Università degli Studi di Ferrara | DE: Department of Engineering Ferrara

Università degli Studi di Ferrara

DOTTORATO DI RICERCA IN
SCIENZE DELL'INGEGNERIA

Ciclo XXXI

Coordinatore: Prof. Stefano Trillo

Advanced modeling of detachment and joints in concrete and wood

Settore Scientifico Disciplinare ICAR/08

Dottorando
Dott. Nicola Orlando

Tutor
Chiar.ma Prof. Elena Benvenuti

Anni 2015/2018

There is no law except the law that there is no law
John Archibald Wheeler

to my family

ABSTRACT

The prediction of the structures failure is one of the most important and yet challenging tasks in civil engineering. Numerical studies are faster and cheaper than experimental studies. For these reasons, numerical models are useful for researchers.

The present work focuses on the Finite Element (FE) simulation of several non-linear 3D engineering problems related to the rehabilitation of concrete and wooden structural elements. In the considered context, the numerical model employed has to be fast, stable and robust to tackle the complexity and the computational burden of the problems to be solved.

The numerical method employed for the simulations is a regularized variant of the eXtendend Finite Element Method (XFEM) proposed by Belytschko and coworkers [1]. The computational model, called REgularized XFEM (3D RE-XFEM), has been developed by Benvenuti [2] in order to study strong and weak discontinuities. Initially, it has been used to study the non-linear evolution of discontinuities in 2D plane-stress problem in concrete [3] and concrete-like [4, 5] materials. Recently, the model has been employed to study linear 3D problems involving planar/curved interfaces [6] and inclusions [7]. Since the previous 2D applications proved the stability and the reliability of the RE-XFEM, in this work, the 3D non-linear formulation (3D RE-XFEM) of the method has been implemented into a parallelized FORTRAN code [8] and successfully applied to several engineering problems.

The thesis collects the results obtained for the modelling of concrete and wooden beams through the 3D RE-XFEM. In particular, the topics covered by this work can be divided into two main parts:

- The first part is devoted to the modelling of the detachment of FRP reinforcements from concrete specimens. Ch. 2 introduces the 3D RE-XFEM approach for concrete and concrete-like materials. Ch. 3 presents the results obtained in the simulation of the detachment process of FRP plates from concrete blocks published in Ref. [9]. Ch. 4 is devoted to

the investigation of FRP reinforced bended beams presented in Refs. [10, 11].

- The second part of the thesis focuses on the simulation of wooden structures. In particular, in Ch. 5 the analyses of end-repaired beams published in Ref. [12] using an orthotropic elasto-damaging model available in literature are discussed. Ch. 6 is devoted to the development of a new unpublished 2D constitutive elasto-damaging plastic model combined with the RE-XFEM for wooden structures.

In the end, Ch. 7 summarizes results and significant aspects achieved in this thesis.

SOMMARIO

La predizione del carico e della modalità di rottura di una struttura è uno degli obiettivi più importanti e impegnativi dell'ingegneria civile. In questo ambito, l'utilizzo di modelli matematici e simulazioni numeriche sta via via assumendo sempre più importanza, visti la maggiore velocità di esecuzione e il minore impatto economico rispetto ai test in laboratorio.

Il lavoro in esame si focalizza sulla simulazione agli Elementi Finiti (FE) di diversi problemi non-lineari nel campo 3D relativi ad interventi di riabilitazione su strutture in calcestruzzo e legno. In questo contesto è necessario che i modelli numerici sviluppati siano veloci, stabili e in grado di descrivere correttamente il comportamento del materiale senza aumentare troppo l'onere computazionale richiesto dalla simulazione.

Per l'esecuzione delle simulazioni è stata usata una variante regolarizzata del metodo *eXtended Finite Element Method (XFEM)* proposto da Belytschko e dai suoi collaboratori [1]. Il modello numerico proposto in questo lavoro, denominato *REgularized XFEM (3D RE-XFEM)*, è stato sviluppato da Benvenuti [2] per lo studio di discontinuità sia di tipo forte che di tipo debole. Inizialmente, il modello è stato utilizzato per l'analisi di problemi piani di tensione relativi al calcestruzzo [3] e a materiali quasi-fragili [4, 5], mentre, recentemente, il modello è stato utilizzato per lo studio in campo lineare di problemi 3D relativi a interfacce planari e curve [6], e ad inclusioni [7]. Dal momento che le precedenti analisi 2D del modello RE-XFEM hanno dimostrato l'affidabilità e la robustezza del sopracitato algoritmo, nel presente lavoro una formulazione 3D non-lineare del modello, denominata 3D RE-XFEM, è stata implamentata in un codice parallelizzato FORTRAN [8] e applicata con successo a diversi problemi ingegneristici.

La tesi raccoglie i risultati ottenuti dalla modellazione di diverse prove su travi in calcestruzzo e legno attraverso il modello 3D RE-XFEM. In particolare, gli argomenti trattati in questo lavoro possono essere divisi principalmente in due parti:

- La prima parte è dedicata alla modellazione del distacco di rinforzi

in FRP da provini in calcastruzzo. Il Cap. 2 introduce la formulazione dell'approccio 3D RE-XFEM nel caso di materiali quasi fragili, quali il calcestruzzo. Nel Cap. 3 vengono presentati i risultati ottenuti dalle simulazione del distacco dei rinforzi in FRP da blocchi di calcestruzzo, pubblicata in Ref. [9]. Il Cap. 4 è invece dedicato all'investigazione di travi rinforzate con FRP soggette a flessione, i cui risultati sono stati pubblicati in Ref. [10, 11].

- La seconda parte della tesi si focalizza sulla simulazione di strutture in legno. In particolare, nel Cap. 5 sono riportate alcune analisi, pubblicate in Ref. [12], effetuate mediante l'uso di un modello di danno ortotropo disponibile in letteratura, relative a travi di legno sottoposte ad un intervento di riabilitazione ad una delle estremità. Il Cap. 6 è dedicato allo sviluppo di un nuovo inedito modello costitutivo 2D che abbina ad un modello ortotropo elasto-plastico-danneggiante alla metodologia RE-XFEM per strutture in legno.

Infine, nel Cap. 7 vengono raccolti e discussi gli aspetti significativi trattati nella tesi.

ACKNOWLEDGMENTS

First of all, I would express my gratitude to my tutor, Prof. Benvenuti, for giving me the opportunity to start my Ph.D. on such an interesting field and for her useful suggestions and patient guidance.

I would like also to acknowledge my thesis reviewers, Prof. Freddi and Prof. Ventura. Thanks for your kind words and your precious suggestions that have been very useful for improving this thesis.

I would thank all my colleagues who shared with me good and bad times, laughs and complaints. In these years, you have been more than just colleagues.

Last but not least, I'm very grateful to all those special people who supported me during this long and intense path. I particularly refer to my family, my girlfriend Alice and all my friends. Let me apologize, my friends, but you are too many to be mentioned one by one. I would like you to know that each contribution, small or big, has been fundamental for me. Every time you made me smile, I have made a step towards my goal. I'm pretty sure that all of this would never have been possible without you.

Thanks.

CONTENTS

1

OUTLINE

The present thesis focuses on a three-dimensional advanced computational methodology aimed at modelling different non-linear 3D engineering problems related to the rehabilitation of concrete and wooden structural elements. The study is organized into two parts. In the first part, the following applications are considered.

- First, the simulation of concrete structures strengthened with plates of Fiber Reinforced Polymer (FRP) is discussed. Single-lap shear tests on FRP-reinforced concrete blocks are often performed to assess the maximum transferable load before the detachment of the FRP plate. On this ground, an effective 3D Regularized eXtended Finite Element Model, called in the following 3D RE-XFEM, has been implemented into a FORTRAN procedure. The introduction of a regularization length and the adoption of a proper mechanical framework lead to an accurate and predictive methodology for smooth simulations of the FRP-detachment process. Moreover, the bending of the FRP plate, the influence of FRP plate width, and the two-way delamination for variable bonding length are assessed.

- Secondly, the 3D RE-XFEM procedure has been also employed to study the detachment of FRP flexural reinforcement from Steel Fiber Reinforced Concrete (SFRC).

  Failure of FRP-strengthened SFRC beams typically occurs after the detachment of the FRP plate and depends on the content of steel fibers. Relevant finite element simulations are few, and, usually, neglect the modelling of the detachment process. On the contrary, the proposed 3D RE-XFEM focuses on the detachment process. In particular, the present

approach takes into account the fiber bridging effect exerted by the steel fibers at the detachment zone, while modelling the detachment through a mechanism-based procedure.

- Thirdly, the case of reinforced-concrete FRP strengthened bended beams has been studied through the proposed 3D RE-XFEM model. In particular, two different experimental campaigns have been modelled. Furthermore, some investigation on the role of thickness and width of the FRP reinforcements has been also carried out.

The second part of the thesis is devoted to the numerical simulation of wooden beams. In particular, the two following issues have been assessed:

- The simulation of end-repaired beams with glued-in rods has been carried out. The numerical analysis has been performed by adopting a 3D orthotropic elasto-damaging model. In collaboration with the Italian Research Council (CNR), the efficacy of different configurations has been investigated.

- A new 2D orthotropic elasto-damaging plastic model combined with the RE-XFEM has been developed in collaboration with the Institute of Structural Analysis of Dresden, Germany. Several tests have been proposed in order to prove the reliability of the proposed model.

The thesis collects the results published in five journal papers, that are:

1. E. Benvenuti, N. Orlando, D. Ferretti, A. Tralli (2016). A new 3D experimentally consistent XFEM to simulate delamination in FRP-reinforced concrete. *Composites Part B: Engineering*. Volume 91. Pages 346-360. (Chapter 3)

2. N. Orlando, E. Benvenuti (2016). Advanced XFEM Simulation of Pull-out and Debonding of Steel Bars and FRP-Reinforcements in Concrete Beams. *American Journal of Engineering and Applied Sciences*. Volume 9, Issue 3. Pages 746-754. (Chapter 4)

3. E. Benvenuti, N. Orlando (2017). Failure of FRP-strengthened SFRC beams through an effective mechanism-based regularized XFEM framework. *Composites Structures*. Volume 172, Pages 345-358. (Chapter 4)

4. E. Benvenuti, N. Orlando (2018). Intermediate flexural detachment in FRP-plated concrete beams through a 3D mechanism-based regularized eXtended Finite Element Method. *Composites Part B: Engineering*, Volume 145, Pages 281-293. (Chapter 5)

5. N. Orlando, Y. Taddia, E. Benvenuti, B. Pizzo, C. Alessandri (2018). End-Repair of timber beams with laterally-loaded glued-in rods: experimental trials and failure prediction through modelling. *Construction and Building materials*. *In press*. (Chapter 6)

The approach and the results contained in Ch. 6.4 are unpublished and are still subject of ongoing research.

2

A COMPUTATIONAL MODEL FOR CONCRETE

The Finite Element non-linear simulation of concrete is a challenging task. Indeed, concrete is a material composed of different coarse aggregate bound together by cement matrix. The material exhibits a very different behaviour under tensile or compressive loading. In particular, the tensile strength, especially with low confining pressures, is very low compared to the compressive strength. Concrete behaviour is very different from homogeneous brittle materials, such as glass and cast iron, where the fracture is attained shortly after the elastic limit is reached.

The microscopic observation showed that in concrete and in concrete-like materials, such as mortar, rocks and ceramics, the fracture is anticipated by the development of a densely distributed micro-crack pattern, the so-called Fracture process Zone (FPZ), that dissipates energy and induces the strain-softening behaviour of the material. The coalescence of the micro-cracks leads to the localization of the strain into a finite band-width in the specimen, estimated to be around three times the size of aggregate with the larger diameter [13], that is usually interpreted as the dominant macro-crack. To highlight the difference with brittle materials where the fracture is obtained immediately after reaching the critical stress, concrete and concrete-like materials are addressed as *quasi-brittle* materials. These materials attain their ultimate strength after developing permanent strains that, while small in absolute terms, are significantly greater than the elastic strains. The permanent deformation is due to several mechanisms, the foremost of which is the opening and closing of cracks.

After an introduction to the state of art about concrete FE computational modelling in Sec. 2.1, this chapter is mainly devoted to the presentation of the non-linear 3D RE-XFEM model adopted in the present work (Sec. 2.2).

A benchmark and an application to a real case study are also proposed in Sec. 2.3

2.1 COMPUTATIONAL MODEL FOR CONCRETE: STATE OF THE ART

During the years, several different techniques have been developed to model the non-linear behaviour of the brittle and quasi-brittle materials, and every model suits in a numerical simulation accordingly to the given problem.

In the following, an overview of the principal constitutive models, with emphasis on fracture models, used for concrete engineering applications is given.

2.1.1 *Continuum Damage Models (CDM)*

In Continuum Damage Mechanics, the progressive deterioration of a loaded concrete specimen is attributed to the formation of micro-cracks, voids and other types of material defects and flaws. The state of deterioration is measured through the damage variable d. In order to model an isotropic damage process is sufficient to consider a scalar damage variable, while tensor damage variables of the second and fourth order are required to account for anisotropic damage [14]. For concrete, an isotropic damage formulation is usually employed.

Let us consider a damaged element characterized by an overall section area $\mathcal{S}$, and let us consider $\widetilde{\mathcal{S}}$ be the effective resisting area purged from the flaws and cavities. By definition, in the case of isotropic damage, the damage variable d is

$$d = \frac{\mathcal{S} - \widetilde{\mathcal{S}}}{\mathcal{S}} \quad . \tag{1}$$

From the mathematical point of view, the damage vanishes as $\widetilde{\mathcal{S}}$ approaches to the value of the section area $\mathcal{S}$(undamaged material), while, if the effective resisting area $\widetilde{\mathcal{S}}$ approaches to $\widetilde{\mathcal{S}} = 0$, the damage value reaches 1 (rupture of the element).

Kachanov [15] pioneered the effective stress concept to take into account the local micro-stress concentration due to the progressive nucleation of micro-cracks.

The effective stress tensor $\widetilde{\sigma}$ is related to the effective resisting area $\widetilde{\mathcal{S}}$ through

$$\widetilde{\sigma} = \sigma \frac{\mathcal{S}}{\widetilde{\mathcal{S}}} = \frac{\sigma}{1-d} \tag{2}$$

Usually, in literature, the degradation of mechanical properties of the concrete is based on the strain equivalence principle, while CDM relying on energy or stress equivalence principle are less diffused.

In the strain equivalence principle, the strain associated with a damaged state under the applied stress is considered equivalent to the strain associated with its undamaged state under the effective stress. This implies that

$$\boldsymbol{\varepsilon} = \boldsymbol{C}\sigma = \boldsymbol{C}^d\widetilde{\sigma} \quad , \tag{3}$$

where $\boldsymbol{C}$ is the compliance matrix of the material and $\boldsymbol{C}^d = (1-d)\boldsymbol{C}$ is the secant compliance matrix. The damage evolution in concrete is obtained defining a softening law $d = g(k)$ and a loading function $f(\boldsymbol{\varepsilon}, k)$ that depends on the strain and the internal state variable k, characterizing the maximum strain level reached in the load history of the material. The loading-unloading conditions in the Kuhn-Tucker form

$$f \leq 0, \quad \dot{k} \geq 0, \quad \dot{k}f = 0 \tag{4}$$

impose that k is never smaller than ε and that k cannot decrease and can grow only if the current values of ε and k are equal to 0.

Due to its simplicity and efficiency, CDM models are largely employed in concrete mechanics [16–21]. As reported in the review proposed by Mazars and Pijaudier-Cabot [22], different model based on continuum damage theory have been proposed for concrete [23].

2.1.2 *Plasticity Model*

Plasticity theories were originally used to model the behaviour of metals. However, many researcher have used plasticity to characterize concrete in different applications [24–34]. Constitutive models formulated within the framework of plasticity theory consists of: (i) a yield function, (ii) a flow rule and

(iii) a hardening/softening law. The inelastic deformations are taken into account by splitting the total strain $\boldsymbol{\varepsilon}$ in the elastic part $\boldsymbol{\varepsilon}^e$ and in the plastic part $\boldsymbol{\varepsilon}^p$

$$\boldsymbol{\varepsilon} = \boldsymbol{\varepsilon}^e + \boldsymbol{\varepsilon}^p \quad , \tag{5}$$

and the stress field is set equal to

$$\boldsymbol{\sigma} = \boldsymbol{D}(\boldsymbol{\varepsilon} - \boldsymbol{\varepsilon}^p) \quad , \tag{6}$$

where $\boldsymbol{D}$ is the stiffness matrix of the Finite Element Method (FEM).

One of the advantages offered by plasticity models is the possibility to include into the formulation pressure and path sensitivity, non-associate flow rule and strain hardening. On the other hand, it is not possible to model the degradation of the material stiffness due to the development of fracture process zones. For this reason, usually, plasticity and damage models are usually coupled. Generally, non-smooth multi-surface plasticity yield functions are employed for quasi-brittle materials [35], then particular iterative algorithms [36] are required for the solution of the problem. The computational burden required by the method is usually high, especially in 3D formulations.

2.1.3 *Discrete crack approach*

Firstly proposed by Ngo and Scordelis [37], the discrete crack approach is particularly suitable for applications that require the study of the propagation of few cracks in the specimen [38–42]. In this model, the crack is forced to propagate along the finite elements boundary by splitting each node crossed by the crack into two nodes. For this reason, according to the crack initiation and the crack propagation criterion employed, a proper remeshing algorithm is required for each iteration of the analysis. If the specimen is characterized by the presence of discontinuities, voids, and inclusions, then the patterns must conform to these geometric entities. The construction of such meshes becomes quite difficult, especially in three-dimensional problems. The difficulty of developing a robust and automatic remeshing algorithm and the computational effort needed for the continuous change in topology are the main disadvantages. In order to overcome these difficulties, usually, the discrete crack approach is employed for modelling the propagation of few main cracks in a structure, while other secondary cracks are modelled with continuous fracture models [43, 44].

2.1.4 *The Extended Finite Element Method (XFEM)*

The Extended Finite Element Method (XFEM) is a powerful and effective tool developed by Belytschko and coworkers (Belytshko and Ventura [1], Moës et al. [45]), that can be successfully used for the solution of problems that involve crack propagation or the evolution of discontinuities in complex geometries.

The principal advantage of this method is that the finite element mesh is independent of the morphology of these entities, as shown in fig. 2.1, then the evolution of crack does not require mesh adaptivity. In general, in the XFEM

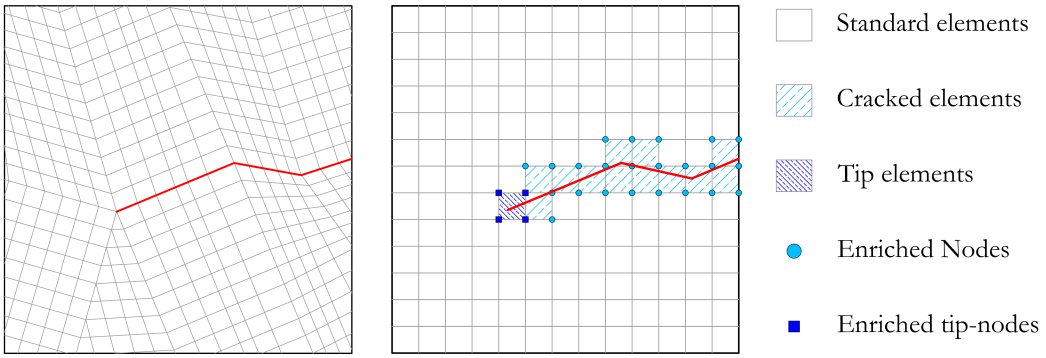

Figure 2.1: Example about the difference of mesh generation between standard FE models (a) and XFEM (b) in problems that involve cracks

the displacement field is approximated by exploiting the concept of Partition of Unity (Melenk and Babuska [46]) to enrich at nodal level the standard FEM solution. A partition of unity is a sets of functions $\phi_I(x)$ such that for each point of the definition domain:

$$\sum_{\forall I} \phi_I(x) = 1 \quad . \tag{7}$$

Standard finite element shape functions satisfy the partition of unity property. Generally, the same functions are used for enrichment and standard finite elements approximations $\phi_I(x) = N_I(x)$. The general formulation of the displacements field using this approach can be written as

$$\boldsymbol{u}(x) = \boldsymbol{u}_{FE} + \boldsymbol{u}_{enr} = \sum_{\forall I} N_I(x) u_I + \sum_{\forall I} N_I(x) \mathcal{H}(x) a_I \quad , \tag{8}$$

where u_I represent the standard nodal degrees values, a_I are unknown parameters that adjust the enrichment so that it best approximates the solution and $\mathcal{H}(x)$ is the heaviside functions defined as

$$\mathcal{H}(d(x)) = \begin{cases} 1\,, & \bar{d}(x) \geq 0 \\ 0\,, & \bar{d}(x) < 0 \end{cases} \quad , \tag{9}$$

where $\bar{d}(x)$ is the distance from the point considered and the discontinuity surface. Numerical integration in XFEM requires special attention. For Heaviside-enriched elements, usually, a sub-triangulation integration scheme is employed, though more efficient integration procedures have been developed [47–49]. The literature is rich in studies on the XFEM methods. Among the others, some applications to concrete structures can be found in the works of Ren et al. [50], Gowleski et al. [51] and Zhang and Bui [52].

2.1.5 *Regularization models*

In each computational model, the stress-strain rule used for the concrete cracking process is characterized by a drop of the stress after the peak stress is reached. As is well known, the use of strain-softening laws leads to an ill-posed boundary value problem [53] and to a pathological non-physical sensitivity of the results to the finite element size of the meshes employed [54]. The mesh-dependency of the results is not acceptable and it must be removed from the numerical model. For engineering applications, the ill-posedness of the problem is usually avoided by adopting a regularization technique. The regularization techniques aim to introduce a characteristic length into the model in order to smear the fracture over a certain domain involving several finite elements. In the following, a brief description of the principal regularization models employed for applications that involve concrete structures is reported.

2.1.5.1 *Cohesive Zone Models (CZM)*

Fictitious crack models or Cohesive Zone Models (CZM), are largely used in problems that involve cracks and discontinuity in concrete structures [55–58].

In cohesive zone models, the complex stress state that arises around the discontinuity edges and near the crack tip, the so-called cohesive zone, is

lumped into a single surface and all the effects are taken into account into the traction-separation law that rules the cohesive interaction across the discontinuity surface. Many different CZM has been developed in order to handle complex problems such as mixed mode crack propagation, scale effects, irreversible deformations and many others. A complete review of these methods can be found in the work proposed by Park and Paulino [59].

2.1.5.2 *Non-local Models*

In non-local models, unlike standard FE codes, the stress at a given quadrature point of the considered finite element does not depend only on the local strain of the point but also on the strain of the surroundings quadrature point. The size of the area where the averaging of the internal variables takes place is a parameter of the model that depends on the material properties and on the specimen geometry. For this reason, this regularization model requires the calibration of the non-local length by inverse analyses. Some example of non-local model use for concrete specimen can be found in [60–62]

2.1.5.3 *Smeared Crack Models*

The main purpose of smeared cracked models is to spread the energy dissipation process of the crack over a localization band of finite width, as firstly proposed in the crack band model by Bazant et al. [63]. The width of the localization band, that is usually smaller than the characteristic size of the finite element mesh, need to be calibrated in order to model the proper amount of dissipated energy in the cracking process. This introduces a characteristic length into the model that depends on the size of the finite element discretization.

The smeared crack models can be classified in fixed crack models and rotating crack models. In the first case, the orientation of the crack is prescribed and is not allowed to change. Since usually, for concrete, the orientation of the crack is typically perpendicular to the principal tensile strain, in rotating crack models, the crack is allowed to propagate accordingly the evolution of the principal strain axis. Smeared crack models often exhibit a so-called mesh alignment sensitivity, as the orientation of the smeared cracks can be dependent on the orientation of the finite element mesh. Some remarkable applica-

tions of smeared crack problems to concrete structures can be found in the works proposed by De Borst and Nauta [64] and Dahlblom and Ottosen [65]

2.1.5.4 *Viscous Models*

The well-posedness of the boundary problem can be restored also introducing a viscosity in the model, even if the introduction is not physically motivated.

In viscous models, the internal length introduced into the formulation in the 1D case is defined by the relationship

$$l = \frac{\eta}{\sqrt{E/d}} \quad , \tag{10}$$

where $\eta\ [kg/(ms)]$ is the viscosity parameter, E is the Young's modulus of the material and $d\ [kg/m^3]$ is the density of the material. The term $c = \sqrt{E/d}$ is usually called propagation velocity. It has been found that the well-posedness of the boundary problem is ensured when the time span of the viscosity t is lower than the critical value $t_0 = l/c$. An example of the application of a viscous model to concrete structures can be found in the work by Faria et al. [66].

2.2 THE REGULARIZED EXTENDEND FINITE ELEMENT METHOD (3D REXFEM)

As assessed by the presence of several computational models, the FE simulation of the non-linear behaviour of concrete-like materials in the presence of strong and weak discontinuities inside the specimen is difficult.

The goal of this work is to develop a computational method able to predict and model in a reliable way the failure mechanisms observed in real application problems.

Here, the regularized variant proposed by Benvenuti and co-workers [2, 67] of the XFEM approach presented in Sec. 2.1.4 is adopted. The method has been employed to study different two-dimensional linear and non-linear problems in quasi-brittle material [3–5]. Some examples on three-dimensional linear problems that involve planar, cylindrical and spherical inclusions have been also presented [6, 7, 68]. Based on the research lines pursued by Benvenuti and co-workers, a 3D non-linear Regularized XFEM formulation has been developed in order to study some engineering problems in concrete. In

the following, an overview of the formulation of the 3D procedure is given. Let us focus the attention on the three-dimensional body Ω shown in Fig. 2.2a characterized by smooth external boundaries $\bar{u}$, a load distribution $\bar{p}$ in Ω_p and an internal plane joint $\partial\Omega_d$ parallel to the plane xy. Between the two

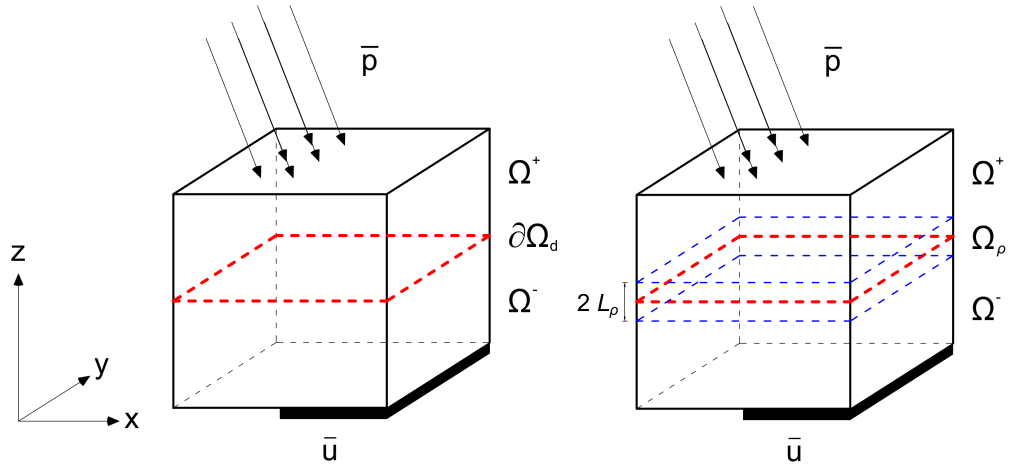

Figure 2.2: Specimen characterized by a surface discontinuity $\partial\Omega_d$ that split the body

disjointed zones denominated Ω^+ and Ω^-accordingly to its position, the displacement $\boldsymbol{u}(x)$ displays a jump $[[\boldsymbol{u}]](x)$

$$[[\boldsymbol{u}]](x) = \begin{cases} (\boldsymbol{u}^+(x) - \boldsymbol{u}^-(x)) \,, & x \in \partial\Omega_d \\ 0 \quad otherwise \end{cases} \quad . \tag{11}$$

where $\boldsymbol{u}^+$ and $\boldsymbol{u}^-$ denote the displacement on the zone Ω^+ and Ω^-, respectively. The displacement field in the body can be expressed as

$$\boldsymbol{u}(x) = \boldsymbol{v}(x) + [[\boldsymbol{u}]]x \quad . \tag{12}$$

Let us introduce the scalar signed distance function $\bar{d}(x)$ of the generic position x defined as

$$\bar{d}(x) = \begin{cases} |\bar{x} - x| \,, & (\bar{x} - x)\, \boldsymbol{n}(x) \geq 0 \\ -|\bar{x} - x| \,, & (\bar{x} - x)\, \boldsymbol{n}(x) < 0 \end{cases} \quad , \tag{13}$$

where $\bar{x}$ is the projection of x in the surface Ω_d and $\boldsymbol{n}$ is the normal vector of the discontinuity surface. In this way the crack surface is defined by $\bar{d}(x) = 0$, i.e. a level set [69]. That allows to treat discontinuities such as cracks without any supplementary data other than at nodal points. As introduce in Eq. 8, in standard XFEM the displacement field of the specimen in Fig. 2.2a can be expressed using the Heaviside function $\mathcal{H}(x)$ as

$$\boldsymbol{u}(x) = \boldsymbol{u}_{FE} + \boldsymbol{u}_{enrichment} = \boldsymbol{v}(x) + \mathcal{H}(x)\ \boldsymbol{a}(x) \quad . \tag{14}$$

In the 3D Regularized eXtended Finite Element method proposed in this work, the discontinuity $\partial\Omega_d$ (Fig. 2.2a) is replaced by the regularized volume Ω_ρ having finite thickness $2L_\rho$ (Fig. 2.2b), where ρ is the regularization length.

The introduction of an internal length leads to restore the well-posedness of the boundary problems and avoid the pathological mesh-dependency of the problems. In the proposed method, the introduction of the regularized volume is also aimed to model physically the development of fracture process zone, that it is particularly suitable for problems in quasi-brittle-materials.

Unlike standard XFEM model where the displacement jump is governed by the Heaviside functions, in the volume Ω_ρ the continuous regularized Heaviside functions $\mathcal{H}_\rho$

$$\mathcal{H}_\rho(x) = \frac{1}{\rho}\int_0^{d(x)} e^{-\frac{|\xi|}{\rho}}\, d\xi = sign(\bar{d}(x))(1 - e^{-\frac{|\bar{d}(x)|}{\rho}}) \tag{15}$$

is used to rule the displacement jumps inside the regularization volume. The Euclidean norm of the gradient of $\mathcal{H}_\rho$ is

$$\|\nabla\mathcal{H}_\rho\| = \gamma_\rho \quad . \tag{16}$$

The function γ_ρ can be interpreted as the micro-crack density function in the regularized volume Ω_ρ. Following the experimental observation carried out by Mihashi and Nomura [70] and Otsuka and Date [71], the function

$$\gamma_\rho(x) = \frac{1}{\rho} e^{\frac{-|\bar{d}(x)|}{\rho}} \tag{17}$$

has been chosen. Fig. 2.3a and Fig.2.3b show the regularized Heaviside function $\mathcal{H}_\rho$ and its derivative γ_ρ for three different values of the regularized parameter ρ, respectively.

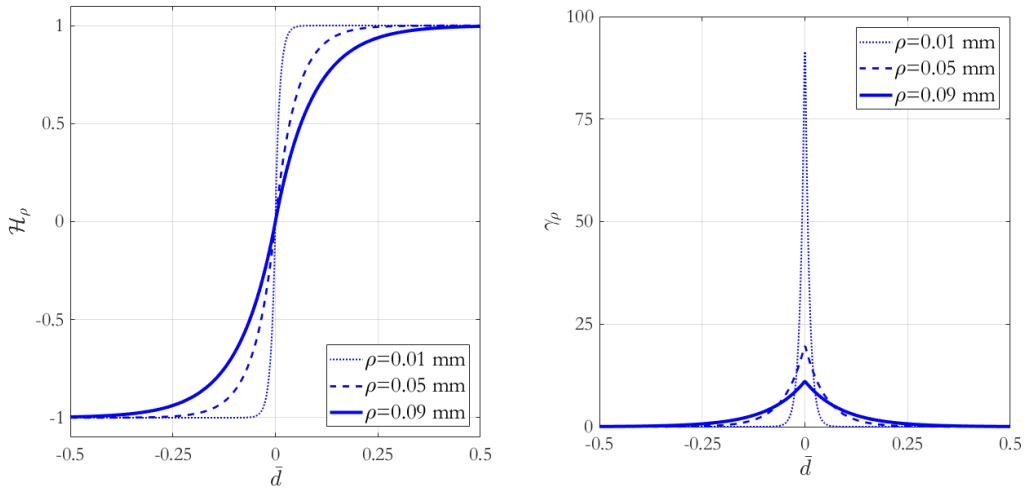

(a) (b)

Figure 2.3: One-dimentional rappresentation of function $\mathcal{H}_\rho$ (a) and γ_ρ for $\rho = 0.09$ (continuos line), $\rho = 0.05$ (dashed line) and $\rho = 0.01$ (dotted line)

Since the regularized Heaviside function $\mathcal{H}_\rho$ and its derivative γ_ρ do not have a compact support, a truncated support $c_\rho = 40\rho$ is obtained by neglecting the contribution of points whose distance $\bar{d}$ is larger than 20ρ. In particular, two cases can occur:

- if the size of the finite element h_e is larger than the truncated support c_ρ, then a sub-elemental enrichment is carried out, which leads to a *thin process zones*, Fig. 2.4a

- if the size of the finite element h_e is smaller than the truncated support c_ρ, then a sub-elemental enrichment is carried out, which leads to a *thick process zone*, Fig. 2.4b

2.2.1 *Incremental finite element formulation*

Let us consider the three-dimensional domain Ω discretized in finite elements connected at $\mathcal{M}$ nodes to be subjected to a loading history $t = [0, T]$ formed by

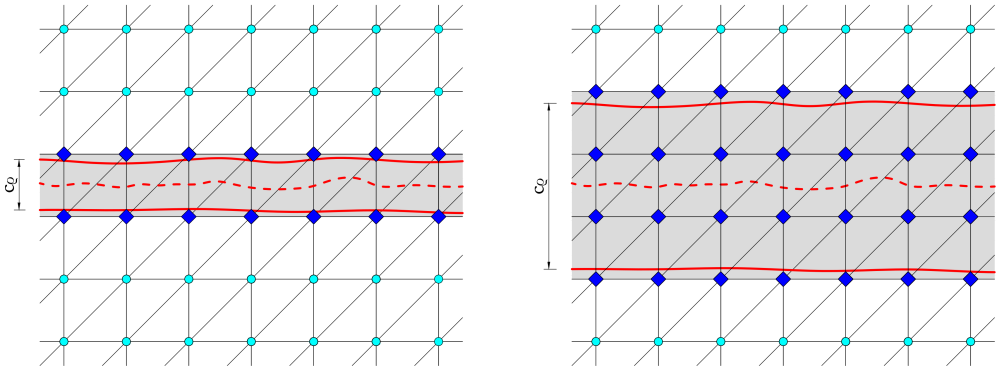

(a) (b)

Figure 2.4: Diferences between thin (a) and thick (b) process zone

$\mathcal{N}$ non-overlapping time intervals. At the instant t_n, the solution of the equilibrium problem is $(\boldsymbol{v}_n, \boldsymbol{a}_n)$. After the increment $\Delta\boldsymbol{p}$ in the interval $[t_n, t_{n+1}]$ the update solution $(\boldsymbol{v}_{n+1}, \boldsymbol{a}_{n+1})$ has to be calculated. The field $\boldsymbol{v}_{n+1}$ is approximated over the set of the $\mathcal{M}$ nodal values v_I, while the displacement jump field $\boldsymbol{a}_{n+1}$ is approximated over the set of the $\mathcal{M}^{enr} \subset \mathcal{M}$ enriched nodal values v_J. The same first order polynomial shape function $\boldsymbol{N}$ is employed for the two fields. According to Eq. 14, the displacement is determined as

$$\boldsymbol{u}_{n+1} = \boldsymbol{N}\boldsymbol{v}_{n+1} + H_\rho \boldsymbol{N}\boldsymbol{a}_{n+1} \quad , \tag{18}$$

where the vectors $\boldsymbol{v}_{n+1} = \{\boldsymbol{v}_1, \ldots, \boldsymbol{v}_\mathcal{M}\}$ and $\boldsymbol{a}_{n+1} = \{\boldsymbol{a}_1, \ldots, \boldsymbol{a}^{enr}_\mathcal{M}\}$ collect the nodal values at the instant t_{n+1}. The compatible strain field is defined as

$$\boldsymbol{\varepsilon}_{\rho_{n+1}} = \boldsymbol{\varepsilon}^a_{n+1} + \boldsymbol{\varepsilon}^b_{\rho,n+1} + \boldsymbol{\varepsilon}^c_{\rho,n+1} \tag{19a}$$

$$\boldsymbol{\varepsilon}^a_{n+1} = \boldsymbol{B}\boldsymbol{v}_{n+1} \tag{19b}$$

$$\boldsymbol{\varepsilon}^b_{\rho,n+1} = H_\rho \boldsymbol{B}\boldsymbol{a}_{n+1} \tag{19c}$$

$$\boldsymbol{\varepsilon}^c_{\rho,n+1} = \gamma_\rho \bar{\boldsymbol{N}}\boldsymbol{a}_{n+1} \quad , \tag{19d}$$

where $\boldsymbol{B} = \nabla\boldsymbol{N}$ is the compatibility operator and the matrix $\bar{\boldsymbol{N}}$ is expressed as

$$\bar{\boldsymbol{N}}\boldsymbol{a}^{n+1} \approx \boldsymbol{N}\boldsymbol{a}^{n+1} \otimes \boldsymbol{n}_l \quad , \tag{20}$$

$\boldsymbol{n}_l$ being the local vector defined based on the mechanism-based levelset explained in the Sec. 2.2.2. Each term of the equation can be seen as the expression of a different mechanical aspect. The strain $\boldsymbol{\varepsilon}^a_{n+1}$ is the same that we can obtain on a body in absence of discontinuity. The second term $\boldsymbol{\varepsilon}_{\rho^b,n+1}$ is due to the jump $\boldsymbol{a}_{n+1}$ and it is defined of the entire solid. The contribution $\boldsymbol{\varepsilon}_{\rho^c,n+1}$, that represents the strain localized over the regularization volume Ω_ρ, is proportional to the function γ_ρ and is different to zero only inside the regularized volume.

2.2.2 *A mechanism-based local level set*

As aforementioned, in concrete-like material, a discontinuity is the result of the coalescence of several micro-crack that take place in a volume of finite width called fracture process zone [54]. The micro-cracks orientation is assumed to be orthogonal to the local maximum principal stress direction $\boldsymbol{n}_l$, as shown in Fig. 2.5 for different load schemes. Besides being corroborated by the experiments, these hypotheses are usual in two-dimensional FE analysis and in numerical models based on one-dimensional bond-stress laws [72, 73].

In the present study, a level set system is adopted, called "global-local level set" system. The "global-local level set" procedure adopts a *global* level set function denoting the surface of the main crack, and a *local* level set system at each Gauss point within the regularized volume V_ρ defined through the vectors orthogonal to the micro-cracks. In order to alleviate the computational burden of the simulation, the field of normal vectors $\boldsymbol{n}_l$ are imposed at the Gauss points accordingly to the expected micro-cracking behaviour. Noteworthy, the solution of the non-linear iterative-incremental procedure will then decide the final directions of the principal stresses, that do not generally coincide with those of $\boldsymbol{n}_l$.

2.2.3 *Constitutive laws and continuous-discontinuous transition*

The 3D RE-XFEM is integrated within an isotropic CDM.

The bulk is made of an isotropic elastic material with constitutive matrix $\boldsymbol{D}$. Two isotropic damage variables, d_{n+1} and d^c_{n+1}, are introduced. The damage d_{n+1} pertains to the bulk material, while d^c_{n+1} is associated to the regularized displacement jump. As usual, the values of the damage variables range from

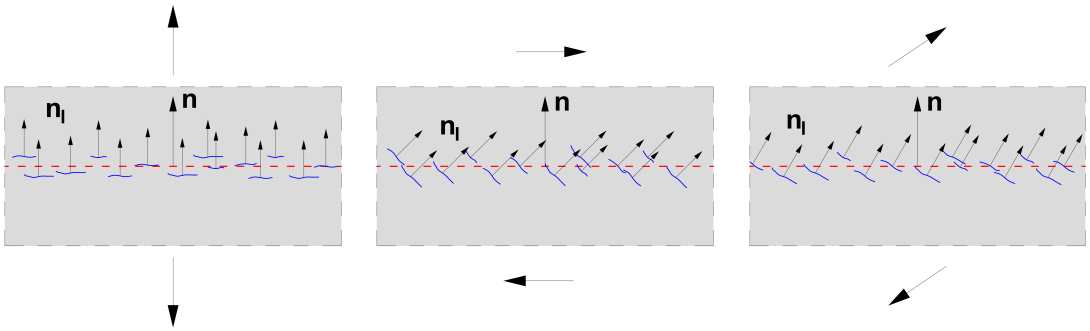

Figure 2.5: Qualitative representation of the FPZ in quasi-brittle materials in a horizontal crack caused by different 2D load schemes: a) mode I, b) mode II and c) mixed mode

0 for sound material up to 1 for completely damaged material. The stress field associated with the bounded part of the strain $\boldsymbol{\varepsilon}^a_{n+1}$ and $\boldsymbol{\varepsilon}^b_{\rho,n+1}$ in the enriched finite elements is governed by the elasto-damaging constitutive law

$$\boldsymbol{\sigma}_{n+1} = (1 - d_{n+1})\boldsymbol{DBv}_{n+1} + (1 - d_{n+1})\boldsymbol{DBH}_\rho \boldsymbol{a}_{n+1} \quad , \tag{21}$$

while the elasto-damaging law

$$\boldsymbol{t}_{n+1} = (1 - d^c_{n+1})\boldsymbol{D}(\bar{\boldsymbol{n}}_l \otimes \boldsymbol{a}_{n+1}) \tag{22}$$

defines the stress related to the localized strain $\boldsymbol{\varepsilon}^c_{\rho,n+1}$. The evolution of the damage variables during the continuous-discontinuous transition has been treated in details in Refs. [4, 5].

Essentially, during the load process, in each finite element of the mesh two regimes can occur:

- In the *continuous regime*, the concrete-like material is modelled through an elasto-damaging constitutive law and the regularized discontinuity description is not activated. In this regime, the material non-linear behaviour is ruled by the damage variable d;
- In the *regularized discontinuous regime*, the local damage d has reached at least in one of the quadrature point the critical threshold d_{cr} and then the regularized discontinuity has been activated. In this regime, the

evolution of the damage d is stopped, while the damage that pertains to the regularized jumps d^c starts to evolve from d_{cr} to 1

It has been proved [5, 74] that this procedure ensures a smooth transition from the CDM model to the 3D RE-XFEM. The simplest damage criterion has been chosen for the material, which is the Galileo-Rankine criterion, often used for brittle and quasi-brittle materials. For a stepwise monotonic damage evolution, the damage variable at the current instant t_{n+1} in the continuous regime is cast as non-decreasing function of the current damage threshold r_{n+1} by means of the loading-unloading conditions [75]

$$\varphi_{n+1} = \tau_{n+1} - r_{n+1} = 0, \quad \Delta d_{n+1} \geq 0, \quad \varphi_{n+1} \Delta d_{n+1} = 0 \quad , \tag{23}$$

where τ_{n+1} is the equivalent stress defined as $\langle \bar{\sigma} \rangle_{n+1}$. The operator $\langle\rangle$ selects the positive value of the maximum principal stress $\bar{\sigma}_1$ associated with the effective stress $\bar{\boldsymbol{\sigma}}_{n+1} = \boldsymbol{DBv}_{n+1}$. Noteworthy, no damage in compression develops with the damage law adopted. At the current instant t_{n+1}, the damage variable d_{n+1} is updated by means the exponential damage law

$$d_{n+1} = \begin{cases} d_n & \phi_{n+1} \leq 0 \\ 1 - \dfrac{r_0}{\tau_{n+1}} exp\left\{ -2H_s \dfrac{\tau_{n+1} - r_0}{r_0} \right\} & \phi_{n+1} > 0 \end{cases} \quad , \tag{24}$$

where H_s is the softening module and r_0 is take equal to the tensile strength of the material. A qualitative representation of the damage law for different value of the softening module is shown in Fig. 2.6.

According to the continuous-discontinuous transition, the damage d_{n+1} rages from 0 to the threshold value d_{cr}. Once the damage reaches the critical threshold at least in one of the quadrature points, the regularized discontinuity is activated in that element. In the regularized discontinuous regime, the damage evolution of d is frozen and the bulk can only elastically unload, while the damage d^c in the regularized volume is governed in a similar way by the loading function

$$\varphi^c_{n+1} = \tau^c_{n+1} - r^c_{n+1} = 0, \quad \Delta d^c_{n+1} \geq 0, \quad \varphi^c_{n+1} \Delta d^c_{n+1} = 0 \quad , \tag{25}$$

where the equivalent stress τ^c_{n+1} is defined as $\langle \bar{\boldsymbol{t}} \rangle_{n+1}$. The effective stress is defined $\bar{\boldsymbol{t}}_{n+1} = \boldsymbol{D}\bar{\boldsymbol{N}}\boldsymbol{a}_{n+1}$ in the case of sub-elemental enrichment and as $\bar{\boldsymbol{t}}^{n+1} = \gamma_\rho \boldsymbol{D}\bar{\boldsymbol{N}}\boldsymbol{a}^{n+1}$ in the case of super-elemental enrichment.

$$d^c_{n+1} = \begin{cases} d^c_n & \varphi^c_{n+1} \leq 0 \\ 1 - \dfrac{r^c_0}{\tau^c_{n+1}} exp\left\{ -2H_s \dfrac{\tau^c_{n+1} - r^c_0}{r^c_0} \right\} & \varphi^c_{n+1} > 0 \end{cases} , \tag{26}$$

where r^c_0 is equal to the tensile strength $f_{t,c}$ of the material.

The damage value d^c_{n+1} range from the value d_{cr} to the maximum value 1 that is associate to the complete damaged material.

$$d^c_{n+1} = \max\{d_{cr}, d^c_{n+1}\} . \tag{27}$$

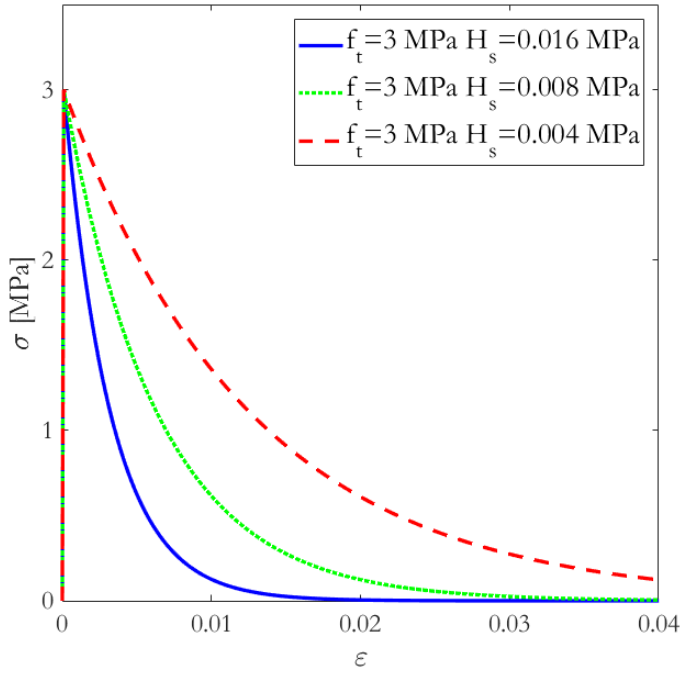

Figure 2.6: Stress-strain damage law adopted for the material in the one-dimensional case for $H_s = 0.016$ MPa (blu continuous line), $H_s = 0.008$ MPa (green pointed line) and $H_s = 0.004$ MPa (red dashed line)

2.2.4 *Variational Formulation*

The discrete form of the virtual power principle is:

$$\int_{\Omega}(1-d_{n+1})\boldsymbol{D}(\boldsymbol{B}\boldsymbol{v}_{n+1}+\mathcal{H}_{\rho}\boldsymbol{B}\boldsymbol{a}_{n+1})^{t}(\boldsymbol{B}\boldsymbol{v}_{n+1}+\mathcal{H}_{\rho}\boldsymbol{B}\boldsymbol{a}_{n+1})d\Omega+$$
$$\int_{\Omega_{\rho}}\gamma_{\rho}(1-d^{c}_{n+1})\boldsymbol{a}^{t}_{n+1}\bar{\boldsymbol{N}}^{t}\cdot\boldsymbol{D}\bar{\boldsymbol{N}}\boldsymbol{a}_{n+1}d\Omega=$$
$$=\int_{\partial\Omega_{d}}\boldsymbol{p}_{n+1}\cdot\boldsymbol{N}\boldsymbol{v}_{n+1}\quad,\quad(28)$$

holds for any $\boldsymbol{v}_{n+1}$ and $\boldsymbol{a}_{n+1}$. The problem of finding $\boldsymbol{v}_{n+1}$ and $\boldsymbol{a}_{n+1}$ such that:

$$\boldsymbol{L}_{v}=\int_{\Omega}\boldsymbol{B}^{t}D\boldsymbol{B}\boldsymbol{v}_{n+1}+\boldsymbol{B}^{t}D\boldsymbol{B}H_{\rho}\boldsymbol{a}_{n+1}d\Omega-\int_{\Omega}\boldsymbol{N}^{t}\boldsymbol{p}_{n+1}d\Omega=0\quad,\qquad(29)$$

$$\boldsymbol{L}_{j}=\int_{\Omega}H_{\rho}\boldsymbol{B}^{t}D\boldsymbol{B}\boldsymbol{v}_{n+1}+{H_{\rho}}^{2}\boldsymbol{B}^{t}D\boldsymbol{B}\boldsymbol{a}_{n+1}d\Omega+$$
$$\int_{\Omega_{\rho}}\gamma_{\rho}\bar{\boldsymbol{N}}^{t}D^{c}\bar{\boldsymbol{N}}^{t}\boldsymbol{a}_{n+1}d\Omega=0\quad.\quad(30)$$

At the equilibrium iteration i within the load step t_{n+1}, the variables are written in the iterative form $\boldsymbol{v}^{i}_{n}=\boldsymbol{v}^{i-1}_{n}+\delta\boldsymbol{v}^{i}_{n}$, $\boldsymbol{a}^{i}_{n}=\boldsymbol{a}^{i-1}_{n}+\delta\boldsymbol{a}^{i}_{n}$ where $\delta\boldsymbol{a}^{i}_{n}$ and $\delta\boldsymbol{a}^{i}_{n}$ are calculated by solving:

$$\boldsymbol{K}\,\boldsymbol{u}_{n+1}=\boldsymbol{p}_{n+1}\quad.\qquad(31)$$

The solving system can be defined as:

$$\left[\int_{\Omega}\boldsymbol{B}^{t}\boldsymbol{D}\boldsymbol{B}d\Omega\right][\boldsymbol{u}_{n+1}]=\left[\int_{\Omega}\boldsymbol{N}^{t}\boldsymbol{p}_{n+1}d\Omega\right]\quad.\qquad(32)$$

To calculate the stiffness matrix when the regularized discontinuity is activated, we can refer to the work of Benvenuti at al. in [6] and [4], where it is proved that:

$$\boldsymbol{K}=\boldsymbol{K}_{\Omega}+\boldsymbol{K}_{\Omega_{\rho}}\quad.\qquad(33)$$

In particular, we can cast the solving system in the next matrix form:

$$\begin{bmatrix}\int_{\Omega}\boldsymbol{K}_{VV}d\Omega & \int_{\Omega}\boldsymbol{K}_{VA}d\Omega\\ \int_{\Omega}\boldsymbol{K}_{AV}d\Omega & \int_{\Omega}\boldsymbol{K}_{AA}d\Omega\end{bmatrix}_{n+1}\begin{bmatrix}\boldsymbol{v}\\ \boldsymbol{a}\end{bmatrix}_{n+1}=\begin{bmatrix}\int_{\Omega}\boldsymbol{N}^{t}\boldsymbol{p}_{n+1}\,d\Omega\\ 0\end{bmatrix}\quad.\qquad(34)$$

2.2.5 *Non-linear solver*

The non-linear problem is solved thanks to the adoption of a arc-length algorithm [76, 77]. The arc-length algorithm is a continuous methods that allows the definition of the equilibrium path of a structure passing limit point. In general, we can express the equilibrium equations as

$$\boldsymbol{g}(\boldsymbol{u}, \lambda) = \boldsymbol{q}_i(\boldsymbol{u}) - \lambda \boldsymbol{p}_{ef} = 0 \quad , \tag{35}$$

where $\boldsymbol{q}_i$ is the internal forces, $\boldsymbol{p}_{ef}$ is the fixed external load and λ is the scalar load multiplier of the vector $\boldsymbol{q}_{ef}$. For this work, the load-level parameter λ is kept fixed and equal to a constant.

Several forms of arc-length methods were developed, all aimed at finding the intersection of equilibrium in Eq. 35 and the arc-length defined as

$$s = \int ds = const \quad , \tag{36}$$

where

$$ds = \sqrt{d\boldsymbol{u}^t d\boldsymbol{u} + d\lambda^2 \psi^2 \boldsymbol{p}_{ef}{}^t \boldsymbol{p}_{ef}} \quad . \tag{37}$$

It has been proved that the scaling parameter ψ has a little effect in practical problems. For this reason, it has been taken equal to zero.

The intersection between the equilibrium path and the arc-length of equation require the solution of the non-linear system defined by

$$\boldsymbol{g}(s) = \boldsymbol{q}_i(\boldsymbol{u}(s)) - \lambda(s) \boldsymbol{p}_{ef} = 0 \quad . \tag{38}$$

A predictor-corrector scheme is used [36]. This is realized by a tangential predictor that replaces the differential form of Eq. 37 with

$$a = (\Delta \boldsymbol{u}^t \Delta \boldsymbol{u} + \Delta\lambda^2 \psi^2 \boldsymbol{p}_{ef}{}^t \boldsymbol{p}_{ef}) - \Delta l = 0 \quad , \tag{39}$$

where Δl is an approximation of the incremental arc-length.

The main feature of the arc-length algorithms is that the load parameter λ becomes a variable of the system. Then, the solving system counts a total of $n + 1$ variables, with n displacements variables and one constraint (Eq. 39).

The $n+1$ equation can be solved by applying the classic Newthon-Raphson method and introducing by a truncated Taylor series:

$$\boldsymbol{g}_n = \boldsymbol{g}_o + \frac{\partial \boldsymbol{g}}{\partial \boldsymbol{u}}\delta\boldsymbol{u} + \frac{\partial \boldsymbol{g}}{\partial \lambda}\delta\lambda = \boldsymbol{g}_o + \boldsymbol{K}_t\delta\boldsymbol{u} - \boldsymbol{p}_{ef}\delta\lambda \quad , \tag{40a}$$

$$a_n = a_o + 2\Delta\boldsymbol{u}^t\delta\boldsymbol{u} + 2\Delta\lambda\delta\lambda\psi^2{\boldsymbol{p}_{ef}}^t\boldsymbol{p}_{ef} = 0 \quad . \tag{40b}$$

Combining the two equations and imposing a_n and $\boldsymbol{g}_n$ equal to zero, $\delta\lambda$ and $\delta\boldsymbol{u}$ can be calculated as

$$\begin{bmatrix}\delta\boldsymbol{u}\\ \delta\lambda\end{bmatrix} = \begin{bmatrix}\boldsymbol{K}_t & -\boldsymbol{p}_{ef}\\ 2\Delta\boldsymbol{u}^t & 2\Delta\lambda\psi^2{\boldsymbol{p}_{ef}}^t\boldsymbol{p}_{ef}\end{bmatrix}^{-1}\begin{bmatrix}\boldsymbol{g}_o\\ a_o\end{bmatrix} \quad , \tag{41}$$

where the matrix is called *augmented stiffness matrix*.

2.2.6 *Linearised Arc-length*

A simple and stable variant of the arc-length can be obtained by the linearisation of Eq. 40b

$$\Delta{\boldsymbol{u}_0}^t\delta\boldsymbol{u} + \delta\lambda(\Delta\lambda_0\psi^2{\boldsymbol{p}_{ef}}^t\boldsymbol{p}_{ef}) = -a_0/2 \quad . \tag{42}$$

Imposing a_0 equal to zero, we obtain that the linearised arc-length is orthogonal to the tangent at the equilibrium path in the point $(\boldsymbol{u}_0, \lambda_0\boldsymbol{p}_{ef})$.

Rearranging the equation of linearised arc-length, we have

$$\delta\lambda(\Delta\boldsymbol{u}_0, \Delta\lambda_0) = \frac{-(a_0/2) - \Delta{\boldsymbol{u}_0}^t\delta\bar{\boldsymbol{u}}}{\Delta{\boldsymbol{u}_0}^t\delta\boldsymbol{u}_t + \Delta\lambda_0\psi^2{\boldsymbol{p}_{ef}}^t\boldsymbol{p}_{ef}} \quad . \tag{43}$$

Despite this linearised version of the arc-length solver is simpler than other algorithms, such as spherical/cylindrical arc-lengths, it has been found that the method is very effective for the simulations carried out in the present contribution.

The final form of the linearised arc-length can be deduced by imposing a vanishing value of the parameter a_0 and ψ

$$\delta\lambda(\Delta\boldsymbol{u}_0, \Delta\lambda_0) = -\frac{\Delta{\boldsymbol{u}_0}^t\delta\bar{\boldsymbol{u}}}{\Delta{\boldsymbol{u}_0}^t\delta\boldsymbol{u}_t} \quad . \tag{44}$$

In order to reduce the issues related to the convergence of the iterative procedure, the non-linear solver algorithm in Eq. 44 is applied to some degrees of freedom of few nodes of the finite element mesh modelled, named *control nodes*, chosen by the user. In this case, we used a *selective* arc-length method. A proper choice of the control nodes for each case study is required to improve for the stability of the non-linear procedure. In general, the degrees of freedom that experience a monotonic behaviour are chosen as control nodes.

2.2.7 *3D non-linear code*

The 3D RE-XFEM model has been implemented into a parallelized FORTRAN code [8]. The flow chart of the final version of the program is reported in Fig. 2.7.

At the beginning, a 3D linear FORTRAN code working with an adaptive quadrature was available [6, 7]. Thence, in order to solve the non-linear problem accordingly to the 3D RE-XFEM presented, several modifications of the initial code and a new non-linear iterative procedure were needed.

The final code is able to perform analysis with tetrahedral and hexahedral finite elements. In order to perform the analysis, the Intel FORTRAN XE Composer numerical library [78] has been used in order to improve dramatically the performance of the code. In particular, to invert the matrix in Eq. 41, the Direct Sparse Solver (DSS) routine of the aforementioned library has been used. This routine, that it is specific for the symmetric sparse matrix, required the definition of the stiffness matrix in a compact form called Compress Sparse Row (CSR) format. In the end, the program has been compiled by means the *ifort* compiler, provided with the Intel's library, in order to optimize the code. The pre-processing modeling of the specimen and the post-process of the results of the simulation are managed by means the free-ware program *GMSH* [79].

2.3 BENCHMARKS AND APPLICATION

In order to test the reliability of the 3D non-linear code, several benchmarks have been carried out. The case of a double notched strip shown subjected to a tensile test is considered.

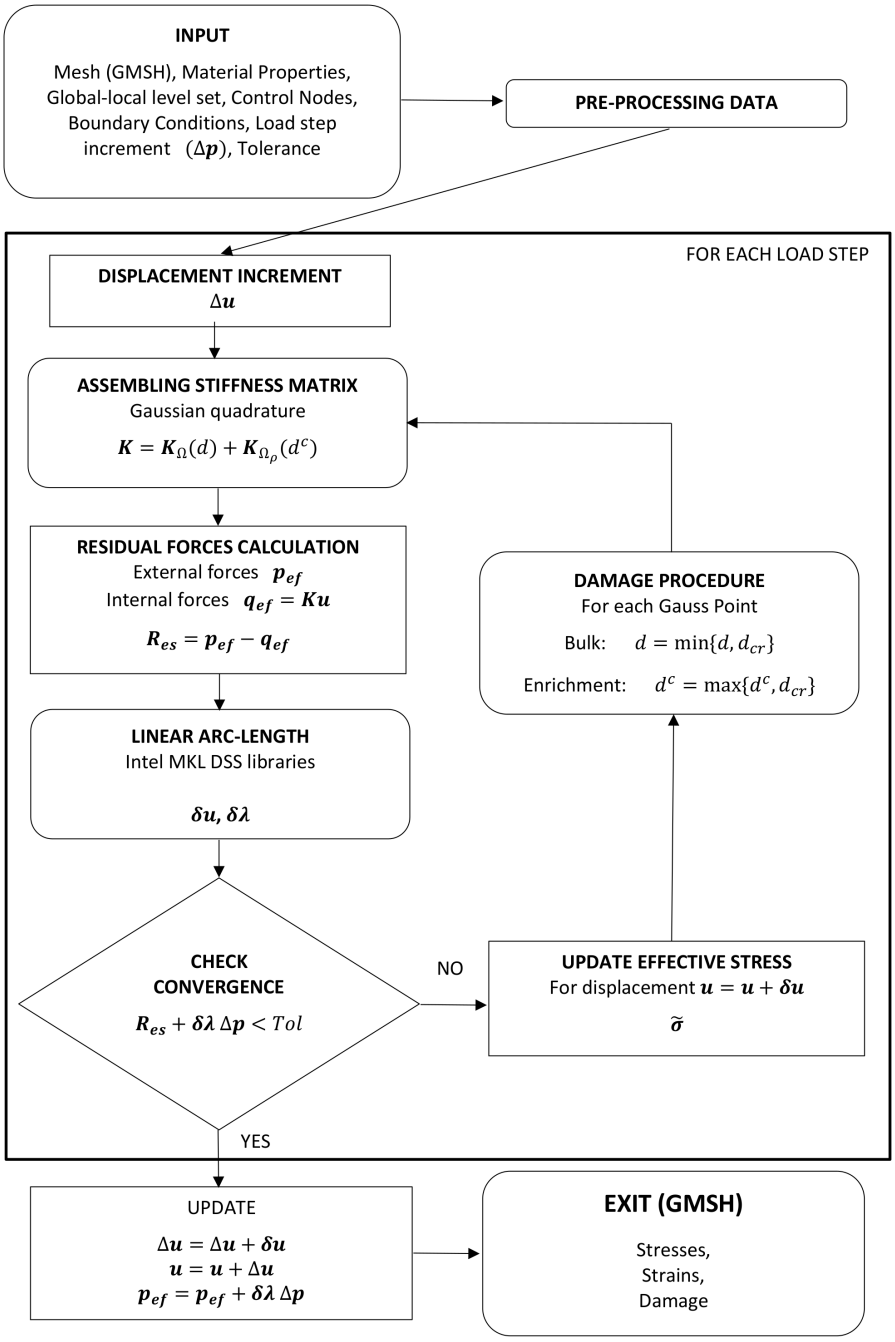

Figure 2.7: Flow chart of the 3D non-linear FORTRAN code implemented

2.3.1 *The Rectangular doubly notched strip*

The case of the notched rectangular strip subjected to a tensile originally proposed by Cervera et al. [75] has been considered for the validation of the 3D procedure. Indeed, the problem has been already studied by Benvenuti and Tralli [5] with the 2D RE-XFEM, and the results have been validated by means the commercial code TNO- Diana. The strip, shown in fig. 2.8, have length $l = 200$ mm, width $b = 100$ mm and thickness $t = 10$ mm. The notches at the middle of the long side are $d = 6$ mm deep and width $w = 3$ mm. The strip is clamped at the bottom and it is subject to an imposed displacement at the top. The same material parameters used in the reference [5] in the

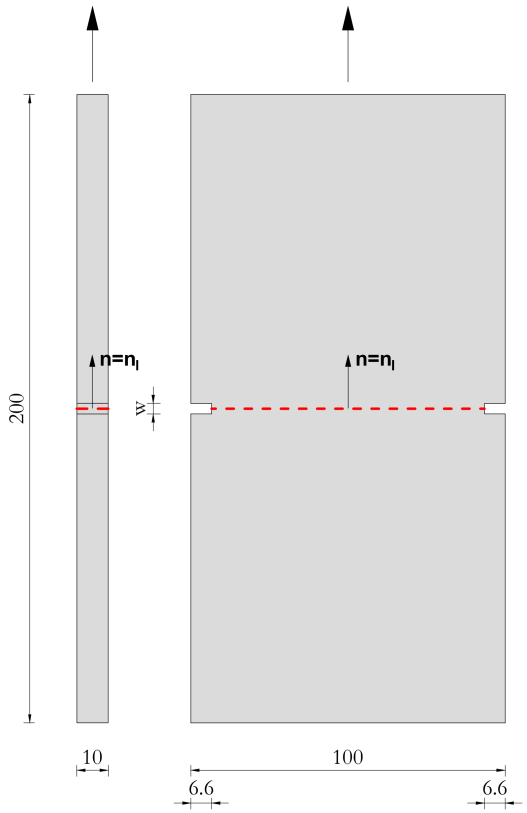

Figure 2.8: Tensile Test: Geometry of the specimen

2D plane-stress simulation has been used. The material is characterised by a Young's modulus $E = 2000$ MPa, a vanishing Poisson's coefficient, a tensile

strength $f_t = 1$ MPa and a softening modulus $H_s = 0.002$ MPa. According to the reference, the critical threshold d_{cr} for the continuous-discontinuous transition has been set to $d_{cr} = 0.001$. A mesh with 12186 tetrahedral finite element with minimum mesh-size of $h_e = 3.3$ mm has been used. The regularization parameter was set equal to $\rho = 0.0825$ mm in order to obtain that the localization band is restricted to a single layer of finite elements. The simulation of the strip, consisting in 10248 dofs, almost require 36 minutes. The computed load vs displacement response is reported in Fig. 2.9. The results

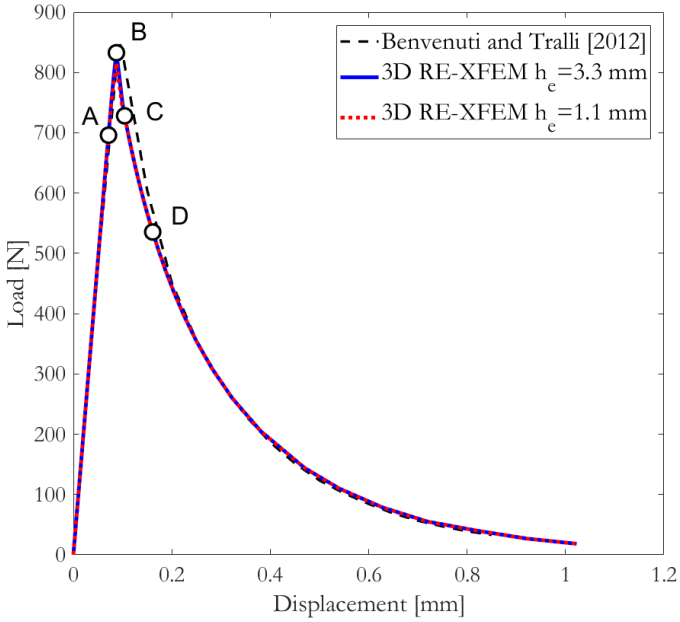

Figure 2.9: Tesile Test: Comparison of the load vs displacement response between the 2D plane-stress analysis carried out by Benvenuti and Tralli [5] (black dashed line) and the solution with the proposed 3D RE-XFEM employing a coarse mesh (blue continuous line) and a fine mesh (red dashed line)

of the simulation are in perfect agreement with the analysis carried out by Benvenuti and Tralli [5]. The strip exhibits a linear elastic behaviour until the peak reached a load $P = 832$ N, and then it shows a clear softening behaviour in the post-critic branch. The contour plots of the damage on the regularized discontinuity d^c for four different steps of the response of the specimen have been reported in Fig. 2.10. The step chosen has been highlighted in the load-displacement response. Step A and Step B have been taken right before and in

correspondence of the peak load, respectively. Instead, Step C and Step D are positioned on the post-peak softening branch of the curve. Fig. 2.10a shows that the damage starts to propagate from the notches before reaching the peak load. At the peak load (Fig. 2.10b), the discontinuity has propagated towards the middle of the strips. The damage of the element near the notches has grown, reaching almost the maximum value. Fig. 2.10c and Fig. 2.10d shown that rapidly, after the peak load, all the element crossed by the discontinuity have been enriched. The damage on the regularized surface has progressively grown according to the stress-strain non-linear damage law defined.

In order to prove the mesh-independence of the results, a test with a mesh having $h_e = 1.1$ mm and fixing all the other problem parameters has been carried out. The result of the simulation is reported in Fig.2.9. The elaboration, that counts 45219 dofs, required 2 hours and 12 minutes. The structural responses obtained with the coarse mesh and the fine mesh are almost overimposed in Fig. 2.9. The peak load obtained with the fine mesh is only about 1.8 % smaller than the previous one.

This confirms the mesh-independency of the method is confirmed.

2.3.2 *Pull-out*

In the present section, the application to a real problem by means of the proposed 3D RE-XFEM approach is presented. In particular, the pull-out test on a steel rebar embedded in a concrete block, proposed in journal paper [80] and in the conference paper [81], has been investigated. As reference results, the experimental findings of Xiao and Falkne [82] have been considered, where two sets of pull-out tests were performed using plain and deformed bars for the specimens shown in Fig. 2.11a. A concrete characterized by compressive strength $f_{c,c} = 43.52$ MPa, a Young's modulus $E_c = 34.2$ GPa and Poisson's ratio $\nu = 0.2$ has been used in the experiments. The plain and the deformed steel rebars have Young's modulus $E_s = 210$ GPa, Poisson ratio $\nu = 0.3$. The experimental plain bar yield strength was equal to $f_{y,s} = 300$ MPa, while for the deformed bar a steel with a yield strength equal to $f_{y,s} = 420$ MPa has been used.

The load was applied by a testing machine to the end of the rebar, while the slip at the free end of the rebar was recorded. In particular, a tube was

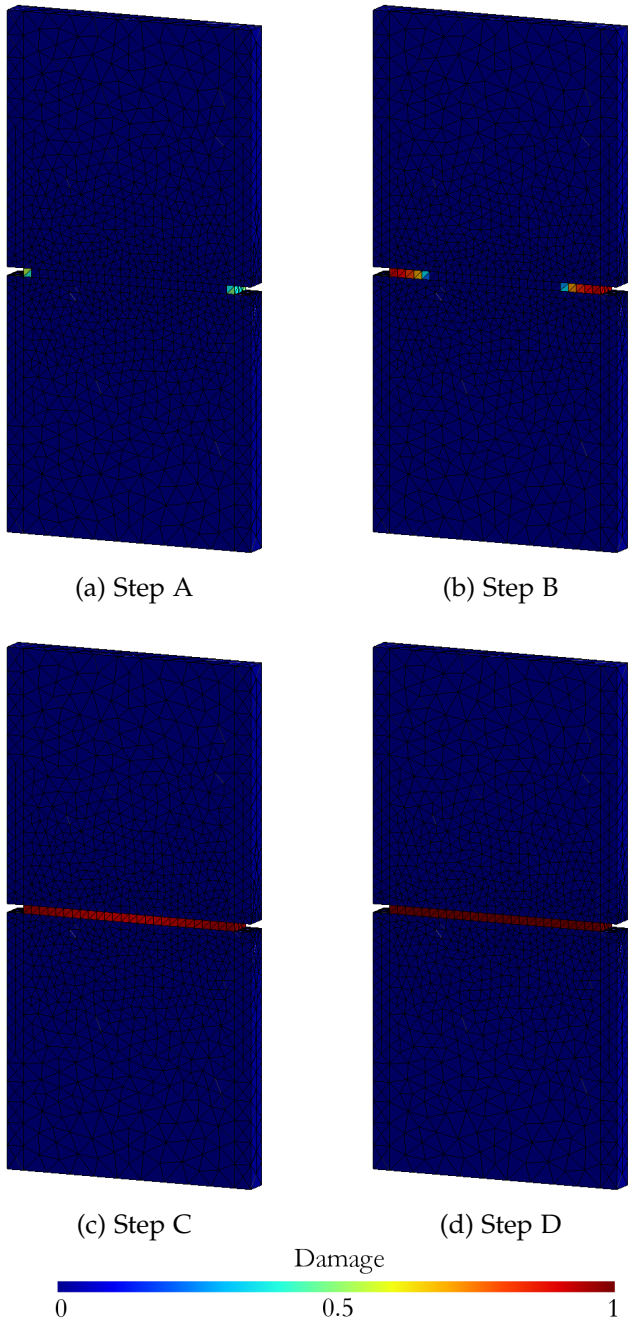

Figure 2.10: Contour plots of the damage in the regularized discontinuity for the steps highlighted in the load vs displacement curve shown in Fig. 2.9

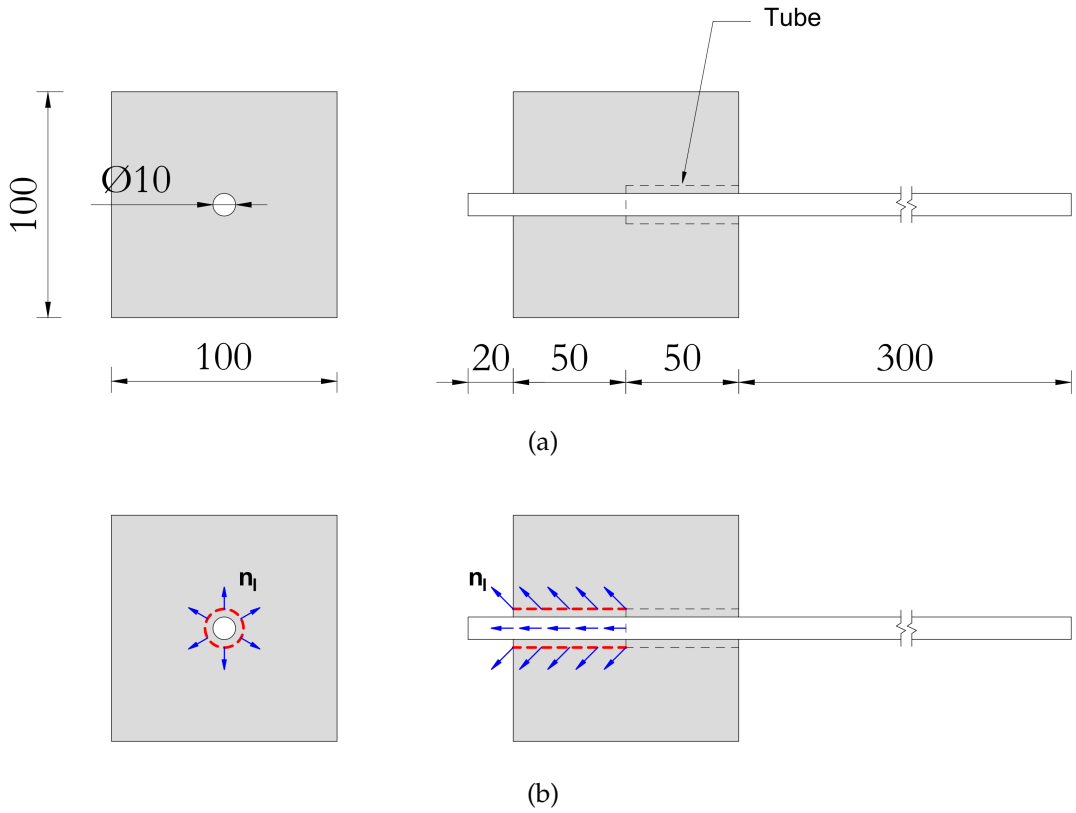

Figure 2.11: Pullout tests: geometry of the specimen employed by Xiao and Falkne [82](a) and qualitative representation of the local-levelset employed for the simulations (b)

inserted in the specimen in order to impose the right embedment length and to prevent the development of incorrect failure mechanisms.

In the numerical simulations, the elastic material values for the materials have assumed. The parameters characterizing the non-linear behaviour of the discontinuity have been calibrated from the tests. In particular, for the plain bar $f_t = 7.0$ MPa and $H_s = 2.5 \cdot 10^{-5}$ MPa have been used, while, for the deformed bar, $f_t = 13.5$ MPa and $H_s = 1.0 \cdot 10^{-4}$ MPa have been imposed.

Since in the experiments the stress in the steel bars does not reach the yield strength of the material, the bars have been modelled as linear elastic. For both the applications, the regularization parameter has been set to $\rho = 0.0250$ mm and only one layer of finite elements having mesh size $c = 1$ mm (thin process

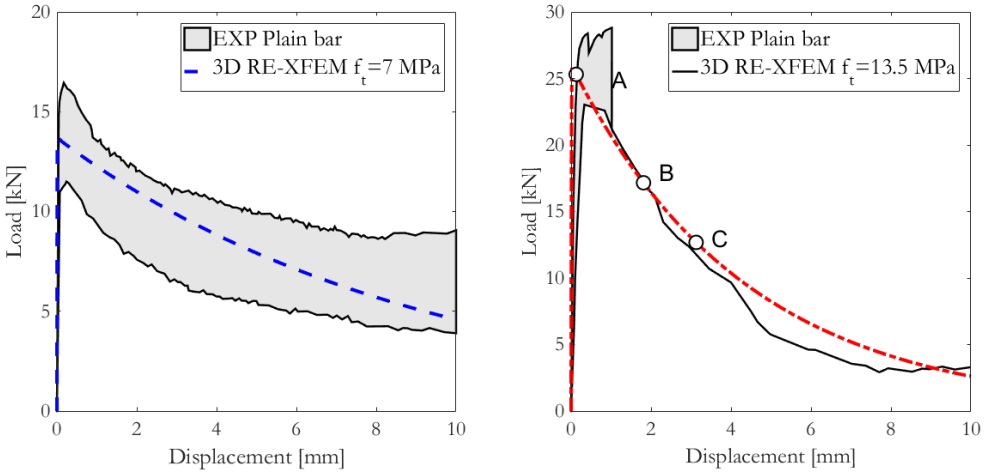

(a) Plain bars (b) Deformed bars

Figure 2.12: Pullout tests: Comparison between the experimental [82] and the numerical load vs displacement curves for the pullout of the plain (a) and deformed (b) bars from concrete blocks

zone) has been enriched. The threshold value of damage d_{cr} has been set to $d_{cr} = 0.001$. The local-levelset adopted for the regularized volume has been reported in Fig. 2.11b, accordingly to the expected micro-cracking behaviour of the specimen. To reduce the computational burden of the simulation, owing to the double symmetry of the problem, only a quarter of the specimen has been meshed. In particular, a mesh formed by 25164 elements and 22662 dofs, characterized by a minimum mesh size $h_e = 1$ mm has been employed in the elaborations. The simulations required 58 minutes for the plain bar and 1 hour and 19 minutes for the deformed bar in a i7-5930k CPU. The numerical and the experimental results are compared in for the plain and the deformed bars area reported in Fig. 2.12a and Fig. 2.12b, respectively. The contour plots of damage on the regularized discontinuity d^c for three representative steps of the deformed bar response curve have been reported in Fig. 2.13. At the peak load, namely Step A, the damage starts to propagate from the loaded end. Then, in post-peak softening branch, the damage propagates towards the free end of the steel rebars (Step B) until it reaches the end of the concrete block (Step C).

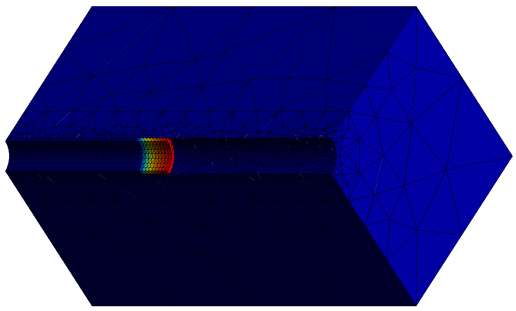

(a) Step A

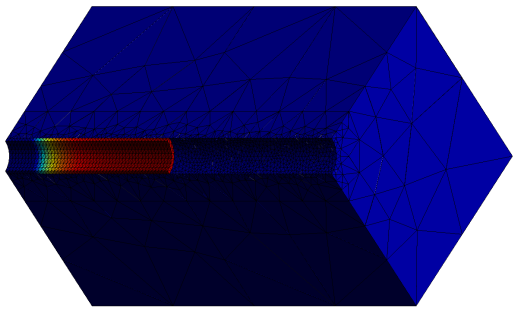

(b) Step B

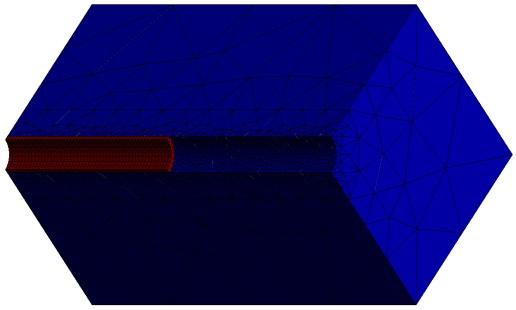

(c) Step C

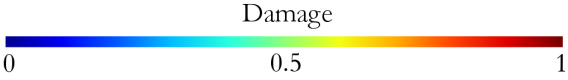

Figure 2.13: Contour plots of the damage for the steps highlighted in the load vs displacement curve shown in Fig. 2.12

The numerical responses obtained for the plain and the deformed bars are in good agreement with the experimental curves. This application confirms that the model is a valid alternative to literature models, such as cohesive zone models, in order to study weak discontinuity in concrete specimen.

2.4 REMARKS

The 3D non-linear Regularized XFEM procedure has been presented. The main aspects of the method can be summarized as:

- In the proposed model, like Standard XFEM, the shape of discontinuities do not have to conform to the FE mesh.
- The internal length introduced into the formulation has a physical meaning. This makes the model suitable for model weak and strong discontinuity in quasi-brittle materials like concrete.
- The mechanism-based local levelset allows taking into account problems that involve mixed mode crack propagation.
- A simple Galileo-Rankine damage law has been chosen. The model does not take into account damage in compression.

After the introduction of the 3D model, the next chapter is dedicated to the presentation of the results obtained in different engineering applications.

3

DEBONDING OF FRP FROM CONCRETE BLOCKS

3.1 INTRODUCTION

Fiber Reinforced Polymers (FRP) reinforcements are increasingly used for the post-seismic structural rehabilitation and to enhance the ultimate strength of concrete structural elements. Single-lap shear tests on FRP-reinforced concrete blocks are often performed to assess the ultimate load before the complete debonding of the FRP plate [83] occurs. Debonding is a complex three-dimensional process, and a challenging issue in computational mechanics [84–86].

Based on experimental results, it is known that the debonding process involves a thin portion of material localized in the concrete layer underlying the FRP plate. Within finite element (FE) approaches, the concrete block is commonly modelled as a two-dimensional body in plane stress state, and the FRP-concrete interface as a one-dimensional interface subjected to distributed tangential stress by means of bond stress-slip laws [72, 87]. However, even if the reinforcement is loaded mainly in shear, the out-of-plane displacements observed during the tests induce tensile and compression stresses orthogonal to the bonding plane [73]. Hence, one-dimensional bond stress-slip relationships have been modified to take into account failure mechanisms relying on mixed fracture modes [88, 89]. Furthermore, experimental tests [90, 91] detected the occurrence of edge regions with high shear strains associated with the stress transfer from FRP to concrete, and highlighted the key role of the peel displacement in the debonding onset and propagation. In particular, a two-way debonding mechanism was observed [73, 92]. For very short bonding lengths, debonding starts at the free end of the FRP plate and propagates towards the loaded end of the plate. For sufficiently long bonding lengths,

debonding starts at the loaded end and propagates towards the free end until a critical bonding length is reached, at which debonding at the free end starts and propagates towards the loaded end. Furthermore, the maximum transferable load is influenced by the FRP plate bending, and the ratio between the widths of the plate and the concrete block.

Width-effects associated with shear-strain-edge-regions cannot be taken into account assuming a plane stress state. For this reason, 3D FE codes [93] have been used, most of them assuming the concrete-FRP surface as a zero thickness interface. Based on these assumptions, 3D FE simulations highlighted the dependence of the concrete stress state on the bending rigidity of the FRP plate and the edge stiffening effect on the shear stress components. To this purpose, the analysis proposed in [94] assumed elastic materials, and a perfect bond between the adhesive and the FRP plate. An elastic-damage interface model governing the inter-laminar stresses acting in the sliding direction was adopted in a more recent study [93]. Furthermore, based on a bond stress-slip law, Neto et al. [95] have introduced an effective bond width that comprehends of both the FRP plate and the contiguous concrete with non-vanishing shear stress.

Despite the use of the XFEM for the 3D modelling of debonding in composite laminates is quite established, 3D RE-XFEM simulations of pull-out tests of FRP plates bonded to concrete specimens seem not to have been presented in the literature.

2D plane-stress simulation of debonding with the regularized XFEM approach was previously carried out by Benvenuti et al. [3]. In particular, the debonding strength was predicted with a sufficient accuracy exploiting just the nominal values of the Young's moduli and the Poisson's coefficients of concrete, glue, and reinforcement.

With respect to the previous 2D model [3], the 3D RE-XFEM formulation proposed in Ch. 2 is characterized by the global-local system of level sets described in Sec, 3.2, that they take into account the edge effects and a fully 3D mixed shearing-peeling debonding mechanism. The main aim of this contribution is not only to fit the experimental results, that are often subjected to several uncertainties, but also to provide a reliable technical tool that can be used for design purposes besides, or in alternative to, experimental tests.

The results shown in this chapter are taken from the published in. [9]. The results obtained for the data sets [73] and [96] are shown in Sec. 3.3. Em-

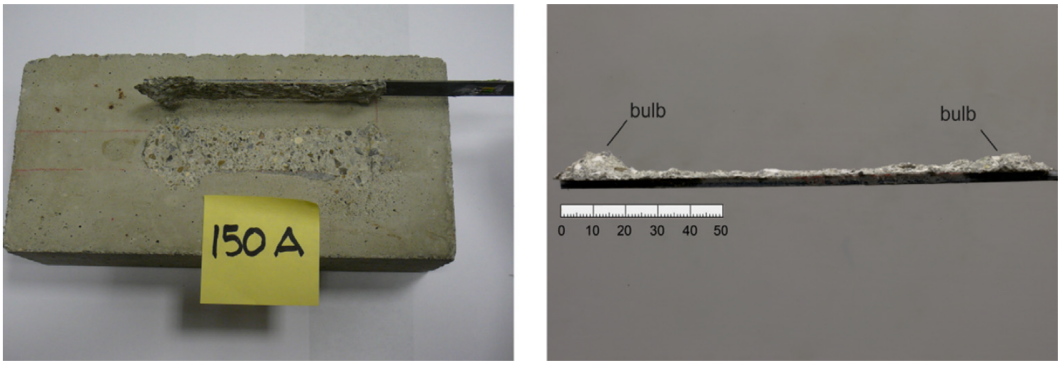

Figure 3.1: Photographs of the detached concrete layer after debonding for the tests of Carrara et al. [73]

phasis is put on the bending of the FRP plate, the presence of the peeling displacements at both the loaded and the free ends of the FRP plate, and the two-way debonding depending on the bonding length. The 3D behaviour of the debonding process is assessed in Sec. 3.4, where the width dependence of the maximum transferable load is also displayed.

3.2 LOCAL-GLOBAL MECHANISMS BASED LEVEL SET

debonding is assumed to take place in a plane parallel to the adhesive layer, as usual in the literature [72, 85]. Such a plane has been located at 1 mm underneath the concrete surface. This corresponds to confine the debonding process in the finite element layer placed immediately below the glue. The hypothesis agrees with the experimental evidence in the central part of the plate (Fig. 3.1), where a layer of concrete $1-3$ mm thick is usually detached [73]. Of course, the concrete bulbs at the ends of the bonded zone are not caught. The global-local level set procedure relies on the fact that we assume: a global level set function denoting the surface of the debonding that is parallel to the adhesive surface and located below the concrete surface, and a local level set system at each Gauss point of the XFEM enriched finite elements, displayed in Fig. 3.2. The global level set surface is defined a priori parallel to the adhesive layer, as usual in two-dimensional FE analysis and in numerical models based on one-dimensional interface laws. As for the local level set system, we have adopted the following path of reasoning. In principle, the $\boldsymbol{n}_l$ vector

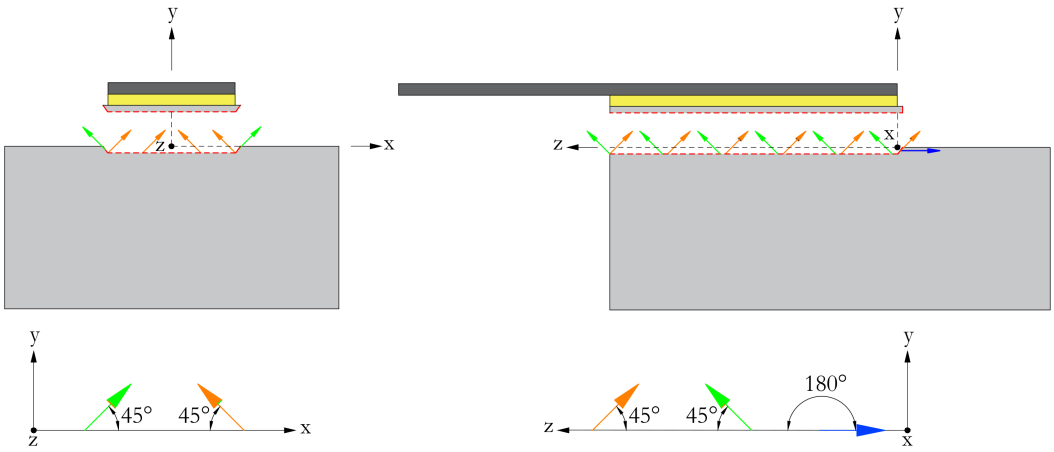

Figure 3.2: Qualitative picture of the vector $\boldsymbol{n}_l$ associated with the local level set adopted

is orthogonal to the crack direction and governed by the maximum tensile principal stress. In this study, we have adopted the simplified local level set shown in Fig. 3.2. Each edge is associated with a local set whose normal vectors are shown in green and blue. The blue normals are oriented at $(0, 0, -1)$ for $x > 0$, $y > 0$, $z > 0$. The green normals are oriented outwards the edges along the direction $(1/\sqrt{3}, 1/\sqrt{3}, -1/\sqrt{3})$ for $x > 0$, $y > 0$, $z > 0$. The local level set adopted inside the enriched layer is associated with a normal field, plotted in orange in the same figure, oriented towards the symmetry plane $y - z$ at $(-1/\sqrt{3}, 1/\sqrt{3}, -1/\sqrt{3})$ for $x > 0$, $y > 0$, $z > 0$, $\boldsymbol{n}_l$ being specular with respect to the $y - z$ plane in the domain $x < 0$, $y > 0$, $z > 0$. This assumption ensures that the debonding process is captured consistently. Noteworthy, the adopted global-local level set system is imposed a priori, but the final directions of the jump vectors at the nodes are computed by the non-linear iterative-incremental procedure and will not generally coincide with that of the superimposed normals. Moreover, the enriched layer of elements has the same width as the FRP plate, and is located 1 mm below the adhesive layer.

3.3 FRP PLATE BENDING, PEELING AND TWOFOLD DEBONDING ONSET

This section is devoted to the discussion on the influence of the FRP plate bending and on the occurrence of peeling at both the ends of the FRP plate

Table 3.1: Material and geometry parameters employed fo the simulation

	Carrara et al. [73]			Chajes et al. [96]		
	FRP	Glue	Concrete	FRP	Glue	Concrete
E [MPa]	108380	1585	33640	168500	3517.3	28700
ν	0.248	0.315	0.2	0.248	0.315	0.2
f_t [MPa]	-	-	3.21	-	-	2.85
Thickness [mm]	1	1	-	1.3	1.3	-
H [mm]	90	90	90	152.4	152.4	152.4
B [mm]	150	150	150	152.4	152.4	152.4
L [mm]	300	300	300	228.6	228.6	228.6
b [mm]	30	30	30	25.4	25.4	25.4

depending on the bonding length. The values of the Young's modulus and the Poisson's coefficient adopted for the FRP plate, the glue, and the concrete used in the model are collected in Tab. 3.1 as indicated in the references of the experimental works.

3.3.1 *Experimental data sets geometry*

For a comparison with experimental results, we will consider the specimens of Chajes et al. [96], often studied in the literature, and the specimens of the tests by Carrara et al. [73]. It is remarkable that, while for the former data set the structural responses lack, for the latter data set, the whole load-displacement curves with softening post-peak branches have been recorded, owing to a stable loading control procedure developed for this purpose. All the data of the geometry and the material parameters of the original tests are collected in Tab. 3.1. In the geometry adopted by Chajes et al. [96] shown in Fig. 3.3, the glue layer starts at the front of the specimen, namely close to the loaded end of the FRP plate. On the contrary, in the geometry of Carrara et al. [73], shown in Fig. 3.4, the FRP plate is bonded at a certain distance from the front of the specimen to avoid the detachment of a concrete wedge when pulling the FRP plate. Moreover, the softening modulus H_s has been set equal

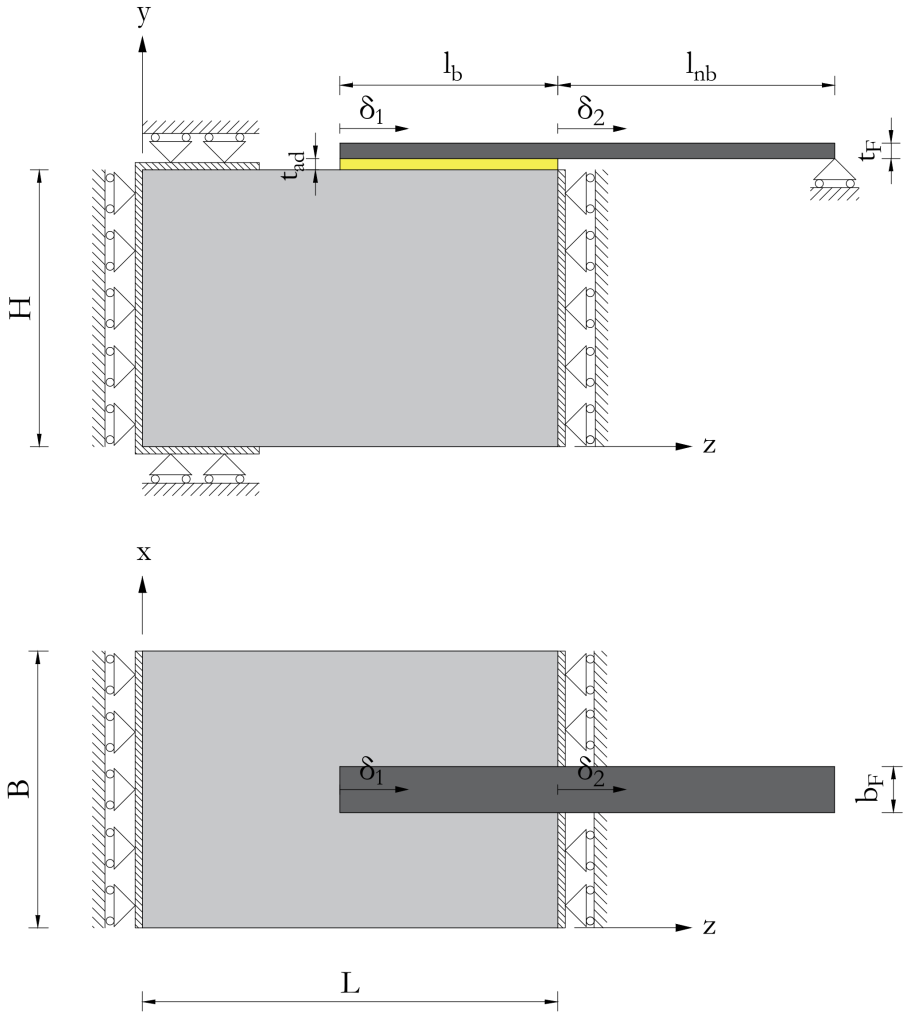

Figure 3.3: Geometry of the specimen used for the single-lap shear test carried out by Chajes et al. [96].

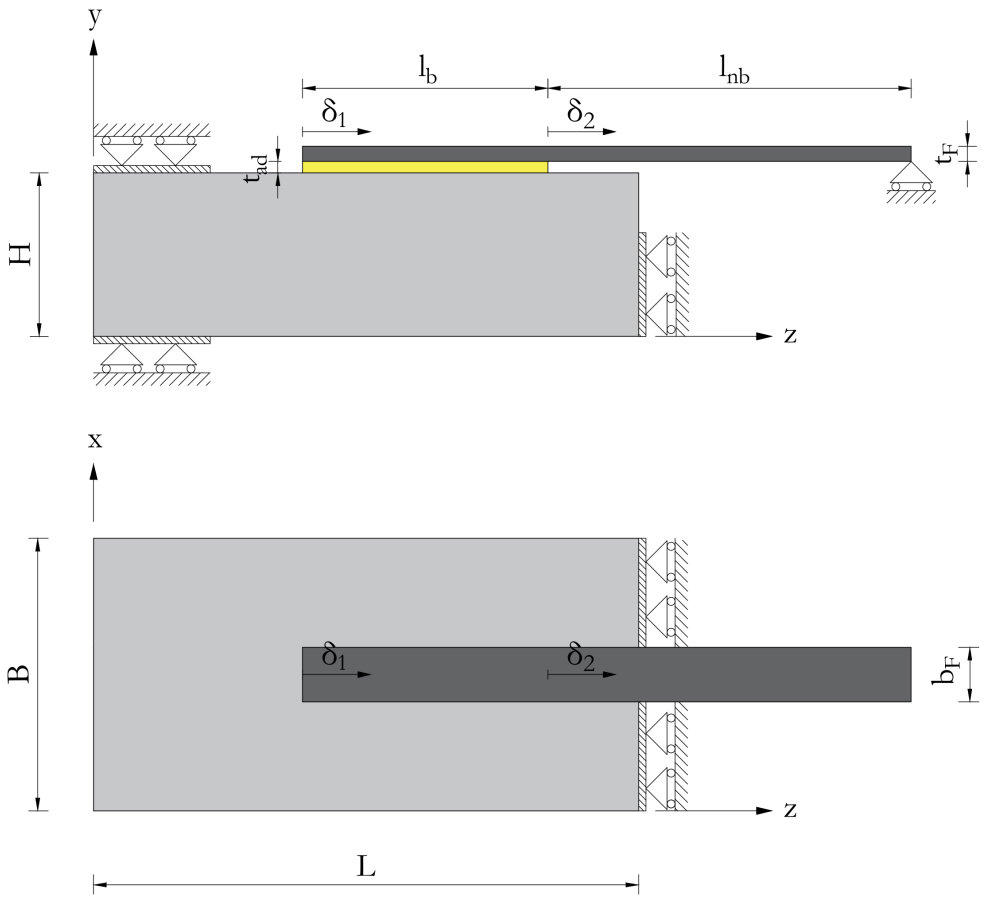

Figure 3.4: Geometry of the specimen used for the single-lap shear test carried out by Carrara et al. [73]

to $H_s = 0.005$ MPa for the Chajes et al. [96] test, and equal to $H_s = 0.008$ MPa for the Carrara et al. [73] test. The regularization parameters has been taken equal to $\rho = 0.0125$ mm and $\rho = 0.016$ mm for the Chajes et al. [96] test and for the Carrara et al. [73] test, respectively.

Based on symmetry reasons, only one half of the specimen has been meshed. Considering that the concrete block stiffness plays an important role in the structural response of the specimen, we have first run some simulations where the real dimensions of the concrete block were modelled. Then, to reduce the computational burden, we have run the same simulations but with a width of the meshed geometry of the concrete block equal to 80 mm. These simula-

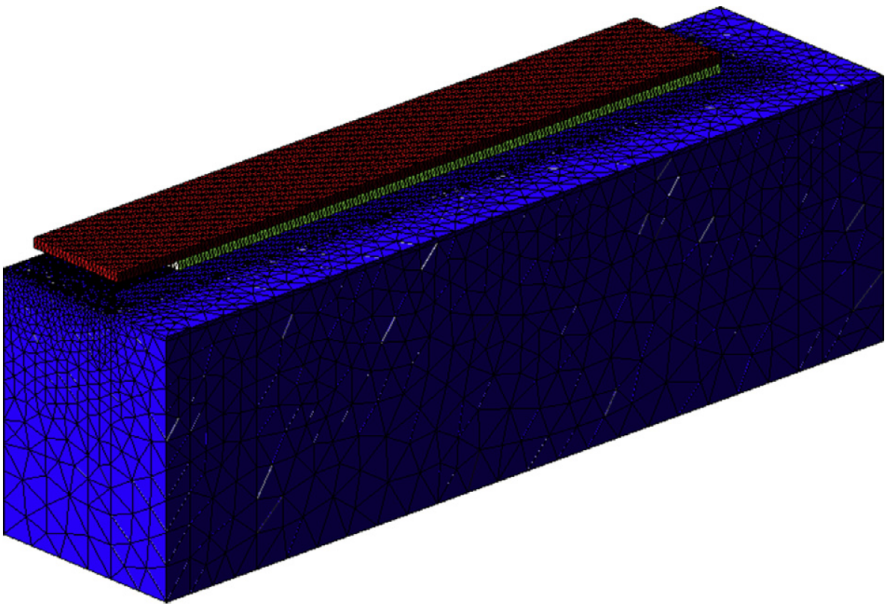

Figure 3.5: Mesh of the half of the Chajes et al. [96] specimen

tions gave the same results of the case with the entire width of the concrete block. Also, the height of the concrete block has been taken equal to 35 mm to reduce the computational effort. The mesh adopted for Chajes et al. [96] in the $L_b = 101.6$ mm case shown in Fig. 3.5 is made of 250548 elements with 243930 total degrees of freedom.

3.3.2 *Structural response*

As the complete data set of Carrara et al. [73] test is available up to the final debonding stage is available, the corresponding debonding process has been assessed for various bonding lengths. To compare the computed structural responses with the experimental ones, we have plotted the load vs both the z displacement δ_2 at the loaded end and the z displacement δ_1 at the free end of the FRP plate, as reported in Figs. 3.3 and 3.4. Different bonding lengths L_b have been from the short length $L_b = 30$ mm, shown in Figs. 3.6 to the longer lengths $L_b = 90$ mm and $L_b = 120$ mm, shown in Figs. 3.7 and Fig. 3.8, respectively. The snap-back in the structural response plotted in terms of the

front-displacement increases as the bonding length increases, as shown in the case of $L_b = 90$ mm in Fig. 3.7a, and in the case of $L_b = 120$ mm in Fig. 3.8a. The maximum transferable loads computed with the present analysis are

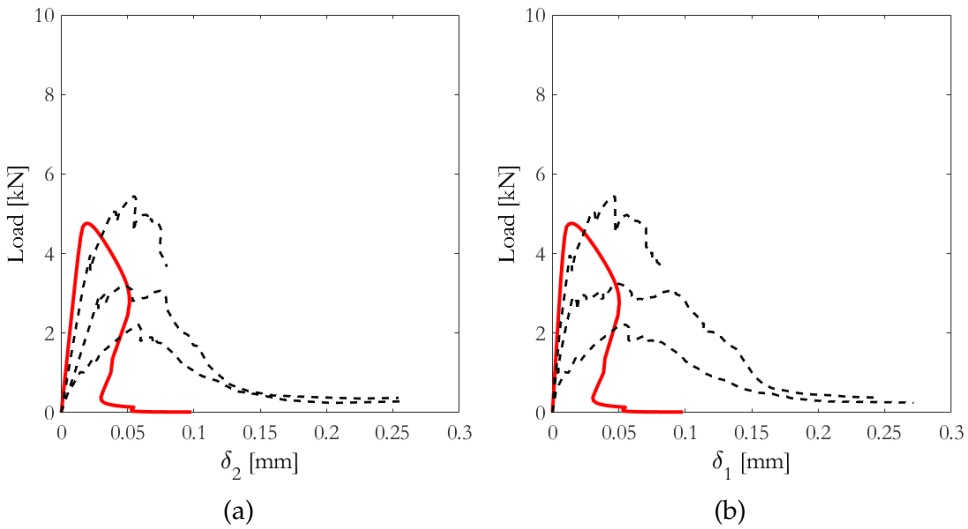

Figure 3.6: Computed (red continuous line) and experimental [73] (black dashed line) load-displacement profiles for $L_b = 30$ mm at the loaded δ_2 (a) and at the free δ_1 end (b)

shown for variable bonding length in Fig. 3.9a. In addition to the previous load-displacement simulations, the structural responses up to the maximum transferable load have been determined for the Chajes et al. [96] geometry too.

For this latter case, the maximum transferable loads vs the bonding length are shown in Fig. 3.9b. The experimental data regarding the structural response of the Chajes et al. [96] are not available, thus a direct comparison with the computed results has not been possible.

3.3.3 *Debonding onset*

The different types of structural behaviour shown in Figs. 3.6, 3.7 and 3.8 are associated with different positions of the debonding onset. Because the detachment is strictly related to the evolution of the damage variable d^c, it

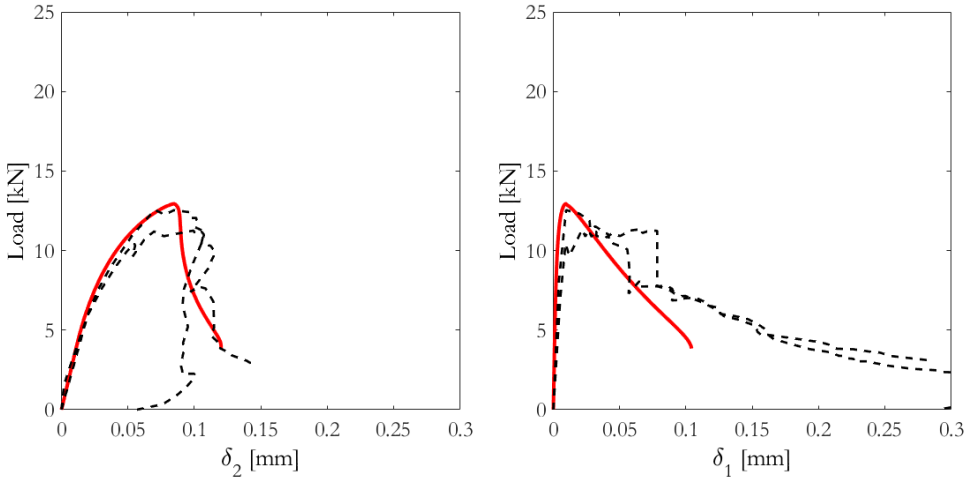

Figure 3.7: Computed (red continuous line) and experimental [73] (black dashed line) load-displacement profiles for $L_b = 90$ mm at the loaded δ_2 (a) and at the free δ_1 end (b)

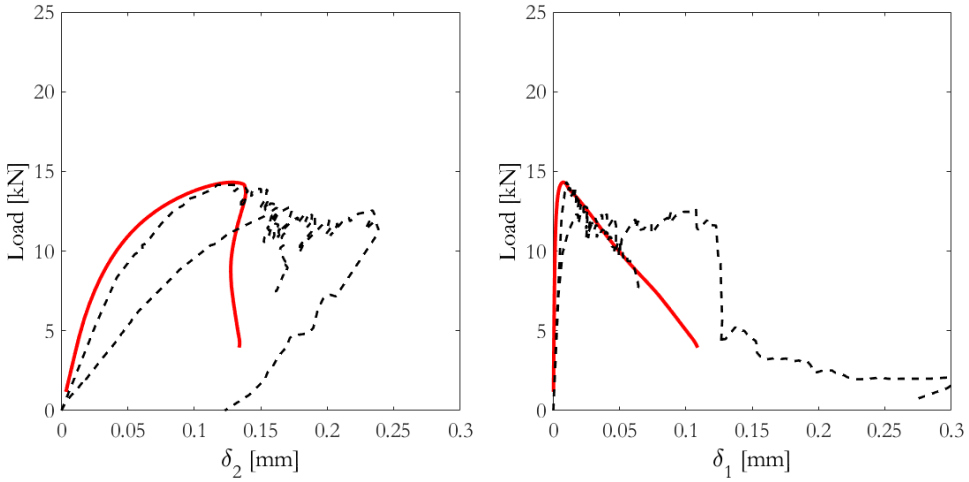

Figure 3.8: Computed (red continuous line) and experimental [73] (black dashed line) load-displacement profiles for $L_b = 120$ mm at the loaded δ_2 (a) and at the free δ_1 end (b)

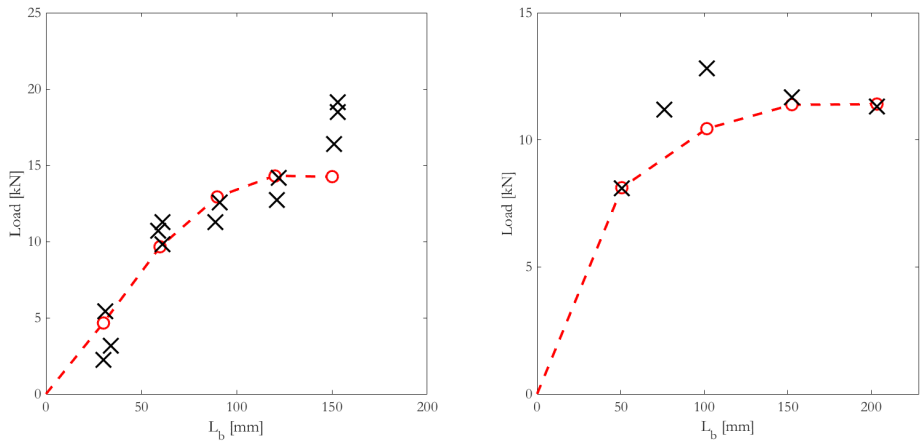

(a) (b)

Figure 3.9: Computed ("'o"') and experimental maximum loads ("'x"') vs bonding length L_b [mm] for the tests [73] (a) and [96] (b).

is thus convenient to consider the evolution of d^c, which is the damage on the concrete surface below the glue. Fig. 3.10 displays the sequence of the contour plots of d^c for $L_b = 30$ mm and $L_b = 90$ mm at the pre-peak, the peak and the post-peak loads, from top to bottom. In the case of short bonding length, $L_b = 30$ mm, damage starts at the free end. On the contrary, for the $L_b = 90$ mm case displayed in Fig. 3.10, the damage evolution is different

Fig. 3.11 shows in detail the evolution of the debonding process for $L_b = 90$ mm in the the pre-peak, peak and post-peak stages. In the firsts stages, the damage develops at both the loaded and the free end of the FRP plate (a, b), and it subsequently propagates from the loaded end towards the free end (c) up to a certain value of the actual bonded length, approximately equal to 30 mm(d). Then, it propagates from the free to the loaded end (e) up to complete debonding (f). For all the investigated bonding lengths, the bending of the FRP plate influences the damage onset and its evolution. Such an influence is shown in Fig. 3.12 for the Chajes et al. [96] test with bonding length $L_b = 50.8$ mm. The same figure shows that, for this bonding length, debonding proceeds from the free end to the loaded end of the FRP plate.

To complete the picture of the 3D debonding process, the tangential stress τ_{yz} and the peel stress σ_{yy} have been evaluated at the Gauss points on the

concrete surface below the glue for the Carrara et al. [73] test. Fig. 3.13 and Fig. 3.14 display the spatial frames of σ_{yy} and τ_{yz} stress components,, respectively, detected at the pre-peak, the peak and the post-peak for the $L_b = 90$ mm case. In particular, in a first stage, the peel stress σ_{yy} is activated at the loaded end (a) and subsequently at the free end (c, e, g). In the final stages (e, g), peeling at the loaded end is predominant. The shearing stress τ_{yz} first propagates from the loaded end to the free end (b,d), then its peak moves from the free to the loaded end (f, h). Moreover, the shear stress τ_{yz} evaluated at the end of the FRP plate reaches values of 15 MPa, which are slightly high with respect to the experimental ones. The profile of τ_{yz} cannot be directly compared to the "shear stress" of one-dimensional shear-stress-slip laws [72], which are average values obtained from the variation of two subsequent strains measured by strain gauges on the plate surface. For instance, an example of shear-stress-slip law equivalent to the experimental one was deduced from the results obtained by means of the regularized XFEM approach in the 2D case [3].

3.3.4 *Strain evolution and deformability*

The strain evolution for various load levels have been compared with the available experimental results for both the experimental data sets. For this purpose, we have obtained from our 3D results a shear strain equivalent to that usually obtained in experiments from the displacements recorded at the strain gauges. In particular, the expression

$$\varepsilon = \frac{u_{z,i+1} - u_{z,i}}{\Delta z} \quad , \tag{45}$$

has been exploited, where z is the longitudinal axis, and $u_{z,i+1}$ and $u_{z,i}$ denote the displacements recorded on the FRP plate at discrete positions z_i and $z_{i+1} = z_i + \Delta z_i$. In Fig. 3.15, the evolution of the strain along the z-axis is shown for the Chajes et al. [96] tests at the maximum transferable load. The post-peak strain profiles have not been reported, because the experimental post-peak data are not available. Profiles of the same colours correspond to the same load level, while the markers indicate the experimental results. For the Carrara et al. [73] experimental data, the strain profiles corresponding to both the pre-peak and the post-peak branches are available. In Fig. 3.16 the strain profiles computed for the two bonding lengths $L_b = 90$ mm and

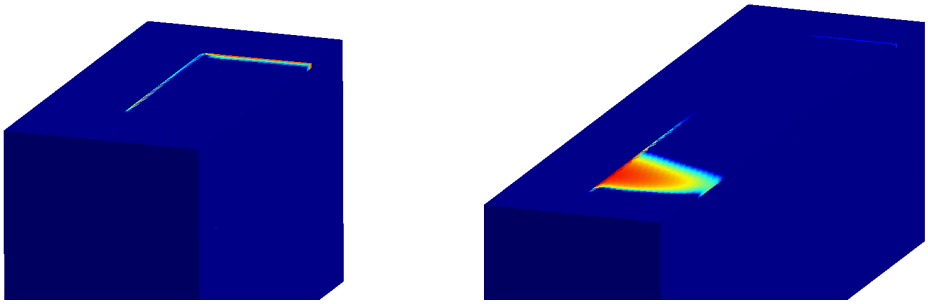

(a) Step A, $L_b = 30$ mm

(b) Step A, $L_b = 90$ mm

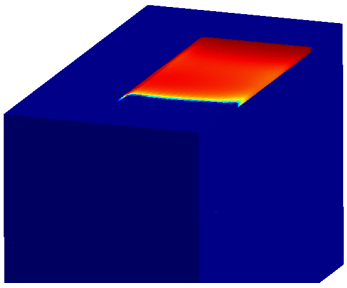

(c) Step B, $L_b = 30$ mm

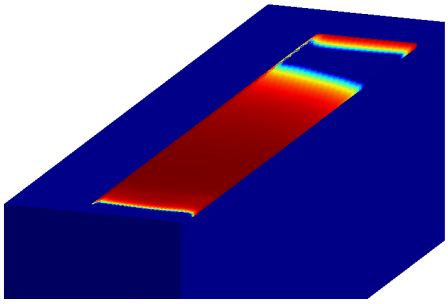

(d) Step A, $L_b = 90$ mm

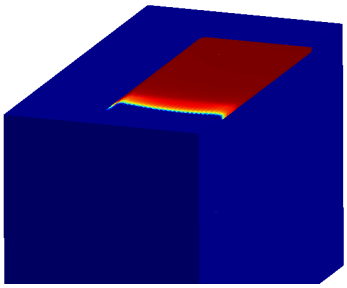

(e) Step C, $L_b = 30$ mm

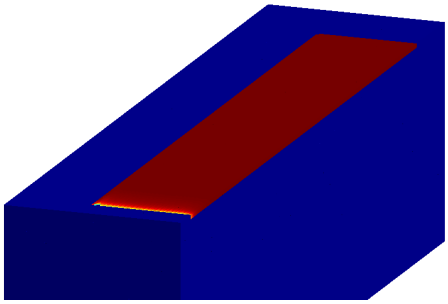

(f) Step A, $L_b = 90$ mm

Figure 3.10: Carrara et al. [73]: Damage and debonding evolution for $L_b = 30$ mm

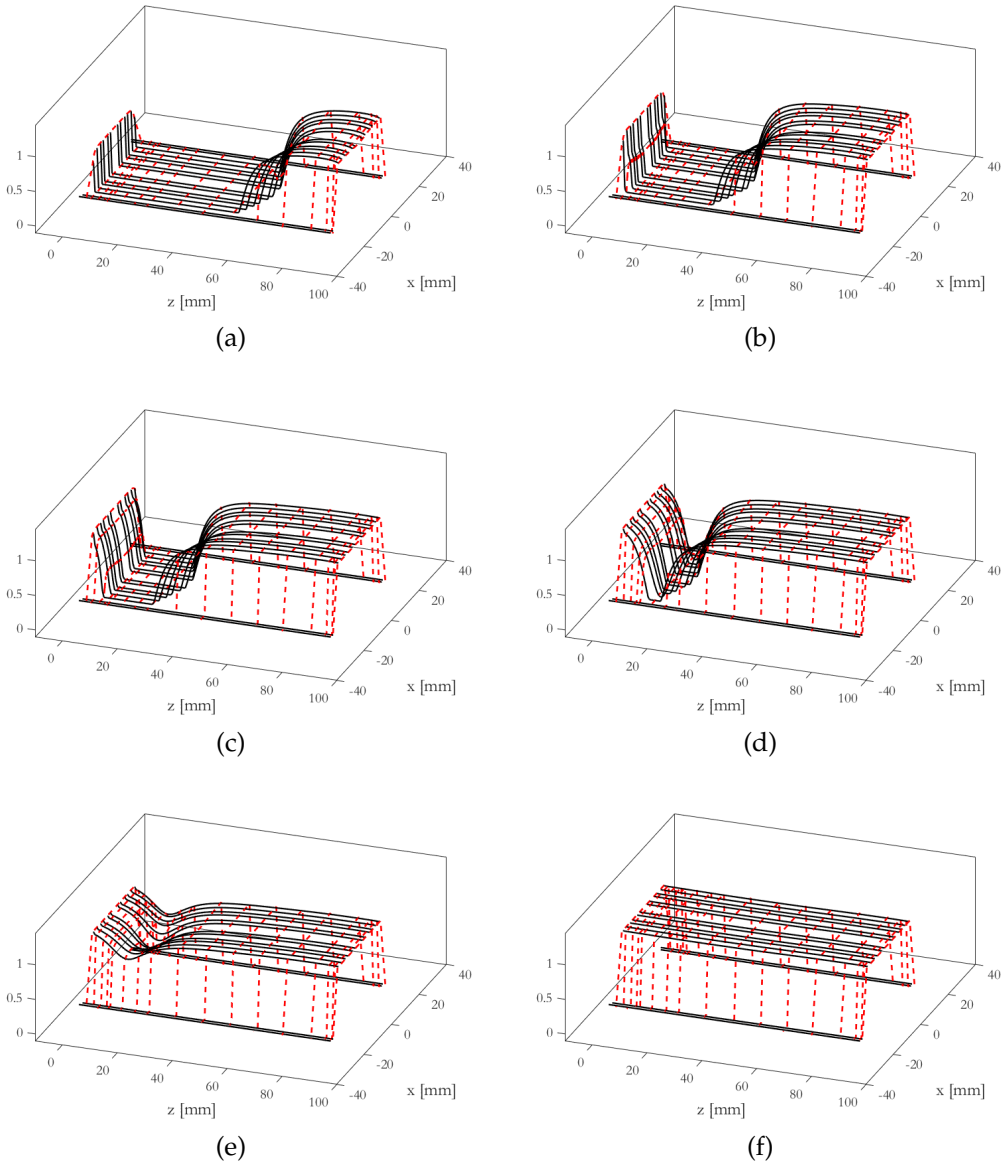

Figure 3.11: Pre-peak (a, b, c), peak (d) and post-peak (e, f) damage profiles for $L_b =$ 90 mm for the test [73]

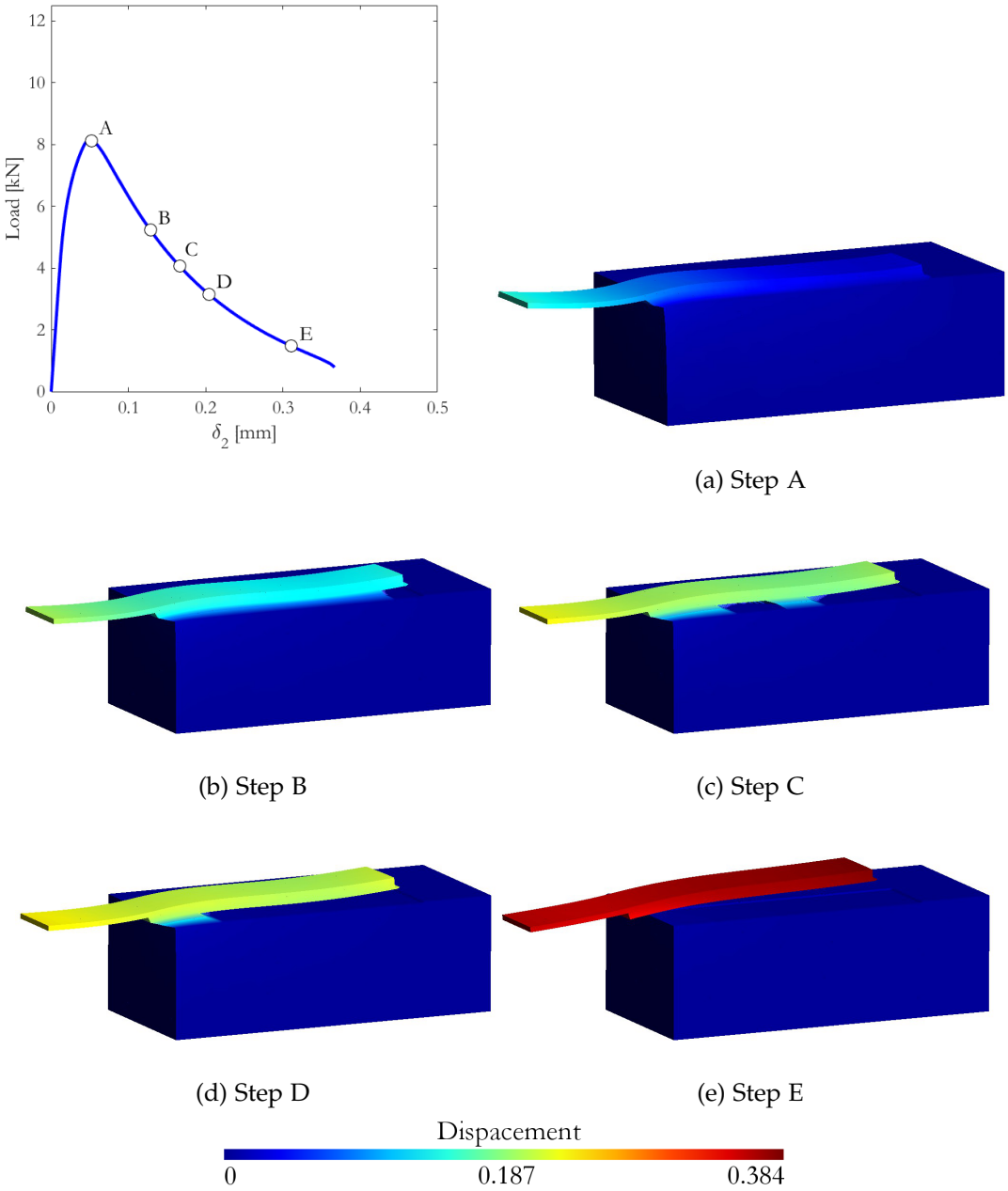

(a) Step A

(b) Step B

(c) Step C

(d) Step D

(e) Step E

Figure 3.12: Computed load-displacement profile for $L_b = 50.8$ mm and corresponding deformed mesh evolution for different time step for the test [96]

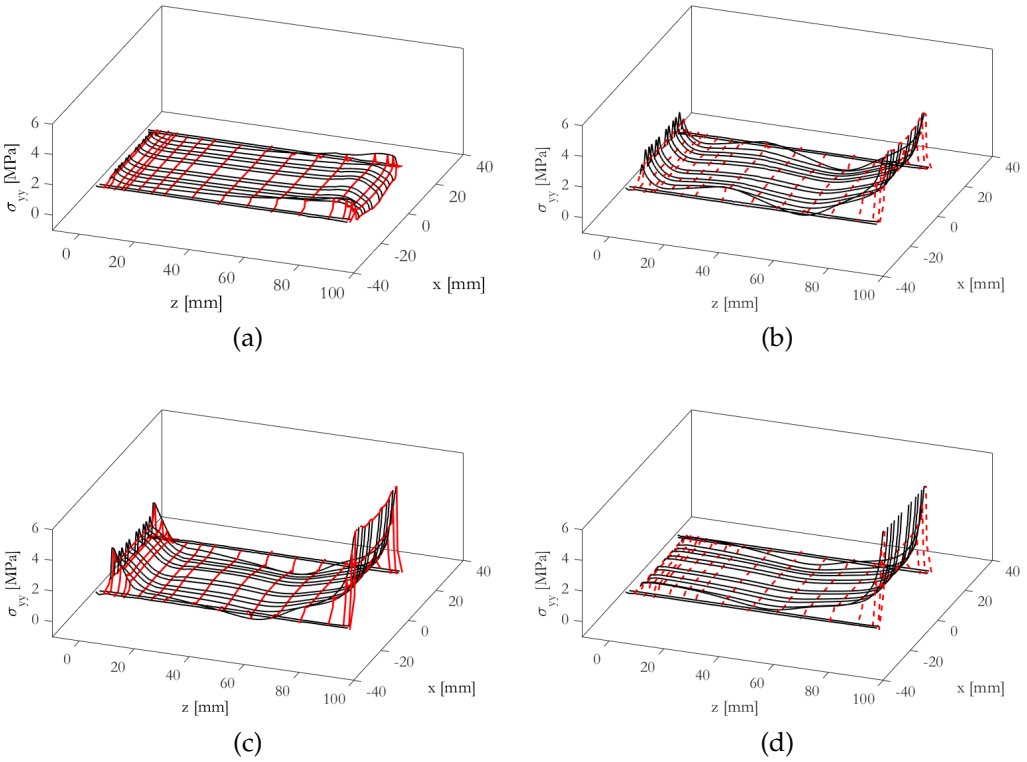

Figure 3.13: Pre-peak (a), peak (b) and post-peak (c,d) profiles of σ_{yy} (peeling) for the test [73] with $L_b = 90$ mm

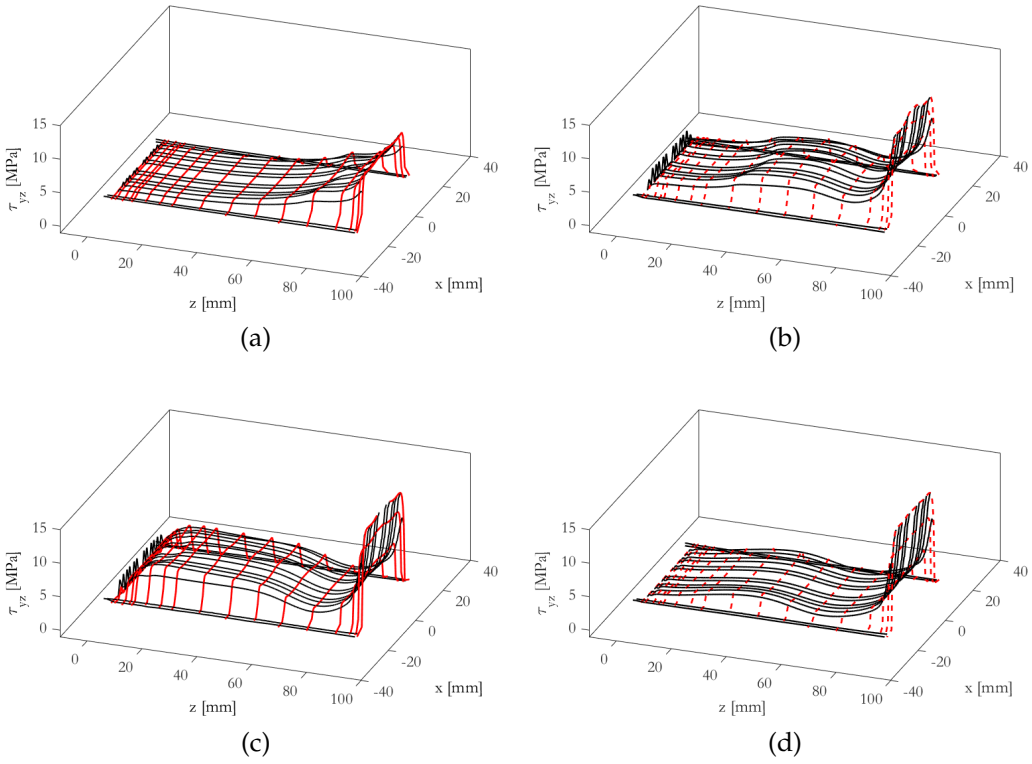

Figure 3.14: Pre-peak (a), peak (b) and post-peak (c, d) profiles of τ_{yz} for the test [73] with $L_b = 90$ mm

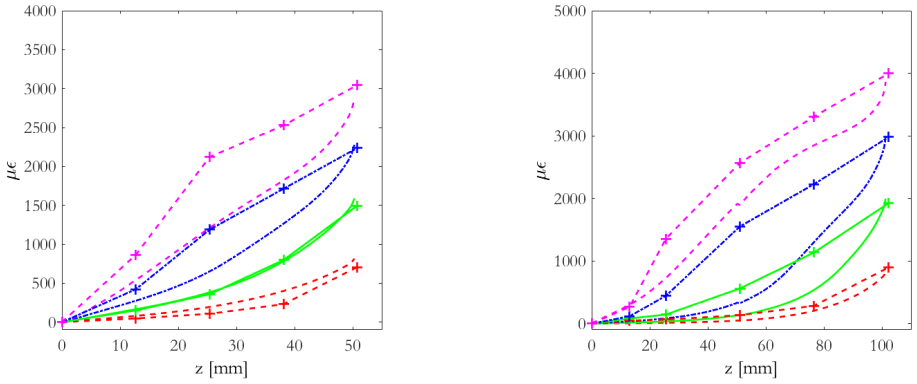

(a) (b)

Figure 3.15: 1D equivalent axial strain along z for the test [96] obtained for $L_b = 50.8$ mm (a) and $L_b = 101.6$ mm (b). The load levels are: $P = 1.94$ kN (red dashed line), $P = 4.06$ kN (green continuous line), $P = 6.01$ kN (blue dash dotted line line), $P = 8.10$ kN (pink dotted line) (a), and $P = 2.23$ kN (red dashed line), $P = 5.03$ kN (green continuous line), $P = 7.71$ kN (blue dash dotted line line), $P = 10.29$ kN (pink dotted line) (b).

$L_b = 120$ mm are compared with the homologous experimental profiles. A good agreement between numerical values and tests is confirmed for both the experimental campaigns.

3.4 3D ASPECTS: WIDTH AND EDGE EFFECT

To highlight the 3D aspects of debonding, this section investigates the profiles of several relevant stress components along the width and the length of the FRP-plate. In Sec. 3.4.1, the influence of the FRP plate width on the structural response is assessed. For this purpose, the Chajes et al. [96] tests are taken into account. In Sec. 3.4.1, the main results obtained for the investigated cases are discussed.

3.4.1 *Influence of the FRP-plate width*

The debonding analysis has been performed for variable FRP plate widths b. For $b/B > 0.5$, the width of the concrete is insufficient to allow a full

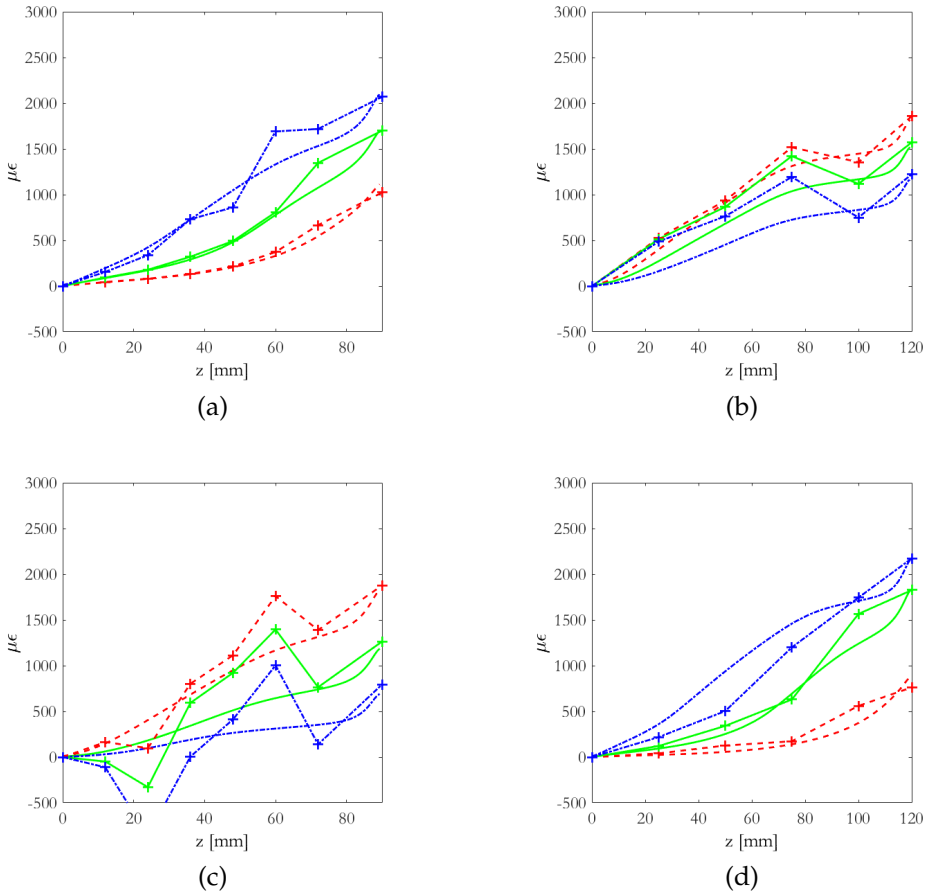

Figure 3.16: 1D equivalent axial strain along z for the test [73] for $L_b = 90$ mm (c) and $L_b = 120$ mm (d), at $P = 6.00$ kN (red dashed line), $P = 10.01$ kN (green continuous line), $P = 12.64$ kN (blue dash dotted line line) in (c), and $P = 5.01$ kN (red dashed line), $P = 12.00$ kN (green continuous line), $P = 14.28$ kN (blue dash dotted line line) (d); $P = 11.15$ kN (red dashed line), $P = 7.47$ kN (green continuous line), $P = 4.67$ kN (blue dash dotted line line) in (e), and $P = 12.21$ kN (red dashed line), $P = 10.33$ kN (green continuous line), $P = 8.04$ kN (blue dash dotted line line) in (f)

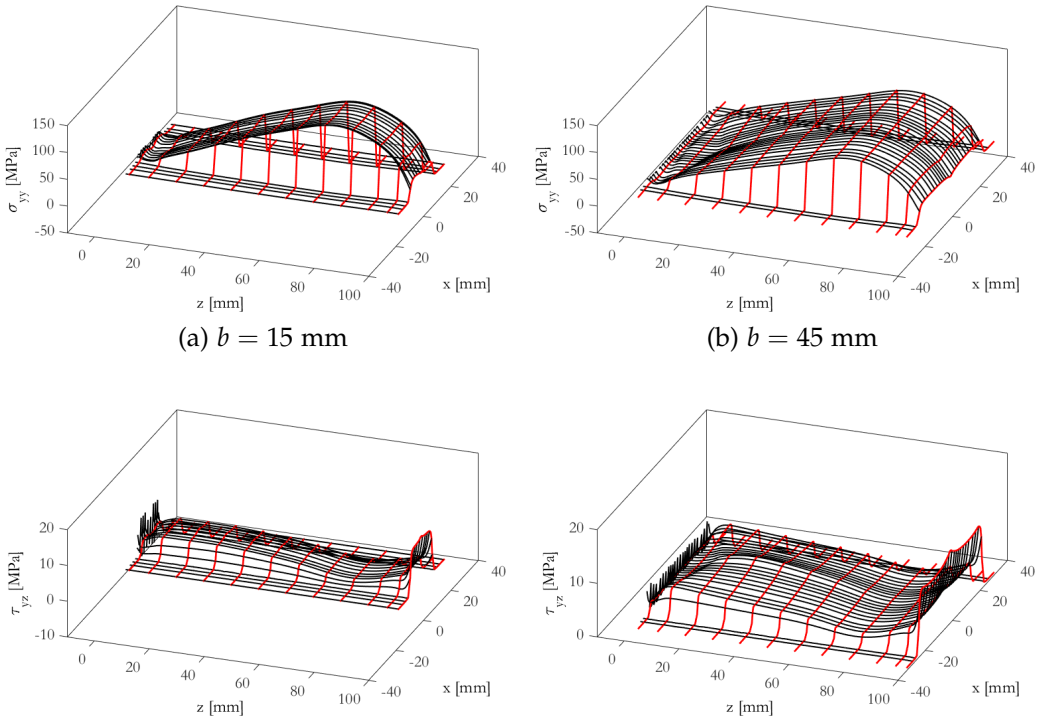

(a) $b = 15$ mm (b) $b = 45$ mm

(c) $b = 15$ mm (d) $b = 45$ mm

Figure 3.17: 3D view of σ_{yy} and τ_{yz} for $b = 15$ mm and $b = 45$ mm with $L_b = 101.6$ mm evaluated at the maximum load for the test [96].

transmission of the stresses from the FRP plate to the concrete substrate [91]. Therefore, the concrete width of the specimen analyzed has been set equal to 80 mm. In particular, the peel stress σ_{yy} and the shearing stress τ_{yz} have been plotted at the Gauss points of the finite elements within the bonded concrete. They are displayed in Fig. 3.17 for two widths of the FRP plate, namely $b = 15$ mm and $b = 45$ mm for the same bonding length $L_b = 101.6$ mm. The profiles have been detected at the peak of the transferable load. Fig. 3.17 displays no appreciable edge effect for both the values of b. The profiles of the shearing and the axial strain components ε_{xz} and ε_{zz}, respectively, have been plotted across the width at different locations along the FRP plate length for $b = 15$ mm, $b = 45$ mm, and $L_b = 101.6$ mm. Fig. 3.18 shows the values detected during the elastic stage, before that the debonding process starts, while

Fig. 3.19 displays the evolution of these specific strain components during the debonding process. The profiles correspond to $z = 0.5$ mm (cyan dotted line), $z = 18.1$ mm (pink dashed line), $z = 38.1$ mm (yellow dash-dotted line), $z = 58.1$ mm (green dotted line), $z = 78.1$ mm (red dashed line) and $z = 95.1$ mm (blu continuous line). During the elastic stage, the profiles of ε_{xz} and ε_{zz} extend over a region significantly larger than b (Fig. 3.18). This confirms that the modelled concrete support must be sufficiently large compared to the FRP plate width to allow a full diffusion of the shearing stress components in the concrete surrounding the FRP plate, as observed by Subramaniam et al. [91]. While ε_{zz} at the centre of the FRP plate are almost constant, ε_{xz} is antisymmetric with respect to the symmetry plane. Both of them display high variations over an edge region approximately 20 mm wide. When the load reaches 90% of the peak load, the damage has been activated at the edges of the concrete substrate underlying the FRP plate. Correspondingly, the ε_{xz} and ε_{zz} shown in Fig. 3.19 display narrower edge regions of width approximately equal to 10 mm, in agreement with the experimental results reported in Ref. [73]. Furthermore, the dependence of the strain profiles on the bonding length has been assessed. Fig. 3.20 displays the strain components during the elastic stage and at the peak, for the bonding lengths $L_b = 152.4$ mm and $L_b = 202.3$ mm. These bonding lengths are close to the asymptotic value predicted by Fig. 3.9b. The strain profiles have been evaluated at a distance from the front of the concrete block of 25.4 mm (blue line), 50.8 mm (red line), and 76.2 mm (green line). The results show that the strain diffusion in the concrete surrounding the FRP is substantially independently of Lb. The widths of the edge regions computed through the present model are smaller than those experimentally detected by Subramaniam et al. [91], who measured edge regions approximately 20 mm wide for both ε_{xz} and ε_{zz}. Analogously to Subramaniam et al. [91], the width of the edge regions measured in this study is independent of b. This width has not been imposed, and has been observed after post-processing the results. Indeed, the enriched layer of elements where the debonding is simulated has a width equal to that of the FRP plate. In Fig. 3.22, the dependence of the maximum stress $\sigma_u = P/(b_f t_f)$ transferable through the FRP plate width is displayed. The same figure displays the results obtained with the CNR-design formula reported in the appendix.
In Fig. 3.22, the dependence of the maximum stress transferable through the

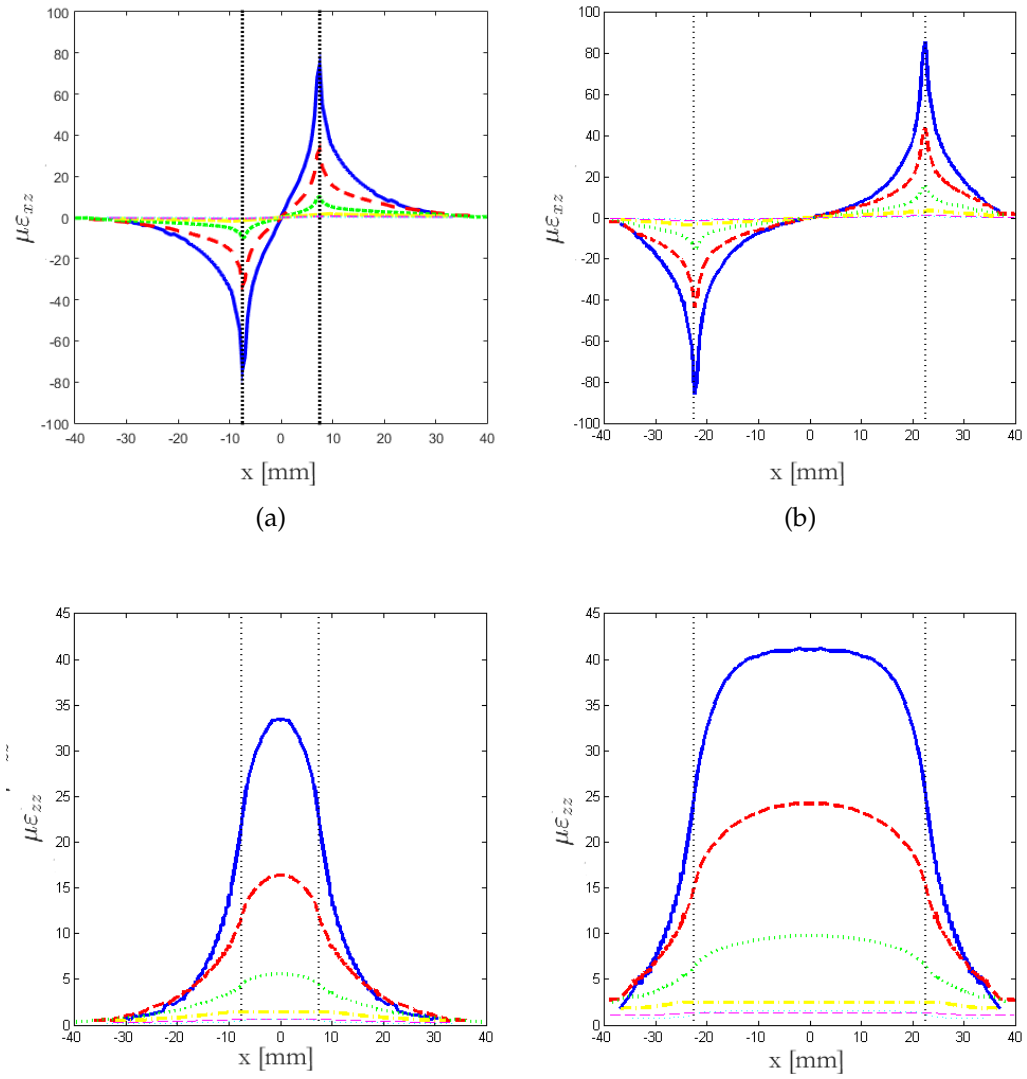

Figure 3.18: Front view of ε_{xz} (a) and ε_{zz} (b) along x during the elastic stage for $b = 15$ mm (on the left) and $b = 45$ mm (on the right) at $z = 0.5$ mm (cyan dotted line), $z = 18.1$ mm (pink dashed line), $z = 38.1$ mm (yellow dash-dotted line), $z = 58.1$ mm (green dotted line), $z = 78.1$ mm (red dashed line) and $z = 95.1$ mm (blu continuous line) for the test [96].

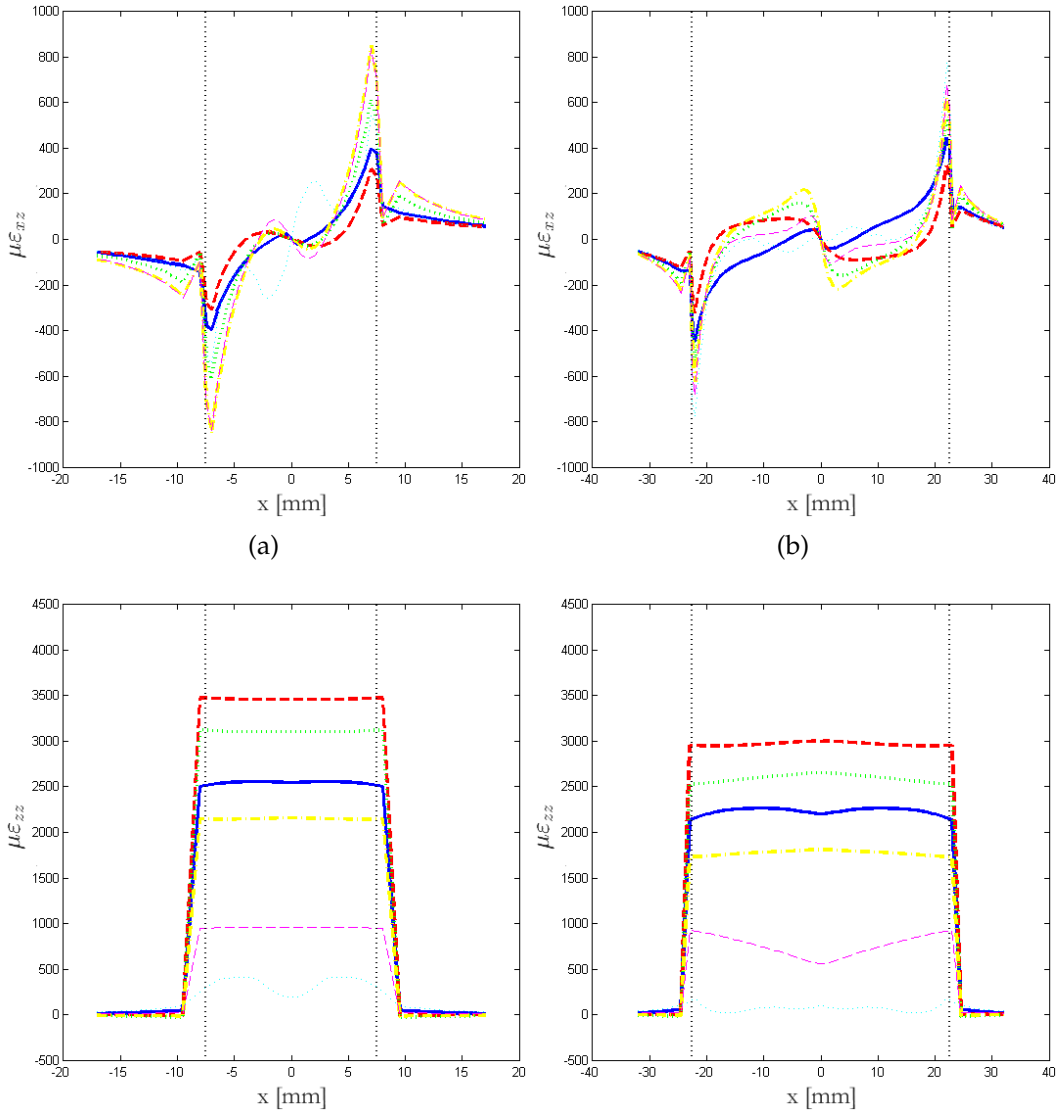

Figure 3.19: Front view of ε_{xz} (a) and ε_{zz} (b) along x at the maximum load for $b = 15$ mm (on the left) and $b = 45$ mm (on the right) in the test [96] (notation as in the previous figure)

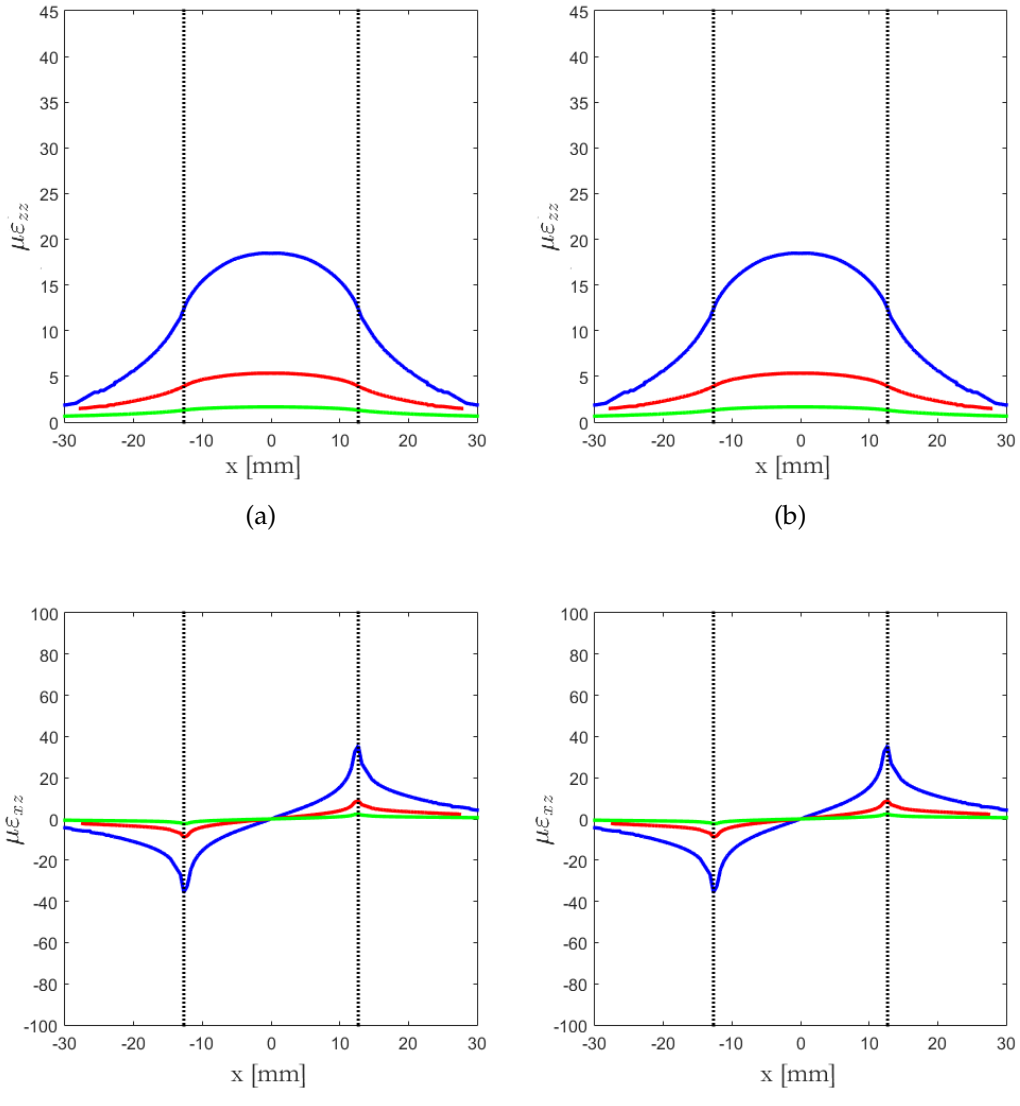

Figure 3.20: Front view of ε_{zz} (a,c) and ε_{xz} (b,d) along x during the elastic stage for $L_b = 152.4$ mm (on the left) and $L_b = 203.2$ mm (on the right) evaluated at a distance from the front of 25.4 mm (blue line), 50.8 mm (red line), and 76.2 mm (green line) for the test [96].

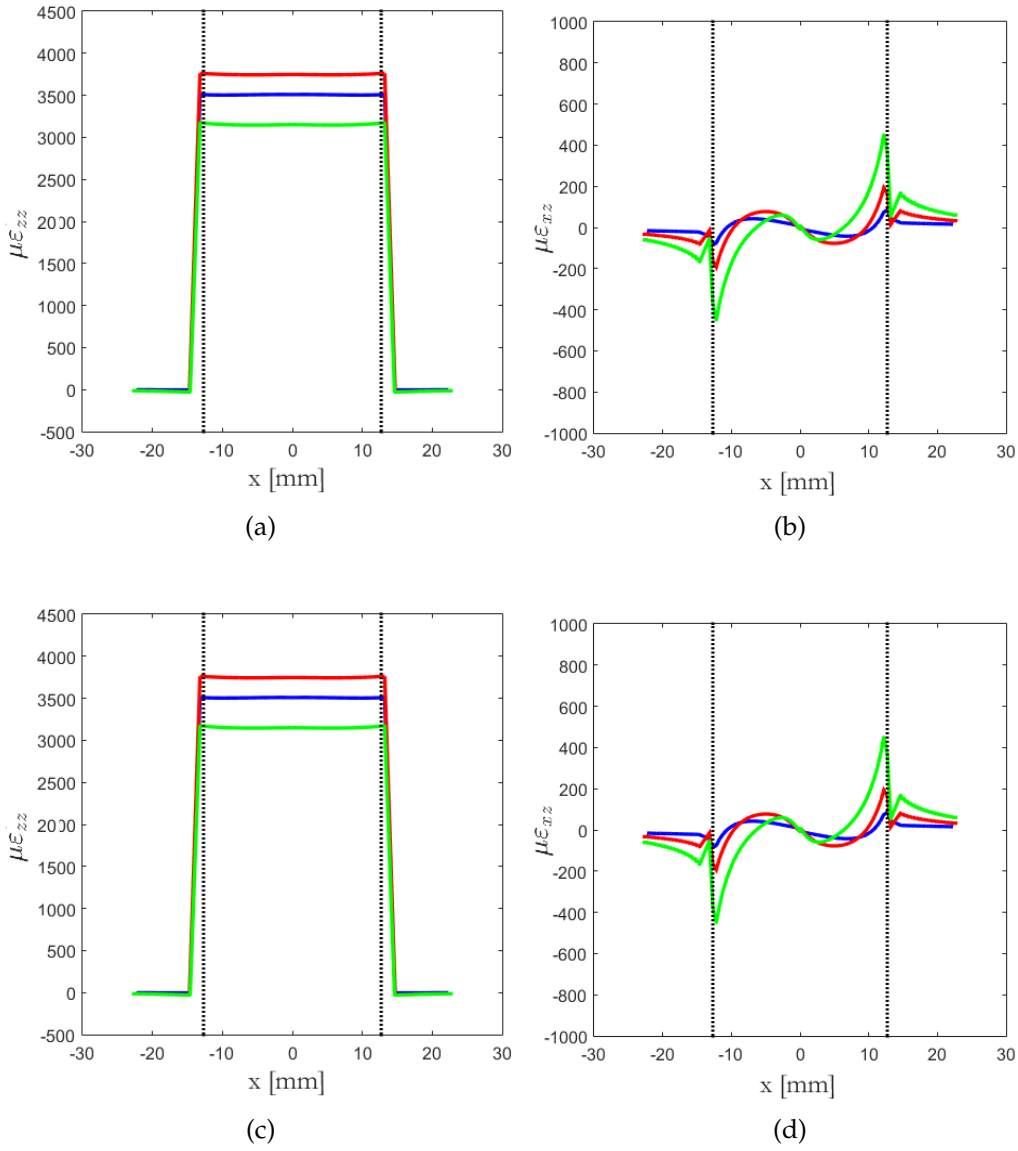

Figure 3.21: Front view of ε_{xz} (a,c) and ε_{zz} (b,d) along x at the peak load for L_b = 152.4 mm (on the left) and L_b = 203.2 mm (on the right) evaluated at a distance from the front of the concrete block of 25.4 mm (blue line), 50.8 mm (red line), and 76.2 mm (green line) for the test [96]

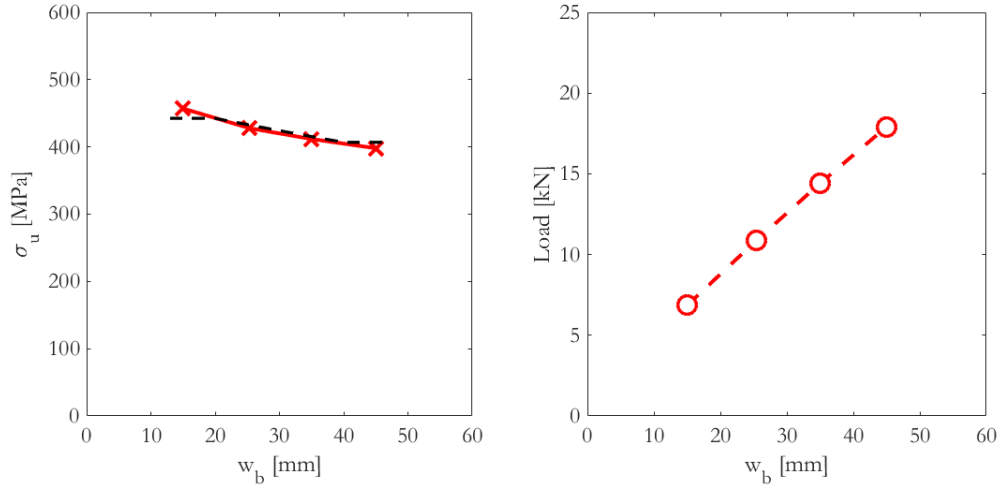

(a) (b)

Figure 3.22: Chajes et al. geometry: nominal stress and maximum load vs width; in Fig. a) the marked line denotes the CNR-design-rule formula setting $\kappa_g = 0.065$

FRP plate width is displayed. The same figure reports the results obtained with the CNR-design formula reported in the Appendix (Eq. 93)

3.4.2 *Discussion*

The agreement with the CNR rule [97] shown in Fig. 3.22a confirms that the developed computational model is a reliable design tool. The computed trend of the maximum transmissible stress shown in Fig. 3.22a is decreasing with increasing FRP plate width b and tends to an asymptote for large widths. On the contrary, based on their experimental tests, where the concrete widths B equal to 52 mm and to 125 mm were taken, Subramaniam et al. [90, 91] concluded that, below the critical value 0.5of the ratio b/B, the maximum transmissible stress increases for increasing width of the concrete support. On the other hand, Fig. 3.22b shows that the maximum transferable load increases with the width b. We have investigated also larger concrete widths B, but the same decreasing trend has been found. A more extensive numerical campaign is necessary to understand whether larger ratios b/B, namely larger concrete

supports, may correspond to an increasing ultimate stress for increasing b. Furthermore, the occurrence of peel stress can potentially affect the results for relatively small bonding lengths, such as in the current case.

To summarize, the results presented in this chapter have shown that:

- Where the FRP plate is still attached to the concrete substrate, the profiles of the strain components ε_{xz} and ε_{zz} along the length of the FRP plate are not uniform across the width, and display high gradients localized at edge regions of the FRP plate comprehensive of both the FRP plate edges and the surrounding concrete.
- Where debonding has been activated, the edge regions, intended as the regions with high gradients, corresponding to the ε_{xz} and ε_{zz} profiles are localized in a narrower zone.
- The edge regions corresponding to the ε_{xz} and ε_{zz} profiles have a width independent of b and L_b
- For the investigated geometries, the maximum transferable load increases for increasing width b of the FRP plate.
- For the assumed b/B ratios, the maximum load increases while the maximum stress transmissible through the FRP plate slightly decreases with the width in agreement with the CNR rules [97].

3.5 CONCLUSIONS

The 3D regularized XFEM approach with an experimentally consistent level set system has been employing for the investigation of two different experimental campaigns of single-lap shear tests. It has been shown that: i) the bending of the FRP plate plays a remarkable role on the debonding of the FRP plate; ii) an edge strengthening effect due to the shear strain localization occurs along the edges of the FRP plate; iii) the common design rules prescribing the variation of the nominal maximum stress with the bonded width of the FRP plates have been confirmed; iv) a two-way debonding can be observed. As for the question whether a 3D or a 2D analysis should be preferred, the obtained results have shown that, while the strain profiles along the FRP plate length, the peeling and the different debonding onset locations can be

detected indifferently through 3D and 2D analyses, the shear and axial strain on the debonded concrete surface display an edge effect that can be captured only by means of a 3D analysis. Moreover, the dependence of the maximum transferable load on the bonding width can be assessed only through a 3D analysis. Finally, the proposed 3D RE-XFEM approach fits, and can be used as an alternative to, experimental single-lap shear tests on FRP-reinforced concrete blocks.

4

DELAMINATION OF FRP FROM CONCRETE BENDED BEAM

4.1 INTRODUCTION

The previous chapter proves the suitability of the proposed 3D RE-XEFEM non linear procedure to study the debonding mechanism of FRP reinforcement of FRP from concrete blocks in pull-off tests. In this chapter, the focus is on the application of the presented model to a real application case such as the flexural strengthening of concrete beams. Experimental tests and numerical analyses have been intensively investigating the strengthening effect induced by FRP plates externally bonded to concrete beams, proving their suitability for the rehabilitation of engineering structures [87, 98]. Experiments have shown that FRP-plated concrete beams typically fail in a brittle manner after the detachment of the FRP plates from the concrete support along a surface a few millimetres thick and parallel to the FRP/concrete surface [99].

The term detachment includes both "debonding", indicating the detachment of the FRP plate due to the fact that the adhesive stops sticking to the FRP plate, and "delamination", intended as the separation of the plies of a composite. As the FRP plate is bonded to the concrete substrate by an adhesive layer, detachment can occur in the adhesive layer, in the concrete substrate, and at the interfaces between the FRP plate and the adhesive or the concrete substrate [99].

Detachment is a three-dimensional mechanism involving both opening and shearing displacements along the detachment surface [73, 88, 91, 100]. While Smith and Teng's [101] one-dimensional analytical interfacial law considers both normal and shear stresses [101], often, the FRP-concrete interface is modelled through bond-stress-slip laws [72], where the normal stress is not ac-

counted for [72]. On the other hand, Finite Element (FE) simulations exploit interfacial laws built-in commercial codes [73]. Thus, the parameters of the aforementioned interfacial stress laws have to be assumed a priori. Moreover, three-dimensional effects, such as the effects of the width of the FRP plate, are neglected. The detachment of FRP strengthened beams is triggered by high stress concentrations such as those arising at material discontinuities, and shear and flexural cracks arising at the end of the FRP plates or at the midspan of the beam [97, 99, 102, 103]. The most typical failure mechanisms being displayed in Fig. 4.1. For instance, in the intermediate-crack-induced interfacial debonding, also referred to as shear-flexural or intermediate detachment, detachment propagates from a region of high stress concentration, such as flexural or shear cracks, towards the plate-end, as shown in Fig. 4.1a. In the plate-end debonding of Fig. 4.1b, detachment propagates from the plate-end towards the midspan, often after concrete cover separation at the level of the longitudinal steel rebars[102, 104]. While plate-end detachment is more typical of steel-plated beams [105], shear-flexural detachment represents the dominant failure mechanism for FRP-plated concrete beams [104, 106–108], especially for comparatively long bonding lengths [109]. A qualitative picture of the distribution of the stresses at the FRP-concrete interface is shown in Fig. 4.2, where the peaks of the stress components σ_{yy}, τ_{yz}, σ_{zz} correspond to flexural or shear/flexural cracks. Detachment involves both opening and shearing of the FRP plate with respect to the concrete substrate. Namely, peeling and shearing stresses are expected along the interface between the FRP plate and the concrete beam [101]. Failure by detachment corresponds to the loss of structural stiffness associated with beginning and propagation of the FRP plate. In most cases, detachment takes place in the concrete [99, 110]. In shear and bending tests, a concrete layer remains attached to the delaminated FRP plate [9, 73, 111]. This concrete layer is sometimes thicker at the ends of the detached concrete layer, or in correspondence with large concrete aggregates [73]. The development of analytical and computational models of the FRP plate detachment from reinforced concrete beams is a complex task. Analytical models compute shearing and normal stresses at the interface between the beam and the FRP plate by the imposition of the equilibrium and compatibility conditions [102, 112–114]. However, most analytical models underestimate the importance of peeling stresses. This underestimation contrasts with what observed in single-lap shear tests on concrete blocks [9, 73], as demon-

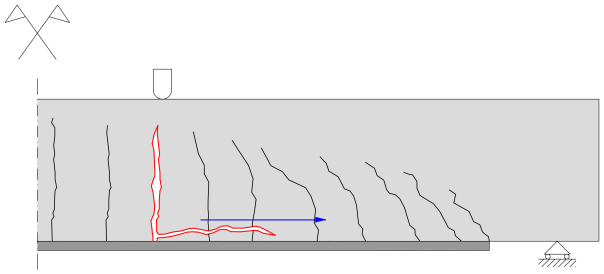

(a) Intermediate crack debonding

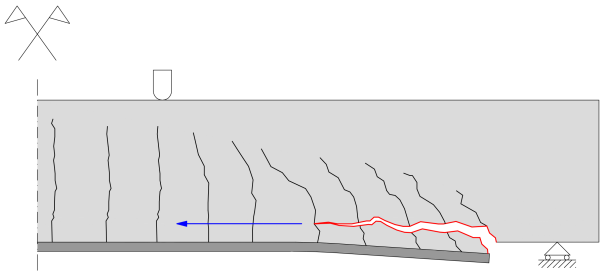

(b) Plate end separation/debonding

Figure 4.1: The main failure modes by FRP-detachment

strated in Ch. 2, where the values of peeling stresses are significant. Analytical interface laws are often implemented in Finite Element (FE) models. In particular, FE models simulate the surface of detachment either through discrete cracks along the element edges [37, 115, 116], or cohesive-crack laws [117–119]. Discrete crack models aim at simulating only dominant cracks. Their main drawbacks are mesh bias and the necessity of mesh adaptation [42]. On the other hand, cohesive-crack laws rule the traction-separation law of the surface of detachment. For the simulation of the debonding of FRP plates, interface elements analogous to cohesive laws have been adopted along the FRP-concrete interface. Most literature studies model the FRP-concrete interface by means of bond-slip laws obtained from pull tests on FRP-to-concrete joints [120, 121]. However, effective bond-slip laws require the knowledge of the fracture energy, the identification of model parameters of difficult determination, and depend on the actual debonding mechanism [109]. Furthermore, loss of convergence of existing FE models is quite common [122]. As for concrete, cracks are typically modeled through smeared cracks [123] and crack-band models [108, 124–127]. The latter overcome the primal mesh-dependency inherent

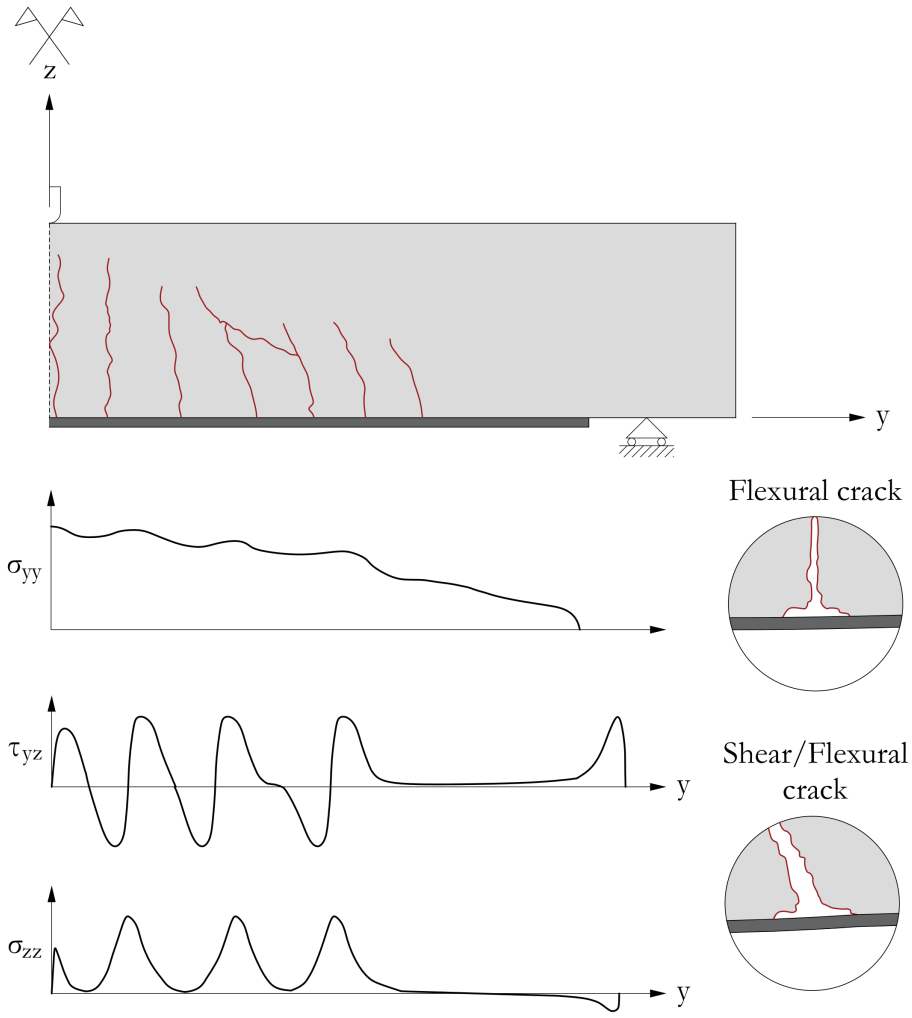

Figure 4.2: Qualitative picture based on [99] of the expected stress profiles at the interface between the FRP plate and the concrete

to the originally proposed smeared crack models by relating the smallest finite element size to the fracture energy [63]. However, both smeared crack and crack-band models distort and spread crack patterns [42]. Moreover, scaling the finite element size with the fracture energy introduces a secondary mesh-size dependency.

With respect to existing FE models based on bond-slip (interfacial) laws of difficult identification, the 3D RE-XFEM presented in Ch. 2 requires few physically-consistent material parameters.

This chapter contains the investigations on flexural detachment of FRP reinforcement from concrete beams by means the 3D RE-XFEM published in the journal papers [10, 11] and in the conference papers [128–131]. In particular, in Sec. 4.2 the flexural detachment of an FRP-strengthened Steel-Fiber-Reinforced-Concrete (SFRC) beam subjected to a three-point bending test is studied. Sec. 4.3 aims to study the detachment failure mechanisms of FRP-reinforced concrete beams under a four-point bending load. In the end, in Sec. 4.4 the main findings of the studies are listed.

4.2 FAILURE OF FRP-STRENGTHENED STEEL-FIBER-REINFORCED-CONCRETE BEAMS

4.2.1 *Introduction to SFRC materials*

Steel-Fiber-Reinforced-Concrete (SFRC) has been intensively used in civil engineering applications, such as tunnel linings, risers, pipes, covers, railways sleepers, repair of highway and airfield pavements, and several others [132]. The addition of steel fibers increases concrete toughness and ductility, and improves durability. Steel fibers induce a crack-bridging effect [133] that delays crack formation, spreads the cracks over a larger process zone while reducing the crack size [111, 132, 134, 135]. Externally-bonded FRP plates increase the strength of SFRC beams. To simulate SFRC beams strengthened with Fiber Reinforced Polymer (FRP) plates, reliable finite element (FE) models should take into account the steel fiber content, and follow the entire structural path. The few pertinent FE analyses focus on the cracking of the concrete by means of smeared-crack approaches [132, 136], while neglecting the detachment of the FRP plate. The present study proposes a regularized eXtended FE Model able to simulate crack pattern and detachment consistent with experiments. Fail-

ure of composite laminates has been intensively simulated through the XFEM by Iarve et al. [137, 138], Motamedi et al. [139], Wang and Waisman [140]. More specifically, in the context of the modelling of FRP-strengthened concrete blocks, the results presented in Ch. 3 have shown that the 3D RE-XFEM correctly captures the mechanism of detachment of the FRP plate, and three-dimensional edge effects.

The goal is to predict the structural behaviour of SFRC beams strengthened with FRP plates subjected to bending tests. The cornerstones of the proposed procedure are: i) the adoption of a regularized kinematics ruled by a regularization length that is related to the bridging effect exerted by the steel fibers; ii) a suitable variational formulation where stress superposition does not hold, iii) and a mechanism-based definition of the level set of the detachment-surface based on the detachment mode experimentally observed in experiments.

The main finding of the present study is that the entire structural path from early cracking to final FRP detachment is captured in perfect agreement with the reference experimental results.

The novelty is that the fiber bridging effect exerted by the fibers in the detachment zone of the FRP plate is captured by means of a regularized kinematics.

One of the advantages of using the proposed method is that the material parameters are directly used, and few model parameters are required.

The peculiarities of the proposed 3D RE-XFEM are already be described in Ch. 2. Sec. 4.2.4 is devoted to the simulation of the SFRC beams. In particular, after a validation of the procedure in the plain concrete case in Sec. 4.2.4.2, cracking pattern and structural results are compared with experimental data in Sec. 4.2.4.3.

4.2.2 *Premises on FRP reinforced SFRC beams*

After their addition to concrete mixtures, steel fibers are randomly distributed and act as crack arrestors [111, 134, 135]). The improvement of the mechanical properties depends on fiber type, and on the content of steel-fibers, from here on expressed as volume fraction V_f. Empirical stress-strain relationships for SFRC concrete are available in the CEB-FIP code [141], and other experimental studies [111, 142, 143]. According to [144], beginning and propagation of the

detachment detected in bending tests on SFRC beams strengthened with FRP plates occur in circumstances similar to that of plain concrete beams, namely detachment begins at the dominant crack and propagates along the direction of propagation that costs less energy. In most cases, a concrete cover of few centimeters remains attached to the detached FRP plate [145]. In a similar context, based on four-point bending tests on notched prisms made of concrete reinforced with steel-polypropylene hybrid fibres, Qian and Stroeven [146] drew that large steel fibers and polypropylene fibers significantly influence the load bearing capacity of fibers-reinforced concrete in the small displacement range, while the steel fibers affect most significantly the energy absorption capacity in the large displacement range.

In the present study, the tensile strength of the SFRC obeys the following empirical formula [143]

$$f_{ct,sp} = 0.63\ (f_{cm})^{0.5} + 0.288\ (f_{cm})^{0.5}\ I_r + 0.052\ I_r\,, \tag{46}$$

where $f_{ct,sp}$ is the splitting tensile strength, f_{cm} is the concrete compressive strength, and $I_r = V_f\ L_f/\phi_f$ is the fiber-reinforcing system index. The tensile strength f_t is deduced from $f_{ct,sp}$ by means of the relationship $f_t = 0.9 f_{ct,sp}$ [141].

4.2.3 *Mechanism-based local level set*

The mechanism of detachment assumed in the present study relies on the physically-consistent hypotheses that: i) the detachment surface is parallel to the adhesive layer and is contained in a concrete layer adjacent to the FRP plate of about 10 mm of thickness, and ii) it is the result of the coalescence of several inclined cracks orthogonal to the maximum principal stress direction $\boldsymbol{n}_l$ [147] (Fig. 4.4). Besides being corroborated by the experiments, these hypotheses are usual in two-dimensional FE analysis and in numerical models based on one-dimensional bond-stress laws [72, 73]. Fig. 4.4 shows the *local* level set adopted on half of the beam, for symmetry. In the figures, the field of the normal vector $\boldsymbol{n}_l$ of the local level set has been reported over the detachment surface. However, it has to be extended to the whole V_ρ. Different colours reflect different directions. The vectors in blue associated with the edges of Ω_ρ are oriented outwards the edge along the direction $(0, -1, 0)$. The vectors in green in the interior of Ω_ρ are oriented along the direction

$(0, -\sqrt{3}/2, 1/2)$. The solution of the non-linear iterative-incremental procedure will then decide the final directions of the principal stresses, that do not generally coincide with those of $\boldsymbol{n}_l$.

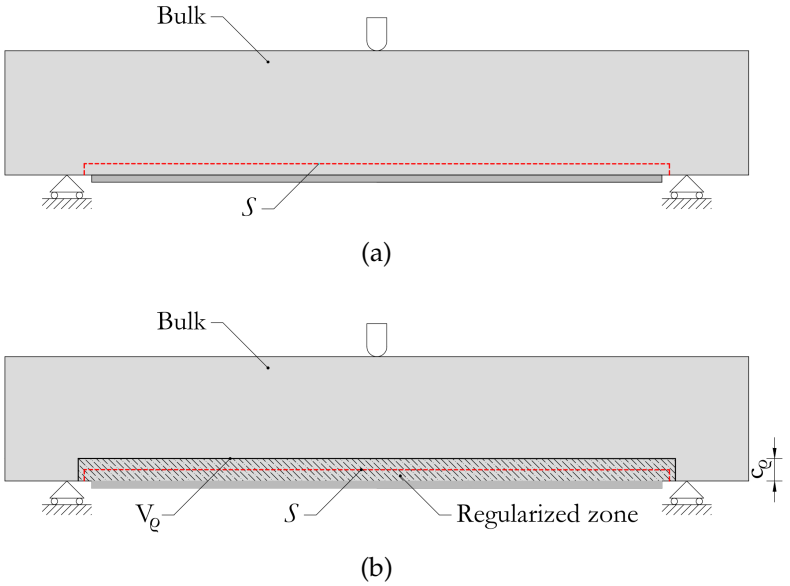

Figure 4.3: Beam reinforced with an FRP plate on the bottom: from the zero-thickness detachment surface (a) to the regularized detachment zone (b)

4.2.4 *Results*

The present section assesses the ability of the proposed approach to correctly capture the load-displacement results for variable steel-fibers content. The model geometry and parameters are defined in Sec. 4.2.4.1. The parameters that change with V_f is ρ, through a linear relationship, and f_t, through the experimentally-determined relationship (46). For the analyses, the vertical displacement of the midspan section has been used for the arc-length control procedure. Noteworthy, a displacement control method cannot be used to reproduce the expected structural profiles.

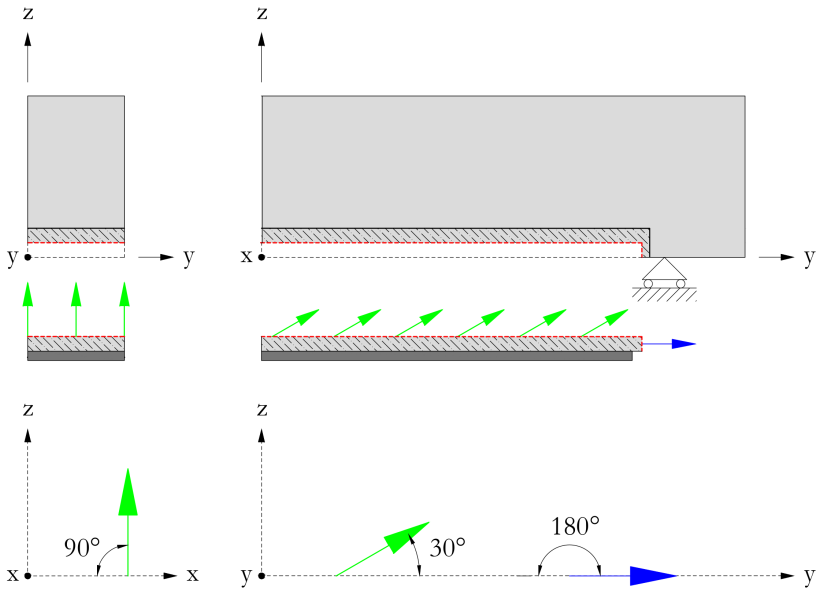

Figure 4.4: Local level set system for the definition of vector $\boldsymbol{n}_f$

4.2.4.1 *Geometry, material and model parameters*

The reference experiment is the series of three-point bending tests carried out by Yin and Wu [144] on the SFRC beam strengthened with an FRP plate in Fig. 4.6. To reduce the computational burden, owing the double-symmetry of the problem, only a quarter of the specimen has been meshed by tetrahedral FE (Fig. 4.7). In the reference experiment, short steel-fibers of length $l_f = 0.30$ mm and diameter $\phi_f = 0.5$ mm were added to the concrete mixture to obtain the SFRC. The elastic moduli of the experimental campaign are assumed. In particular, the concrete has Young modulus $E_c = 25$ GPa and Poisson ratio ν=0.2. The tensile strength of the concrete $f_t = 2.89$ MPa has been estimated through Eq. (46). Moreover, the FRP plate has Young modulus $E_{FRP} = 230$ GPa, thickness $s = 0.11$ mm, and Poisson ratio $\nu = 0.248$. Whereas the concrete and the detachment zone are assumed made of a homogeneous elasto-damaging material, the FRP is assumed linear elastic. In the simulations, the only model parameters to be identified are the regularization length ρ, the softening parameter H_s of the damage law, and the critical damage threshold d_{cr}. Parameter H_s has been set equal to 0.008 and the tensile strength of the SFRC $f_t = 2.89$ MPa. The damage threshold has been chosen

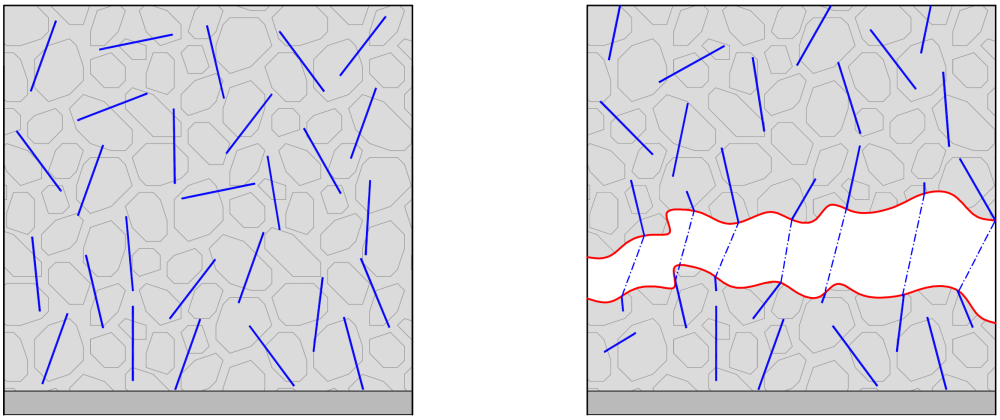

(a) SFRC fiber bridging

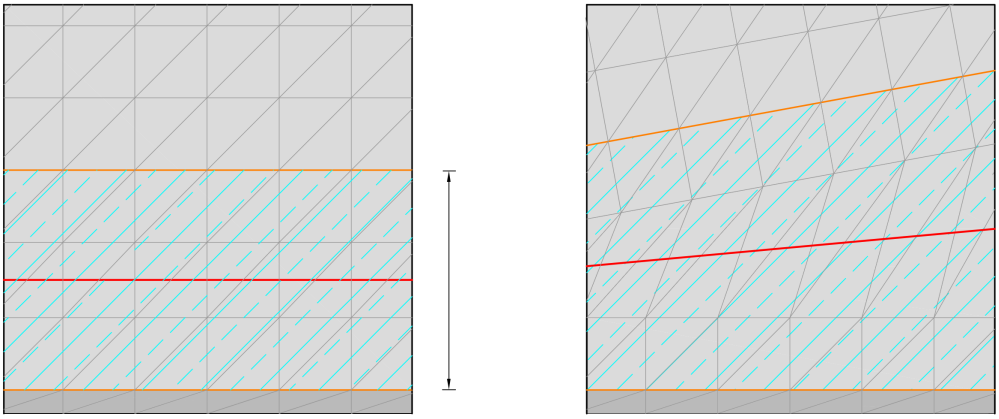

(b) 3D RE-XFEM Model

Figure 4.5: Model of the fiber bridging effect of the SFRC material during the detachment process: from the real physics (a) to the 3D RE-XFEM approach (b)

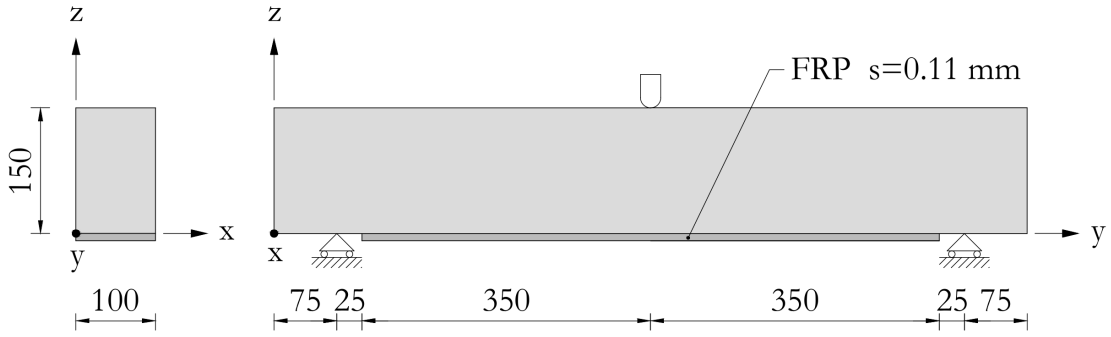

Figure 4.6: Geometry of the specimen of Yin and Wu [144] with dimensions in mm

equal to 0.99. Keeping the value of ρ fixed and varying the mesh size, both sub-elemental and super-elemental enrichment strategies described in detail in Sec. 2.2 have been adopted.

The failure recorded in the experiments for V_f =1.0% occurs by rupture of the FRP plate, possibly due to a flaw of the FRP plate. This failure mode is not taken into account in the present analysis, because of the hypothesis of linear elasticity for the FRP.

4.2.4.2 *Validation of the 3D RE-XFEM formulation on a beam of plain concrete reinforced with an FRP plate*

The current section validates the results obtained by means of the 3D RE-XFEM developed in the previous sections. This goal is accomplished through the comparison with the experimental results in the case where the steel fibres are absent. In particular, the three-point bending test of Sec. 4.2.4.1 is considered. The goal of the section is to show that crack development, detachment and structural response are correctly captured.

As described in Ch. 2, the adoption of softening damage laws in FE models leads to possible mesh-size dependence of the computed structural results, because the structural response converges to elastic unloading for decreasing size of the mesh of the process zone [148]. An additional source of mesh-dependence arises because the detachment of the FRP plate from the concrete beam implies a sudden loss of the structural stiffness for decreasing mesh size. The former source of mesh dependence, namely that associated with softening damage laws, can be tackled by means of regularization models [61,

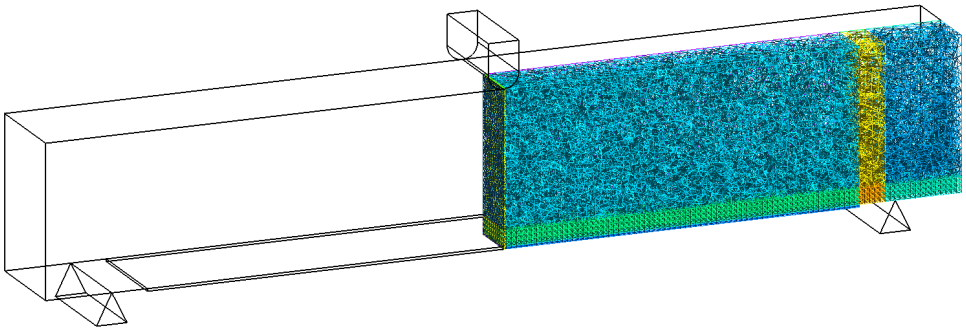

(a) Mesh

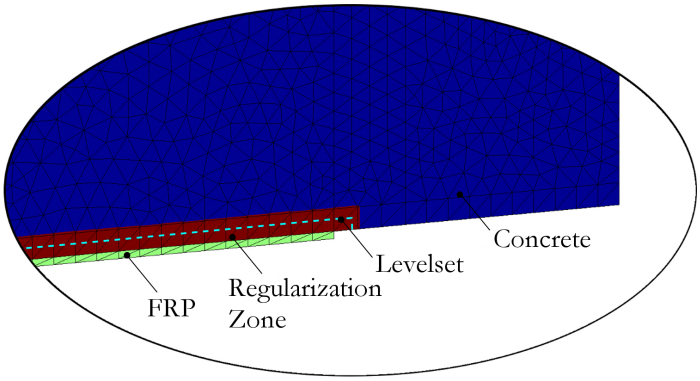

(b) Coarse mesh

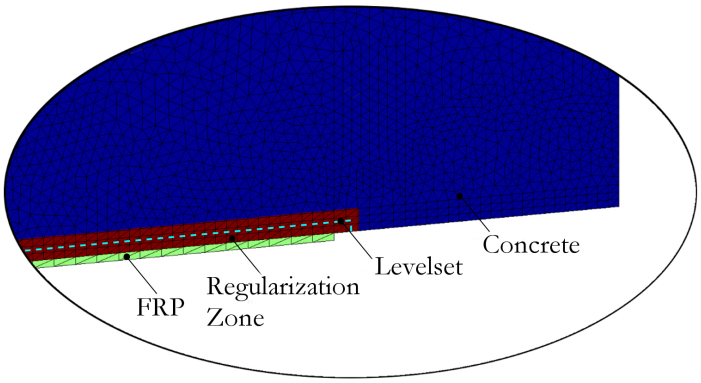

(c) Fine mesh

Figure 4.7: Plain concrete: coarse and fine mesh employed for the mesh independence analysis

148–151], or, in alternative, by means of the 3D RE-XFEM developed for strain localization problems [4]. In the present study, only the latter source of mesh dependence, namely that associated with the loss of stiffness during the detachment of the FRP plate, is tackled by means of the 3D RE-XFEM approach illustrated in Ch. 2. This choice is based on the assumption, to be verified in the following, that the detachment of the FRP plate is the main source of sharp snap-backs of the structural response. To verify the reliability of the proposed model, the mesh-independence of the results has been investigated. For this purpose, the two meshes of 83701 and 234638 elements of Fig. 4.7 have been adopted. Fig. 4.8 compares the load vs midspan deflection curve with the homologous experimental profiles. The agreement is highly satisfying. The computed structural response is almost independent of the mesh size. Fig. 4.9 shows that, in the fine mesh, the damage is more localized in narrow strips than in the coarse mesh. This is not surprising as the damage law of the concrete has not been regularized. However, the obtained results are satisfying for the following reasons. First, the structural behavior has been correctly reproduced. Second, the crack pattern of the concrete is consistent with the experimental results, whereas regularized damage laws like nonlocal damage or smeared-crack based laws would spread the concrete damage in wide regions [132, 136, 144] that do not fully correspond to the crack pattern observed experimentally. It remains to prove that the implemented continuous-discontinuous procedure ensures a smooth process of detachment of the FRP plate. To this aim, a comparative analysis for variable ρ has been carried out, whose results are reported in Fig. 4.10. If a vanishing ρ is adopted, or if ρ is too small, namely if a strong discontinuity formulation without regularization is adopted, a spurious failure can be observed in the structural response. Failure corresponds to the almost vertical dotted branches in which the structural profiles terminate. On the contrary, increasing values of ρ delay the final failure and make the detachment of the FRP plate possible. Namely, it is the presence of the FRP plate that delays the failure of the beam, and the regularization ensures that the detachment of the FRP plate is reached smoothly so to prevent initial brittle failure of the beam. For $\rho = 0.1875$ mm, Fig. 4.11, 4.12, 4.13, and 4.14 display the crack pattern in the deformed configuration, and the stresses computed at the FRP-concrete interface for different stages of the structural response, denoted A, B, C, and D in Fig. 4.8. The computed crack pattern is consistent with the experimental results. Fig. 4.11 and

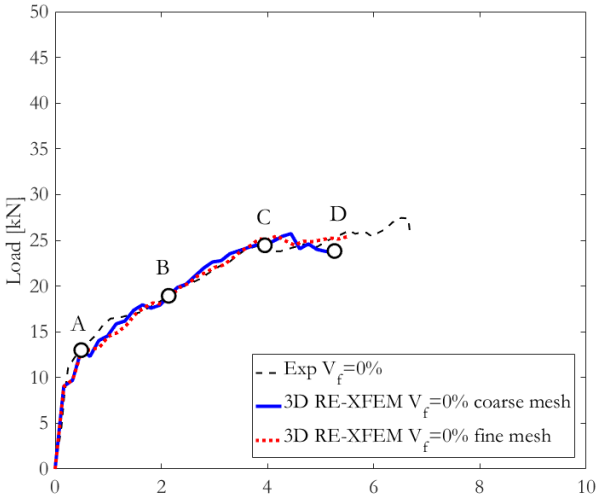

Figure 4.8: Plain Concrete: comparison among the experimental and numerical load vs midspan-deflection curves, where the black dashed line, the blue continuous line, and the red dotted line indicate the experimental test [144], the 3D RE-XFEM result for the coarse mesh, and the 3D RE-XFEM result for the fine mesh, respectively

Fig. 4.12 illustrate the stages of crack beginning and crack propagation. Like in the experimental test, the first cracks of the concrete develop at the midspan of the specimen, followed by two main lateral flexural cracks. Fig. 4.13 and Fig. 4.14 show respectively the initial and final stage of the detachment process. Detachment propagates from the flexural cracks towards the FRP plate end. As the detachment is complete, the beam fails by brittle failure.

4.2.4.3 *The case of variable V_f*

The structural responses of SFRC beams strengthened with the FRP plate computed for $V_f = 0.25\%, 0.50\%, 1.00\%$ have been compared with the experimental results. According to Eq. (46), the tensile strength f_t are equal to 3.1 MPa, 3.3 MPa, and 3.75 MPa for increasing V_f. The remaining material properties are the same as that used for plain concrete. To account for the presence of the steel fibers, the linear relationship of Fig. 4.15 between regularization parameter ρ and volume fraction V_f is adopted. The load vs midspan deflection curves of the numerical and the experimental results for

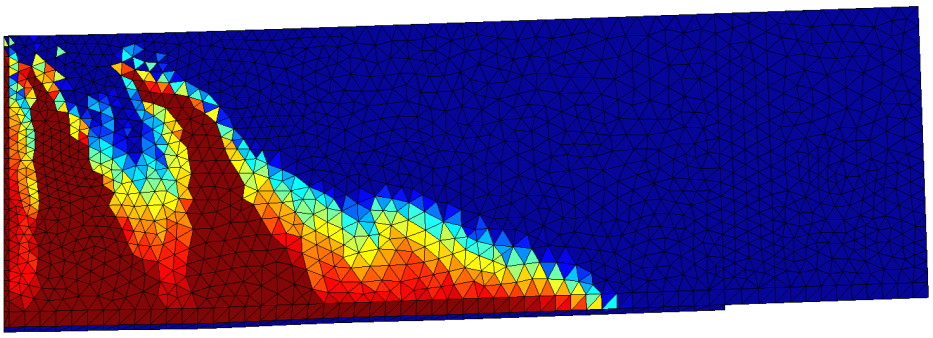

(a) Coarse Mesh

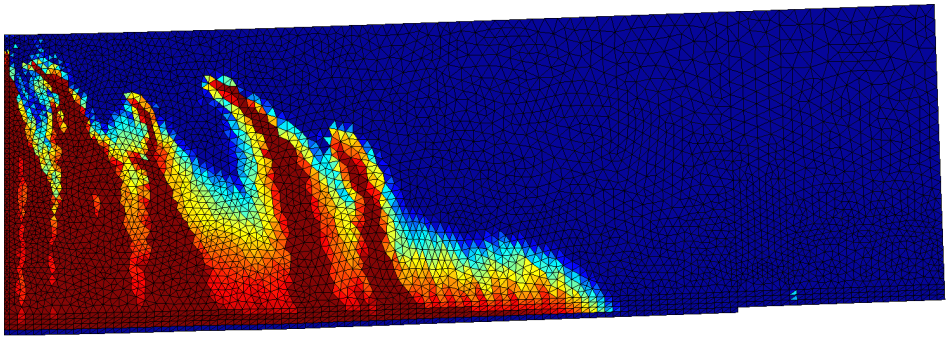

(b) Fine Mesh

Figure 4.9: Plain concrete: comparison between the damage pattern computed with the coarse (a) and the fine mesh (b) at the beginning of detachment (Step C in Fig. 4.8)

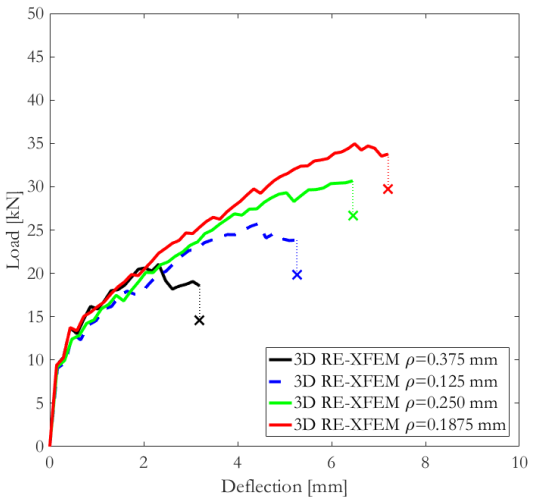

Figure 4.10: Influence of the regularization parameter ρ on the structural response of the FRP-reinforced beam for $\rho = 0.125$ mm (black thick continuous line), $\rho = 0.1875$ mm (blue thin dashed line), $\rho = 0.250$ mm (green continuous line) and $\rho = 0.375$ mm (red thick dashed line)

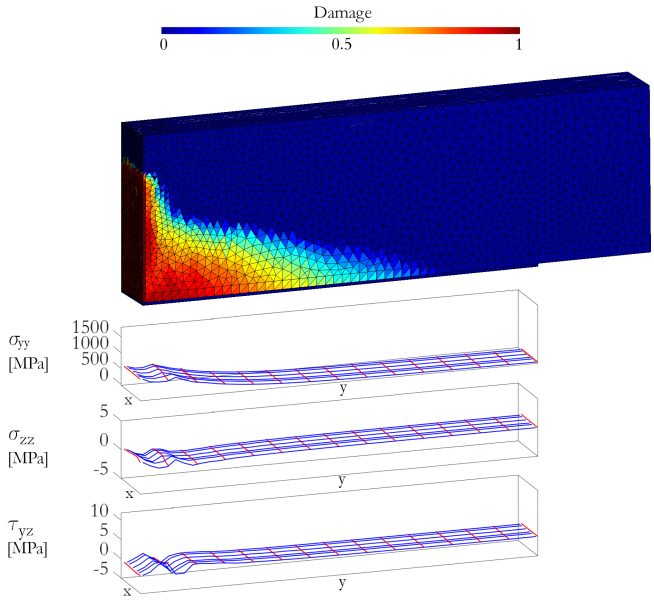

Figure 4.11: Plain Concrete: damage and stresses σ_{yy},σ_{zz} and τ_{yz} at step A of Fig. 4.8 on the top of the FRP plate

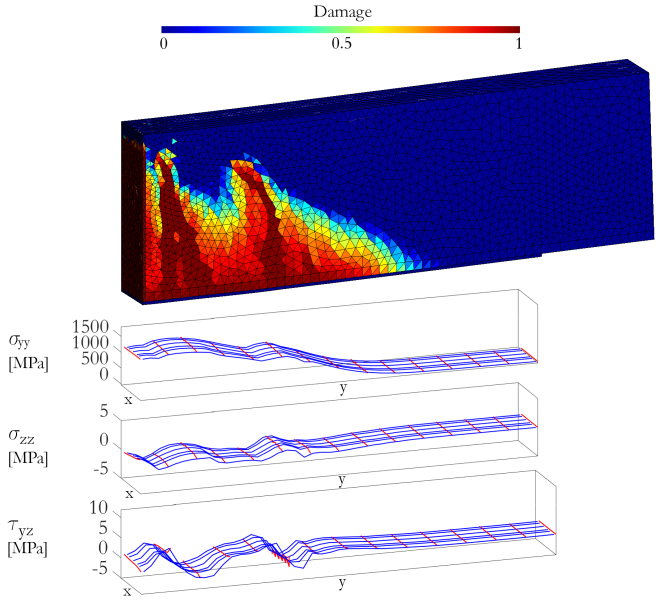

Figure 4.12: Plain Concrete: damage and stresses σ_{yy},σ_{zz} and τ_{yz} at step B of Fig. 4.8 on the top of the FRP plate

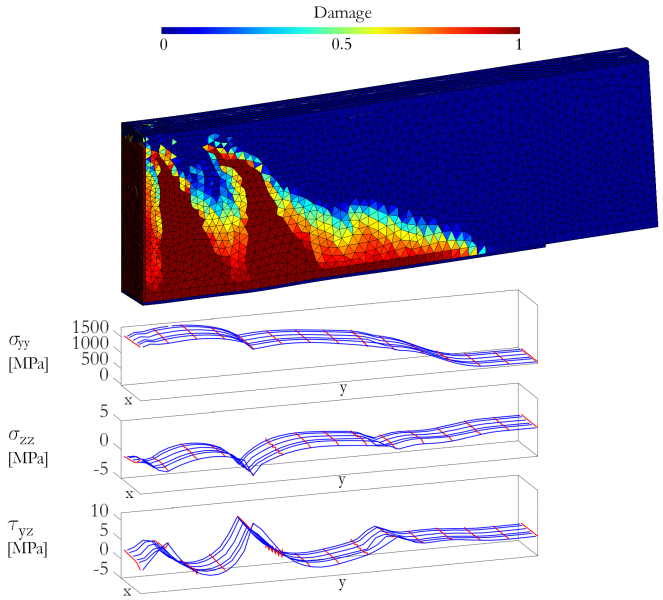

Figure 4.13: Plain Concrete: damage and stresses σ_{yy},σ_{zz} and τ_{yz} at step C of Fig. 4.8) on the top of the FRP plate

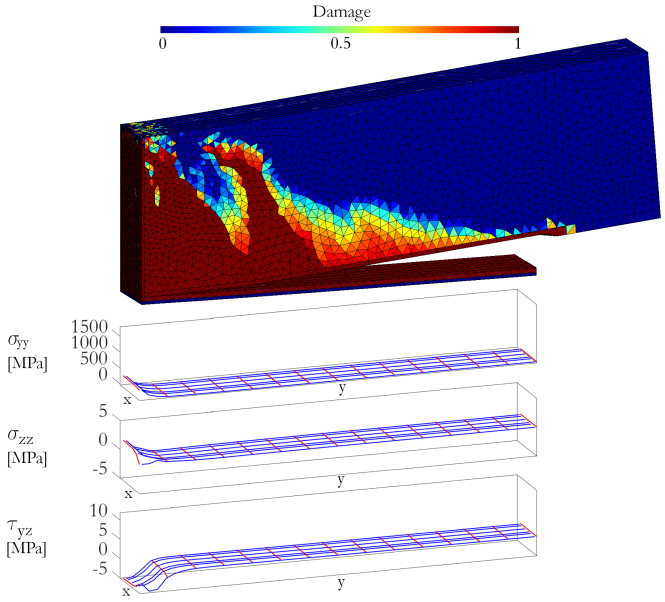

Figure 4.14: Plain Concrete: damage and stresses σ_{yy},σ_{zz} and τ_{yz} at step D of Fig. 4.8) on the top of the FRP plate

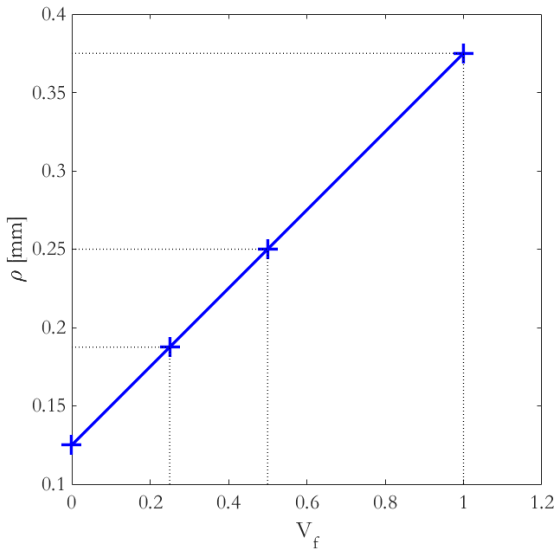

Figure 4.15: Adopted linear relationship between V_f and the regularization parameter ρ

$V_f = 0.25\%, 0.50\%, 1.00\%$ are available in Fig.4.16. The agreement between numerical and experimental load vs midspan deflection is satisfying. In both

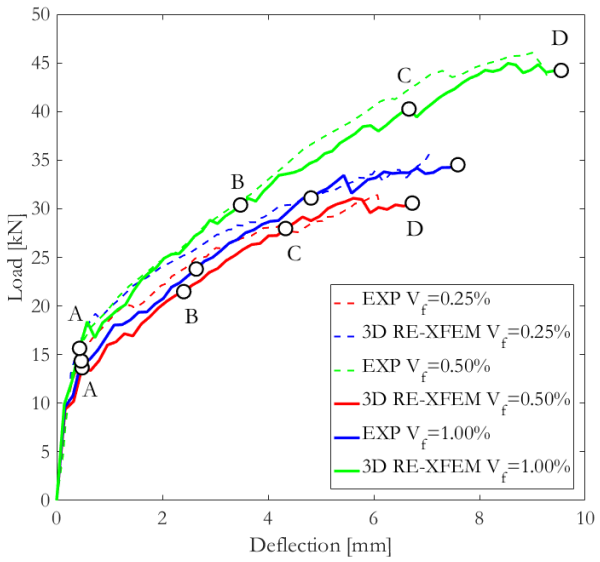

Figure 4.16: SFRC: Comparison between experimental test and numerical results of the load-midspan deflection curve for $V_f = 0.25\%$, $V_f = 0.50\%$, and $V_f = 1.00\%$

experiments and simulations, crack activation and propagation and final detachment detected for $V_f = 0.25\%, 0.50\%$ are similar to that observed for $V_f = 0\%$, except for the fact that, for increasing V_f, cracks multiply and are more distributed along the beam. In particular, damage and stress profiles have been detected at stages A, B, C, and D in Fig. 4.16. The results of Fig. 4.17, 4.18, 4.19, and 4.20 display the crack pattern and the stress profiles along the FRP plate surface computed for $V_f = 0.25\%$. Analogous profiles for the maximum $V_f = 1\%$ are shown in Figs. 4.21, 4.22, 4.23 and 4.24. For increasing load, diagonal cracks form towards the lateral beam support, followed by the development of micro-cracks at the FRP-concrete interface. Finally, the detachment progresses rapidly along the detachment surface up to subsequent beam failure.

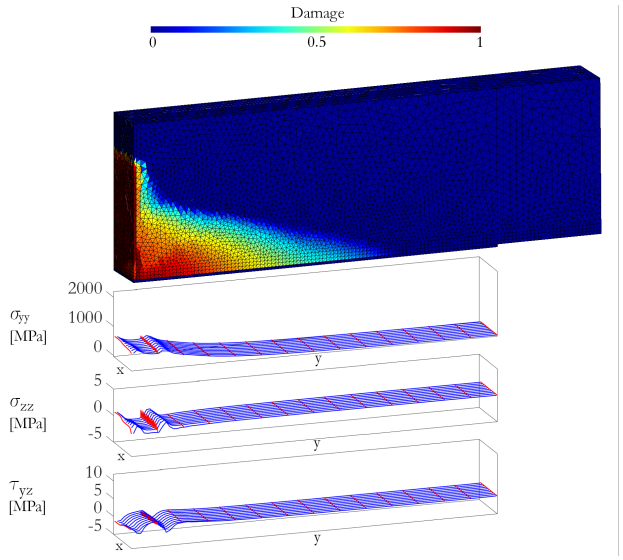

Figure 4.17: SFRC: Damage and stresses σ_{yy}, σ_{zz} and τ_{yz} for $V_f = 0.25\%$ at step A of Fig. (4.16) plotted on the top of the FRP plate

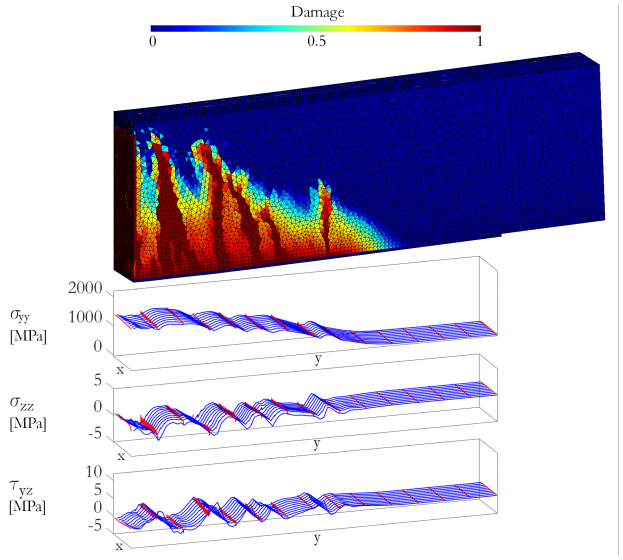

Figure 4.18: SFRC: Damage and stresses σ_{yy}, σ_{zz} and τ_{yz} for $V_f = 0.25\%$ at step B of Fig. (4.16) plotted on the top of the FRP plate

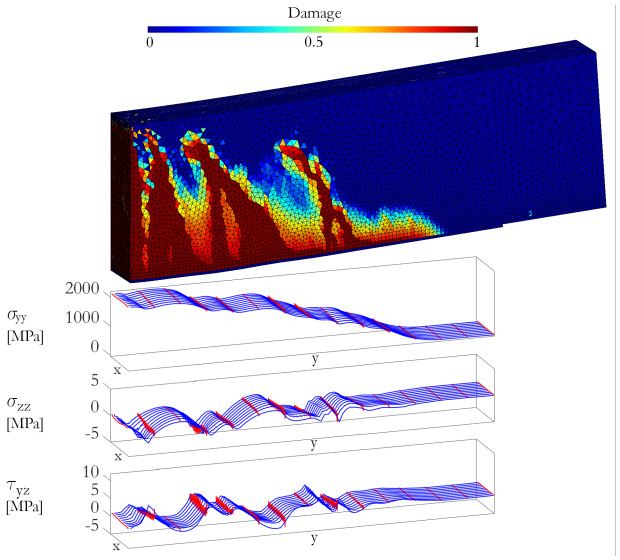

Figure 4.19: SFRC: Damage and stresses σ_{yy}, σ_{zz} and τ_{yz} for $V_f = 0.25\%$ at step C of Fig. (4.16) plotted on the top of the FRP plate

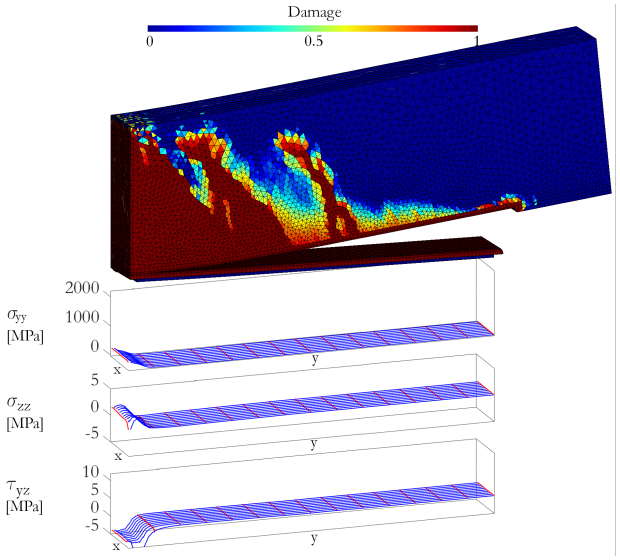

Figure 4.20: SFRC: Damage and stresses σ_{yy}, σ_{zz} and τ_{yz} for $V_f = 0.25\%$ at step D of Fig. (4.16) plotted on the top of the FRP plate

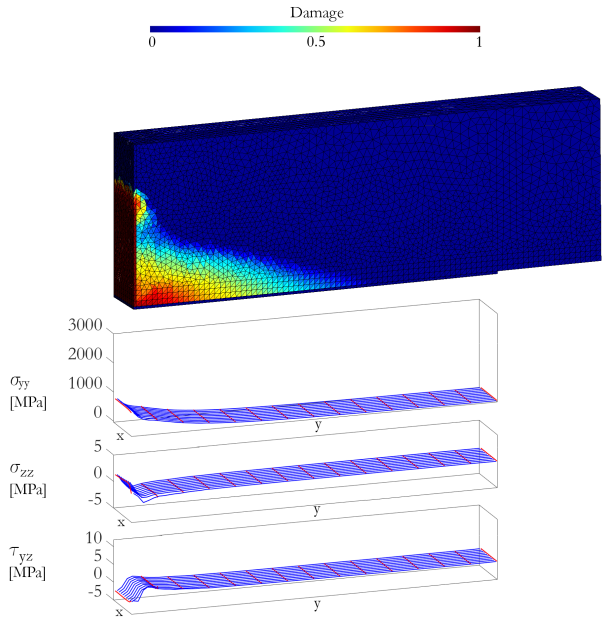

Figure 4.21: SFRC: Damage and stresses σ_{yy}, σ_{zz} and τ_{yz} for $V_f = 1\%$ at step A of Fig. (4.16) plotted on the top of the FRP plate

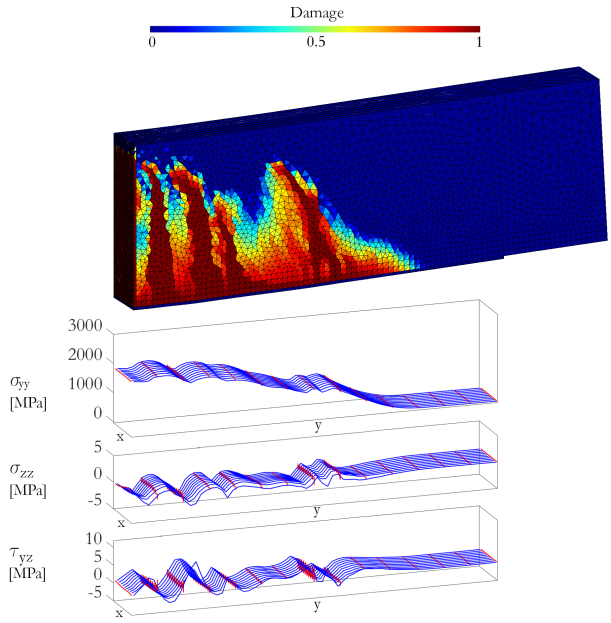

Figure 4.22: SFRC: Damage and stresses σ_{yy}, σ_{zz} and τ_{yz} for $V_f = 1\%$ at step B of Fig. (4.16) plotted on the top of the FRP plate

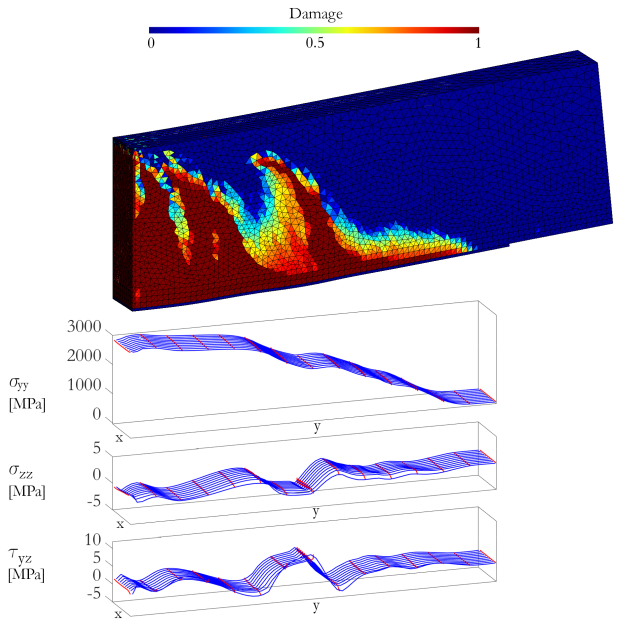

Figure 4.23: SFRC: Damage and stresses σ_{yy}, σ_{zz} and τ_{yz} for $V_f = 1\%$ at step C of Fig. (4.16) plotted on the top of the FRP plate

4.2.4.4 *Remarks*

In the experimental results [144], the addition of steel-fibers into the concrete mixture significantly increased the maximum load, and enhanced the ductility of the post-peak branch. Moreover, for increasing V_f, the cracks tended to be more distributed and numerous. Detachment started at the midspan section and moved towards the plate ends. Failure was reached due to the detachment of the FRP plate, except in the case of $V_f = 1.0$ %, where failure occurred by breakage of the FRP plate at the midspan section. In the remaining cases, failure came after formation of a diagonal flexural/shear cracks, followed by sudden detachment of an FRP-concrete cover approximatively 1 cm thick. The values of the normal stress component σ_{yy} experimentally detected on the FRP plate at the beginning of the detachment process for $V_f = 0.25\%$ and $V_f = 1.00\%$ were 1900 MPa and 3000 MPa, respectively.

In the simulations, the detachment of the FRP plate occurs mainly by shearing and opening along the FRP plate. Moreover, the computed maps of the damage delineate flexural and flexural/shear cracks. After total detachment

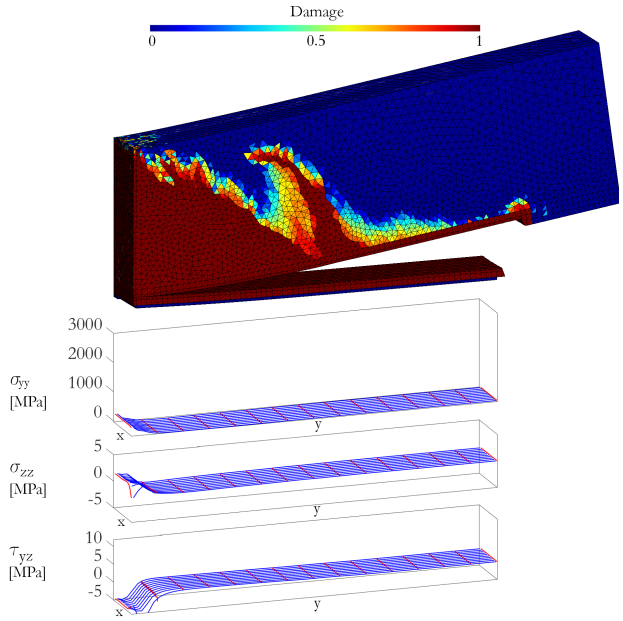

Figure 4.24: SFRC: Damage and stresses σ_{yy}, σ_{zz} and τ_{yz} for $V_f = 1\%$ at step D of Fig. (4.16) plotted on the top of the FRP plate

of the FRP plate, the failure of the beam is brittle. In the simulations, detachment starts in correspondence with flexural and shear-flexural cracks and not at the FRP plate ends. This can be ascribed to the fact that the thickness of the FRP plate, and, thus, its flexural stiffness, are very small compared to the beam.

Numerical and experimental load-displacement profiles are almost coincident. The simple linear law $\rho - V_f$ assumed in the model makes it possible to perfectly capture the increase of maximum loads and midspan deflection at failure detected in the experiments. Noteworthy, the numerical damage map and the experimental crack pattern are compared in Fig. 4.25, where the crack lines detected in the experimental tests [144] are in black, and the red zone indicates where the damage variable $d = 1$. The damage map almost superposes with the experimental crack pattern. Fig. 4.19 and 4.23 display values of the peaks of stress component σ_{yy} very close to the experimental ones.

Unlike existing FE analyses based on smeared-crack models or non-local models [132, 136, 144], where the detachment of the FRP plate is not explicitly modelled, and the crack pattern in the concrete is spread over large regions,

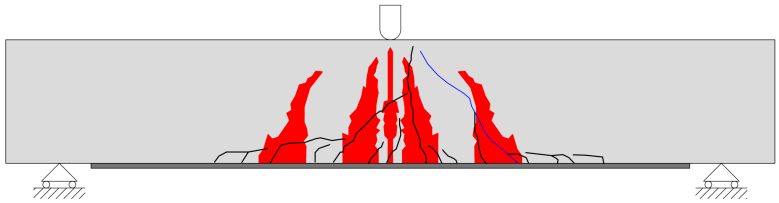

(a) $V_f = 0.00\%$

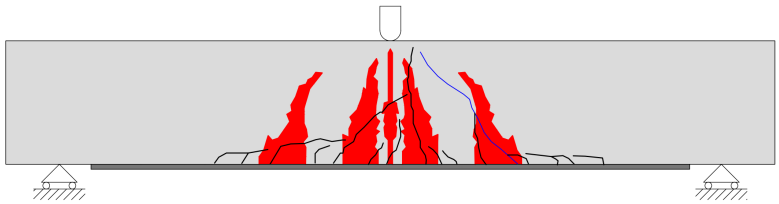

(b) $V_f = 0.25\%$

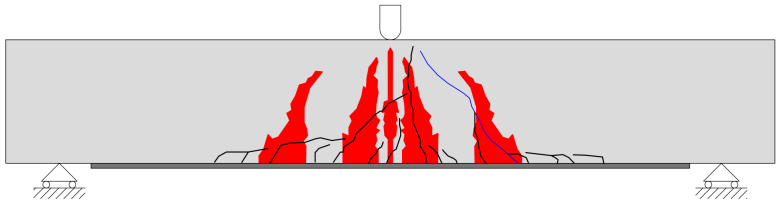

(c) $V_f = 0.50\%$

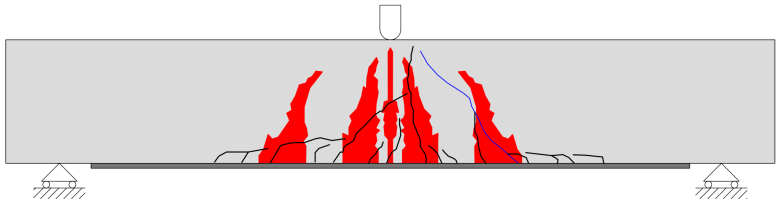

(d) $V_f = 1.00\%$

Figure 4.25: Superposition of the experimentally detected crack pattern [144] (black cracks) and the numerically obtained damage map (in red, for damage 1) for $V_f = 0\%, 0.25\%, 0.5\%, 1\%$, from the top to the bottom

the present 3D RE-XFEM procedure is more consistent with the crack pattern experimentally detected and makes it possible to follow the entire load-displacement path, comprehensive of both crack development and FRP plate detachment.

The main limitation of the present approach is that no damage in compression is taken into account for the concrete. However, the proposed 3D RE-XFEM procedure can accommodate any desired elasto-damaging constitutive law, such as that proposed by Comi [149] for concrete damage in tension and compression. Moreover, this assumption does not jeopardize the ability of the proposed model to capture the salient features of the structural response.

4.3 FOUR POINT BENDING

The mechanism-based 3D RE-XFEM has succeeded in modeling single-shear lap tests in Ch. 3 [3, 9] and three-point bending tests carried out on steel-fibre-reinforced concrete beams in Sec. 4.2 [10]. This section is dedicated to applied for the first time the proposed methodology to FRP-strengthened RC beams. What makes the present application different from the previous ones is the interplay between the strengths of the concrete, the FRP plate and the steel rebars.

4.3.1 *The mechanism-based detachment mode*

As already assessed, the surface of detachment results from the coalescence of meso-cracks developing in the concrete along a direction almost orthogonal to the direction $\boldsymbol{n}_I$ of the maximum principal tensile stress [109, 152]. In mixed-mode loadings, these meso-cracks are not orthogonal to the macro-surface of detachment [109, 147]. A possible qualitative picture of the expected meso-cracks developing in the detachment zone for the expected detachment mode is displayed in Fig. 4.26. In the mechanism-based 3D RE-XFEM, the

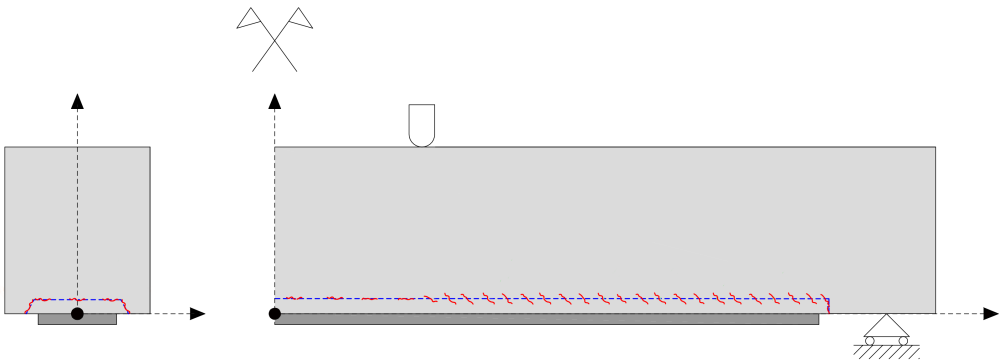

Figure 4.26: Qualitative description of the cracks diffused along the detachment surface

knowledge of the vector field $\boldsymbol{n}_I$ is crucial to the computation of the stress fields, as explained in Ch. 2. To this purpose, the directions of the expected meso-cracks are assumed, and, thus, the vector $\boldsymbol{n}_I$ is taken perpendicular to

the directions of the assumed meso-cracks. This way, the computation of the principal stresses at each integration points is avoided, and $\boldsymbol{n}_l$ becomes a sort of model vector, that allows unblocking the detachment of the enriched layer. Fig. 4.27 shows the field of vector fields $\boldsymbol{n}_l$ above the FRP plate in the detachment zone. The different directions of $\boldsymbol{n}_l$ are highlighted with different colors. In particular, $\boldsymbol{n}_l$ between the loadings is aligned along the yellow $(0, 0, 1)$ vectors. In the span from the loading point to the plate end, the direction of $\boldsymbol{n}_l$ coincides with that of the green $(0, 1/2, 3/2)$ vectors. To allow for plate end detachment, at the back edge and along the side edges, $\boldsymbol{n}_l$ is aligned with vectors $(0, 1, 0)$, in blue, and $(3, 1, 3)$, in orange, respectively.

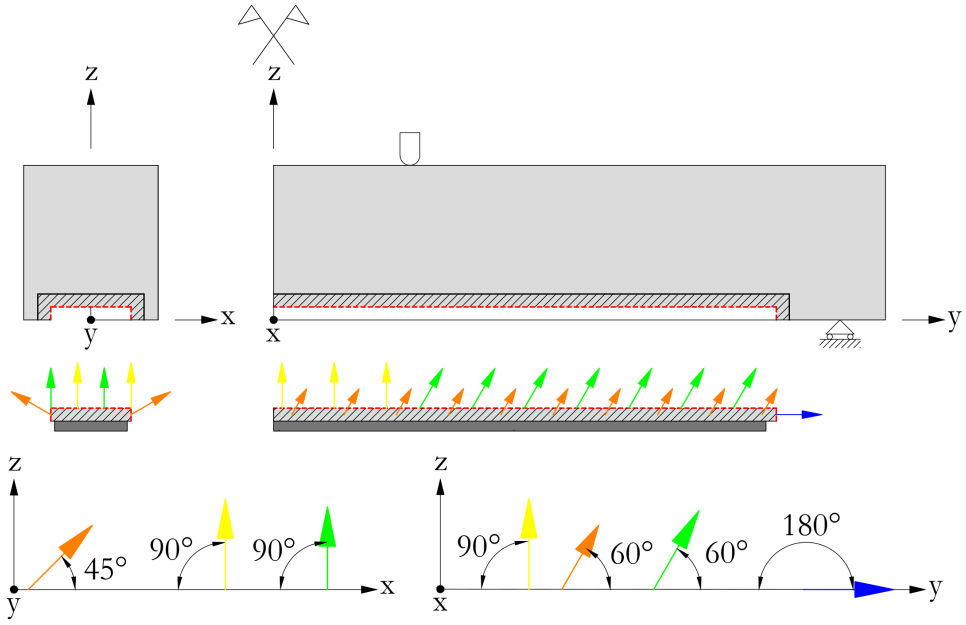

Figure 4.27: Scheme of the vectors $\boldsymbol{n}_f$ for the mechanism-based detachment

4.3.2 *Steel constitutive law*

The non-linear behavior of steel is modeled through a well-known elasto-damaging law based on a modified version of Ramberg-Osgood's law for ductile plastic damage [153, 154]. For instance, in the one-dimensional case,

the plastic strain ϵ_p and the steel damage d are related to the von Mises stress σ_{eq} trough

$$\epsilon_p = \left[\frac{\sigma_{eq}}{(1-d)K}\right]^{\frac{1}{n}}, \tag{47}$$

where K and n are material coefficients. In Eq. (47), ϵ_p and ϵ_R denote the one-dimensional strain at damage threshold and at failure, respectively. The intrinsic value of damage at failure D^c is assumed to be material properties [153]

$$\begin{cases} d = 0 & \epsilon_p \leq \epsilon_D \\ d = D^c \dfrac{\epsilon_p - \epsilon_D}{\epsilon_R - \epsilon_D} & \epsilon_D < \epsilon_p \leq \epsilon_R \\ d = D^c & \epsilon_p \geq \epsilon_R \end{cases}. \tag{48}$$

Fig. 4.28 displays a one-dimensional representation of the stress-strain of the steel for one-dimensional tension for $K = 1200$, $n = 0.08$, $D^c = 0.98$, ϵ_d=0.01, and ϵ_r=0.04.

4.3.3 *Validation of the mechanism-based 3D RE-XFEM*

The present section presents the results obtained in the simulation of four point bending tests of FRP strengthened beams carried out on several beam geometries for both plated and unplated configurations [106, 155]. For the whole set of simulations, the experimentally determined material properties have been adopted. In fact, the concrete elasto-damaging model and the continuous-discontinuous transition procedure require few model parameters that can be deduced from the producer's data. The values of the regularization parameters ρ, indicated in Tab. 4.1, have been kept constant during the simulations. Considering that the computed thickness of the detachment zone turns out being 40ρ, ρ has been identified based on the experimental structural paths, and assuming a thickness of the detachment process zone of about $1 - 2$ cm. Noteworthy, for fixed ρ, the results of the present 3D RE-XFEM formulation were previously shown to be independent of the mesh size.

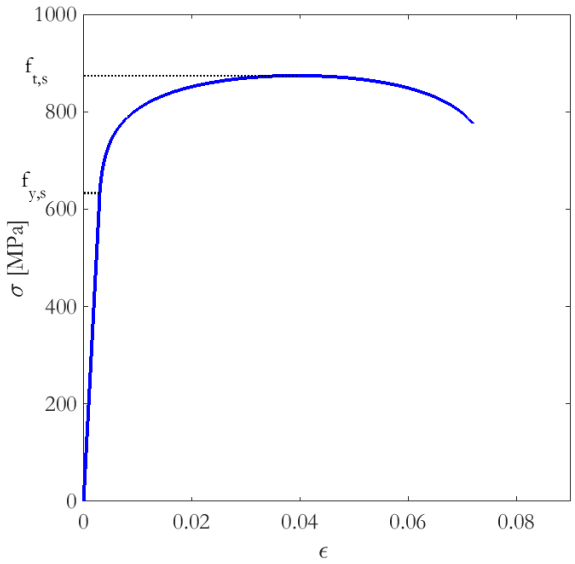

Figure 4.28: Qualitative one-dimensional representation of the damage laws adopted for the steel rebars with $K = 1200$, $n = 0.08$, $D^c = 0.98$, ϵ_d=0.01, and ϵ_r=0.04

4.3.3.1 *Thick beam: geometry and material parameters*

The experimental test performed by Barros et al. [155] has been modelled. It is based on the beam of Fig. 4.29a with l/h of about 5, and a shear span to depth ratio of 1.76.

The concrete material parameters are taken directly from the reference experimental data [155] and are collected in Tab. 4.1. Young's modulus and tensile strength were estimated through the expressions contained in [156] $E = 22000\,[f_{cm}/10]^{0.3} = 34360$ MPa and $f_{ctm} = 0.30 f_{cm}^{2/3} = 3.28$ MPa, with $f_{cm} = 44.2$ MPa.

The material parameters and mechanical properties of the steel of the rebars and the FRP plate are gathered in Tabs. 4.2 and 4.3. To avoid an excessive mesh refinement, the FRP plate thickness has been taken equal to 2 mm. Consequently, an effective Young's modulus $\bar{E}_{FRP} = E_{FRP}\, t_{FRP}\, b_{FRP}/2$ has been set.

The mesh made of 109264 tetrahedral finite elements is shown in Fig. 4.30a. Only the first layer of finite elements above the FRP plate has been enriched.

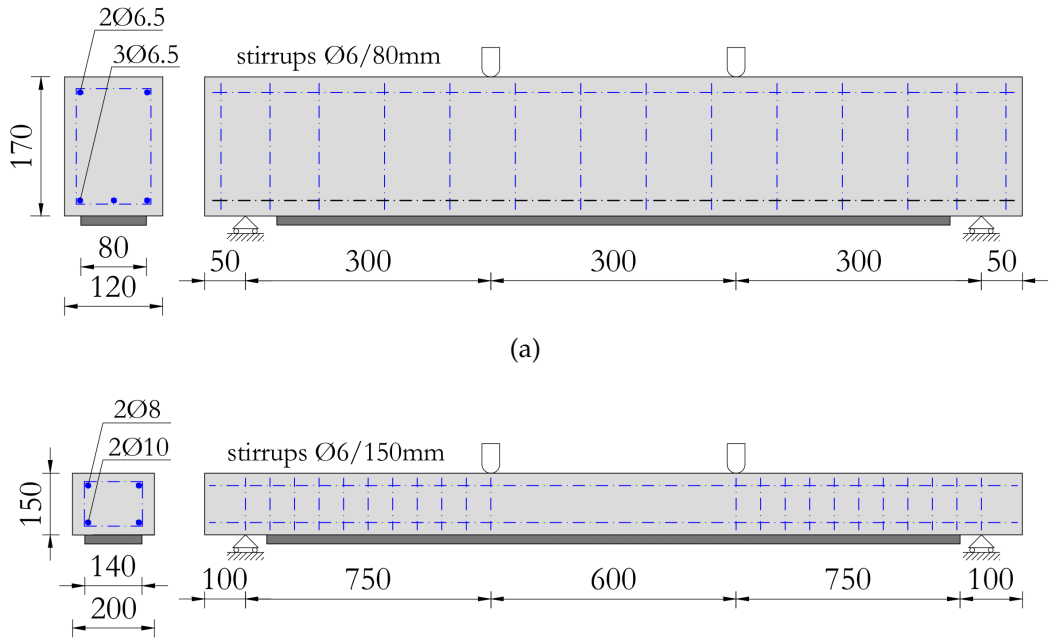

Figure 4.29: Geometry of the thick ($l/h \simeq 5$) and the thin ($l/h \simeq 15$) beams tested in [155] (a) and [106] (b), respectively

	Exp. set [155]	Exp. set [106]
E [MPa]	34360	25000
ν	0.2	0.2
f_{ctm} [MPa]	3.28	2.8
H_s	0.008	0.01
ρ [mm]	0.15	0.45
d_{cr} [mm]	0.999	0.999

Table 4.1: Mechanical properties and parameters of the concrete

	Exp. set [155]	Exp. set [106]
E [MPa]	210000	210000
ν	0.3	0.3
f_{ts} [MPa]	765	575
K	1000	640
n	0.10	0.03
D^c	0.98	0.98
ϵ_D	0.020	0.005
ϵ_R	0.040	0.05

Table 4.2: Mechanical properties and parameters of the steel

	Exp. set [155]	Exp. set [106]
E_{FRP} [MPa]	240000	127000
ν_{FRP}	0.3	0.3
t_{FRP} mm	0.33	0.8
b_{FRP} mm	80	140

Table 4.3: Mechanical properties and geometry of the FRP plate

In the enriched layer, the characteristic mesh-size is 6 mm. To reduce the computational burden and exploit the symmetries of the beam, a quarter of the specimen has been modelled. The surface of detachment is in the concrete at a distance of 3 mm from the upper surface of the FRP plate. Furthermore, a regularization parameter equal to $\rho = 0.15$ mm has been used.

On an i7-5930k PC with 6 3.50 GHz cores, the numerical simulation of the complete structural path has required almost 20 hours.

4.3.3.2 *Thin beam: geometry and material parameters*

The numerical model has been applied to the experimental test [106]. The geometry of the beam having $l/h \simeq 15$ is shown in Fig. 4.29b. The material properties deduced from the experimental data are reported in Tabs. 4.1- 4.3.

A regularization length of $\rho = 0.45$ mm has been adopted leading to a regularized layer whose thickness includes three rows of enriched finite elements. The mesh employed for numerical analysis, reported in Fig. 4.30b, is made of 243771 tetrahedra with a characteristic size of 6 mm in the most refined part. With the same processor used for the thick beam, the entire simulation run for 3 days. The simulation is three times that of the previous test, because the number of enriched elements is three times larger as well, while the number of finite elements is double. The surface of detachment has been imposed at a distance of 9 mm from the upper surface of the FRP plate.

4.3.3.3 *Structural results*

Fig. 4.31 displays the experimental and computed load-midspan-deflection curves for the thick (a) and the thin (b) beams.

The post-detachment structural path of the thick beam exhibits a brittle drop eventually joining the path of the control beam in the unplated configuration, up to exhaustion of the strength of the steel rebars. On the contrary, the failure of the thin beam is reached as soon as the FRP plate detaches, because the steel bars had previously failed. In both the thin and the thick beam, in the first stage of the structural path, the response of the beam is almost elastic until the occurrence of the early cracks. Then, flexural and shear cracks develop within the concrete with subsequent loss of structural stiffness, while the progressive propagation of cracks increases the stress on the tensile steel rebars. In the last part of the structural response, the rebars gradually yield until

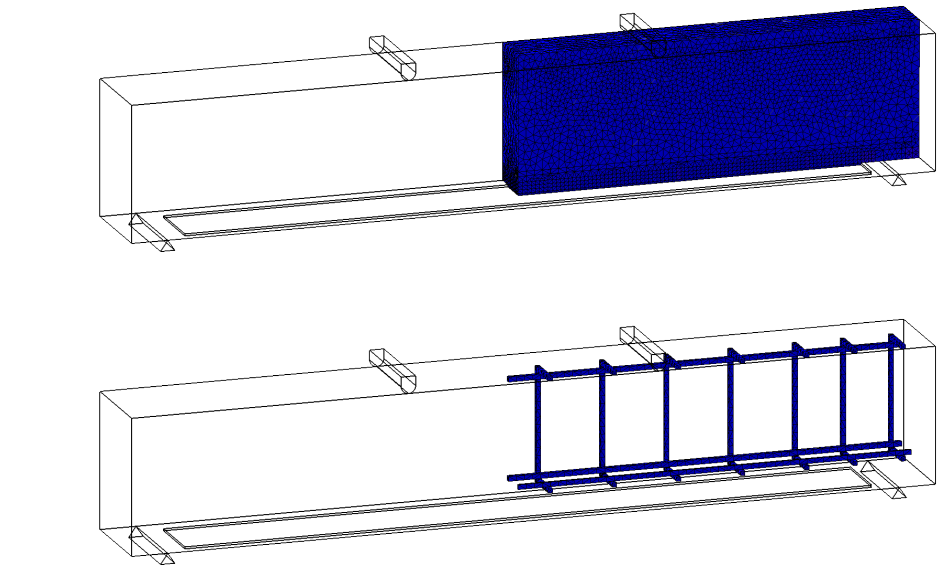

(a)

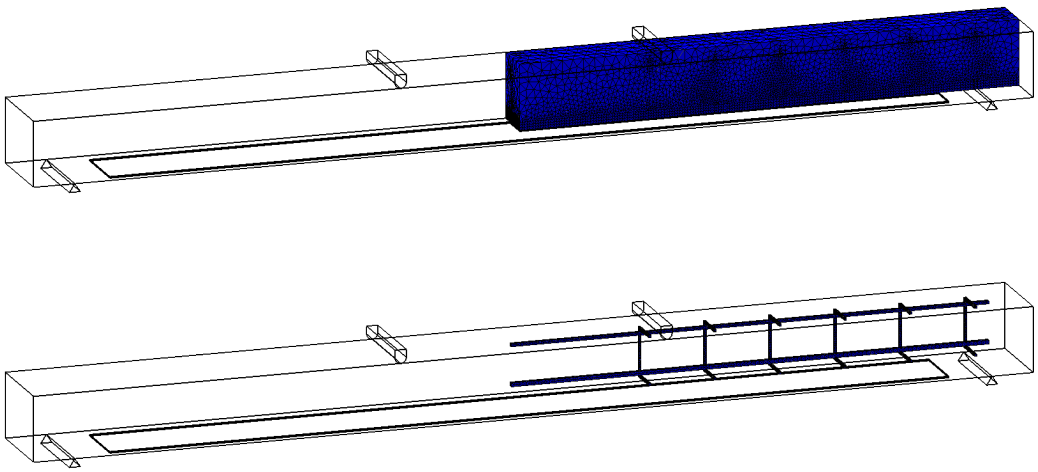

(b)

Figure 4.30: Meshes and details of the steel reinforcement for the two studied beams: a) 108354 elements with 70704 dofs for the beam tested in [155]; b) 243771 elements with 157809 dofs for the beam tested in [106]

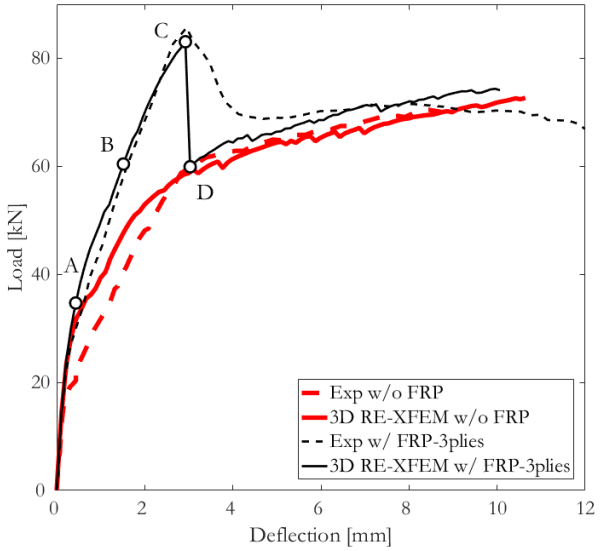

(a) Thick beam

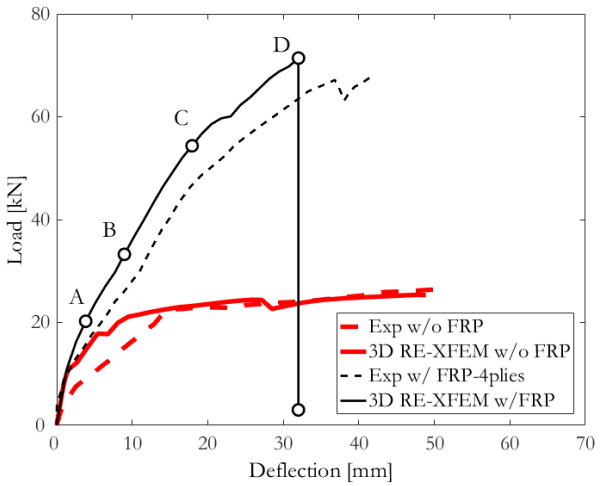

(b) Thin beam

Figure 4.31: Comparison between experimental and numerical load-midspan-deflection curves for the beams tested in [155] (a) and [106] (b), respectively

failure. The gain in maximum load and stiffness obtained after application of the FRP plate is remarkable. The FRP reinforced systems shows higher performance on maximum load and flexural stiffness. However, failure changes from ductile to brittle. The experimental failure loads are properly estimated by the numerical procedure, with a discrepancy less than 6%.

4.3.3.4 *Detachment mechanism*

Detachment occurs by an intermediate flexural detachment mechanism. This can be deduced from Fig. 4.32, which displays the contour plots of the damage d in the concrete matrix and in the steel reinforcements for three representative load steps of the test [155]. The early macro-cracks occur under the applied load (Step A). Then, cracks develop within the concrete bulk (Step B). The concrete damage starts at the midspan and propagates towards the plate-end (Step B). At a certain distance from the plate-end, the damage-front stops and a new damage-front develops from the plate-end to the beam midspan (Step C). Finally, the FRP plate fully detaches from the RC beam In a single load step (Step D).

Fig. 4.33 illustrates the contour plots of the damage in the thin beam over the detachment surface at steps A, C, and D. This confirms the same intermediate flexural cracking detachment mechanism already observed in the thick beam. On the right, the damage in the longitudinal rebars is shown to be localized at the flexural cracks.

The evolution of damage d on the defined surface of detachment for both experimental tests is shown in Fig. 4.34. The damage evolution starts from the midspan and propagates towards the plate-end at step A. At a certain distance from the plate-end, a secondary front of damage arises propagating from the plate end to the beam midspan (step B); failure and total detachment coincide and occurs at steps C-D. In this figure, the elements in red are those where the 3D RE-XFEM has been activated.

4.3.4 *Role of thickness and width of the FRP plate*

To study the influence of the geometries of FRP reinforcement on the structural behavior of the beam, variable thicknesses and widths of the FRP plate have been considered. To the author's knowledge, numerical studies of the

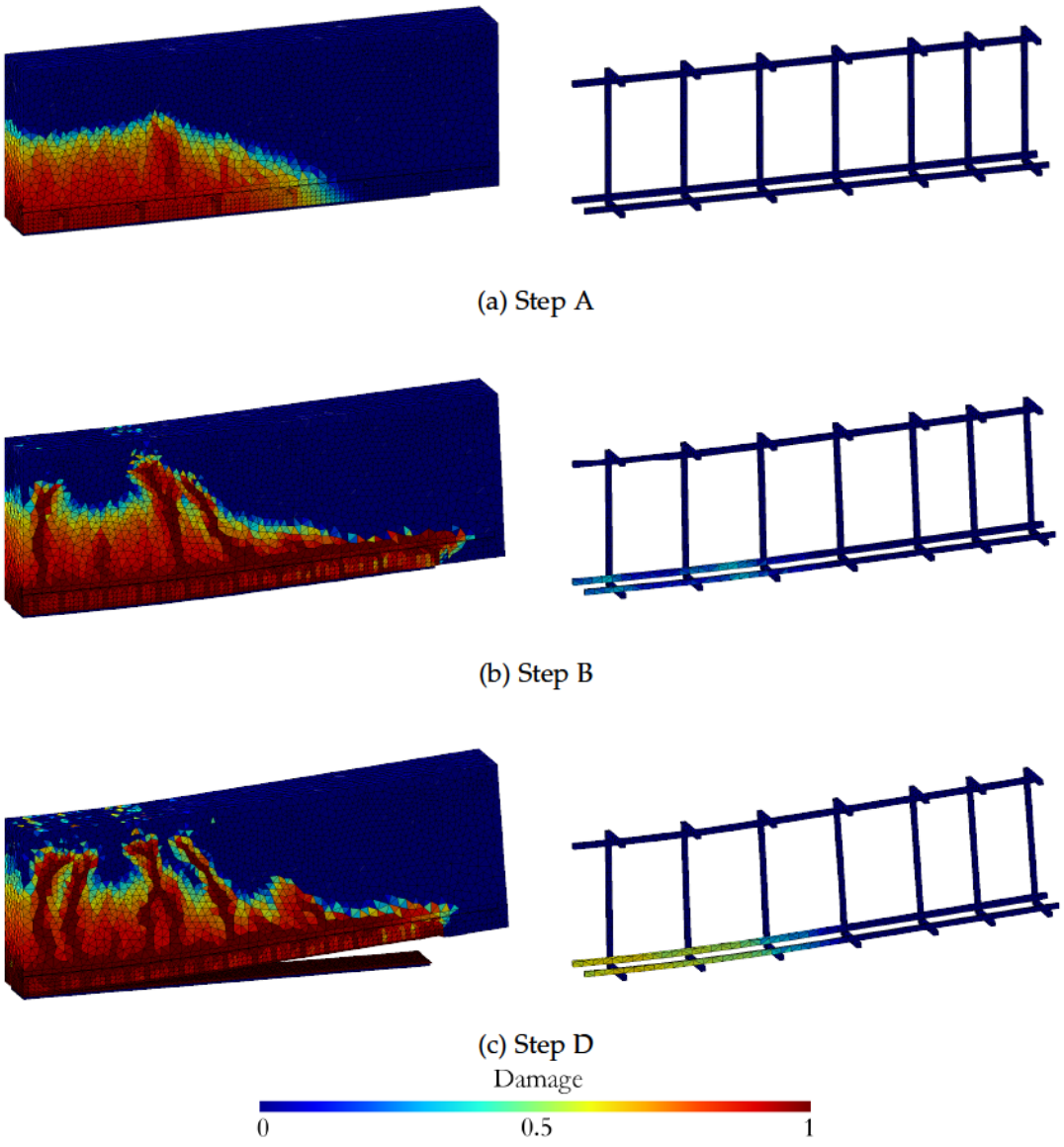

(a) Step A

(b) Step B

(c) Step D

Figure 4.32: Contour plots of the damage at steps A, B and D of Fig. 4.31a for the beam tested in [155]

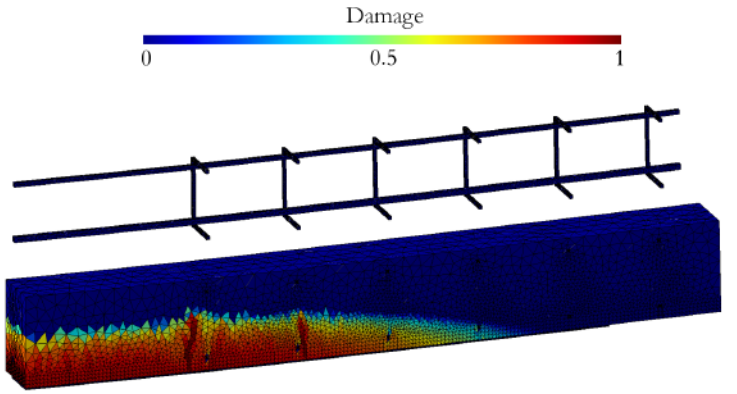

(a) Step A

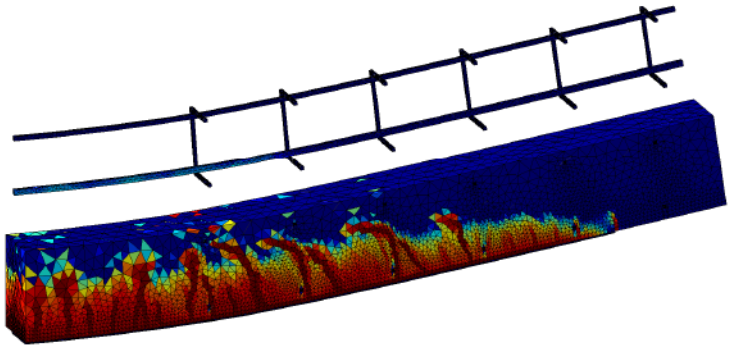

(b) Step B

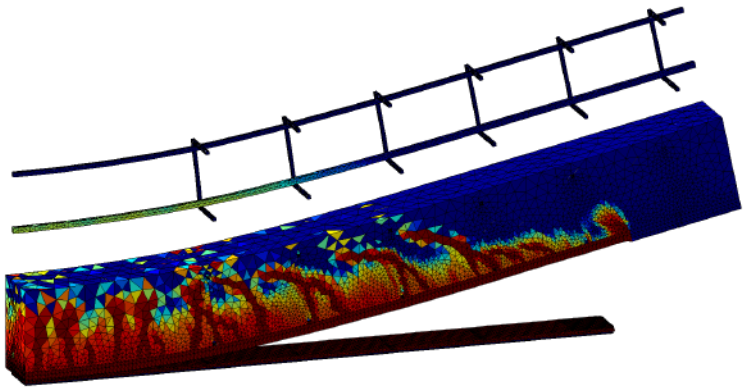

(c) Step C

Figure 4.33: Contour Plots of the damage at steps A, B and D of Fig. 4.31b for the beam tested in [106]

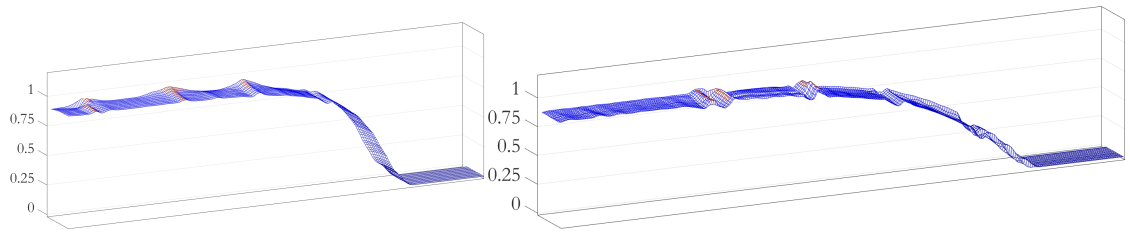

(a) Thick beam, Step A

(b) Thin beam, Step A

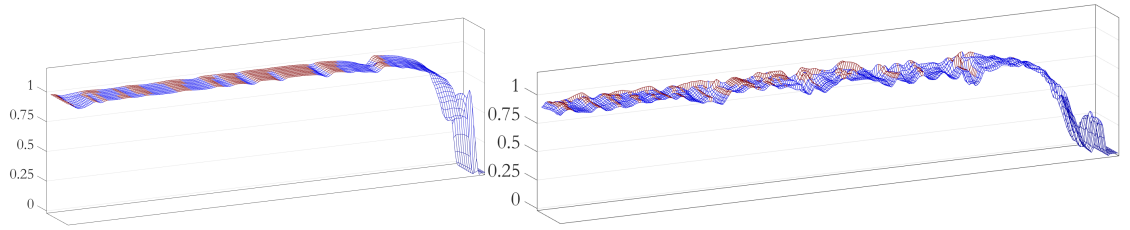

(c) Thick beam, Step B

(d) Thin beam, Step B

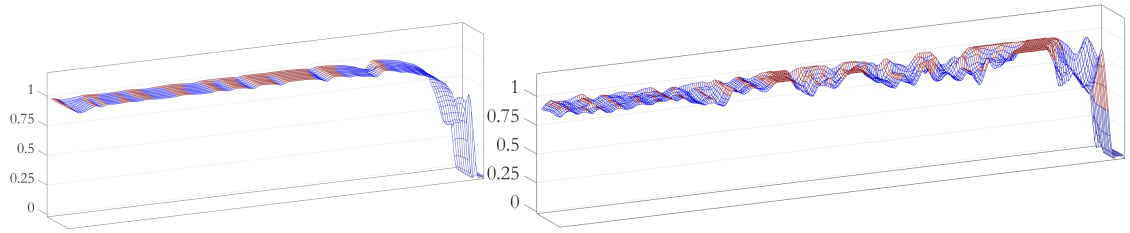

(e) Thick beam, Step C

(f) Thin beam, Step D

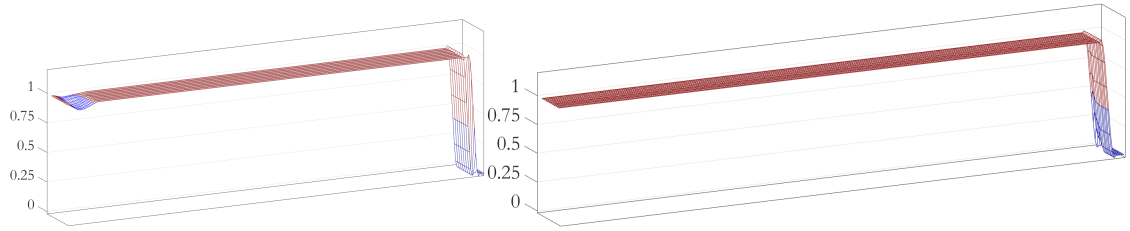

(g) Thick beam, Step D

(h) Thin beam, Step D

Figure 4.34: Damage evolution for the beams tested in [155] (a) and [106] (b), respectively, corresponding to stages A, B, C, and D of Fig. 4.31

influence of the FRP plate width b_{FRP} are only available for shear debonding of FRP sheets from concrete [90].

4.3.4.1 *Structural effects*

For the case of the experimental test of Fig. 4.29b, the behaviour of the reinforced system for different values of the FRP thickness t_{FRP} has been evaluated and compared with the experimental results whenever available, namely for $t_{FRP} = 0.8$ mm and $t_{FRP} = 1.2$ mm. To extend the numerical analysis and identify a trend, $t_{FRP} = 0.4$ mm has also been simulated for constant beam cross section. The experimental and the numerical load vs deflections curves are reported in Fig. 4.35 for variable t_{FRP}. In particular, beams with thicker FRP plates exhibit higher stiffness. Both simulations and experiments detected almost the same failure load and the same intermediate crack debonding mode irrespective of the FRP thickness. However, the thicker the FRP plate, the higher the beam stiffness and the less ductile the structural path. In other experimental tests [107], a similar trend was observed.

In Fig. 4.36, the contour plots of the damage of the steel reinforcements are reported at failure for $t_{FRP} = 1.2$ mm (a) and $t_{FRP} = 0.4$ mm (b). It can be observed that the thinner the FRP plate, the more damaged the steel rebars. The structural influence of the width of the FRP plate has been also investigated for the thick beam for the FRP widths $b_{FRP} = 20$, 40, 80, and 120 mm. The computed load vs deflection profiles are shown in Fig. 4.37. It can be drawn that failure loads and ductility slightly increase with b_{FRP}. An analogous increase of the failure load with the plate width was detected in previous studies [105]. For the specimen with $b_{FRP} = 80$ mm, the numerical and the experimental maximum loads differ by the 3%. The experimental failure loads for different FRP-widths are not available.

4.3.5 *Design loads*

The current subsection suggests how to draw from the simulations an indication about the design loads and the corresponding maximum strain of the FRP plate for variable FRP width and thickness and constant beam cross section. To this purpose, a comparison with a reference design rule [97, 157] has been carried out. The reference design rule, detailed in the Appendix, aims to

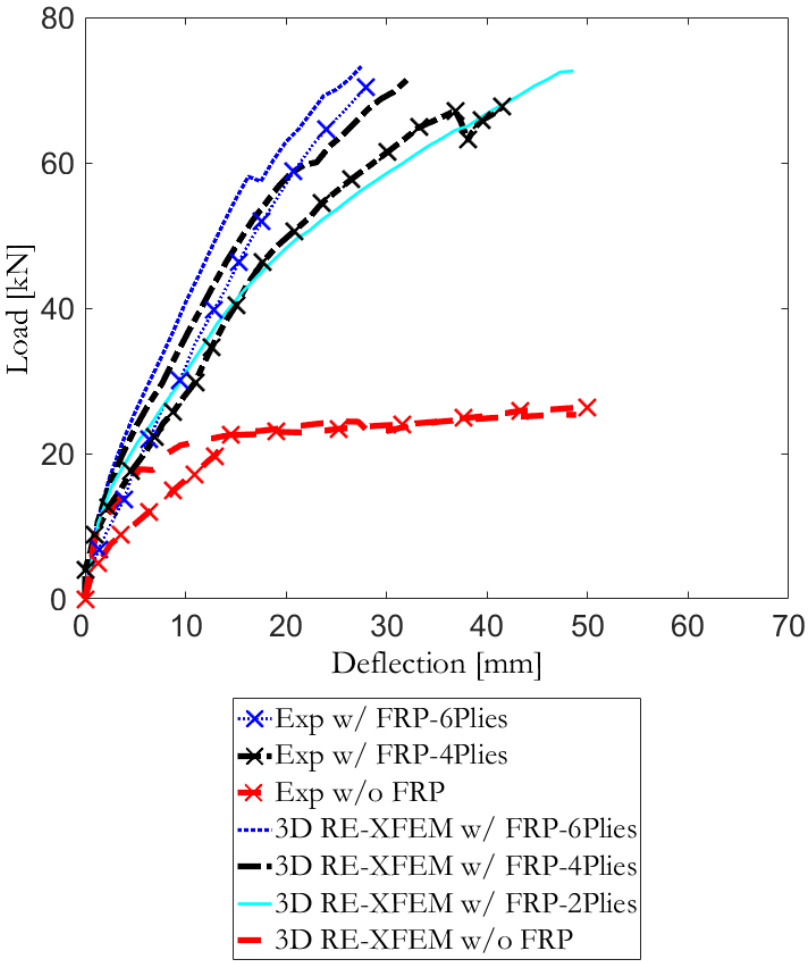

Figure 4.35: Comparison between experimental and numerical load-midspan-deflection curves for variable FRP plate thickness t_{FRP} and the test [155]

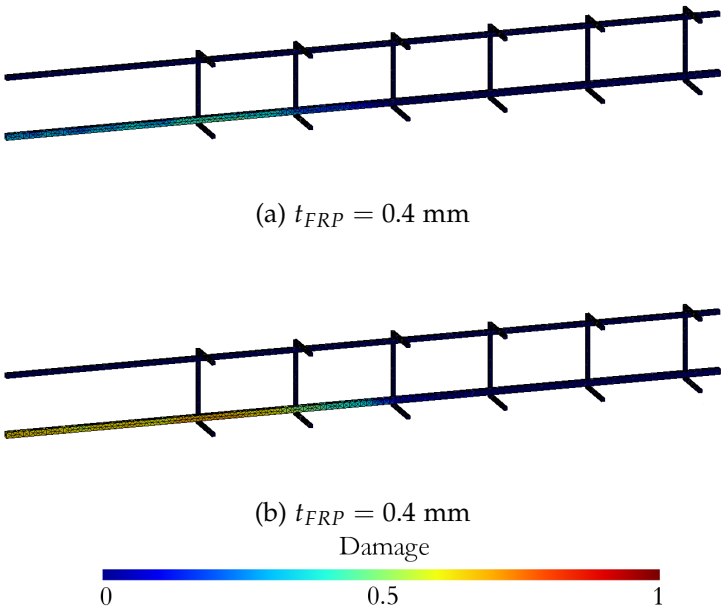

(a) $t_{FRP} = 0.4$ mm

(b) $t_{FRP} = 0.4$ mm

Figure 4.36: Comparison between the damage in the steel bars at the peak load for $t_{FRP} = 1.2$ mm (a) and $t_{FRP} = 0.4$ mm (b) for the test [106]

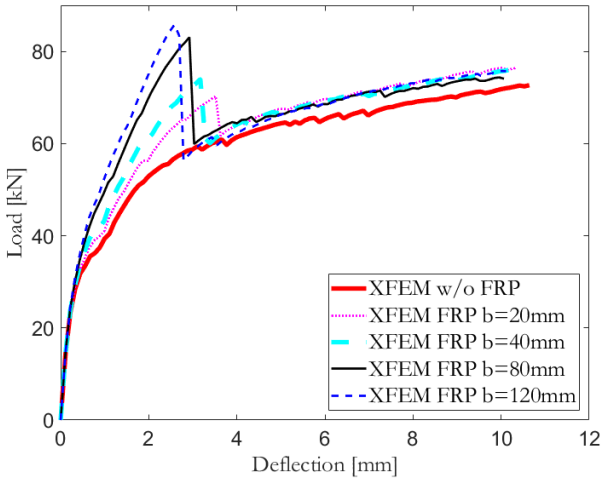

Figure 4.37: Load-midspan-deflection curves for variable FRP plate width b_{FRP} for the beams tested in [155]

design FRP-reinforced systems with a fair safety factor. Hence, the reference design loads have been compared to the loads detected at the occurrence of the early macro-cracks rather than to the computed failure loads. For the thin beam [106], Figs. 4.38a and 4.38b compare the computed loads and maximum FRP strain for variable FRP-thickness t_{FRP} with the corresponding values evaluated through the reference design rule. In particular, the values computed at the occurrence of the first and second macro-crack in the concrete beam have been considered. These values are plotted with dashed lines marked with "x" and dash-dotted lines marked with "$\square$", respectively. The reference values fall within the range of the values computed when the first and second beam macro-cracks are detected. Noteworthy, the design rule leads to design loads and FRP strains increasing for decreasing thickness of the FRP plate. This is in contrast with the present results, and with the fact that the computed and experimental failure loads have been shown to increase with t_{FRP}. For variable width b_{FRP} and in the case of the thick beam [155], the numerical and the corresponding FRP maximum strain, evaluated at the occurrence of the first macro-crack, are displayed together with the reference values in Fig. 4.38a–b, respectively. In this case, the simulations are in good agreement with the design rule. In both computed and reference values, the larger the FRP plate the higher are the design loads and the smaller the FRP maximum strain.

4.3.6 *Discussion of the results*

The present results show that, in the investigated examples, the damage process of the detachment zone above the FRP plate is triggered by the early flexural crack developing in the concrete under the load. Damage proceeds from the central part of the beam to the plate end until the concrete cracking pattern reaches the plate end itself. Then a new damage front is activated proceeding very fast from the plate end to the center, subsequently joining the previous damage front. At this point, the FRP plate detachment is complete. In fact, either the detected structural failure is brittle and almost simultaneous with the FRP plate detachment, or the post-detachment path joins that of the unplated beam.

As expected, the structural failure of the simulated plated beams depends on the interplay among the strengths of the concrete beam, the steel bars, and the FRP plate. In particular, the structural failure is postponed with re-

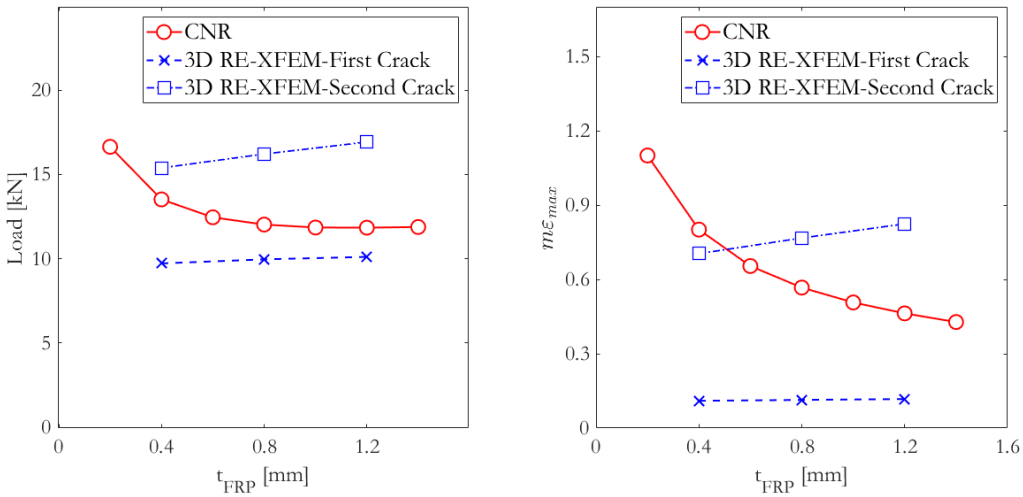

Figure 4.38: Comparison between numerical and design values [97] for variable thickness in terms of loads(a) and maximum FRP axial strain (b), obtained for the beam tested in [106]

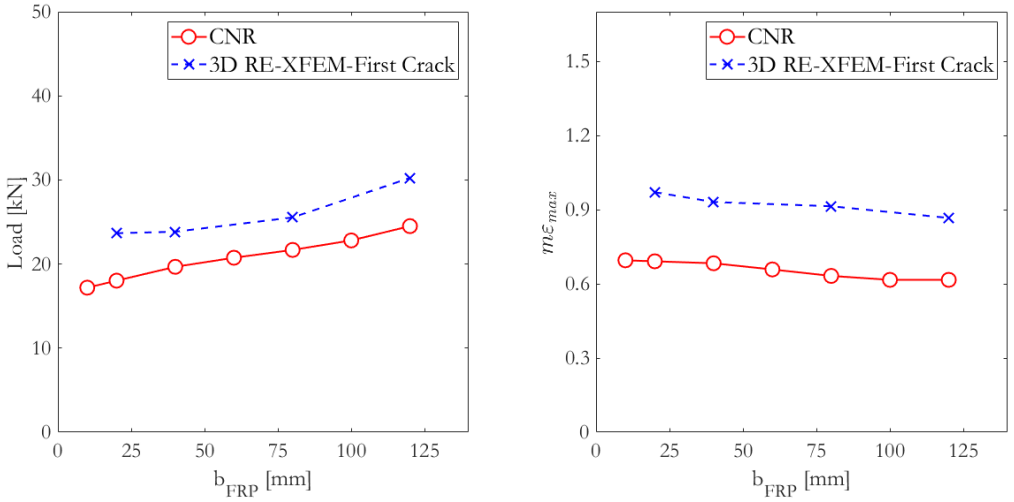

Figure 4.39: Comparison between numerical and design values [97] for variable width of the FRP plate in terms of loads (a) and maximum FRP axial strain (b), obtained for the beam tested in [155]

spect to the FRP plate detachment, provided that the steel transverse reinforcement is correctly placed in the loaded region, and the yielding of the steel rebars is not complete. This is the case of the thick beam [155], having a shear span to depth ratio less than 2, where the steel reinforcements carry the load after the FRP detachment. On the contrary, in the tests by Rahimi and Hutchinson [106], with a shear span to depth ratio of about 6, the sections were adequately reinforced for the load history carried by the unplated beams, whereas they resulted under-reinforced with respect to the load levels reached by the plated beams, based on Rahimi and Hutchinson's assumption that only under-reinforced beams presumably require further reinforcements, hence the lack of stirrups at the beam centre. The experimentally detected failure mode for the plated beam was shear failure followed by concrete cover separation and FRP detachment. The failure occurred suddenly, as usual in the case of shear failure of the concrete beam. The simulations closely reproduce the experimentally detected failure mode, as proved by the fact that the computed post-failure path displays a sudden significant loss of stiffness from step C, eventually loses convergence immediately after step D, and does not join the structural path of the unplated beam. Therefore, the simulations confirm that, depending on the steel reinforcement, the strengthening effect induced by the FRP plates on under-reinforced concrete beams can change the failure mode of the unplated beam into brittle shear failure, where the FRP plate detachment follows, instead of preceding, the beam failure. The loads computed at the first crack are not significantly sensitive to the width and thickness of the FRP plate. On the contrary, it is in the post-elastic regime that the structural behaviour displays its dependency on the width and thickness of the FRP plate. In particular, the loads at which the FRP plate detaches increase with the FRP plate width, while they are not remarkably influenced by the FRP plate thickness. On the other hand, the midspan deflection at detachment increases with the thickness in all the modeled beams, though more markedly in the thin beam. Finally, the present study suggests that the loads corresponding to the occurrence of the early macro-cracks in the concrete beams can be assumed as design loads. Such an estimate has been shown to be reasonably close to that provided by the reference design rule [97].

4.4 CONCLUSIONS

Numerical models that compute the structural behavior of FRP plated beams abound in the relevant literature. However, most of them require the definition of interfacial laws to be identified a priori, often lose convergence, and are unable to satisfactorily capture the concrete cracking pattern and the complete FRP plate detachment. The proposed mechanism-based 3D RE-XFEM overcomes the previous limitations. In fact, it requires only basic material properties and few model parameters, allows for a smooth transition from the continuum to the detachment, and models the mixed-mode fracture process zone in a physically consistent way.

It has been shown that:

- The model reproduces the experimental mixed opening-shearing mechanism of detachment
- The bridging effect exerted by the steel fibers at the detachment surface through can be taken into account with the regularization parameter
- The crack pattern obtained in the concrete beam is consistent with experiments
- The model allows to follows the entire structural path up to beam failure
- If the goal is to increase the deflection and moderately improve the detachment load, FRP plates made of two or three-plies and almost $20 - 40$ mm wide should be used.
- Larger thicknesses and widths enhance the detachment load and reduce the ultimate deflection.
- Surprisingly, an increase of thickness and width of the FRP plate has negligible effects on the values of the midspan deflection and the load at which early cracks occur.
- Design loads increase by less than 2% when doubling the FRP plate width, and are quite constant for variable thickness.

Hence the proposed 3D RE-XFEM is an effective and predictive tool of the behavior of SFRC beams reinforced with FRP plates.

5

MODELLING OF WOODEN BEAMS

5.1 INTRODUCTION

In this second part of the thesis, the focus of the research switches from the investigation of the debonding mechanisms of FRP reinforcements in concrete specimens to the study of the structural response of wooden structures. In particular, this research was motivated by the request of the Italian National Research Council (CNR) to numerically study the efficiency of reinforcing interventions employed for old decayed wooden beams. After an introduction on the wood behaviour and on the state of art in wood modelling (Sec. 5.2), the 3D non-linear orthotropic CDM employed for the simulation is presented in Sec. 5.4. The experimental tests carried out by the CNR and the numerical simulations on the repaired wooden beams are reported in Sec. 5.5. In particular, the effect of the use of screws and passing screws on the reparation intervention are highlighted in Sec 5.5.3 and Sec. 5.5.4, respectively. In the end, in Sec. 5.6 the main findings of the studies are listed. The results presented in this chapter have been proposed for publication. The article is currently in press [12].

5.2 PREMISES ON WOOD

Wood is a natural material with a complex composite cellular microstructure (Fig. 5.1). Due to its nature, wood is an inhomogeneous, anisotropic and porous material with moisture-, temperature- and time-dependent behaviour.

Despite being an anisotropic material, wood is commonly modelled as an orthotropic material. The three main directions of the material are denoted

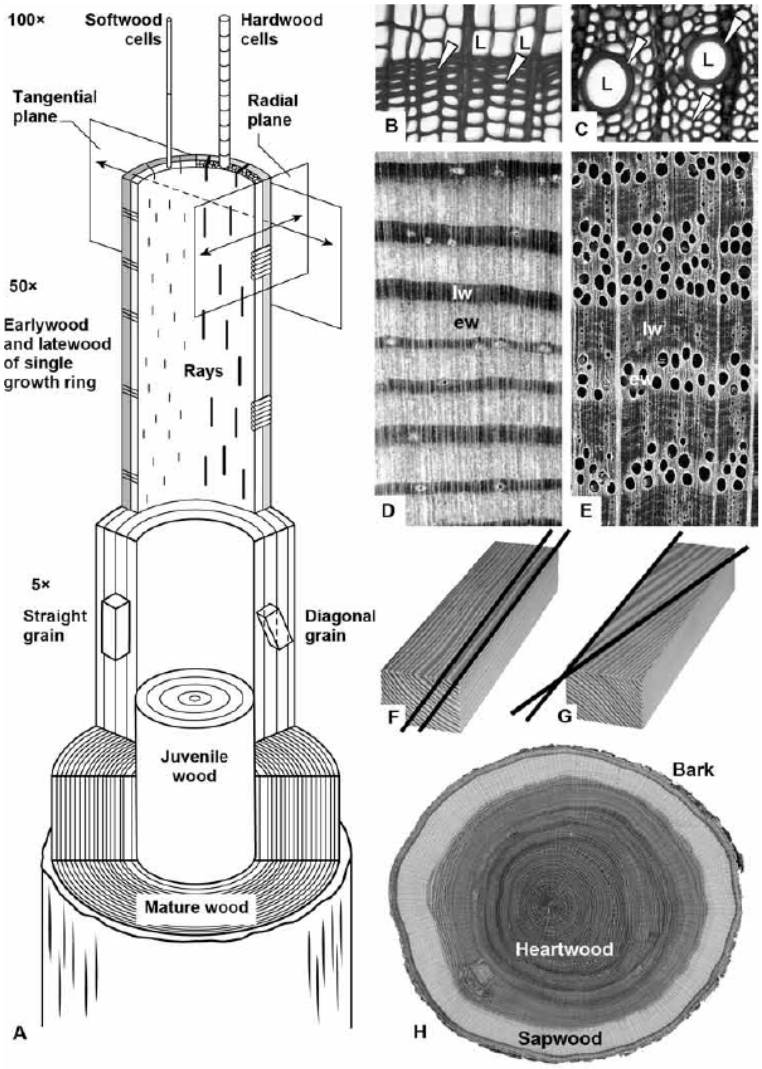

Figure 5.1: Illustration of the wood macro-to-micro structure taken from the Handbook [158]. In the following, the elements contained in the picture are listed. Illustration of a cut-away tree at various magnifications (A). Microscopic views of the wood cell walls of a softwood (B) and a hardwood (C). Hand-lens views of growth rings, each composed of earlywood and latewood, in a softwood (D) and a hardwood (E). A straight-grained board (F). Diagonal-grained board (G). The gross anatomy of a tree trunk, showing bark, sapwood, and heartwood (H).

as longitudinal (L), radial (R) and tangential (T). In the dedicated literature, the longitudinal direction is also known as the "parallel-to-grain" direction. Moreover, the terminology "perpendicular-to-grain" is used to including both of the radial and the tangential directions, since usually there is no significant difference between the properties along them.

The material modelling of wood has to tackle several issues. First of all, all the wood species differ at the micro-scale in the anatomy. Furthermore, the presence of inhomogeneities, such as grain deviations and knots, affects the material behaviour. Thence, the availability and the reliability of the engineering parameters usually employed for the material formulation are troublesome. Moreover, strength properties of wood significantly differ for compressive, tensile and shear loading.

5.2.1 *Tension*

In tension, wood shows a quasi-brittle failure. The brittle failure modes can be clearly seen in Fig. 5.2, where the typical load-displacement curves of tension tests where the load direction is parallel-to-grain (Fig. 5.2a) and perpendicular-to-grain (Fig. 5.2b) carried out on spruce specimen [159, 160] are reported. The qualitative tensile behaviours parallel and perpendicular to the grain are similar, but the ultimate tensile stress capacity is very different.

5.2.1.1 *Fracture Process Zone in wood*

On the microscopic scale, as shown in Fig. 5.3, it has been found that brittle failure occurs at annual ring level in the earlywood, the low-density part of the annual rings that forms during the spring, or in the interface earlywood/latewood [163, 164]. The fibers bridging plays a key role in the energy dissipation process, spreading the cracking process within a Fracture Process Zone. Murata et al. [163], estimates that the thickness of the process zone ranges between 0.3 to 0.5 mm in a spruce specimen (annual ring width 0.89 mm), assuming a constant and uniform dissipation over the fracture process zone.

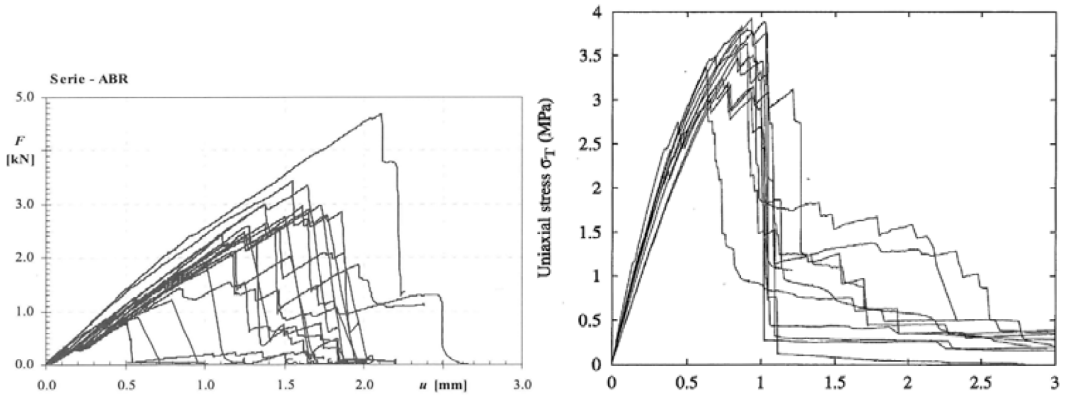

(a) (b)

Figure 5.2: Uniaxial tensile tests parallel-to-grain (a) and perpendicular-to-grain (b) carried out on spruce (Picea abies) specimens by Franke [161] and Poulsen [160], respectively

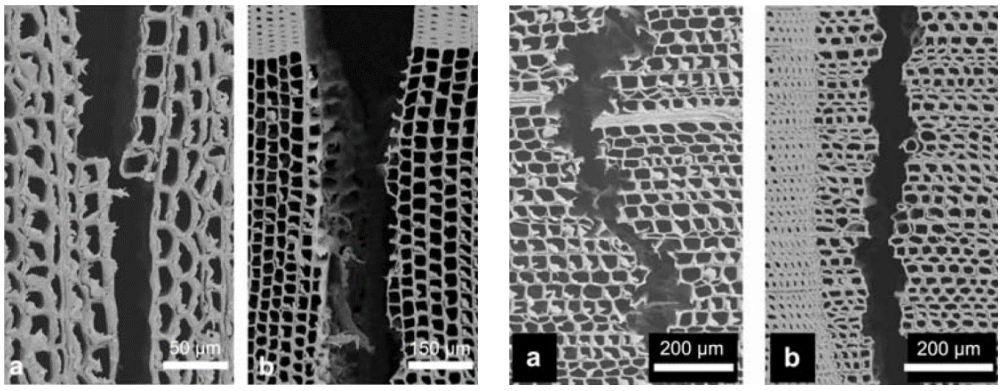

(a) (b)

Figure 5.3: Particular at the micro-scale of the effect of a tensile load along the R-direction (a) and the T-direction [162]

5.2.2 *Compression*

The behaviour in compression exerted by wood is completely different from the quasi-brittle result in tension. Wood in compression is ductile with a distinct plastic behaviour, as shown in Fig. 5.4. At the micro-scale, it has been drawn that, in compression, the cells are structurally acting as columns which are failing by kinking. The non-linearity before the decrease in strength is due sliding and microscopic buckling phenomena. After the incipient kinking, a steady plateau is developing where the material is yielding without gaining higher stresses. Fig. 5.5 shows the kink band angle on the tangential face of specimens of different size loaded in parallel-to-grain compression.

The cell buckling is usually starting in earlywood, where the cell walls are thinner and thus are more susceptible to stability problems due to compression loads.

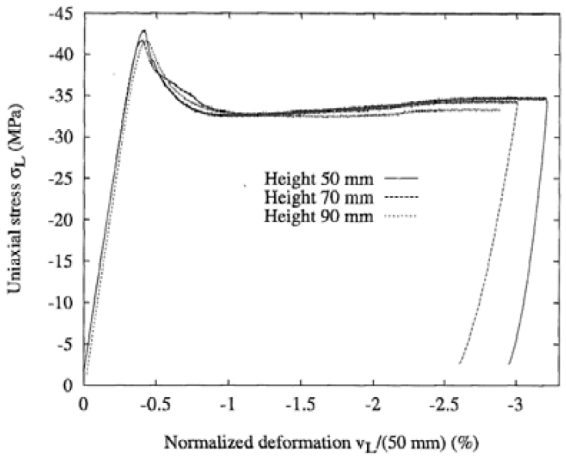

Figure 5.4: Uniaxial compression parallel-to-grain test on a spruce (Picea abies) specimen carried by Poulsen [160]

5.2.3 *Shear*

Generally, wood shows a quasi-brittle failure due to shear, similar to the tensile failure. Shear failure always happens in the LT- or LR-plane and usually follows the annual rings separating earlywood from latewood as this is the

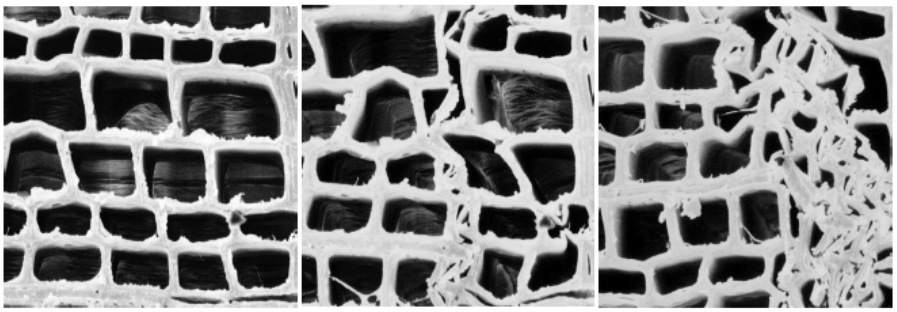

Figure 5.5: Effect of a progressive compressive (from the left to the right) load at the micro-scale level [162]

weakest part. Microscopically, as shown in Fig. 5.6, shear failures show the same rupture mechanisms as tension perpendicular to the grain.

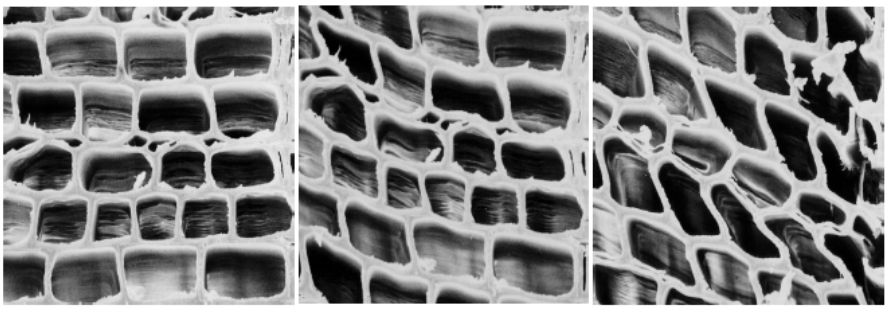

Figure 5.6: Effect of a progressive shear load (from the left to the right) at the micro-scale level [162]

5.3 STATE OF ART ON WOOD MODELLING

A reliable constitutive FE model for timber has to be anisotropic/orthotropic and to account for both the difference in strength between tension and compression and, at the same time, the simultaneous presence of ductile and brittle failure modes. State-of-the-art-literature on FE constitutive models mostly provides anisotropic plasticity models based on Tsai and Wu [165] and Hill [166] failure criteria. For instance, Bouchaïr and Vergne [167], Clouston and Lam [168] developed single-surface plasticity models by combining the classical flow theory of plasticity with the elliptical Tsai and Wu failure surface for anisotropic

materials [165, 169]. Other examples of single-surface plasticity models are based on the failure surfaces proposed by Hoffman [170], e.g. [171]. Although single-surface plasticity models are able to predict the failure loads of the material, they fail to reproduce different failure modes and do not satisfactorily describe the structural behaviour. Therefore, multi-surface plasticity model have been developed [35, 172]. However, the parameters employed for the mathematical description of the multi-surfaces may lack of direct physical meaning, while the computational transition from one surface to another one is prone to numerical instabilities. Eventually, multi-surface plasticity models are coupled to fracture models, such as CZM or interface element [173].

An alternative approach to plasticity models consists in adopting orthotropic constitutive laws in the context of Continuum Damage Mechanics (CDM). In CDM models, as introduced in 2.1.1, the progressive deterioration of the mechanical strength due to the development of micro-cracks, voids and other types of defects is modelled through the introduction into the stiffness matrix of damage variables representative of the state of degradation of the material, ranging from 0 for sound material to 1 for completely broken material. Thus, CDM is suitable to model materials whose constitutive law exhibits a brittle softening post-peak branch and failure mainly occurs by strain localization. Recently, Sandhaas et al. [174] have developed a simplified effective 3D material model suitable for modelling localized ruptures observed in timber structures. For a complete 3D description of wood as an orthotropic material, CDM model is based on eight types of brittle and ductile failure modes governed by six damage variables [14], while ductile plastic-like behaviour under compression is simulated by means of an elasto-damaging law displaying a horizontal stress threshold beyond a critical strain. This approach overcomes the emergence of mesh-dependency induced by the presence of softening constitutive laws through the adoption of the crack-band model [63]. The adoption of the aforementioned crack-band model is an acceptable compromise between simplicity of implementation and accuracy. Furthermore, in the Sandhaas and van de Kuilen model [14], a fictitious-viscosity-based stabilization term had to be used to tackle the occurrence of fast snap-back and snap-through points encountered during the loading process. Although permanent plastic deformations are not captured, it has been successfully applied to the modelling of timber specimens subjected to monotonic tension, compression and dowel embedment [174]. More recent contributions, such as those by Sirumbal-Zapata

et al. [175], for cyclic loads, and Khenanne et al. [176], for large plastic deformations, have proposed elasto-damaging plastic orthotropic constitutive laws, with the limitation that isotropic damage laws are used, thus precluding a physically consistent representation of the complex damage state occurring in repaired timber beams.

5.4 AN ORTHOTROPIC ELASTO-DAMAGING CONSTITUTIVE MODEL

Wood is an orthotropic material and its damaging process is also orthotropic. Let consider the reference system shown in Fig. 5.7, where the x-axis, the y-axis and the z-axis are aligned to the longitudinal (L), the radial (R) and the tangential (T) directions of the wood, respectively. According to the reference

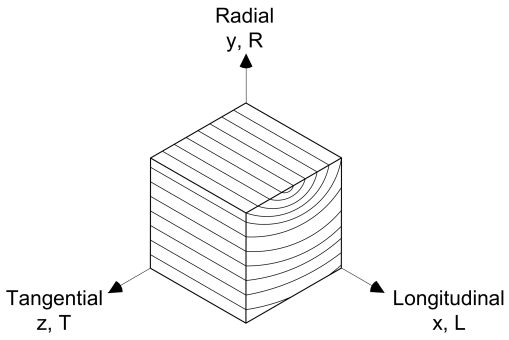

Figure 5.7: Reference system adopted

system adopted, using the Voigt notation, the stress can be expressed as

$$\boldsymbol{\sigma} = \left[\sigma_{xx}, \sigma_{yy}, \sigma_{zz}, \sigma_{xy}, \sigma_{yz}, \sigma_{xz}\right]^t \equiv \left[\sigma_L, \sigma_R, \sigma_T, \sigma_{LR}, \sigma_{RT}, \sigma_{LT}\right]^t \quad . \tag{49}$$

The orthotropic non-linear behaviour of the wood has been modelled in the CDM framework according to Sandhaas et al. [14]. In particular, six independent damage variables, one for each stress component, have been introduced and collected in the vector

$$\boldsymbol{d} = \left[d_L, d_R, d_T, d_{LR}, d_{RT}, d_{LT}\right]^t \quad . \tag{50}$$

We define the effective stress vector $\widetilde{\sigma}$ as the stress that acts on the effective resisting area, deprived of damaged parts, i.e.

$$\widetilde{\sigma} = \boldsymbol{M}\boldsymbol{\sigma} \quad , \tag{51}$$

where

$$\boldsymbol{M} = \begin{bmatrix} \frac{1}{(1-d_R)} & 0 & 0 & 0 & 0 & 0 \\ 0 & \frac{1}{(1-d_T)} & 0 & 0 & 0 & 0 \\ 0 & 0 & \frac{1}{(1-d_L)} & 0 & 0 & 0 \\ 0 & 0 & 0 & \frac{1}{(1-d_{RT})} & 0 & 0 \\ 0 & 0 & 0 & 0 & \frac{1}{(1-d_{RL})} & 0 \\ 0 & 0 & 0 & 0 & 0 & \frac{1}{(1-d_{TL})} \end{bmatrix} \quad . \tag{52}$$

For the subsequent derivations, it is convenient to define the damaged compliance matrix $\boldsymbol{C}^d$ of wood as

$$\boldsymbol{C}^d = \begin{bmatrix} \frac{1}{(1-d_R)E_{11}} & -\frac{\nu_{21}}{E_{22}} & -\frac{\nu_{31}}{E_{33}} & 0 & 0 & 0 \\ -\frac{\nu_{12}}{E_{11}} & \frac{1}{(1-d_T)E_{22}} & -\frac{\nu_{32}}{E_{33}} & 0 & 0 & 0 \\ -\frac{\nu_{13}}{E_{11}} & -\frac{\nu_{23}}{E_{22}} & \frac{1}{(1-d_L)E_{33}} & 0 & 0 & 0 \\ 0 & 0 & 0 & \frac{1}{(1-d_{RT})G_{12}} & 0 & 0 \\ 0 & 0 & 0 & 0 & \frac{1}{(1-d_{RL})G_{13}} & 0 \\ 0 & 0 & 0 & 0 & 0 & \frac{1}{(1-d_{TL})G_{23}} \end{bmatrix} \quad . \tag{53}$$

The nominal stress σ is defined by the equation

$$\boldsymbol{\sigma} = \boldsymbol{D}^d \boldsymbol{\varepsilon} \quad , \tag{54}$$

where the damaged stiffness matrix is obtained as $\boldsymbol{D}^d = \left(\boldsymbol{C}^d\right)^{-1}$. Eight different failure criteria are considered in the adopted model, each one corresponding to a failure surface in the principal stress space, as detailed in the following paragraphs.

- Criterion I - Failure in parallel-to-grain tension: Brittle failure mode caused by tensile stress parallel-to-grain $\tilde{\sigma}_L > 0$ and is governed by the damage variable d_L. It obeys the loading-unloading inequality

  $$F_I(\sigma) = \frac{\tilde{\sigma}_L}{f_{t,L}} - 1 \leq 0 \quad , \tag{55}$$

  where $f_{t,L}$ is the tensile strength along the longitudinal direction.

- Criterion II - Failure in parallel-to-grain compression: Ductile failure mode caused by compressive stress parallel-to-grain $\tilde{\sigma}_L < 0$ that affects the damage variable d_L. The failure is associated with the loading-unloading inequality

$$F_{II}(\sigma) = \frac{-\tilde{\sigma}_L}{f_{c,L}} - 1 \leq 0 \tag{56}$$

  where $f_{c,L}$ is the compressive strength along the longitudinal direction.

- Criteria III/IV - Failure in perpendicular-to-grain tension: Brittle failure modes governed by tensile perpendicular-to-grain ($\tilde{\sigma}_R > 0$ and $\tilde{\sigma}_T > 0$), longitudinal shear ($\tilde{\sigma}_{LR}$, $\tilde{\sigma}_{LT}$) and rolling shear $\tilde{\sigma}_{RT}$ stresses. They are characterized by the development of splitting cracks in LR-plane and LT-plane, respectively, and are related to the damage variables d_R, d_T, d_{LR} , d_{LT} and d_{RT}. The quadratic loading-unloading inequalities:

$$\begin{aligned} F_{III}(\sigma) &= \frac{\tilde{\sigma}_R^2}{{f_{t,R}}^2} + \frac{\tilde{\sigma}_{LR}^2}{{f_v}^2} + \frac{\tilde{\sigma}_{RT}^2}{{f_{roll}}^2} - 1 \leq 0 \\ F_{IV}(\sigma) &= \frac{\tilde{\sigma}_T^2}{{f_{t,T}}^2} + \frac{\tilde{\sigma}_{LT}^2}{{f_v}^2} + \frac{\tilde{\sigma}_{RT}^2}{{f_{roll}}^2} - 1 \leq 0 \end{aligned} \quad , \tag{57}$$

  are adopted, where $f_{t,R}$ is the tensile strength along the radial direction, $f_{t,T}$ is the tensile strength along the tangential direction, $f_{v,LR}$ is the shear strength along the LR plane, $f_{v,LT}$ is the shear strength along the LT plane, and, finally, $f_{v,RT}$ is the rolling shear strength of the material.

- Criteria V/VI - Failure in perpendicular-to-grain compression: Ductile failure modes caused by the compressive stress along the radial or the longitudinal direction ($\tilde{\sigma}_R < 0$ and $\tilde{\sigma}_T < 0$), and governed by the damage variables d_R and d_T. They are associated with the following loading-unloading inequalities

$$\begin{aligned} F_V(\sigma) &= \frac{-\tilde{\sigma}_R}{f_{c,R}} - 1 \leq 0 \\ F_{VI}(\sigma) &= \frac{-\tilde{\sigma}_T}{f_{c,T}} - 1 \leq 0 \end{aligned} \quad , \tag{58}$$

  where $f_{c,R}$ and $f_{c,T}$ are the compressive strength along the radial and the longitudinal direction of the material, respectively

- Criteria VII/VIII - Shear failure: Brittle failure modes induced by the longitudinal shear stresses $\tilde{\sigma}_{LR}$, $\tilde{\sigma}_{LT}$ and the rolling shear stress $\tilde{\sigma}_{RT}$, in the case that a compressive perpendicular-to-grain ($\sigma_R < 0$ or $\sigma_T < 0$) occurs. They are governed by the damage variables d_{LR}, d_{LT} and d_{RT}. The current case is governed by the quadratic loading-unloading inequalities:

$$\begin{aligned} F_{VII}(\sigma) &= \frac{\tilde{\sigma}_{LT}^2}{{f_v}^2} + \frac{\tilde{\sigma}_{RT}^2}{{f_{roll}}^2} - 1 \leq 0 \\ F_{VIII}(\sigma) &= \frac{\tilde{\sigma}_{LT}^2}{{f_v}^2} + \frac{\tilde{\sigma}_{RT}^2}{{f_{roll}}^2} - 1 \leq 0 \end{aligned} \quad . \tag{59}$$

In general, the loading-unloading Kuhn-Tucker condition for the $m-th$ surface of the CDM model is cast as

$$\phi_m(\boldsymbol{\sigma}, k_m) = F_m - k_m \leq 0 \quad \dot{k_m} \geq 0 \quad \phi_m \dot{k_m} = 0 \quad , \tag{60}$$

where k_m is the state variable related to the $m-th$ failure criteria, and $\dot{k_m}$ denotes the increment of k_m evaluated with respect to a fictitious time parameter.

In order to simulate both brittle and ductile failure modes, the Sandhaas et al. model [174] considers two damaging laws. In particular, Fig. 5.8a shows a qualitative representation of the adopted stress-strain law adopted for each case of ductile failure modes, such as failure by compression in the parallel-to-grain and perpendicular-to-grain directions. In this case, and the relevant damage variable, that is activated when the loading function is greater than zero, is calculated as

$$d_i(k_m) = 1 - \frac{1}{k_m} \qquad i = L, R \quad . \tag{61}$$

For each brittle failure mode induced by tensile and/or shear stresses, the bilinear softening stress-strain law displayed in 5.8b is used. In this case, the damage variables related to the tensile failure modes are computed according to

$$d_i(k_m) = 1 - \frac{1}{f_{t,i} - 2g_{f,i}E_i}\left(f_{t,i} - \frac{2g_{f,i}E_i}{k_m}\right) \qquad i = L, R, T \quad , \tag{62}$$

while, for shear failure modes, the damage variables are defined as

$$d_i(k_m) = 1 - \frac{1}{f_{v,i} - 2g_{f,v,i}G_i}\left(f_{v,i} - \frac{2g_{f,v,i}G_i}{k_m}\right) \qquad i = LR, LT, RT \quad , \tag{63}$$

where $g_{f,i}$ and $g_{f,v,i}$ being the specific fracture energies for the tensile and the shear failure modes, respectively. Mesh-dependency is alleviated by adopting the crack band model [63], where the specific fracture energy g_f of the single FE e is related to the fracture energy of the material G_f and to the characteristic size of the finite element h_e through

$$g_F = \frac{G_f}{h_e} \quad . \tag{64}$$

In our case, fracture energies have been taken from Sandhaas and van de

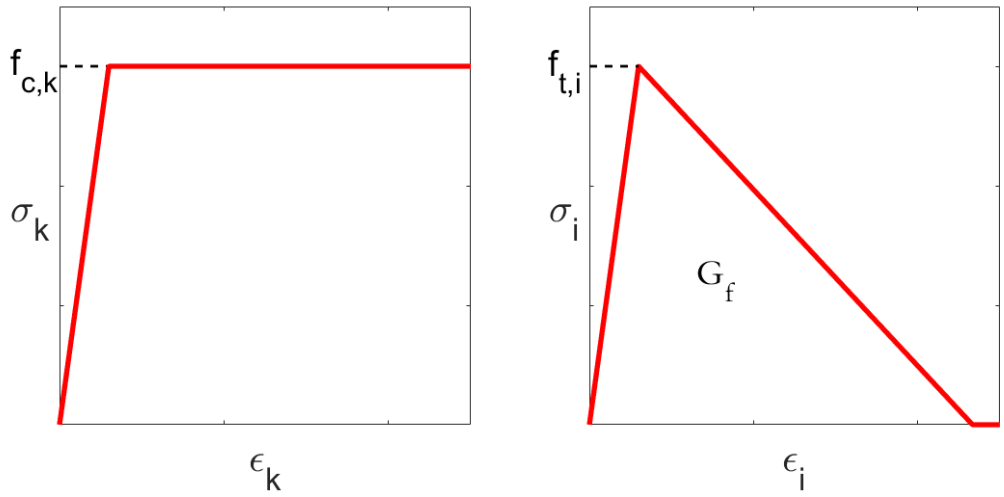

Figure 5.8: Qualitative representation of the stress-strain law adopted for: a) ductile failure modes, where $k = L, R, T$; b) brittle failure modes, where $i = L, R, T, LR, LT, RT$.

Kuilen [14] and Mackenzie-Helnwein et al. [172] and the other properties from the Handbook [158](Tab. 5.1). Based on the 3D FORTRAN code presented in Ch. 2, a 3D non-linear FE code hass been developed following the

Elastic Properties [MPa]				
E_L	E_T	E_R	$G_{LT} = G_{LR}$	G_{RT}
11000	500	800	690	50
Strengths [MPa]				
$f_{t,L}$	$f_{c,L}$	$f_{t,R} = f_{t,T}$	$f_{c,L} = f_{t,T}$	$f_{rol} = f_v$
45-65	25-35	0.5-2.5	3.8	4-6.9
Fracture Energies [N/mm]				
$G_{f,L}$	$G_{f,T}$	$G_{f,vR}$	$G_{f,vT}$	$G_{f,roll}$
2	0.3	1.2	1.2	0.6

Table 5.1: Material parameter of Norway spruce employed for the numerical simulations

mathematical formulation presented. The flow chart of the code can be found in Fig. 5.9.

The procedure has been validated by modelling experimental 4-point bending tests carried out on four integer Norway spruce beams. The experimental and numerical structural responses were in close agreement. In particular, not only the load vs displacement curves were highly comparable (general shape, peak loads and displacements at failure correctly predicted), but also the failure mode associated with bending failure was consistently reproduced: indentation under the anvils, damage slowly growing at extrados due to compressive stress, damage due tension quickly propagating at the intrados under the loaded zone in the post-peak regime (data not shown).

5.5 CASE STUDY: END-REPAIRED BEAM

A large number of timber structures is part of the human heritage, and in recent years the new timber constructions have impressively grown as manufacturing volumes and have attracted ever more interest in the building sector. However, during their service life timber elements may need reinforcing in-

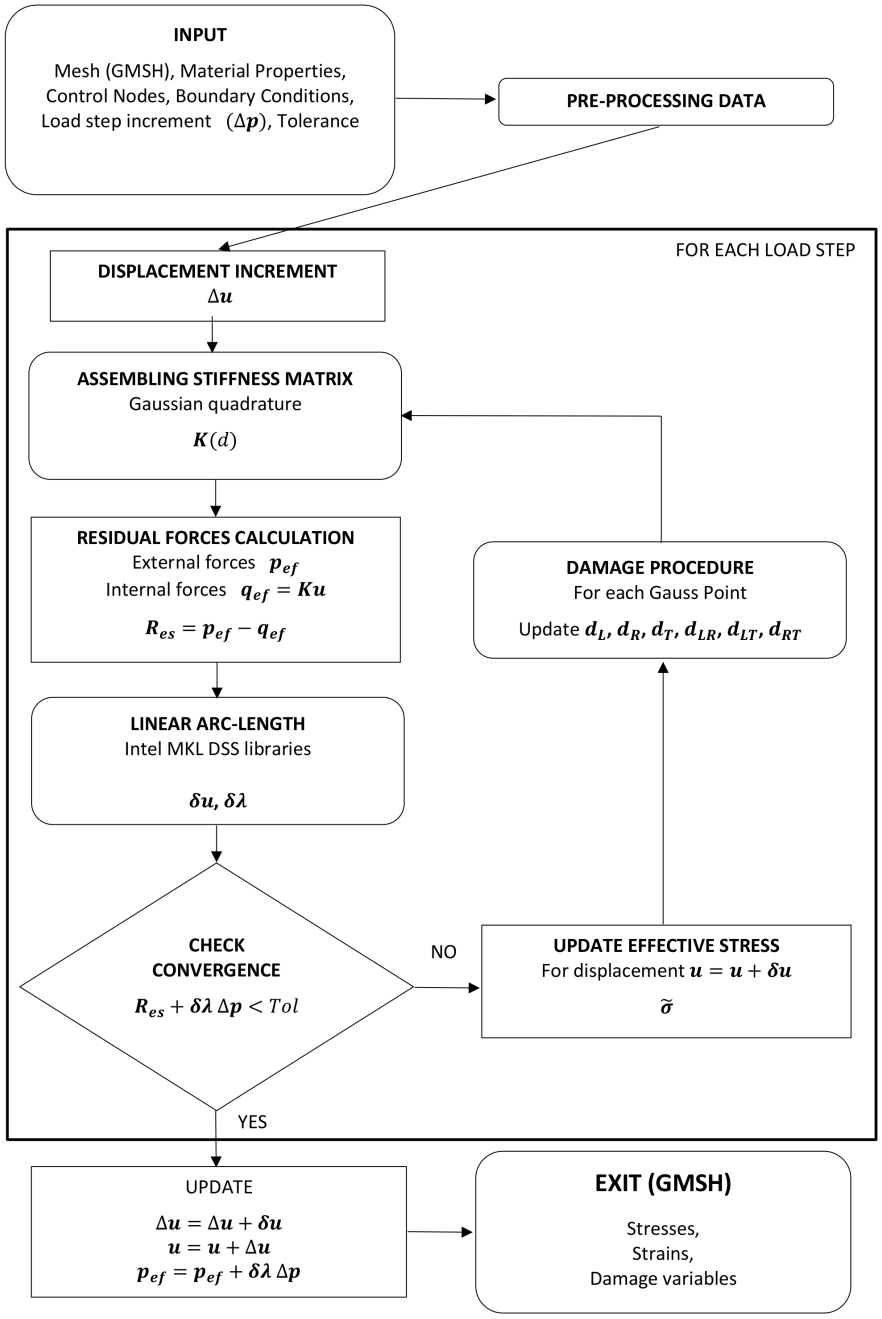

Figure 5.9: Flow chart of the 3D non-linear FORTRAN FE code implemented based oh the orthotropic damage model assumed [14]

terventions due to several reasons (e.g., an increase in load-bearing capability owing to modified service conditions in buildings), including repair when decay has occurred [177]. In fact, specific parts of timber elements (such as the ends, usually in contact with masonry) are under high risk of biotic attack because excessive levels of humidity may possibly develop in walls (e.g., after malfunctioning of rain-collecting systems, associated to lack of adequate maintenance) [178]. In the events mentioned above, which can be related to both old and new buildings, the use of glued-in rods (GIR) placed into predrilled holes or slots and bonded with structural adhesives, represents a good solution for possible interventions; in fact, the joints prepared with GIR are considered to possess high strength and stiffness along the rod axis, low cost for the preparation, improved fire resistance and good aesthetic appearance, due to both hidden connecting elements and low loss of original timber [179, 180]. This latter characteristic is most important in the conservation of timber elements in heritage monuments, as in this case the safeguarding authorities prescribe that the original parts are maintained integer as much as possible, even when structural upgrading is needed (in fact, in many cases the timber surface may be decorated e.g. with paints). Thus, the use of interventions making use of GIR is a realistic and successful alternative to the replacement of whole elements that are only partially decayed, provided that these interventions are consistent with heritage conservation principles [181]. However, the majority of research carried out on GIR has been oriented towards rods glued into wood elements under purely axial loading. Already in these conditions bars are subjected to both uneven stress distribution along their length (peaks at both rod ends) and stresses perpendicular to the axis [182–184]. Furthermore, in lateral loading conditions, such as those characterising the interventions on beam-ends or on spliced beams (both are moment resisting connections), a multiaxial system of forces is involved, which makes the stress distribution much more complex to manage. In fact, mechanical response of wood under multi-axial stress states has been considered only rarely [185], and little is known about failure behaviour of timber under combined stresses [186]. It is worthwhile observing that even in the case of uniaxial forces nominally acting on the bars the design approach is not fully established among researchers, and no unique design codes exist at European level for this typology [187]. Actually, Eurocode 5 (EN 1995-2 [188]) does not take into account this specific type of connection. Thus, it can be easily un-

derstood how no reliable rules to predict the mechanical performance are yet available for the case of multiaxial stress distribution. Accordingly, the usual approach encountered in the scientific literature to characterise the load bearing capacity of such connections is based on developmental-type investigations sometimes associated to Finite Element (FE) modelling. Experimental trials were carried out on both new and old timber beams where one of the two ends were cut and re-connected using GIR inserted in slots, so as to simulate a repair intervention on biologically decayed ends [189]. The prepared beams were tested in bending (thus, rods were laterally loaded), and results evidenced that specimens invariably failed at the repaired side and the collapse mechanism was wood splitting close to rods, which was unexpected according to the adopted design approach. A combined effect of shear and orthogonal-to-grain tensile stresses was suggested as possible causes of collapse [189]. Splitting induced by non-axial loading was also observed in other cases of laterally loaded bars. For instance, recent tests [190] were carried out on Sitka spruce spliced beams, connected with glued-in basalt fibre reinforced polymer (BFRP) rods and subjected to pull-bending tests (combination of axial and bending forces). Results displayed that several specimens failed prematurely due to the occurrence of splitting, and in these cases a lower failure strength was observed with an average drop of almost 8% [190]. Splitting of GIR reinforced wood is usually attributed to: a) short edge distances; b) rod misalignment; c) excessive loading perpendicular to the grain. This failure mode can be prevented by transversely reinforcing the connection in the proximity of bars, e.g. by means of screws [180]. This solution was already adopted in tests carried out on glued-laminated spliced beams of Norway spruce loaded in bending [191]. Moreover, new spruce beams with ends cut and repaired using steel bars and transversal screws passing from the intrados to the extrados evidenced a 30% load-bearing capacity increase compared to the series without the screws [192]. The mechanical behaviour of such prostheses is made even more complex by the fact that in GIR-based connections the joint strength depends on parameters affected by both the mechanical and the geometrical factors of three different materials: wood, adhesive, and reinforcing/connecting element. Thus, FE modelling is often taken into consideration to interpret the results obtained in experimental tests. Focus of present work is to analyse in more detail the mechanical behaviour of timber beams repaired by means of solid wood prosthesis connected with steel GIR and to

evaluate possible improvements of such behaviour by using screws, as suggested in [192]. In our case, differently than what was done before, the use of short screws locally reinforcing the elements in the perpendicular-to-grain direction and placed close to the rod insertion areas is considered in the attempt of limiting the use of long screws (mostly impacting for large-sized beams). The effect of the local reinforcement was also evaluated by using different inclination (45° and 90° with respect to the geometrical axis of the beam) of the cut executed to connect the prosthesis to the rest of the beam. Four-point-bending tests were carried out in the Laboratory on spruce repaired beams up to the final collapse. Each test was documented by photogrammetric surveys through which it was possible to follow the whole deformation process of the beam. Such experimental tests offered the opportunity of validating the mentioned 3D-CDM model to predict the load carrying capacity (also in bending) of repaired beams. In fact, to the authors' knowledge, FE simulations of timber beams end-repaired with wood prosthesis, GIR steel bars and reinforcing screws have yet to be done. At this regard, a high-performance 3D and parallelised Finite Element FORTRAN code has been developed to carry out large-scale numerical simulations of the experimental tests and to obtain numerical results to compare with the experimental ones.

5.5.1 *Experimental tests*

A total of 15 glulam, simply supported beams (cross section $120x160\ mm^2$; span length 1800 mm), graded as GL24 and made of Norway spruce (Picea abies Karst.) were analysed in 4-points bending tests (Fig. 5.10a, 5.10b, 5.10c). The various specimens were cut close to one end and then the two parts were re-sewed using 4 steel bars (S275, nominal diameter 10 mm, length 400mm) glued into specifically prepared slots by means of epoxy adhesive (Mapewood Paste 140). In this way, the variability related to wood characteristics (density, slope of grain, moisture content, ageing effects etc.) on joint performances was kept to a minimum. The transversal geometry of specimens is shown in Fig. 5.11. Rods were placed parallel to wood grain, and slots had a square section, as usual in interventions carried out onsite [193, 194]. Bars were centred along each slot using stoppers, thus ensuring an equal anchorage length between the two parts of the beam. Additionally, to arrange a proper centring, O-rings were used at rod ends. Beams were divided into three groups

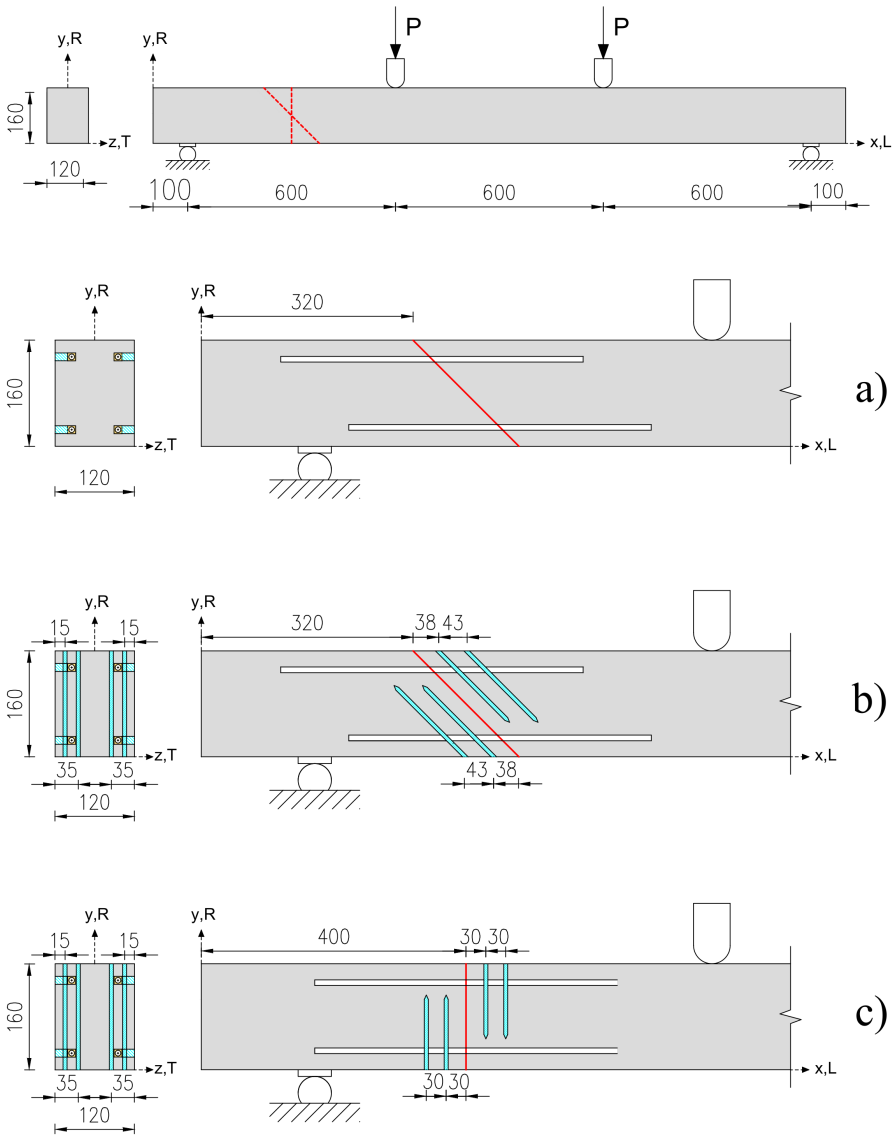

Figure 5.10: Specimen configurations and test arrangements: (a) the reference one (cut inclined 45°, no reinforcing screws); (b) same as (a) but with the use of reinforcing screws inclined 45° compared to wood grain; (c) configurations with vertical cut and perpendicular-to-grain reinforcing screws

(each consisting of five specimens) (Fig. 5.10): i) (configuration 45/*refer*) cut inclined 45° with respect to the geometrical axis. Considering that in normal practice no reinforcing screws are used, this configuration is assumed as the reference one for beams with 45° inclined cut (Fig. 5.10a) both in experimental and numerical tests; ii) (configuration 45/45) cut inclined 45° and use of 16 reinforcing screws (Φ6 mm, length 160 mm), 8 on each part of the beam, also inclined 45° compared to the wood grain/geometrical axis. The screws insertion pattern is shown in Fig. 5.10b. The length of reinforcing screws (160 mm) was selected based on previous tests [189], which showed that in the reference configuration the majority of specimens failed under the upper bar of the main part (the longer one) of the beam and above the lower bar of prosthesis (the shorter one) [189]. Therefore, the screws are stopped before the opposite rod; iii) (configuration 90/90) cut inclined 90° (vertical) and use of 16 reinforcing screws (Φ6 mm, length 120 mm), 8 on each part of the beam, inserted perpendicular to the wood grain. The screws insertion pattern is shown in Fig. 5.10c. The length of the screws was chosen with the same rationale as described in point (ii). It is worth noting that beams with 90° inclined cut, but without screws, were not tested because previous experiences proved the irrelevant influence of the cut orientation on the mechanical behaviour of the whole beam [192]. Beams were left to cure for a minimum of 15 days in standard conditions (20°C and 65% r.h.). The 4-points bending tests were configured so as to make appreciable the shear stress close to the repaired end-parts (Fig. 5.10), as usually occurs in real cases (where prostheses are close to walls). Tests were carried out on a Z600 universal testing machine (produced by Zwick/Roell) with 600 kN load capacity (load cell accuracy ±1%). Firstly, beams were subjected to 2 preliminary load steps from 0 to 12 kN; then, the load was gradually increased at a load-bar rate of 7.5 mm/min up to collapse. The load-displacement curve was acquired using the built-in LVDT transducer provided with the dynamometer; thus, the displacement of the upper loading anvils was actually measured. The results of the tests carried out in the Laboratory are shown in Tab 5.2 and in Fig. 5.12. As usual for timber elements, the data showed a certain variability. In series 45/45 and 90/90 this variability also increased due to failures starting from defects occurring in the wood beams (such as knots, localized grain deviations and presence of finger joints in lower lamellas) and hence not directly related to the presence of bars. This occurrence clearly indicated that the presence of short screws did not improve

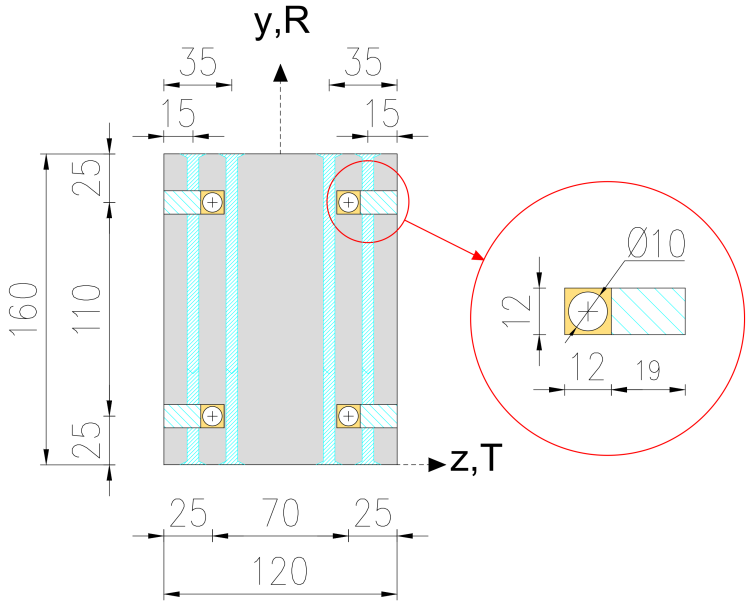

Figure 5.11: Scheme of the transversal section of all repaired beams. The position of the screws is also visible in the cross section

the mechanical performance of repaired elements, but they left unaltered both the load at collapse and the stiffness of reinforced beams. Looking at the failure mode, it was observed that beams of series 45/*refer* collapsed due to the occurrence of splitting invariably localised under the upper rods of the main (longer) part of the beam, similar to Pizzo et al. [189] This mechanism was also associated to the pull-out of lower bars, which occurred at the moment of collapse. Instead, in both 45/45 and 90/90 series cracks due to wood splitting moved down towards lower bars, localised at the tips of screws (mechanism ALBB in Tab. 5.2). Thus, the presence of screws (although short) affected the failure mechanism of repaired beams.

5.5.2 *Numerical Results*

The three experimental typologies showed in Fig. 5.10 have been simulated, and the main mechanical parameters obtained after numerical analysis shown in Tab. 5.1. The steel rods and the adhesive have been modelled as elasto-plastic isotropic materials with the material parameters provided by the man-

Configurations	Sample	P_{max} [kN]	Deflection [mm] @ P_{max}	Failure modes
$45/refer$	T6	65.64	19.7	**UUBB**;POLB
	T9	59.01	18.1	**UUBB**;POLB
	T10	65.08	19.7	**UUBB**;POLB
	T12	57.00	19.8	**UUBB**;POLB
45/45	T1	51.26	14.7	**T**
	T5	63.36	17.7	**ALBB**;POLB
	T8	49.87	15.4	**T**
	T11	65.30	18.1	**ALBB**;POLB
	T13	66.67	N.A.	**ALBB**;POLB
45/45	T2	55.94	23.1	**T**
	T15	62.35	28.5	**ALBB**
	T16	56.23	17.5	**ALBB**
	T17	64.46	21.4	**ALBB**
	T18	58.89	18.2	**ALBB**

Table 5.2: Experimental results obtained for end-repaired beams. UUBB = under the upper bar of the main (longer) part of the beam; ALBB = above the lower bar of the main part of the beam; POLB = pull-out of the lower bars; T = timber-related defects (knots, localised grain deviation, rupture in finger joints etc.). In bold the mechanism observed in the pre-peak regime.

(a) Failure mode UUBB (b) Failure mode ALBB

Figure 5.12: Examples of failure modes for representative elements: a) UUBB; b) ALBB.

ufacturers. In particular, the steel and adhesive Young's moduli are 210000 and 4000 MPa, respectively, while the Poisson coefficients are 0.3 and 0.35, respectively. Moreover, steel S275 has been used in all the simulations, except in the case of passing screws as illustrated in Sec. 5.5.4, where both steel S275 and B450C have been used. For the sake of simplicity, a perfect adhesion has been assumed at the steel-adhesive and the adhesive-wood interfaces. A thin layer made of a linear elastic isotropic material with reduced Young's modulus has been introduced to simulate the unilateral contact at the cut-interface. As for wood, the parallel-to-grain compressive strength, $f_{c,L}$, and the tensile strength, $f_{t,L}$, have been set to 35 and 65 MPa, respectively, whereas the other parameters are shown in Tab. 5.1. More comments on the model sensitivity to the material parameters are given in Sec. 5.5.5. A three-dimensional mesh with 228599 tetrahedrons and a characteristic mesh size of 2 mm has been used. The numerical test took 13 hours. Owing to the symmetry with the respect to the LR-plane, only one half of the specimen has been modelled. The experimental and the numerical load vs displacement curves for the $45/refer$ configuration of Fig. 5.10a are displayed in Fig. 5.13. It can be drawn that the response of the repaired beam is brittle. Fig. 5.14 displays the contour plots of the cumulative damage greater than 10^{-3} evaluated at the development of the first macro-crack (Step A), at the peak load (Step B) and at complete failure (Step C). Before the load peak, the contour map of the cumulative damage at Step A displays two horizontal cracks located below the upper bar in the

Configurations	P_{max} [kN]	Deflection @ P_{max} [mm]	Failure modes
$45/refer$	62.02	17.1	Pull-out of the lower bar in the main beam combined with horizontal crack above the lower bars in the main part of the beam
45/45	61.72	16.46	Pull-out of the lower bar in the main beam combined with horizontal crack above the lower bars in the main part of the beam
$90/refer$	52.78	15.03	Yielding of the lower bars
90/90	56.43	18.14	Horizontal crack above the lower bars in the main beam
90/90 passing screws S275	60.02	20.38	Yielding of the lower bars
90/90 passing screws B450C	66.64	22.79	Pull-out of the lower bar in the main beam combined with horizontal crack above the lower bars in the main part of the beam
$45/refer$ $f_{t,R} = 0.50$ MPa $f_v = 6.9$ MPa	57.16	17.70	Shear cracks across the cut and horizontal crack above the lower bars in the main beam
$45/refer$ $f_{t,R} = 0.50$ MPa $f_v = 6.9$ MPa	62.86	18.19	Pull-out at the end of the lower bar in the main beam
$45/refer$ $f_{t,R} = 0.50$ MPa $f_v = 6.9$ MPa	63.87	17.77	Pull-out at the end of the lower bar in the main beam

Table 5.3: Peak loads, displacements at peaks and failure modes for each numerically simulated configuration.

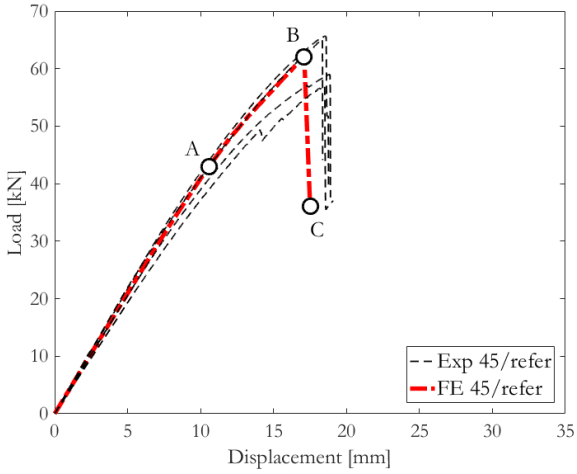

Figure 5.13: Comparison between experimental (black dashed line) and numerical (red point-dashed line) load vs deflection curves obtained for $45/refer$ beam and obtained with $f_{t,L} = 35$ MPa, $f_{c,L} = 65$ MPa, $f_{t,R} = 1.25$ MPa, $f_v = 4$ MPa.

main part of the beam and above the bottom bar in the prosthesis. Furthermore, an indentation process develops under the loaded area. Then, at step B corresponding to the peak reached at load 62.02 kN, the compression generated by the bending starts damaging the upper side of the beam section, while the aforementioned horizontal cracks further propagate. In addition, a damaged zone close to the left end of the lower bar is activated. This latter damage zone spreads at failure, reached at Step C, possibly, as a consequence of the pull out of the bars. Fig. 5.13 and Fig. 5.14 display a good agreement between the numerical and the experimental results. Both the failure mode and the structural response obtained from the numerical simulation are consistent with those observed in the experimental tests. Particularly interesting is the agreement with the cumulative damage at Step A, where the cracks developing before the maximum load is attained (evidenced both in present, Fig. 5.12, and previously reported tests [189], are correctly predicted.

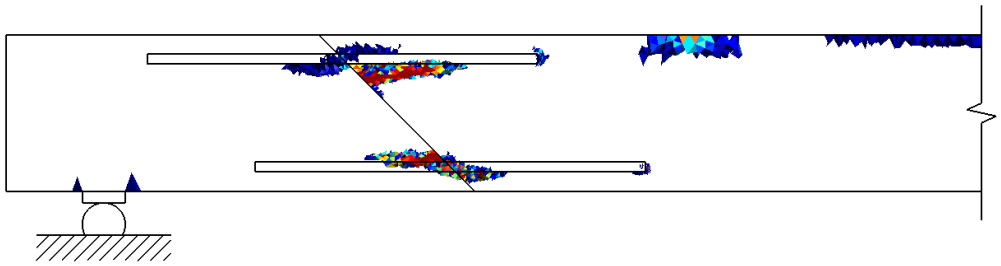

(a) Step A

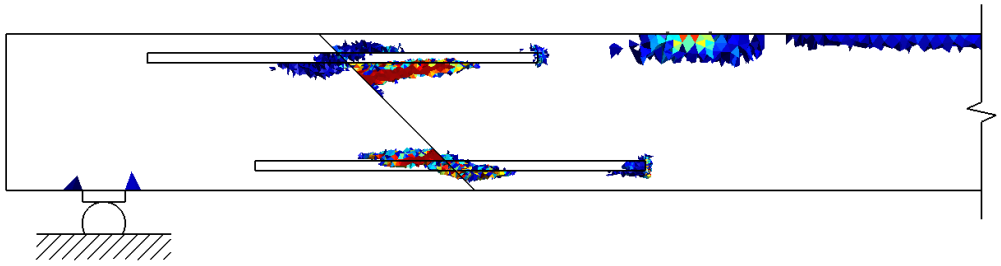

(b) Step B

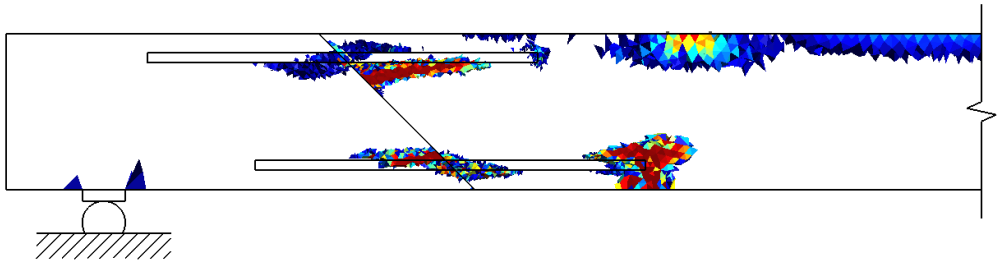

(c) Step C

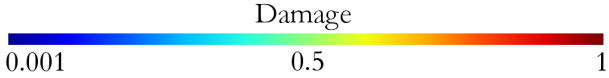

Figure 5.14: Contour plots of the cumulative damage for the 45/*refer* beam (Fig. 5.10a) at different steps of the load vs displacement curve (Fig. 5.13).

5.5.3 *Influence of screws*

The simulation of the two numerical models related to configurations 45/45 and 90/90 (respectively Fig. 5.10b and Fig. 5.10c) was made by 315484 and by 297092 tetrahedrons, respectively. It has taken almost 19 hours for the 45/45 configuration and 17 hours for the 90/90 one on a PC i7-5930k CPU. The numerical and the experimental load vs deflection curves are reported in Fig. 5.15. For the sake of completeness, the results obtained for the configuration without reinforcing screws have also been reported. It can be deduced that the screws do not significantly affect the peak load and the brittleness of the structural response of the 45/*refer* end-repaired beams, whereas they increase the peak load by only 6% in the 90/90 configuration. Fig. 5.16 and Fig. 5.17 show the contour plots of the cumulative damage for the 45/45 and 90/90 configurations, respectively. In particular, the displayed contour plots correspond to the stages immediately before (a) and at failure (b), namely at Steps B and C (Fig. 5.15) according to the notation adopted for the 45/*refer*. Furthermore, a detail of the cumulative damage at failure in the screws section is reported in Fig. 5.16c and Fig. 5.17c. These contour plots show that, in both the considered configurations, the reinforcing screws stop the crack propagation below the upper rods of the main part of the beam, whereas some damage develops at the screws tips. Moreover, failure occurs around steel bars, as a consequence of either yielding or pull-out-related tensions.

5.5.4 *Numerical assessment of the effect of passing screws*

Numerical investigation was also used to assess to which extent the usage of passing screws (Fig. 5.18) might further improve the structural performance of the end-repaired beams. For this purpose, simulations have been carried out for the case of the 90° cut. In detail, two simulations have been run, one with a steel with yielding stress equal to 275 MPa, the same as used on the experimental tests, and another one with a steel yielding at 450 MPa, the same used in [192], with the aim of assessing the influence of the steel strength on the increase of the peak load. The failure modes detected in the simulations are presented in Tab. 5.3. Fig. 5.19 shows that, with respect to the 90/*refer* beam, the passing screws increase the failure load by 14% in the case of steel *S*275, namely from 52.78 kN to 60.02 kN, and by 26% in the case of steel

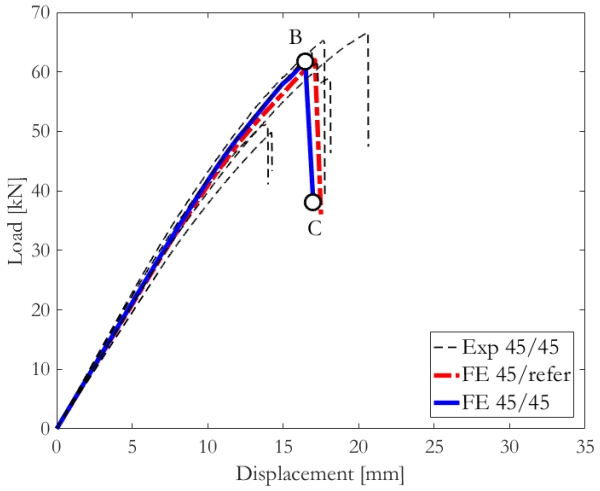

(a)

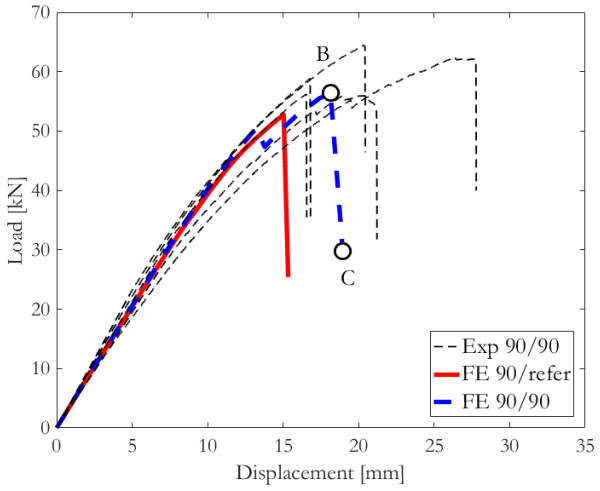

(b)

Figure 5.15: Comparison between experimental (black dashed line) and numerical load vs displacement curves for: a) the 45/*refer* (red point-dashed line) and the 45/45 (blu continuous line); b) the 90/*refer* (red continuos line) and the 90/90 (blu dashed line) configurations. $f_{t,L} = 35$ MPa, $f_{c,L} = 65$ MPa, $f_{t,R} = 1.25$ MPa, $f_v = 4$ MPa

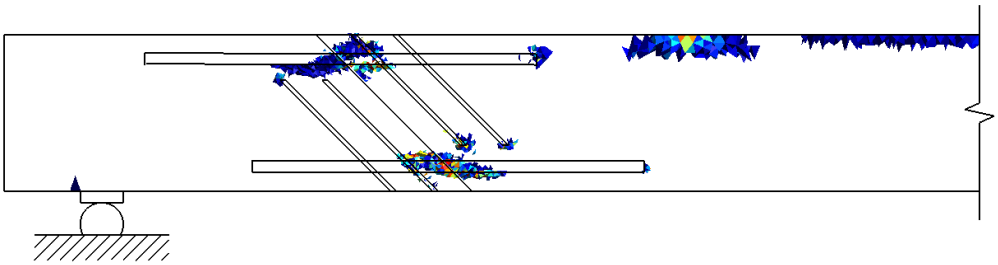

(a) Step B

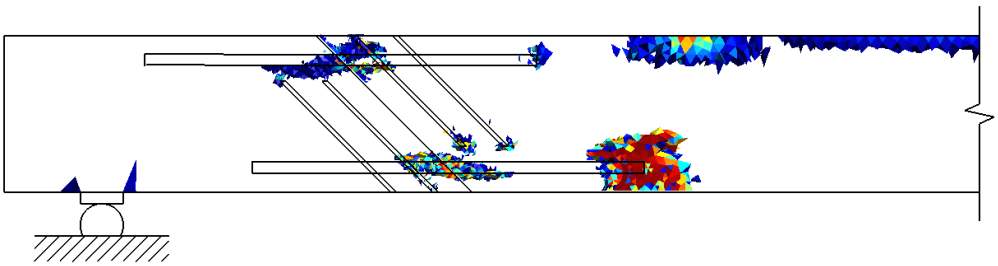

(b) Step C

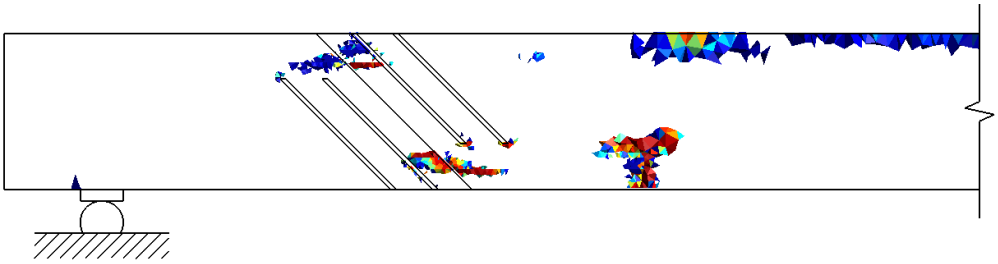

(c) Step C, screws section

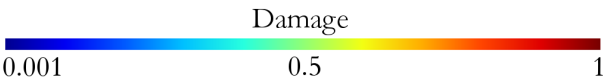

Figure 5.16: Contour plots of the cumulative damage immediately before (a) and at failure (b) for the 45/45 configuration (Fig. 5.10b). In (c), the cumulative damage at failure in the screws section is shown.

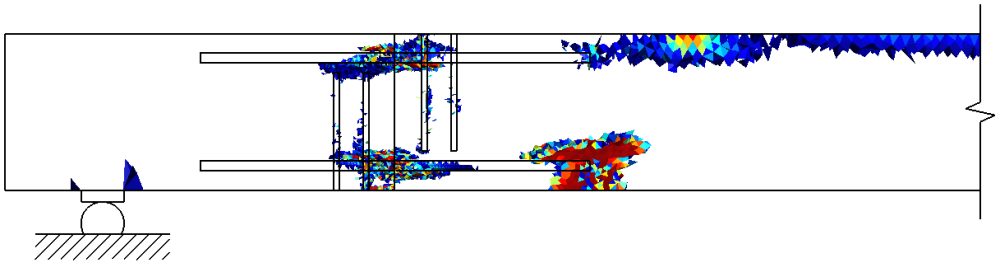

(a) Step B

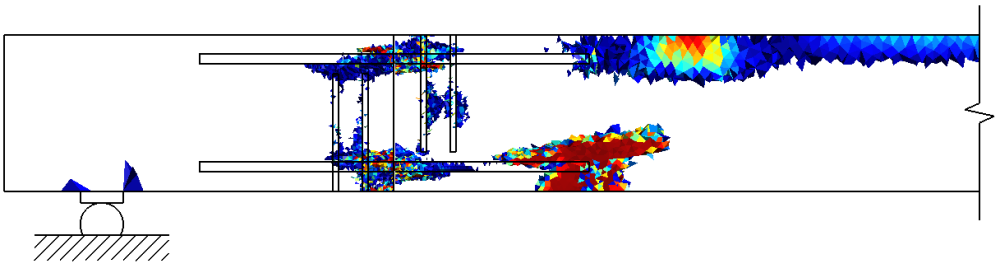

(b) Step C

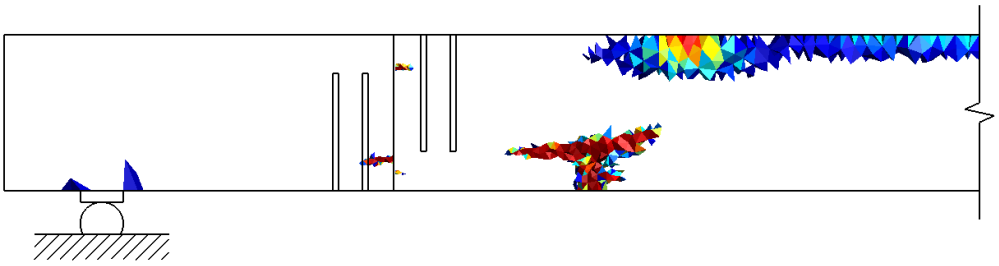

(c) Step C, screws section

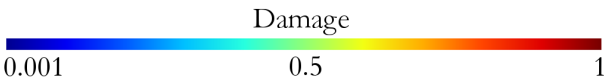

Figure 5.17: Contour plots of the cumulative damage immediately before (a) and at failure (b) for the 90/90 configuration of Fig. 5.10c. In (c), the cumulative damage at failure in the screws section is shown.

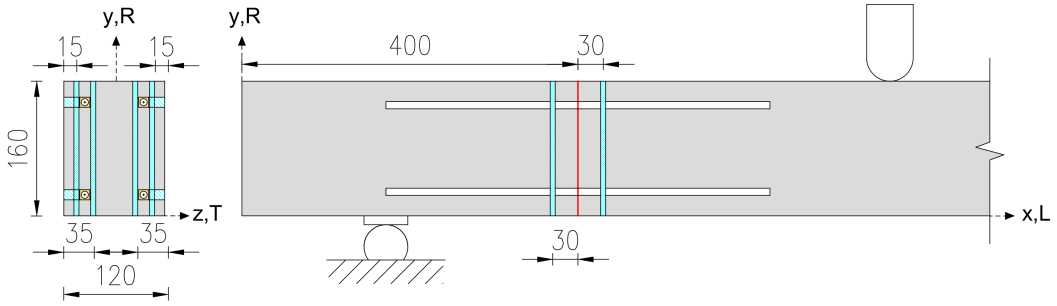

(a) Step A

Figure 5.18: The configuration with 90° cut and passing screws simulated in the numerical investigation

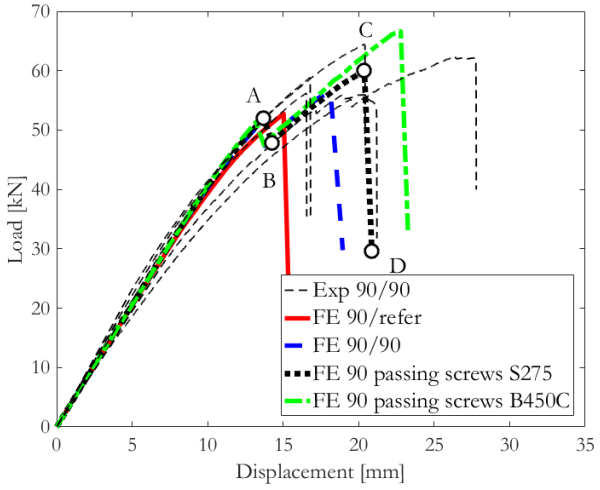

Figure 5.19: Comparison between numerical load vs displacement curves for the 90 cut beam with passing screws in both cases of steel S275 and B450C, the 90/90 configuration with non-passing screws (experimental tests), and the $90/refer$ beam. $f_{t,L} = 35$ MPa, $f_{c,L} = 65$ MPa, $f_{t,R} = 1.25$ MPa, $f_v = 4$ MPa.

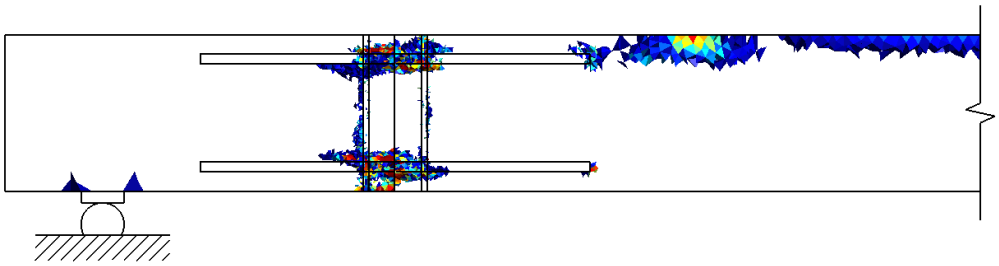

(a) Step A

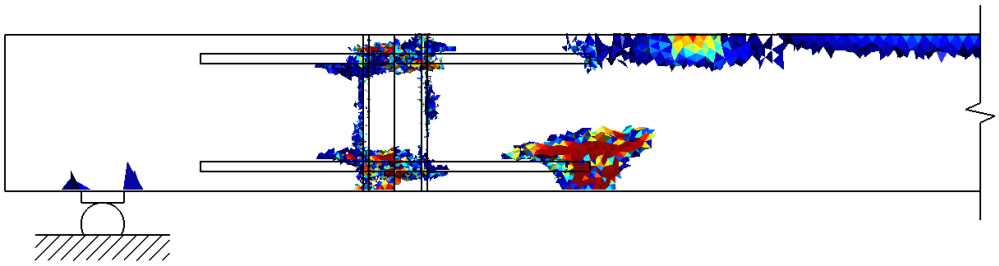

(b) Step B

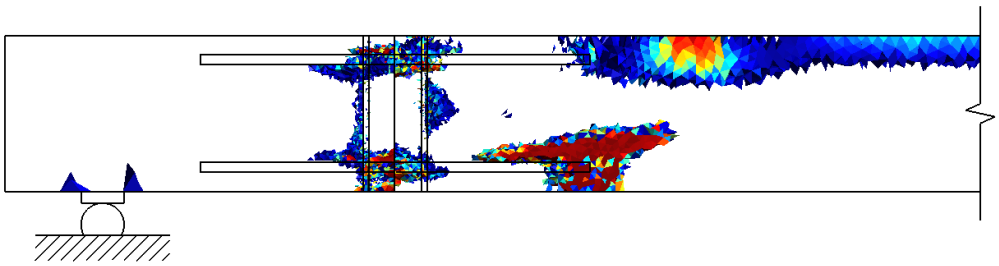

(c) Step C-D

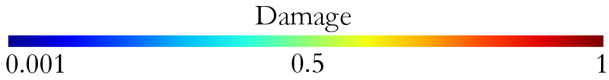

Figure 5.20: Contour plots of the cumulative damage for the 90° cut beam with passing screws and steel S275.

*B*450*c*, that is from 52.78 kN to 66.64 kN. The damage maps illustrated in Fig. 5.20 display that, analogously to the non-passing screws, the presence of the passing screws inhibits damage in their surrounding zone: failure starts at Step C, completes at step D and occurs by yielding and/or pull-out of the steel bars. On the other hands, it is worth noting that, when screws made of *B*450*C* are simulated, the damaged zone developing above the lower bar in the main part of the beam is larger, and failure mainly occurs by pull-out of the lower bar, while the yielding of the latter is still present but to a lesser extent.

5.5.5 *Numerical sensitivity analysis to the orthogonal to the grain tensile strength*

A sensitivity analysis has been carried out on the $45/refer$ configuration to assess the influence of the strength properties along the direction orthogonal to the grain, having fixed all the remaining material parameters. In particular, the cases where $f_{t,R} = 0.50, 1.25, 2.50$ MPa with $f_v = 6.9$ MPa have been considered. Fig. 5.21 compares the experimental and the structural paths computed with the aforementioned parameters. It can be drawn that changing the strength in the radial direction does not significantly alter the load-displacement curves. The corresponding damage maps at failure are displayed in Fig. 5.22, and they evidence that the respective damage patterns are markedly different, especially in the case of $f_{t,R} = 0.50$ MPa, for which the model predicts diffused shear cracks across the cut that, however, have not been experimentally observed. This occurrence implies that the characteristic value of 0.5 MPa recommended in codes for class GL24 (the same used in present tests) is highly precautionary and not suitable for numerical codes. The failure modes computed for the whole set of constitutive parameters are collected in Tab. 5.3. A satisfying correspondence between the numerical and the experimental failure modes can be evidenced.

5.6 CONCLUSIONS

Some experimental tests were aimed at evaluating the effectiveness of short screws inserted in beams repaired at one end with the use of GIR, to locally reinforce timber in the perpendicular-to-grain direction. Moreover, a comprehensive numerical analysis was carried out in order to interpret the experi-

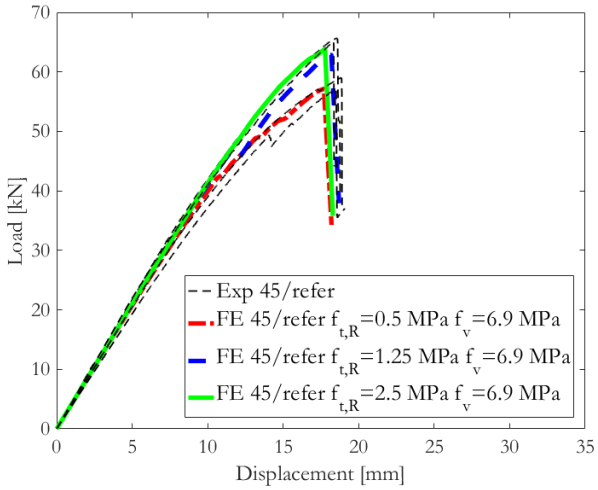

Figure 5.21: Sensitivity analysis: Influence of the radial tensile strength $f_{t,R}$ obtained with $f_{t,L} = 35$ MPa, $f_{c,L} = 65$ MPa.

mental behaviour of both reinforced and unreinforced beams. Results showed that short screws were not able to substantially improve the load capacity of repaired elements, for both configurations 45/45 and 90/90. However, the presence of screws (although short) affected the failure mechanism of repaired beams: the movement of the due-to-splitting cracks towards the lower bars (of the main part of the beam) was observed in the two screw-reinforced configurations, differently from the $45/refer$ series where splitting was localised below the upper bars. Numerical simulation agreed to a very good extent with experimental results (for both screw-reinforced and unreinforced configurations): both the load-displacement curves and the obtained damage maps observed in mechanical tests were correctly predicted. Moreover, even when applied to the case, already reported in the literature, of screws passing from extrados to intrados, the numerical model predicted a load capacity increase very close to the one previously reported. Finally, sensitivity analysis allowed establishing that the experimentally observed failure mechanism is related to the failure criteria III/IV, which in fact provides a combination of tension perpendicular-to-grain, longitudinal shear and rolling shear stresses.

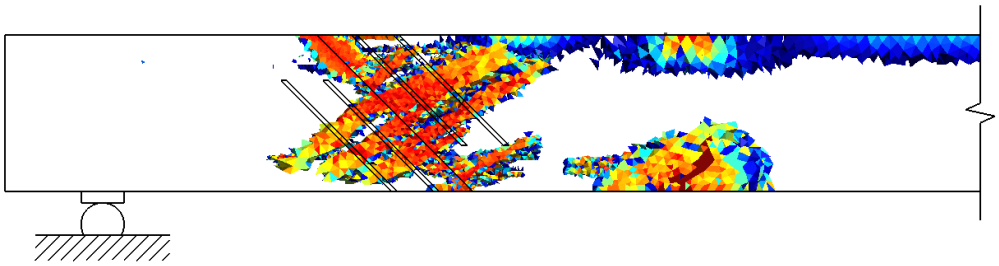

(a) a) $f_{t,R} = 0.50$ MPa

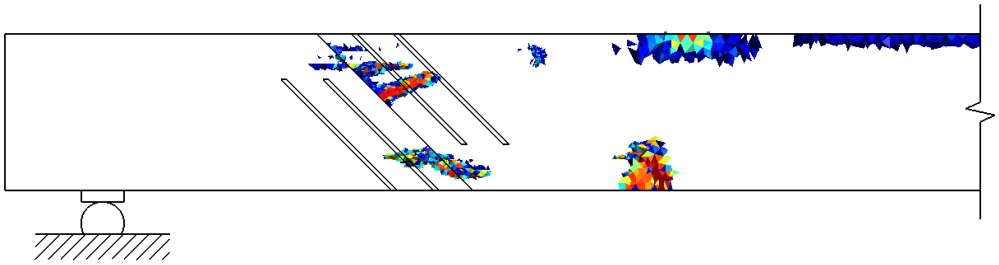

(b) a) $f_{t,R} = 1.25$ MPa

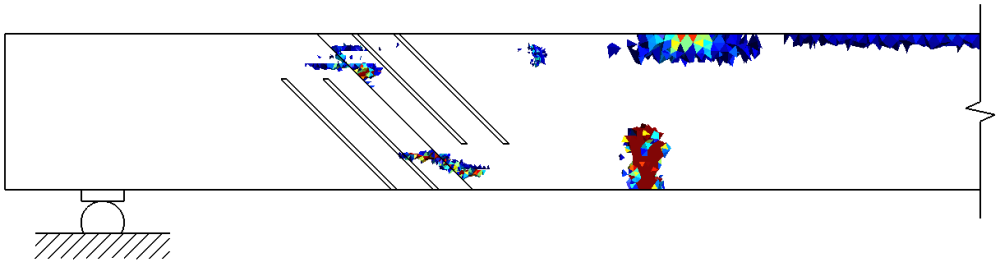

(c) a) $f_{t,R} = 2.50$ MPa

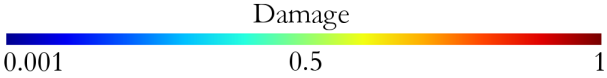

Figure 5.22: Contour plots of the cumulative damage at failure for the $45/refer$ beam for variable $f_{t,r}$.

6

A NEW ORTHOTROPIC ELASTO-PLASTO-DAMAGE MODEL FOR WOODEN BEAMS AND ITS IMPLEMENTATION IN THE RE-XFEM CONTEXT

In Ch. 5, the orthotropic CDM model proposed by Sandhaas et al. [14] has been used to study the structural response of end-repaired wooden beams. The simulations, reported in Sec. 5.5, showed that the CDM model is able to model in a suitable way the brittle behaviour of end-repaired wooden beams and, in particular, to capture correctly the position of the damaged zones. However, the proposed 3D orthotropic CDM model has some weaknesses.

The weak points of the model are mainly related to the compressive behaviour of the material and to the strain localization. Indeed, wood in compression exhibits a complex plastic non-linear behaviour, that cannot be fully described by the ductile damaging law of CDM [14]. In this sense, multi-surface plasticity models have to be preferred for simulations involving plasticity and damage under compression.Furthermore, in CDM model [14], the crack process zone tends to be spread over large areas.

This chapter presents a new constitutive model developed in collaboration with Prof. Michael Kaliske of the *Institute of Structural Analysis* of Dresden is presented. The collaboration is aimed to propose a new 2D elasto-damaging plastic constitutive law for wood where discontinuities are modelled through a suitable RE-XFEM.

After a brief introduction to the multi-surface plasticity models developed for wooden structures by Kaliske and coworkers in Sec. 6.1, the motivations and the key aspects of the new computational model are presented in Sec. 6.2. Some numerical tests on benchmarks and experimental tests are shown in Sec. 6.4. In the end, some remarks on the firsts result obtained and on the future developments are discussed in Sec. 6.5 and in Sec. 6.6, respectively.

6.1 MULTI-SURFACE PLASTICITY MODEL

In order to model the non-linear behaviour of wood, Schmidt and Kaliske [35] proposed a 3D multi-surface plasticity model. This constitutive model consists of 7 different flow rules f_m, each one have the form

$$f_m(\boldsymbol{\sigma}, \alpha_m) = \boldsymbol{a_m^t}\boldsymbol{\sigma} + \boldsymbol{\sigma}^t \boldsymbol{B}_m \boldsymbol{\sigma} + q_m(\alpha_m) - 1 = 0 \qquad m = 1, \ldots, 7 \quad , \tag{65}$$

where $\boldsymbol{a}_m$ and $\boldsymbol{B}_m$ are the strength tensors set on the basis of a large experimental campaign on biaxial tests (Eberhardsteiner [185]), q_m is a scalar parameter that rules the non-linear evolution of the plastic surface and α_m is the internal plastic state variable. The seven flow rules, each one corresponding to a failure mode, are

- Tension in Radial direction $(m = 1)$
- Compression in Radial direction $(m = 2)$
- Tension in tangential direction $(m = 3)$
- Compression in tangential direction $(m = 4)$
- Tension in Longitudinal direction $(m = 5)$
- Compression in longitudinal direction $(m = 6)$
- Shear $(m = 7)$

In general, in the method proposed by Schmidt and Kaliske [35], the softening behaviour associated with a brittle failure modes, such as tension and shear failure is defined through the function

$$q_m = [1 - exp(-\eta_m \alpha_m)] \quad , \tag{66}$$

where the parameter η_m determines the shape of the softening function. In particular, for tensile failure modes,

$$\eta_m = \frac{f_{t,i} l_c}{G_{f,i}} \qquad i = L, R, T \quad , \tag{67}$$

where l_c is the characteristic length taken equal to the finite element size and $G_{f,i}$ is the fracture energy of the tensile failure mode along the direction i. For the shear failure mode

$$\eta_7 = \frac{f_v l_c}{G_{f,v}} \quad , \tag{68}$$

where f_v is the shear strength of the specimen and $G_{f,v}$ is the fracture energy related to the shear failure mode.

For ductile failure modes, the evolution of the stress-strain relationship is governed by the function

$$q_m = (1 - k_m)\left[1 - exp(-\eta_m \alpha_m)\right] - \psi_m \frac{(\alpha_m - \alpha_{m,d})^2}{\alpha_{m,max} - \alpha_m} \quad , \tag{69}$$

where k_m is a parameter that rules the hardening, ψ_m is a scalar form factor, and $\alpha_{m,d}$, $\alpha_{m,max}$ and η_m are shape parameters. Figs. 6.1a and b show the effects of the shape parameters for the stress-strain behaviours at compression perpendicular-to-grain and parallel-to-grain, respectively. Parameters need to be calibrated in order to model the correct stress-strain response.

In order to implement a non-smooth multi-surface model, an iterative return mapping algorithm has to be implemented. In particular, the closest point projection algorithm proposed by Simo and Hughes [36] has been used.

Several investigation has been carried out in order to take into account the presence of inhomogeneities, the effect of humidity, thermo-higro-mechanical coupling [173, 195, 196]. However, at this stage of the research, these additional effects have not been considered.

6.2 A 2D ORTHOTROPIC MULTI-SURFACE ELASTO-PLASTO-DAMAGE MODEL COMBINED WITH RE-XFEM

In this section, a 2D new constitutive model for wood is presented. The new model relies on two assumptions:

- Failure modes in compression are modelled by means a multi-surface plasticity models. In particular, the multi-surface plasticity model proposed by Schmidt and Kaliske [35] and described in the previous section has been considered.

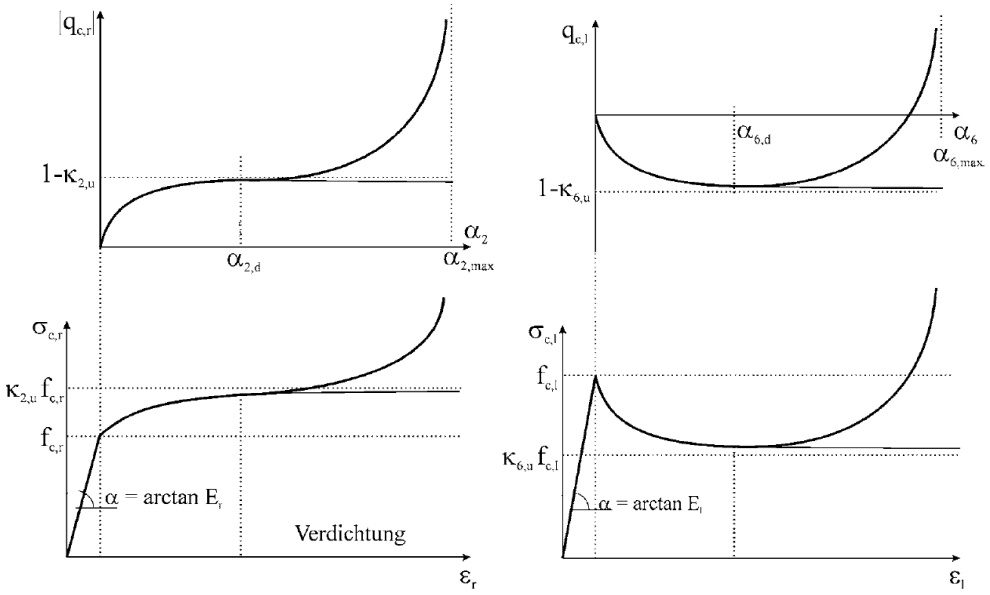

(a) (b)

Figure 6.1: Qualitative stress-strain behaviour at compression perpendicular-to-grain (a) and parallel-to-grain (b) adopted by Schmidt and Kaliske [35]

- Quasi-brittle failure modes, such as failure modes in tension and shear, are modelled by means the orthotropic CDM model proposed by Sandhaas et al. [14]. The cracks development is modelled with a suitable RE-XFEM, that is combined to the orthotropic CDM by the adoption of a continuous-discontinuous transition.

The final constitutive model consists in an orthotropic 2D multi-surface elasto-plasto-damage model, where interfaces are modelled through an orthotropic RE-XFEM.

Let us consider plane-stress problems where the x-axis and the y axis are aligned with the longitudinal (L) and the radial direction (R),

$$\boldsymbol{\sigma} = \left[\sigma_{xx}, \sigma_{yy}, \sigma_{xz}\right]^t \equiv \left[\sigma_L, \sigma_R, \sigma_{LR}\right]^t \quad . \tag{70}$$

In the two-dimensional case, six independent damage variables have been introduced into the model, namely

$$\boldsymbol{d} = \left[d_L, d_R, d_{LR}\right]^t \quad \text{and} \quad \boldsymbol{d^c} = \left[d_L^c, d_R^c, d_{LR}^c\right]^t \quad , \tag{71}$$

where the three variables collected in $\boldsymbol{d}$ pertain to the bulk, while the variables collected in $\boldsymbol{d}^c$ pertain to the Regularized XFEM.

During the load process two regimes can occur:

- in the *continuous regime* the material is governed by a multi-surface elasto-plasto-damage constitutive model until one of the damage variables of the bulk d_L, d_R, d_{RL} reaches the critical threshold d_{cr}

- in the *regularized discontinuous regime*, in the regularized volume, the bulk is ruled by an multi-surface elasto-plasto-damage model, while the regularized discontinuity is activated. The damage variables are d_L^c, d_R^c and d_{RL}^c start to grown from the critical value d_{cr} up to the maximum value 1.

In the following, a detailed description of the two regimes is reported.

6.2.1 *Continuous regime*

In the orthotropic CDM proposed by Sandhaas, the damaged compliance matrix $\boldsymbol{C}^d$ for the 2D plane-stress is defined as

$$\boldsymbol{C}^d = \begin{bmatrix} \frac{1}{(1-d_L)E_L} & -\frac{\nu_{LR}}{E_R} & 0 \\ -\frac{\nu_{LR}}{E_L} & \frac{1}{(1-d_R)E_R} & 0 \\ 0 & 0 & \frac{1}{(1-d_{RL})G_{RL}} \end{bmatrix} \quad , \tag{72}$$

where the damaged stiffness matrix is obtained $\boldsymbol{D}^d = (\boldsymbol{C}^d)^{-1}$.

The nominal stress $\boldsymbol{\sigma}$ is defined by the elasto-damaging plastic constitutive equation

$$\boldsymbol{\sigma} = \boldsymbol{D}^d(\boldsymbol{\varepsilon} - \boldsymbol{\varepsilon}^p) \quad , \tag{73}$$

where $\boldsymbol{\varepsilon}^p$ are the plastic deformations due to compressive failures. Furthermore, the effective stress field $\tilde{\boldsymbol{\sigma}}$ that takes into account the micro stress concentrations due to damage is define as

$$\tilde{\boldsymbol{\sigma}} = \boldsymbol{M}\boldsymbol{\sigma} \quad , \tag{74}$$

where $\boldsymbol{M}$ is the damage operator defined as

$$\boldsymbol{M} = \begin{bmatrix} \frac{1}{(1-d_L)} & 0 & 0 \\ 0 & \frac{1}{(1-d_R)} & 0 \\ 0 & 0 & \frac{1}{(1-d_{RL})} \end{bmatrix} \quad . \tag{75}$$

The proposed constitutive model consists in 5 different failure surfaces, as detailed in the following.

- Failure in tension along the longitudinal direction is a brittle failure mode caused by tensile stress parallel-to-grain $\tilde{\sigma}_L > 0$ and is governed by the damage variable d_L. The relevant criterion obeys the loading-unloading inequality

  $$F_I(\sigma) = \frac{\tilde{\sigma}_L}{f_{t,L}} - 1 \leq 0 \quad , \tag{76}$$

  where $f_{t,L}$ is the tensile strength along the longitudinal direction.

- Failure under compression along the longitudinal direction is a ductile failure mode governed by the plastic flow rule

$$f_{II}(\boldsymbol{\sigma}, \alpha_{II}) = \boldsymbol{a}_{II}^t \boldsymbol{\sigma} + \boldsymbol{\sigma}^t \boldsymbol{B}_{II} \boldsymbol{\sigma} + q_{II}(\alpha_{II}) - 1 = 0 \qquad , \tag{77}$$

$$\boldsymbol{a}_{II} = \begin{bmatrix} \frac{1}{f_{c,L}^2} & 0 & 0 \end{bmatrix}^t \qquad \boldsymbol{B}_{II} = \begin{bmatrix} 0 & \frac{0.33}{f_{c,R}^2} & \frac{0.25}{f_{v,RL}^2} \end{bmatrix} \boldsymbol{I} \quad . \tag{78}$$

- Failure in tension along the radial direction is a brittle failure mode governed by tensile stress along the radial direction $\tilde{\sigma}_R > 0$ and longitudinal shear ($\tilde{\sigma}_{LR}$) stress. It is characterized by the development of splitting cracks in LT-plane, and is related to the damage variables d_R, d_{LR} . The quadratic loading-unloading inequalities:

$$F_{III}(\sigma) = \frac{\tilde{\sigma}_R^2}{{f_{t,R}}^2} + \frac{\tilde{\sigma}_{LR}^2}{{f_v}^2} - 1 \leq 0 \qquad , \tag{79}$$

  are adopted.

- Failure in compression along the longitudinal direction is a ductile failure mode governed by the plastic flow rule

$$f_{IV}(\boldsymbol{\sigma}, \alpha_{IV}) = \boldsymbol{a}_{IV}^t \boldsymbol{\sigma} + \boldsymbol{\sigma}^t \boldsymbol{B}_{IV} \boldsymbol{\sigma} + q_{IV}(\alpha_{II}) - 1 = 0 \qquad , \tag{80}$$

  where

$$\boldsymbol{a}_{IV} = \begin{bmatrix} 0 & \frac{0.4}{f_{c,R}^2} & 0 \end{bmatrix}^t \qquad \boldsymbol{B}_{IV} = \begin{bmatrix} \frac{-0.25}{f_{c,L} f_{t,L}} & 0 & \frac{0.33}{f_{v,RL}^2} \end{bmatrix} \boldsymbol{I} \quad , \tag{81}$$

  are introduced.

- Failure by shear is a brittle failure mode induced by the longitudinal shear stress $\tilde{\sigma}_{LR}$ when the compressive radial stress $\sigma_R < 0$ occurs. It is governed by the damage variables d_{LR}. The current case is governed by the quadratic loading-unloading inequalities:

$$F_V(\sigma) = \frac{\tilde{\sigma}_{LR}^2}{{f_v}^2} + -1 \leq 0 \qquad . \tag{82}$$

Fig. 6.2 shows the 2D representation of the surface failures defined in the multi-surface plasticity model [35] and in the in the multi-surface elasto-damaging plastic model proposed compared with the experimental values obtained by Eberhadsteiner [185] on spruce specimens having $f_{t,L} = 65$ MPa, $f_{c,L} = -50.3$ MPa, $f_{t,R} = 3.75$ MPa, $f_{c,R} = 6$ MPa, $f_{V,LR} = 6.34$ MPa. The failure surfaces at compression have been reported with a red pointed line, while the failure surfaces in tension in the multi-surface plasticity model [35] and in the proposed model have been with a black continuous line and with a blue dashed line, respectively. In the plasticity model proposed by Schmidt and Kaliske [35], the tensile stress at failure along a direction decreases for increased stress along the other direction. On the other hand, in the orthotropic damage model assumed in the proposed model, the tensile stress at failure is constant and equal to the tensile strength of the material. Considering the scattered values obtained from the experimental campaign [185], the assumption of constant tensile failure stress seems justified. In Fig. 6.3, the 3D envelope of the failure surfaces on the stress space is reported.

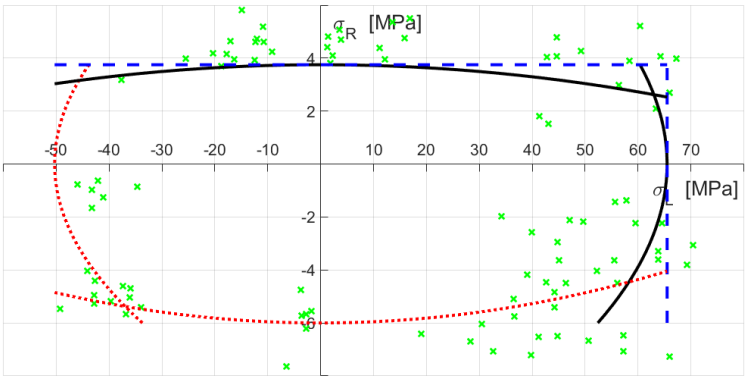

Figure 6.2: 2D representation of the surface failures defined in the multi-surface plasticity model [35] (black continuous line) and in the in the multi-surface elasto-plasto-damage model proposed (blue dashed line) compared with the experimental values obtained by Eberhadsteiner [185] (green "x" markers) on spruce specimens having $f_{t,L} = 65$ MPa, $f_{c,L} = -50.3$ MPa, $f_{t,R} = 3.75$ MPa, $f_{c,R} = 6$ MPa, $f_{V,LR} = 6.34$ MPa.

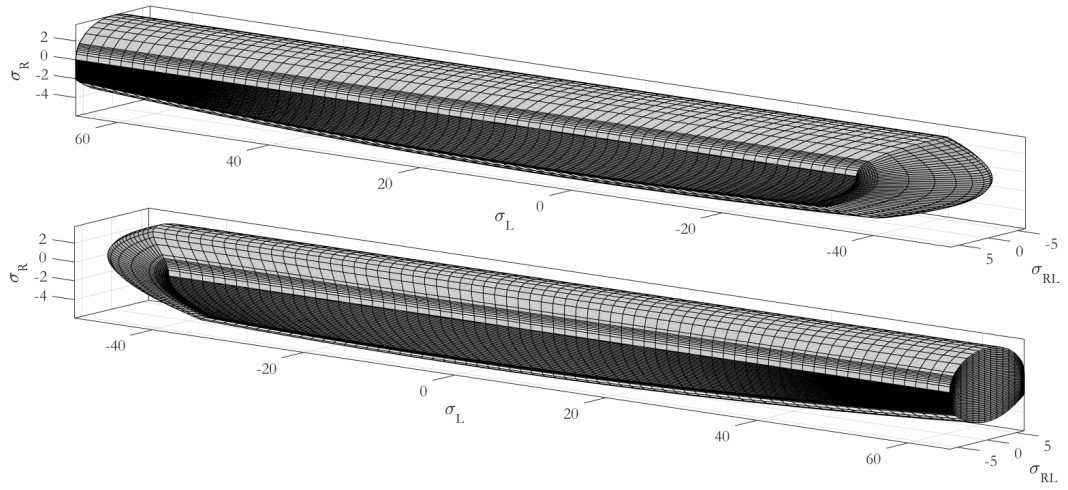

Figure 6.3: 3D representation of the multi-surface failure domain for $f_{t,L} = 65$ MPa, $f_{c,L} = -50.3$ MPa, $f_{t,R} = 3.75$ MPa, $f_{c,R} = 6$ MPa, $f_{V,LR} = 6.34$ MPa

6.2.2 *Damage and Plasticity evolution*

Each of the damage variables $d_{L,n+1}, d_{R,n+1}, d_{L,n+1}$ at the current instant t_{n+1} in the continuous regime is cast as a non-decreasing function of the correspondent current damage $r_{L,n+1}, r_{R,n+1}, r_{LR,n+1}$ by means of the loading-unloading conditions

$$\varphi_{i,n+1} = \tilde{\sigma}_{i,n+1} - r_{i,n+1} = 0, \quad \Delta d_{i,n+1} \geq 0, \quad \varphi_{i,n+1} \Delta d_{i,n+1} = 0 \quad . \tag{83}$$

Moreover, each damage variable evolves according the exponential damage law [2]

$$d_{i,n+1} = \begin{cases} d_{i,n} & \phi_{i,n+1} \leq 0 \\ 1 - \dfrac{f_{t,i}}{\tilde{\sigma}_{i,n+1}} exp\left\{ -2\dfrac{\tilde{\sigma}_{i,n+1} - f_{t,i}}{2G_{f,i}E_i - f_{t,i}} \right\} & \phi_{i,n+1} > 0 \end{cases} \quad , \tag{84}$$

where $G_{f,i}$ is the fracture energy of the correspondent failure mode and i=L,R,LR.

Like in the multi-surface plasticity model proposed by Schmidt an Kaliske [35], the evolution of the plastic stress-strain behaviour is governed by

$$q_m = (1 - k_m)\left[1 - exp(-\eta_m \alpha_m)\right] - \psi_m \frac{(\alpha_m - \alpha_{m,d})^2}{\alpha_{m,max} - \alpha_m} \quad m = II, IV \quad , \tag{85}$$

where the shape parameters have to be calibrated base on the experimental uniaxial compression tests.

6.2.3 *Regularized discontinuous regime*

The damage compliance matrix $C^{d,c}$ is defined as

$$\boldsymbol{C}^{d,c} = \begin{bmatrix} \frac{1}{(1-d_L^c)E_L} & -\frac{\nu_{LR}}{E_R} & 0 \\ -\frac{\nu_{LR}}{E_L} & \frac{1}{(1-d_R^c)E_R} & 0 \\ 0 & 0 & \frac{1}{(1-d_{RL}^c)G_{RL}} \end{bmatrix} \quad . \tag{86}$$

The damaged stiffness matrix is obtained $\boldsymbol{D}^{d,c} = (\boldsymbol{C}^{d,c})^{-1}$. As soon as one of the three damage variables d_L, d_R, d_{LR} reaches the critical threshold d_{cr} in one of the Gauss quadrature point of the considered finite element, the regularized XFEM is activated in that element, the evolution of the damage variables $\boldsymbol{d} = [d_L, d_R, d_{RL}]$ stopped and the material is governed by an elasto-plastic constitutive model.

The effective stress is defined $\bar{\boldsymbol{t}}_{n+1} = \boldsymbol{D}\bar{\boldsymbol{N}}\boldsymbol{A}_{n+1}$ in the case of sub-elemental enrichment and as $\bar{\boldsymbol{t}}^{n+1} = \gamma_\rho \boldsymbol{D}\bar{\boldsymbol{N}}\boldsymbol{A}^{n+1}$ in the case of super-elemental enrichment. Like in the continuous regime, the loading-unloading conditions

$$\varphi_{i,n+1}^c = \tilde{t}_{i,n+1} - r_{i,n+1}^c = 0, \quad \Delta d_{i,n+1}^c \geq 0, \quad \varphi_{i,n+1}^c \Delta d_{i,n+1}^c = 0 \quad . \tag{87}$$

hold, while each of the damage variables evolve according to

$$d_{i,n+1}^c = \begin{cases} d_{i,n}^c & \varphi_{i,n+1}^c \leq 0 \\ 1 - \frac{f_{t,i}}{\tilde{t}_{i,n+1}} exp\left\{ -2\frac{\tilde{t}_{i,n+1} - f_{t,i}}{2G_{f,i}E_i - f_{t,i}} \right\} & \phi_{i,n+1} > 0 \end{cases} \quad , \tag{88}$$

where i stands for L, R or LR.

6.3 2D FORTAN PROCEDURE

The 2D orthotropic multi-surface elasto-damaging plastic model combined with the RE-XFEM has been implemented in FORTAN code [8]. The flow chart of the final code is reported in Fig. 6.4. The implementation work is

started by the codification of a 2D version of the 3D non-linear FORTRAN RE-XFEM code presented in Sec. 2.2.7. After that, step by step all the modifications and the new algorithms required by new 2D orthotropic multi-surface elasto-plasto-damage model coupled to the RE-XFEM has been implemented. In particular, a massive work has been required for the implementation of the iterative radial-return mapping algorithm for non-smooth multi-surface plasticity model [36]. Furthermore, a new procedure for the definition of the internal forces by the integration of the stresses has been required.

The same non-linear iterative solver scheme an the same Intel's numerical lybrary [78] see in the 3D RE-XFEM (Sec. 2.2.7) have been used. The code works with both triangular and quadrilateral FE.

6.4 VALIDATION TESTS

In order to prove the potential of the proposed model, some validation tests on 2D problems with a well-known crack path has been investigated. The results of the simulation has been presented in the conference paper [197].

6.4.1 *Double Cantilever Beam (DCB) tests*

As first validation test, the Double Cantilever Beam (DCB) test has been considered. This test is usually employed to compute the mode I fracture energy and strength of the material in the direction perpendicular-to-grain. The numerical test carried out by Danielsson and Gustafsson [198] by means of a cohesive zone model and the experimental test carried out by Moura et al. [199], shown in Fig. 6.5, have been simulated.

The simulation carried out by Danielsson and Gustafsson considered [198] a Norway spruce specimen (Fig. 6.5a). The material parameters used in the reference [198], reported in Tab. 6.1, have been adopted. The simulation, carried out on a 2D mesh having 4850 dofs with a characteristic mesh size equal to $h_e = 1$ mm, required 38 minutes on a PC i7-5930k CPU.

The comparison between the reference and the obtained results is reported in Fig. 6.6, where the load-displacement profile obtained with the Multi-Surface plasticity model developed by Schmidt and Kaliske [35] is also proposed.

As drawn from the load-vs-displacement curves, the adopted model is able to simulate the structural response of the specimen. A perfect match between

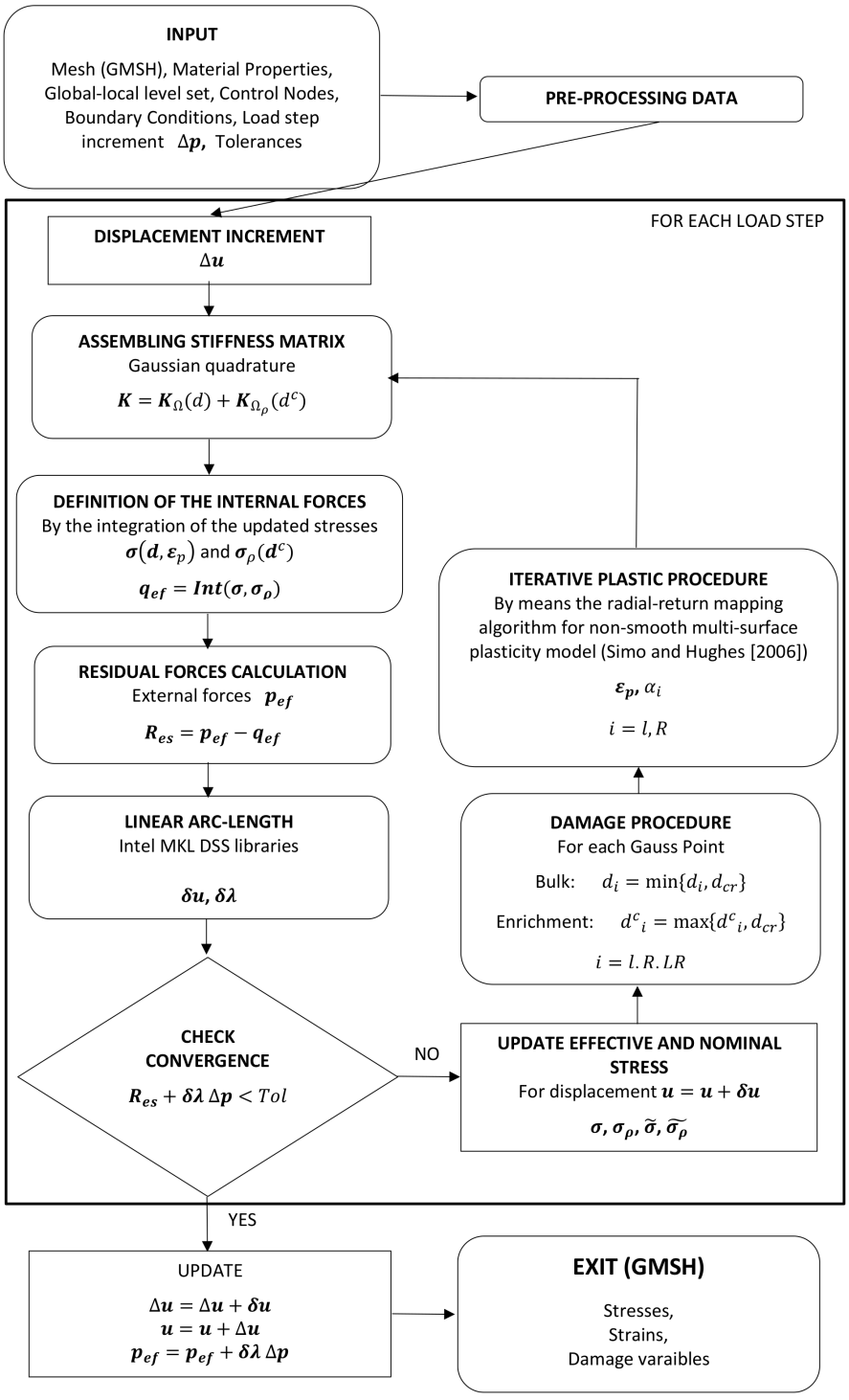

Figure 6.4: Flow chart of the 2D orthotropic multi-surface elasto-damaging plastic model coupled to the RE-XFEM FORTRAN code

Elastic properties [GPa]					
	E_L	E_R	G_{LR}	ν_{RL} $[-]$	
Norway Spruce, Fig. 6.5a	12	0.8	0.7	0.02	
Maritime Pine, Fig. 6.5b	15.13	1.01	1.12	0.033	
Spruce (Picea abies), Fig. 6.11a	9.9	0.73	0.5	0.32	
Birtch, Fig. 6.11a	8.5	0.66	0.44	0.03	
Spruce (Sitka), Fig. 6.14	10.5	0.8	0.7	0.03	
Strength Properties [MPa]					
	$f_{t,L}$	$f_{c,L}$	$f_{t,R}$	$f_{c,R}$	f_v
Norway Spruce, Fig. 6.5a	40	-40	3	-4	6
Maritime Pine, Fig. 6.5b	87	-53	2.5	-2.2	10
Spruce (Picea abies), Fig. 6.11a	65.5	-50.3	3	-2.8	6.34
Birtch, Fig. 6.11a	73	-33	5.25	-6	6.2
Spruce (Sitka), Fig. 6.14	40	-40	2.5	-4	6
Fracture Energies [N/mm]					
	$G_{f,L}$	$G_{f,R}$	$G_{f,RL}$		
Norway Spruce, Fig. 6.5a	1.65	0.3	0.9		
Maritime Pine, Fig. 6.5b	1.65	0.2	0.9		
Spruce (Picea abies), Fig. 6.11a	1.65				
Birtch, Fig. 6.11a	1.65	0.1	0.77		
Spruce (Sitka), Fig. 6.14	1.65	0.3	0.77		

Table 6.1: Material properties employed for the numerical simulations of wooden beams reported in Secs. 6.4.1, 6.4.2 and 6.4.3

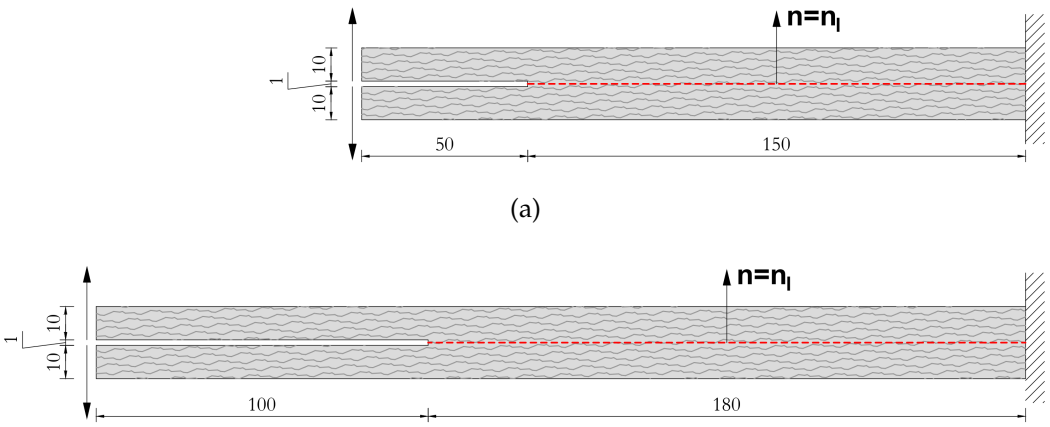

(a)

(b)

Figure 6.5: Geometry of the wood specimens used in the DCB tests carried out by Danielsson and Gustafsson [198] (a) and Moura et al. [199] (b) with dimensions in mm

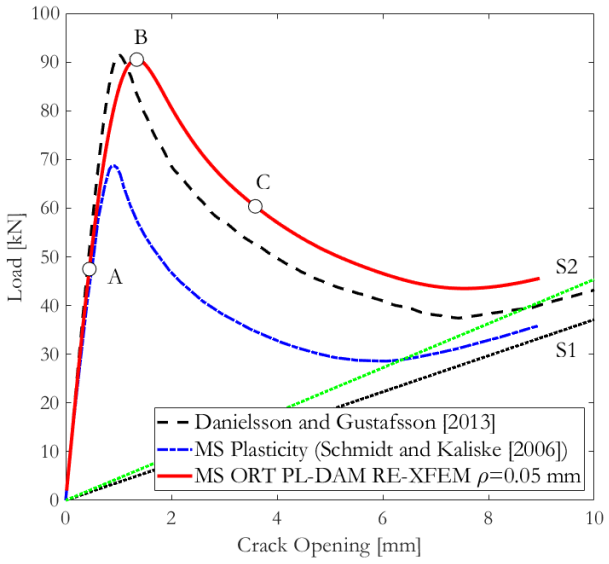

(a)

Figure 6.6: Comparison between the numerical simulation of the DCB test [198] with some numerical solution available in literature

the reference and the simulated peak load is obtained with $\rho = 0.05$ mm. The contour plots of three different steps of the structural response are plotted in Fig. 6.7. The results show that before the peak load (Step A) the crack on the TL plane starts to propagate from the notch towards the clamped part of the beam. At the peak (Step B) the crack rapidly propagates following the predefined crack. In the post-peak part of the structural response (Step C), the specimen is almost divided into two parts by the crack. For this reason, on the load-vs-displacement curve the post-peak stiffness of the system tends asymptotically to the bending stiffness of half of the specimen. From this point of view, there is a clear difference between the numerical models considered in the comparison in Fig. 6.6. Indeed, in the CZM used by Danielsson and Gustaffsson [198] and in the multi-surface plasticity model by Schmidt and Kaliske [35], the residual stiffness in the post-peak part of the response tends to the bending stiffness named $S_1 = 220.42$ N/mm. On the other hand, the proposed XFEM model, the residual bending stiffness of the structural system is higher, and it tends to the stiffness $S_2 = 269.39$ N/mm. As shown in Fig. 6.8, the difference between the two different residual bending stiffness is due to the small layer having thickness $s = 1$ mm. In particular, in the CZM [198] and in the plasticity model [35], the contribute of the layer to the bending stiffness vanishes. Since that the FPZ is thinner than the layer, in the elasto-damaging XFEM model the contribute of the remaining part of the layer after the crack propagation to the bending stiffness makes the stiffness S_2 higher than S_1.
The second considered DCB test is the one carried out by Moura et al. [199] on a maritime pine specimen, shown in Fig. 6.5b. In the simulation, the elastic properties of the material used in the reference have been assumed. Since the strength properties of the wood specimen have not been reported in the reference work [199], the material parameters of the maritime pine suggested by National laboratory of civil engineering of Portugal (LNEC) have been used (Tab. 6.1). For the elaboration, a 2D mesh having 5913 dofs and characteristic mesh size equal to $h_e = 1$ mm has been employed. The simulation required 46 minutes on the aforementioned PC. The comparison between the numerical simulation with the experimental tests is reported in Fig. 6.9. The agreement between the numerical and the experimental results is very good. The contour plots of different steps at the structural response are reported in Fig. 6.10. The structural behavior is similar to the one observed in the previous DCB test.
As expected from the experimental results, it is not possible to make some

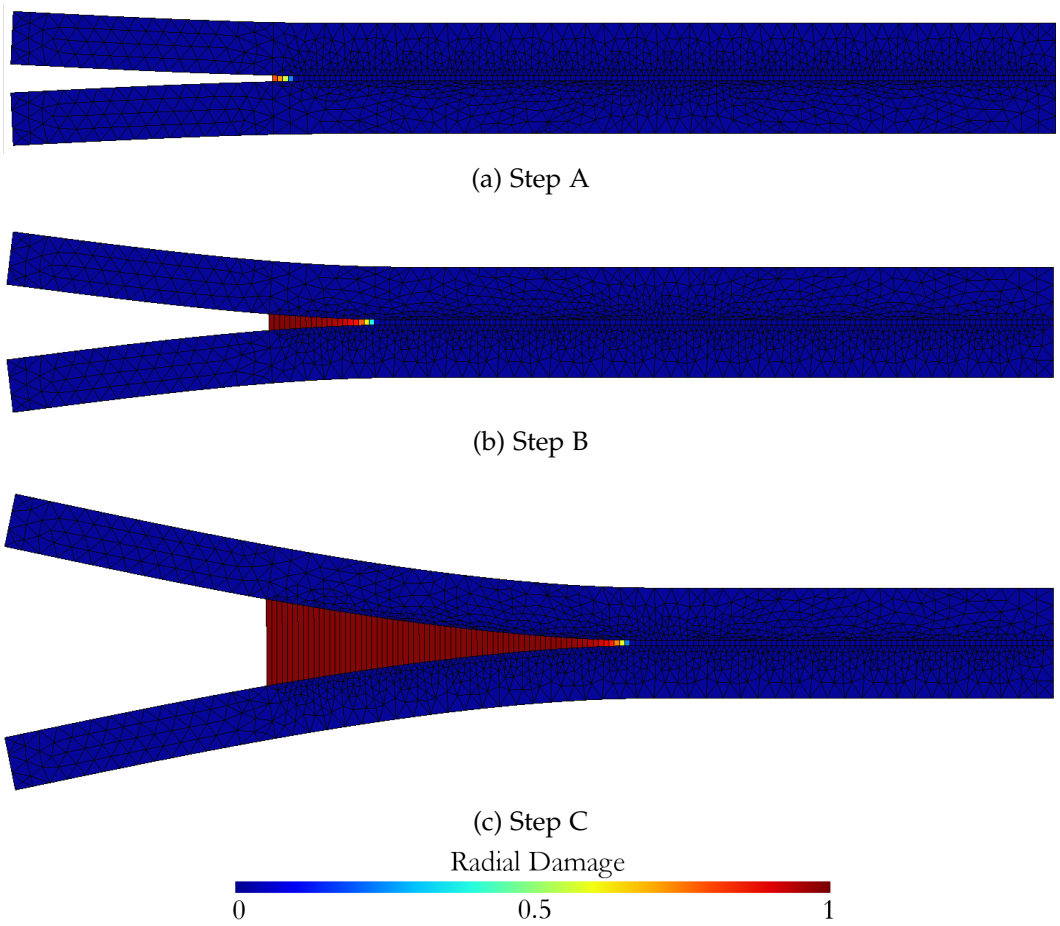

Figure 6.7: Contour plots of the radial damage d_R^c for three representative steps of the load vs displacement curve in Fig. 6.6

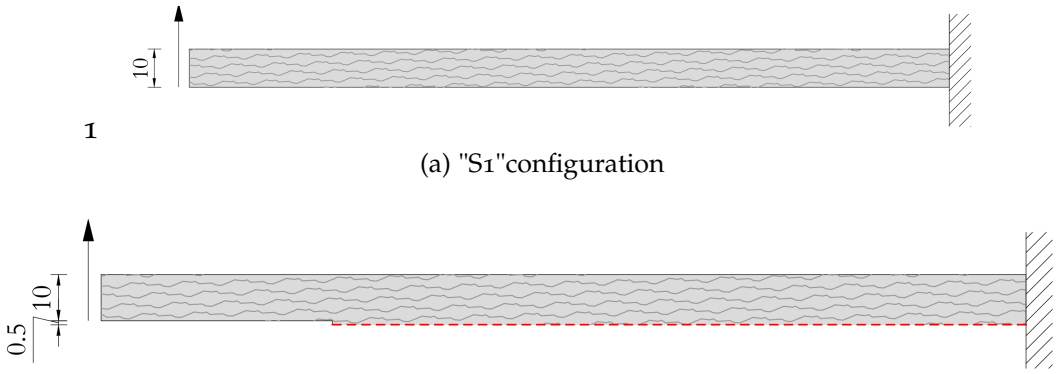

(a) "S1"configuration

(b) "S2"configuration

Figure 6.8: Different scheme of the residual stiffness in the DCB test in the post-peak behavior between the reference models (a) and the proposed XFEM model (b)

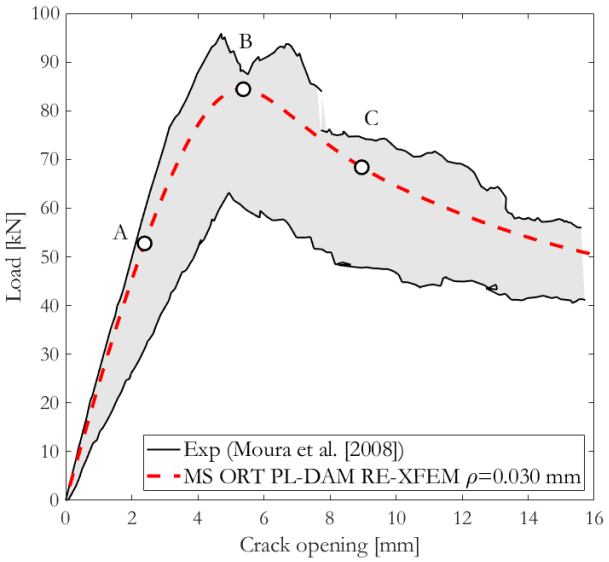

Figure 6.9: Comparison between experimental and computed load profiles for the DCB tests carried out by Moura et al. [199]

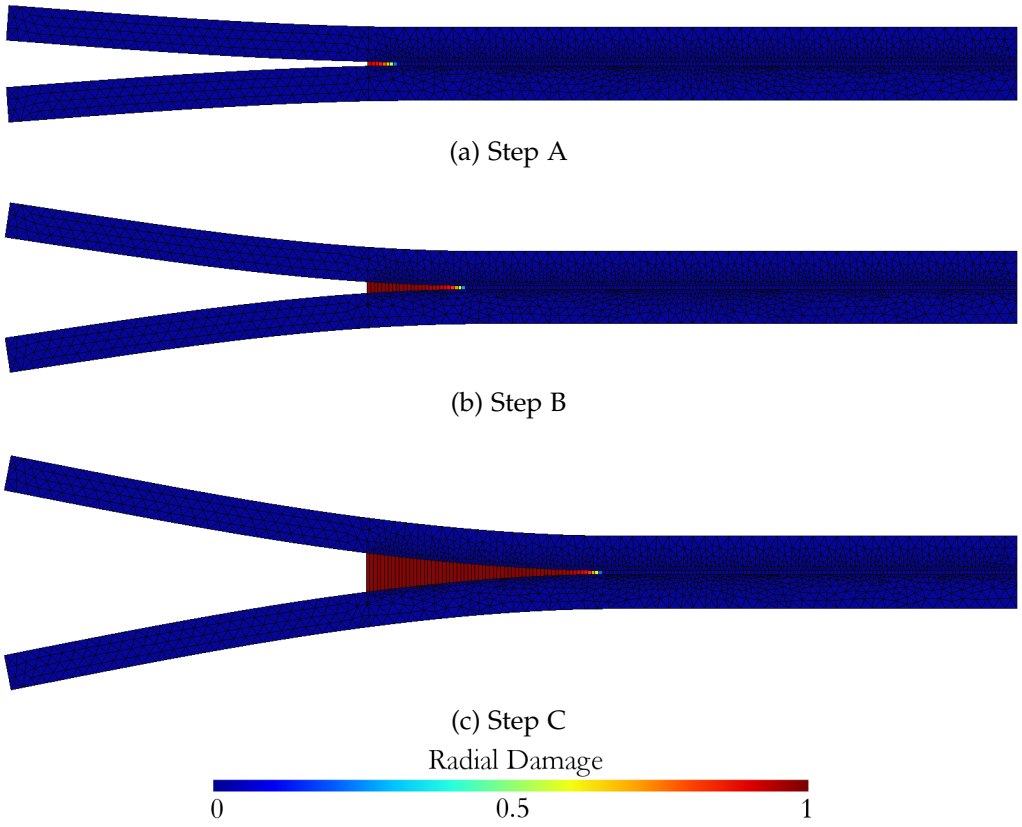

Figure 6.10: Contour plots of the radial damage d_R^c for three representative steps of the load vs displacement curve in Fig. 6.9

statements about the residual bending stiffness because the specimen broke at crack opening of 16 mm.

6.4.2 *Single-Edge-Notched Beam tests*

Analogously to the DCB test, the Single-Edge-Notched Beam (SENB) test is usually carried out to calculate the fracture properties of the wood specimen. In this test, a beam, composed by glueing together 3 different part of wood, is subjected to a three-point bending load. Furthermore, in order to pre-define the crack path, a deep notch is cut in the middle of the beam.

The experimental tests carried out by Dourado et al. [200] on a spruce specimen and by Franke at al. [161] on a birch specimen have been simulated. The geometries of the two set of tests are reported in Fig. 6.11

The material parameters employed for the simulations have been reported in Tab. 6.1. The material properties for the spruce (Picea Abies) defined by Dourado et al. [200] have been assumed, while, due to the unavailability of the experimental material parameters for the second SENB test, the literature values for birtch available in [158] have been used.

The two meshes used for simulation have 4215 dofs and 4116 dofs and required for the computation 47 minutes and 43 minutes, respectively. The comparison between the computed and the references load-displacement curves is reported in Fig. 6.12. The computed response is in optimal agreement with the experimental results. In particular, a regularization length of $\rho = 0.035$ mm and $\rho = 0.045$ mm has been used in the two cases, respectively. Since the structural response in the two tests is similar, only the contour plots of the radial damage d_R^c of the test carried out by Dourado et al. [200] has been reported in Fig. 6.13. After the linear elastic stage, the crack starts to propagate from the notch in the middle of the beam (Step A). With increasing the load, the crack propagates rapidly towards the loaded zone. At the peak (Step B), half of the resistant middle section is crossed by the crack.

6.4.3 *End-Notched Beam test*

Finally, we considered the end-notched beam (ENB) test carried out by Rautenstrauch et al. [201] on a Spruce (Sitka) beam. In this test, the beam with the geometry shown in Fig. 6.14 is subjected to a three-point bending load. Due to

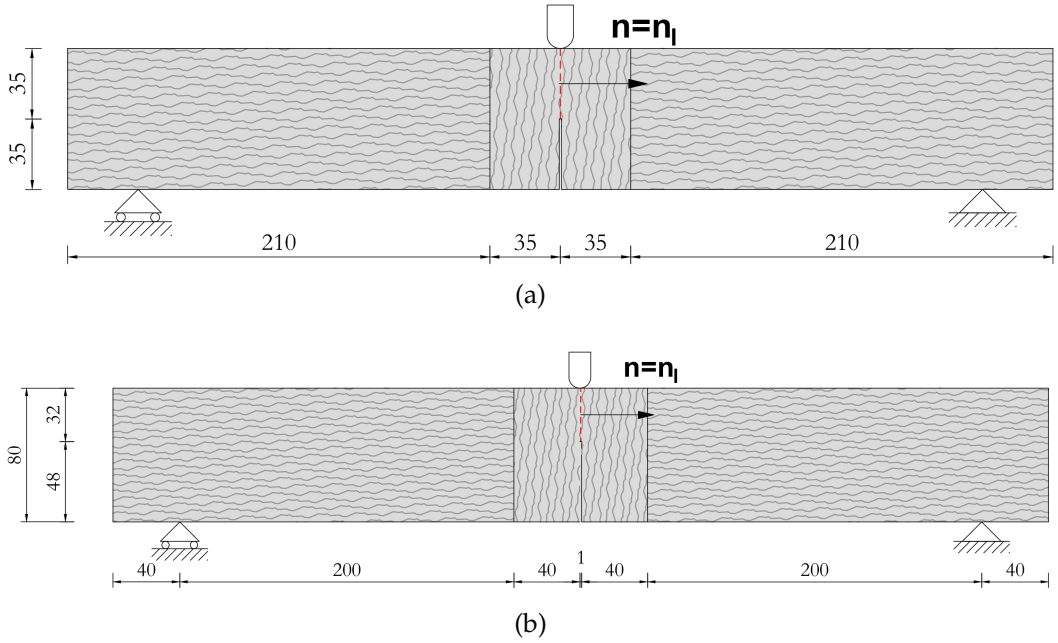

Figure 6.11: Geometry of the wood specimen used in the SENB test carried out by Dourado et al. [200] (a) and by Franke at al. [161] (b) with dimensions in mm

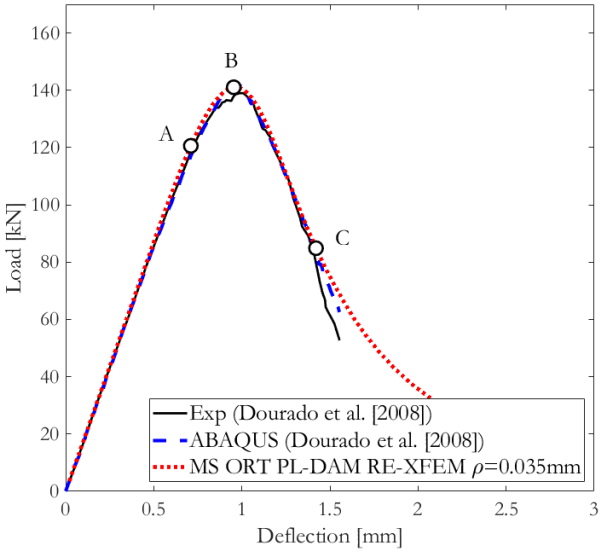

(a)

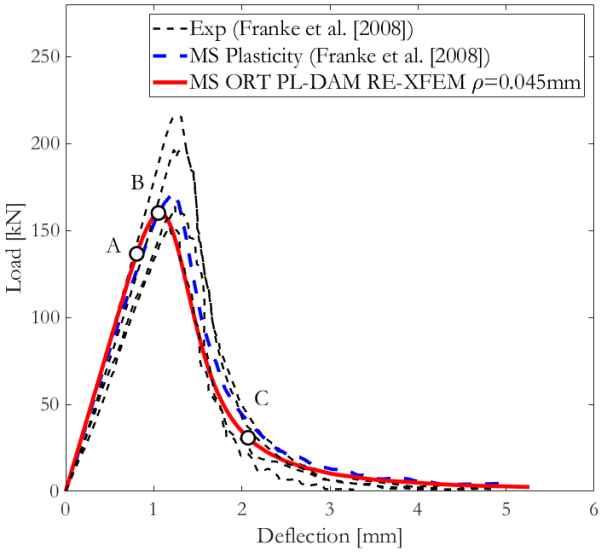

(b)

Figure 6.12: Comparison between experimental and computed load profiles for the DCB tests carried out by Dourado et al. [200] (a) and by Franke at al. cite-franke2008 (b)

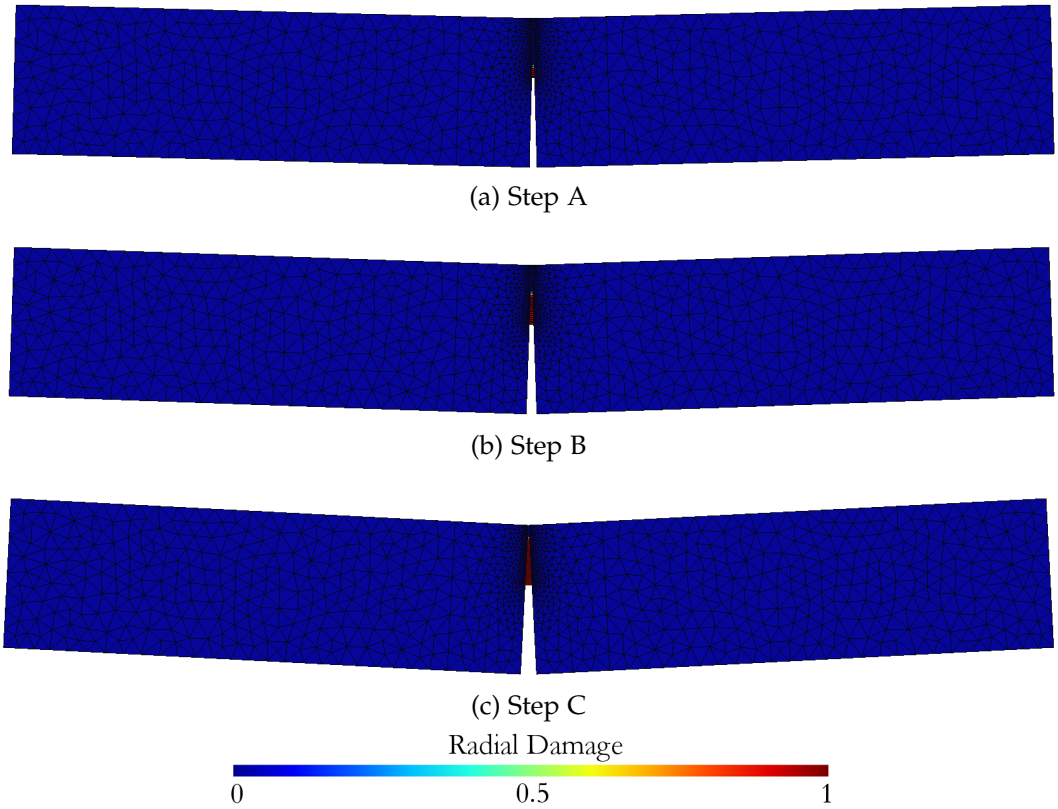

Figure 6.13: Contour plots of the radial damage d_R^c for three representative steps of the load vs displacement curve in Fig. 6.12a

the presence of the end-notch, a mixed mode crack is expected to propagate from the notch towards the centre of the beam on the TL plane.

Like in the local-global level set presented in Ch. 2 for the RE-XFEM, the mixed mode propagation has been modelled adopting a local levelset $\boldsymbol{n}_l$ at Gauss point level in the regularized volume as reported in Fig. 6.14. A mesh of 101487 dofs having characteristic mesh size $h_e = 1$ mm has been employed. The simulation required almost 27 hours. The comparison between the numerical and the experimental responses is shown in Fig.6.15.

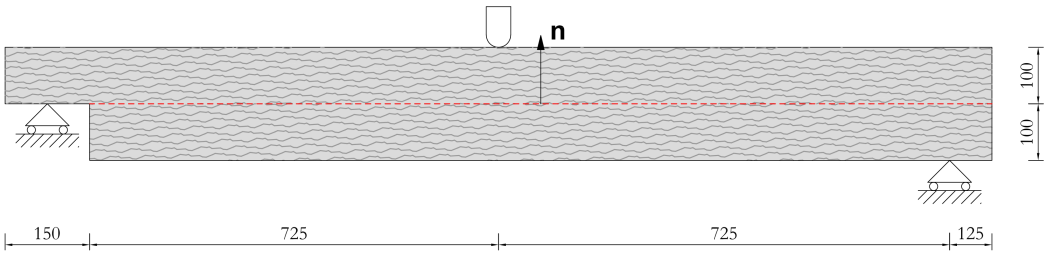

Figure 6.14: Geometry of the wood specimen used in the ENB test carried out by Rautenstrauch et al. [201] with dimensions in mm

A good agreement with the experimental data is obtained with a regularization parameter $\rho = 0.045$ mm. The contour plots of the radial d_R^c and the shear d_{RL}^c damage are reported in Fig. 6.16 and Fig. 6.17, respectively. As expected, a crack propagates from the end-notch towards the centre of the beam.

6.5 DISCUSSION OF THE RESULTS

The validation tests aimed to prove the reliability of the proposed 2D orthotropic elasto-damaging plastic model combined with the RE-XFEM. In particular, mode I and mixed mode crack propagation along the TL plane have been simulated in wooden beams with a pre-defined crack path.

In all the tests, a good agreement between the experimental and the numerical results has been observed using the material parameters taken from the references or from the literature for the wooden species considered.

The approach is original and offers several advantages respect to the models available in literature. First of all, the complex compressive failure modes are tackled by a suitable multi-surface plasticity formulation. At the same time,

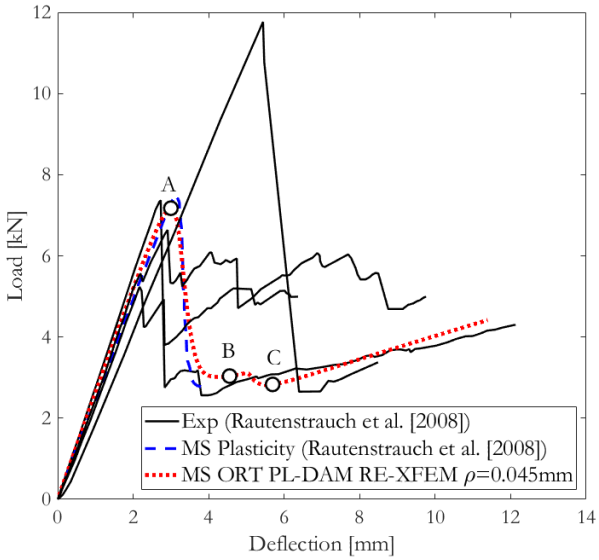

Figure 6.15: Comparison between experimental (black continuous line) and computed (red dotted line) load-vs-displacement profiles for the DCB tests carried out by Rautenstrauch et al. [201]

the tensile behaviour is modelled by means an orthotropic damage model, that have been proved to be effective on the simulations of wooden fracture processes in Ch. 5. Furthermore, the mesh-dependency is avoided owing to the presence of the regularization length. As can be drawn from Tab. 6.2, a regularization length between $\rho = 0.03$ mm and $\rho = 0.05$ mm has been used in the simulations. In the RE-XFEM, the ρ governs the width of the regularization volume and, in particular, the 99% of crack dissipation process take place in a volume having thickness 10ρ. From the physical point of view, the regularization length is linked to the width of the fracture process zone and to the micro-structure of wood. This hypothesis is confirmed by the work proposed by Murata et al. [163], where the width of the fracture process zone in a spruce specimen has been estimated to range between 0.3 to 0.5 mm.

6.6 FUTURE DEVELOPMENTS

In the numerical tests, the 2D plane-stress of experimental test with a well-known pre-defined crack path have been analysed.

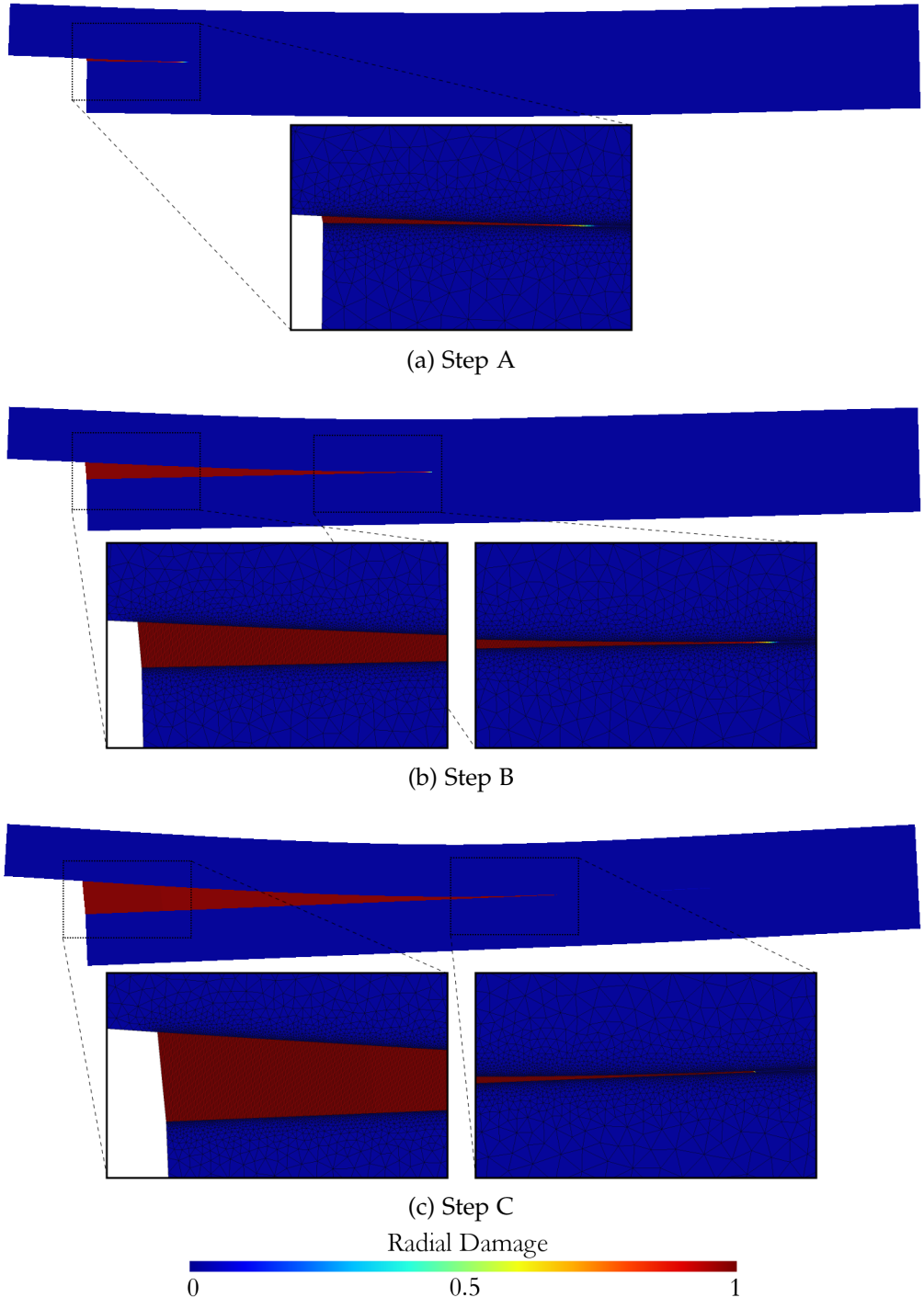

(a) Step A

(b) Step B

(c) Step C

Figure 6.16: Contour plots of the radial damage d_R^c for three representative steps of the load vs displacement curve in Fig. 6.15

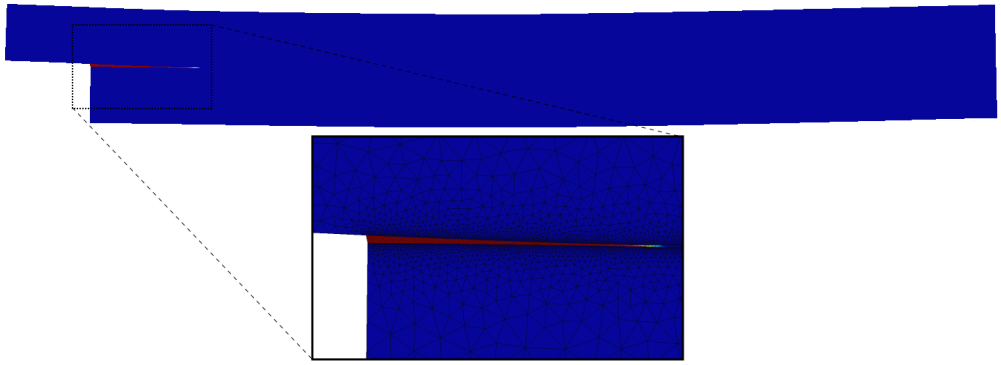

(a) Step A

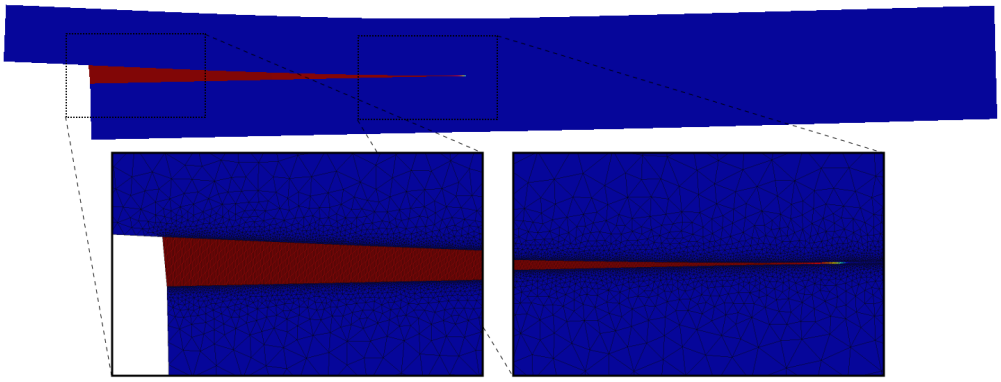

(b) Step B

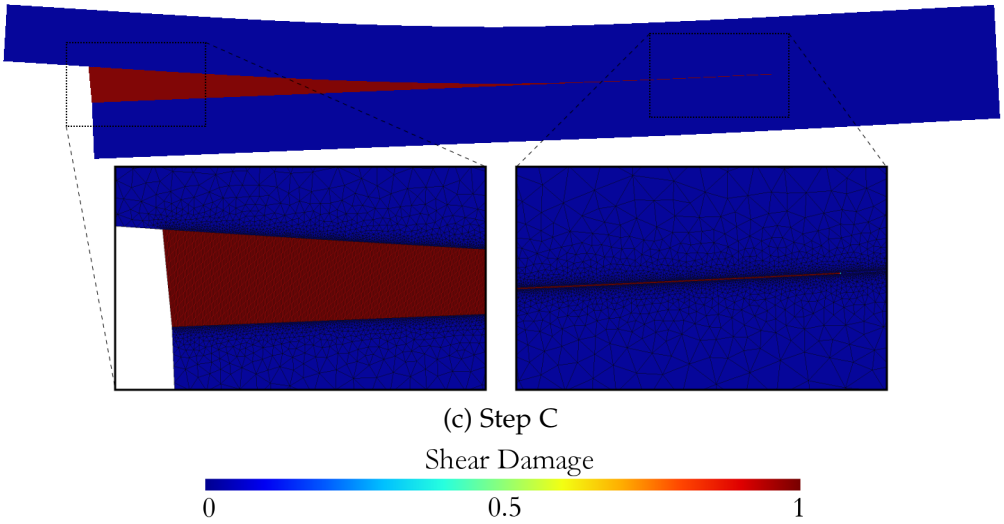

(c) Step C

Figure 6.17: Contour plots of the shear damage d^c_{RL} for three representative steps of the load vs displacement curve in Fig. 6.15

Wood Species	ρ [mm]
Norway Spruce, Fig. 6.5a	0.05
Maritime Pine, Fig. 6.5b	0.03
Spruce (Picea abies), Fig. 6.11a	0.035
Birtch, Fig. 6.11a	0.045
Spruce (Sitka), Fig. 6.14	0.035

Table 6.2: Values of the regularization length ρ employed in the simulations

One of the possible future developments of the methods is the extension of the method to the 3D case. The formulation of the method, presented in Sec. 6.2 for 2D plane-stress problems, is easily extensible to the 3D case. As demonstrated in Ch. 5 for the end-repaired beams, the three-dimensional simulation of wooden joints and discontinuities is essential to capture the system behaviour.

Another important improvement is the definition of a proper crack tracking algorithm suitable for wood. Until now, only case-studies with a pre-defined crack path have been modelled by means the continuous-discontinuous transition imposing the discontinuity surface, but, in general, the crack path in wooden structures is not known a priori.

7

CONCLUSIONS

The thesis focused on the 3D advanced FE modelling of discontinuities in quasi-brittle materials by means a regularized variant of the XFEM method. This method, originally developed by Benvenuti [2] and used to study 2D non-linear [3–5] has been implemented into a robust 3D non-linear procedure [8], presented in Ch. 2, to study several engineering problems.

The thesis has been organized into two parts. In the first part, the focus has been on failure by the detachment of the reinforcements in FRP-reinforced concrete structures. In particular:

- In Ch. 3 the case of the FRP-debonding from concrete blocks subjected to single-shear lap have been simulated [73, 96]. Results have shown that the detachment of the FRP plates involves 3D effects that need to be taken into account to design the FRP reinforcement. Furthermore, the simulation has clarified the difference in the detachment mode between long and short FRP reinforcing plates.

- Ch. 4 has been devoted to the detachment of FRP flexural reinforcements from concrete beams. The cases of three-point bending tests on FRP-plated Steel Fibres Reinforced Concrete beams and four-point bending tests on FRP plated Reinforced concrete beams have been studied. The numerical investigations, based on different experimental campaigns [106, 144, 155], have shown the reliability of the model in the simulation of mixed-mode crack propagation. In particular, it has been proved that the model has been able to follow the entire structural path up to the detachment of the FRP flexural reinforcements from the beam. The experimentally observed crack patterns have been also correctly captured by the procedure. Furthermore, the role of the thickness and of the width

of the FRP flexural reinforcements on the detachment failure have been emphasized. It has been found that larger thicknesses and widths of the FRP reinforcements enhance the detachment load at failure but have a negligible effect on the deflection at failure.

The second part of the thesis has been dedicated to the study of the wooden structures. In particular:

- Ch. 5 concerns to study end-repaired beams. The end-repaired beams have been modelled by means a 3D non-linear FORTRAN procedure developed by the candidate adopting a 3D orthotropic damage model available in literature [174]. The numerical simulations, have been able to reproduce the failure mechanisms and the failure loads obtained in the experimental tests carried out at the CNR-IVALSA laboratory. In particular, the role of additional screws used for the reparation has been analysed and clarified.

- Finally, Ch. 6 has been focused on the development of a new model for wooden structures. In collaboration with the Institute of Structural Analysis of Dresden (Germany), a new 2D orthotropic elasto-plasto-damage model combined to a suitable Regularized XFEM has been presented. A validation campaign based on several experimental and numerical tests have been carried out. Results proved the reliability and the suitability of the new 2D elasto-damaging plastic model for wooden structures in the presence of mode I and mixed mode interfaces.

The main aspects of novelty of this research activity are listed as follows.

- Based on the 3D RE-XFEM, a 3D FORTRAN non-linear code [8] has been implemented. The procedure is robust and stable and is able to handle the computational burden required by real applications in a reasonable time, using a standard i7-5930K CPU.

- The 3D FORTRAN with RE-XFEM non-linear model makes it possible to investigate the three-dimensional effects of FRP reinforcements on a concrete specimen. In particular, the role of the width and the thickness of the FRP reinforcement has been numerically investigated. An optimal agreement between numerical and experimental data has been obtained

- The structural behaviour of FRP-reinforced SFRC beams has been successfully simulated through the aforementioned procedure. In particular, a simple linear relationship between the regularization length and the fiber volume content has been effective for the simulations.
- An orthotropic 3D damage model [14] has been implemented into the 3D FORTRAN code in order to investigate the response of end-repaired beams. The computed crack patterns and failure loads agree in a reliable way to the experimentally observed results. Furthermore, the role of screws on the structural behaviour of the repaired beams has been assessed.
- A new 2D elasto-damaging-plastic model for wood has been proposed. The model combines a multi-surface plasticity model [35] with an orthotropic damage model [14], using the RE-XFEM to study the propagation of discontinuities. Several validation tests have been presented.

7.1 FUTURE DEVELOPMENTS

Possible future developments on the research lines pursued involve:

- The implementation of a crack tracking algorithm for crack propagation in general geometries and loadings in the presence of multiple crack-branching.
- The extension to the 3D domain of the new elasto-plasto-damage model.

A

APPENDIX: FRP DESIGN RULES

Strengthening of concrete structures by means of externally bonded reinforcement is an efficient technique that relies on the composite action between a reinforced or pre-stressed concrete element and externally bonded reinforcement. To guarantee the overall structural safety of the strengthened member it is important that proper FRP externally bonded reinforcement systems are used, correctly designed, detailed and executed. The design of the reinforcement system must fulfil the requirements of serviceability, durability and resistance to collapse. In case of fire, to guarantee the strength of the reinforcement, it must be adapted to the exposure time designed. The reinforcement system must be placed in areas where it is necessary to withstand tensile stresses, the composite must not be entrusted compression efforts.

According to the guide provide by the CNR, structures and structural members strengthened with FRP shall be designed to have design strength R_d at all sections at least equal to the required strength E_d calculated for the factored loads and forces,

$$E_d \leq R_d \quad . \tag{89}$$

The generic design capacity R_d can be expressed by:

$$R_d = \frac{1}{\gamma_{Rd}} R\left\{X_{d,i}, a_{d,i}\right\} \quad , \tag{90}$$

where γ_{Rd} is the partial factor that takes into account the uncertainties of the mechanical model considered (Tab. A.1). The parameter $a_{d,i}$ is the nominal value of the geometrical parameters considered in the model while $X_{d,i}$ is

Resistence Model	γ_{Rd}
Flexion/Buckling	1.0
Shear/Torsion	1.2
Confinement	1.0

Table A.1: Value of partial factor γ_{Rd} [97]

Failure model	Partial factor	Type A application	Type B application
FRP ropture	γ_f	1.10	1.25
FRP debonding	γ_f, d	1.20	1.50

Table A.2: Value of partial factor γ_m for strengthening system certified *Type A* and strengthening system uncertified *Type B* [97]

the value for the calculation of the existing materials and FRP. The generic calculation of the property X_d is expressed by:

$$X_d = \eta \frac{X_k}{\gamma_m} \quad , \tag{91}$$

where η is the conversion factor, X_k is the characteristic value of the property considered and γ_m is the partial coefficient of FRP material (Tab. A.2).

When concrete members are reinforced with FRP composites, the role of bond between concrete and FRP is of great relevance due to the brittleness of the failure mechanism by debonding (loss of adhesion). According to the capacity design criterion, such a failure mechanism shall not precede flexural or shear failure of the strengthened member. The loss of adhesion between FRP and concrete may concern both laminates or sheets applied to reinforced concrete beams as flexural strengthening. As shown in figure A.1, debonding may take place within the adhesive, between concrete and adhesive, in the concrete itself, or within the FRP reinforcement (e.g. at the interface between two adjacent layers bonded each other). When a proper installation is performed, because the adhesive strength is typically much higher than the concrete tensile strength, debonding always takes place within the concrete

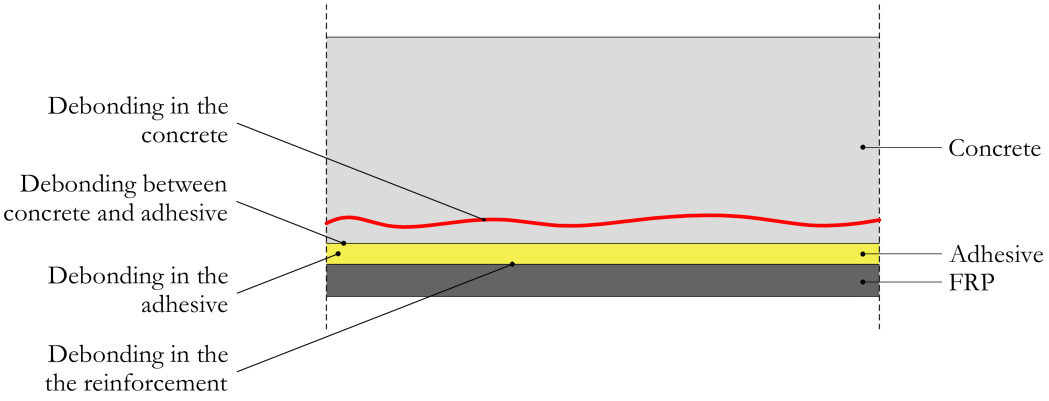

Figure A.1: Debonding between FRP and concrete ([97])

itself with the removal of a layer of material, whose thickness may range from few millimetres to the whole concrete cover.

Debonding failure modes for laminates or sheets used for flexural strengthening may be classified in the following four categories, schematically represented in Fig. A.2

- Mode 1: Laminate/sheet end debonding
- Mode 2: Intermediate debonding, caused by flexural cracks
- Mode 3: Debonding caused by diagonal shear cracks
- Mode 4: Debonding caused by irregularities and roughness of concrete surface

To design FRP flexural reinforcements is required that flexural capacity M_{Rd} and factored ultimate moment M_{Sd} satisfy the inequation

$$M_{Sd} \leq M_{Rd} \quad . \tag{92}$$

The fundamental hypothesis at the base of the method are:

- Cross-beam sections, perpendicular to the beam axis prior to deflection, remain still plane and perpendicular to the beam axis after deflection

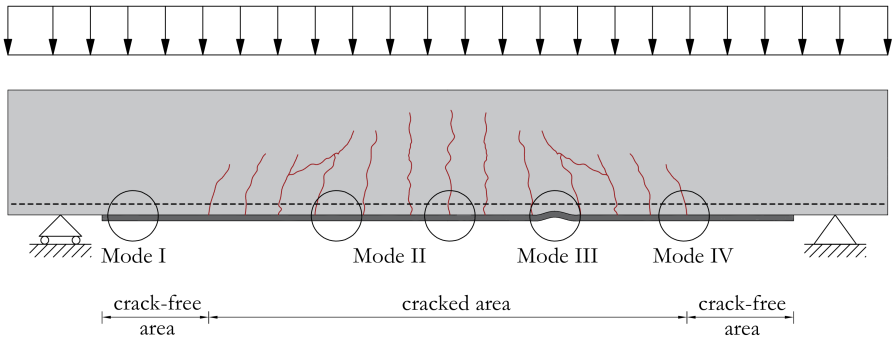

Figure A.2: FRP flexural strengthening: Schematic view of the debonding modes [97]

- Perfect bond exists between FRP and concrete, and between steel and concrete
- Concrete does not react in tension
- Constitute laws for concrete and steel are accounted for according to the building code while FRP is considered a linear elastic material up to failure

For bond length l_b longer than the optimal bonded length l_e, the ultimate design debonding strength can be calculated as

$$f_{dd} = \frac{1}{\gamma_{f,d}\sqrt{\gamma_c}}\sqrt{\frac{2\,E_{FRP}\,\Gamma_{Fk}}{t_f}} \quad , \tag{93}$$

where E_f is the Poisson's modulus of the FRP reinforcement and t_f is the FRP thickness. For flexural intermediate debonding failure, the design rule specifies the ultimate design strength as $f_{dd,2} = k_{cr} f_{dd}$ where $k_{cr} = 3$.

Γ_{Fk} is the specific fracture energy of the FRP-concrete interface may be expressed as

$$\Gamma_{Fk} = 0.003 k_b \sqrt{f_{ck} f_{ctm}} \quad . \tag{94}$$

Here, f_{ctm} is the average tensile strength of the concrete, f_{ck} is the characteristic compressive strength of the concrete and the geometric parameter k_b can be evaluated as:

$$k_b = \sqrt{\frac{2 - \frac{b_f}{b}}{1 + \frac{b_f}{400}}} \geq 1 \quad , \tag{95}$$

where b_f is the width of the FRP reinforcemnet and b the width of the specimenand $b_f/b \geq 0.33$. The optimal bonded length l_e may be estimated as follows

$$l_e = \sqrt{\frac{E_f t_f}{2 f_{ctm}}} \quad . \tag{96}$$

For $l_b \leq l_e$, the ultimate strength has to be reduced according to

$$f_{dd,rid} = f_{dd} \frac{l_b}{l_e} \left(2 - \frac{l_b}{l_e}\right) . \tag{97}$$

REFERENCES

[1] T. Belytschko, R. Gracie, and G. Ventura. "A review of extended/generalized finite element methods for material modeling". In: *Modelling and Simulation in Materials Science and Engineering* 17 (2009), p. 043001.

[2] E. Benvenuti. "A regularized XFEM framework for embedded cohesive interfaces". In: *Computer Methods in Applied Mechanics and Engineering* 197 (2008), pp. 4367–4378.

[3] E. Benvenuti, O. Vitarelli, and A. Tralli. "Delamination of FRP-reinforced concrete by means of an extended finite element formulation". In: *Composites Part B: Engineering* 43 (2012), pp. 3258–3269.

[4] E. Benvenuti. "Mesh-size-objective XFEM for regularized continuous–discontinuous transition". In: *Finite Elements in Analysis and Design* 47 (2011), pp. 1326–1336.

[5] E. Benvenuti and A. Tralli. "Simulation of finite-width process zone in concrete-like materials by means of a regularized extended finite element model". In: *Computational Mechanics* 50 (2012), pp. 479–497.

[6] E. Benvenuti, G. Ventura, N. Ponara, and A. Tralli. "Variationally consistent eXtended FE model for 3D planar and curved imperfect interfaces". In: *Computer Methods in Applied Mechanics and Engineering* 267 (2013), pp. 434–457.

[7] E. Benvenuti. "XFEM with equivalent eigenstrain for matrix–inclusion interfaces". In: *Computational Mechanics* 53 (2014), pp. 893–908.

[8] N. Orlando. "3D REgularized XFEM FORTRAN procedure (3D RE-XFEM)". The code is available for anyone who is interested (nicola.orlando@unife.it). 2018.

[9] E. Benvenuti, N. Orlando, D. Ferretti, and A. Tralli. "A new 3D experimentally consistent XFEM to simulate delamination in FRP-reinforced concrete". In: *Composites Part B: Engineering* 91 (2016), pp. 346–360.

[10] E. Benvenuti and N. Orlando. "Failure of FRP-strengthened SFRC beams through an effective mechanism-based regularized XFEM framework". In: *Composite Structures* 172 (2017), pp. 345–358.

[11] E. Benvenuti and N. Orlando. "Intermediate flexural detachment in FRP-plated concrete beams through a 3D mechanism-based regularized eXtended Finite Element Method". In: *Composites Part B: Engineering* 145 (2018), pp. 281–293.

[12] N. Orlando, Y. Taddia, E. Benvenuti, B. Pizzo, and C. Alessandri. "End-repair of timber beams with laterally-loaded glued-in rods: experimental trials and failure prediction through modelling". In: *Construction and building materials* (in press).

[13] Z. P. Bazant and J. Planas. *Fracture and size effect in concrete and other quasibrittle materials*. Vol. 16. CRC press, 1997.

[14] C. Sandhaas and J. Van de Kuilen. "Material model for wood". In: *Heron* 58.3 (2013), p. 173.

[15] L. Kachanov. "On the time to failure under creep conditions, Izv". In: *AN SSSR, Otd. Tekhn. Nauk* 8.26-31 (1958), p. 8.

[16] I. Carol, E. Rizzi, and K. Willam. "A unified theory of elastic degradation and damage based on a loading surface". In: *International journal of solids and structures* 31.20 (1994), pp. 2835–2865.

[17] J.-L. Chaboche. "Continuous damage mechanics—a tool to describe phenomena before crack initiation". In: *Nuclear Engineering and Design* 64.2 (1981), pp. 233–247.

[18] C. Chow and J. Wang. "An anisotropic theory of continuum damage mechanics for ductile fracture". In: *Engineering Fracture Mechanics* 27.5 (1987), pp. 547–558.

[19] D. Krajcinovic. "Damage mechanics". In: *Mechanics of materials* 8.2-3 (1989), pp. 117–197.

[20] J. Lemaitre. "A continuous damage mechanics model for ductile fracture". In: *Journal of engineering materials and technology* 107.1 (1985), pp. 83–89.

[21] J. Simo and J. Ju. "Strain-and stress-based continuum damage models—I. Formulation". In: *Mathematical and Computer Modelling* 12.3 (1989), p. 378.

[22] J. Mazars and G. Pijaudier-Cabot. "Continuum damage theory—application to concrete". In: *Journal of Engineering Mechanics* 115.2 (1989), pp. 345–365.

[23] G. Ruocci, P. Argoul, K. Benzarti, and F. Freddi. "An improved damage modelling to deal with the variability of fracture mechanisms in FRP reinforced concrete structures". In: *International Journal of Adhesion and Adhesives* 45 (2013), pp. 7–20.

[24] P. A. Vermeer and R. De Borst. "Non-associated plasticity for soils, concrete and rock". In: *HERON, 29 (3), 1984* (1984).

[25] P. Grassl, K. Lundgren, and K. Gylltoft. "Concrete in compression: a plasticity theory with a novel hardening law". In: *International Journal of Solids and Structures* 39.20 (2002), pp. 5205–5223.

[26] W.-F. Chen. *Plasticity in reinforced concrete*. J. Ross Publishing, 2007.

[27] P. Grassl and R. Rempling. "A damage-plasticity interface approach to the meso-scale modelling of concrete subjected to cyclic compressive loading". In: *Engineering Fracture Mechanics* 75.16 (2008), pp. 4804–4818.

[28] E. Hansen, K. Willam, and I. Carol. "A two-surface anisotropic damage/plasticity model for plain concrete". In: *Fracture Mechanics of Concrete Structures. Balkema, Lisse* (2001), pp. 549–556.

[29] J. Lee and G. L. Fenves. "Plastic-damage model for cyclic loading of concrete structures". In: *Journal of engineering mechanics* 124.8 (1998), pp. 892–900.

[30] J. Lubliner, J. Oliver, S. Oller, and E. Onate. "A plastic-damage model for concrete". In: *International Journal of solids and structures* 25.3 (1989), pp. 299–326.

[31] G. Meschke, R. Lackner, and H. A. Mang. "An anisotropic elastoplastic-damage model for plain concrete". In: *International journal for numerical methods in engineering* 42.4 (1998), pp. 703–727.

[32] Y. Tao and J.-F. Chen. "Concrete damage plasticity model for modeling FRP-to-concrete bond behavior". In: *Journal of composites for construction* 19.1 (2014), p. 04014026.

[33] G. Z. Voyiadjis, Z. N. Taqieddin, and P. I. Kattan. "Anisotropic damage–plasticity model for concrete". In: *International journal of plasticity* 24.10 (2008), pp. 1946–1965.

[34] S. Yazdani and H. Schreyer. "Combined plasticity and damage mechanics model for plain concrete". In: *Journal of engineering mechanics* 116.7 (1990), pp. 1435–1450.

[35] J. Schmidt and M. Kaliske. "Zur dreidimensionalen Materialmodellierung von Fichtenholz mittels eines Mehrflächen-Plastizitätsmodells". In: *Holz als Roh-und Werkstoff* 64.5 (2006), pp. 393–402.

[36] J. C. Simo and T. J. Hughes. *Computational inelasticity*. Vol. 7. Springer Science & Business Media, 2006.

[37] D. Ngo and A. Scordelis. "Finite element analysis of reinforced concrete beams". In: *Journal Proceedings*. Vol. 64. 3. 1967, pp. 152–163.

[38] J. Gálvez, J. Červenka, D. Cendon, and V. Saouma. "A discrete crack approach to normal/shear cracking of concrete". In: *Cement and concrete research* 32.10 (2002), pp. 1567–1585.

[39] I. Carol, P. C. Prat, and C. M. Lopez. "Normal/shear cracking model: application to discrete crack analysis". In: *Journal of engineering mechanics* 123.8 (1997), pp. 765–773.

[40] M. Prasad and C. Krishnamoorthy. "Computational model for discrete crack growth in plain and reinforced concrete". In: *Computer methods in applied mechanics and engineering* 191.25-26 (2002), pp. 2699–2725.

[41] Z. Yang and J. Chen. "Fully automatic modelling of cohesive discrete crack propagation in concrete beams using local arc-length methods". In: *International Journal of Solids and Structures* 41.3-4 (2004), pp. 801–826.

[42] R. d. Borst, J. J. Remmers, A. Needleman, and M.-A. Abellan. "Discrete vs smeared crack models for concrete fracture: bridging the gap". In: *International Journal for Numerical and Analytical Methods in Geomechanics* 28.7-8 (2004), pp. 583–607.

[43] H. B. Pham, R. Al-Mahaidi, and V. Saouma. "Modelling of CFRP–concrete bond using smeared and discrete cracks". In: *Composite Structures* 75.1-4 (2006), pp. 145–150.

[44] V. Lotfi and R. Espandar. "Seismic analysis of concrete arch dams by combined discrete crack and non-orthogonal smeared crack technique". In: *Engineering Structures* 26.1 (2004), pp. 27–37.

[45] N. Moës, J. Dolbow, and T. Belytschko. "A finite element method for crack growth without remeshing". In: *International Journal for Numerical Methods in Engineering* 46 (1999), pp. 131–150.

[46] J. Melenk and I. Babuska. "The Partition of Unity Finite Element Method: Basic Theory and Applications". In: *Computer Methods in Applied Mechanics and Engineering* 139 (1996), pp. 289–314.

[47] G. Ventura, R. Gracie, and T. Belytschko. "Fast integration and weight function blending in the extended finite element method". In: *International journal for numerical methods in engineering* 77.1 (2009), pp. 1–29.

[48] G. Ventura. "On the elimination of quadrature subcells for discontinuous functions in the extended finite-element method". In: *International Journal for Numerical Methods in Engineering* 66.5 (2006), pp. 761–795.

[49] G. Ventura, N. Orlando, and E. Benvenuti. "An equivalent Polynomial Library for Accurate Quadrature of the Regularized Heaviside Enrichment Function". In: *14th International Conference on Computational Plasticity, Fundamentals and Applications*. Barcelona, Spain, 2017.

[50] Q. Ren, Y. Dong, and T. Yu. "Numerical modeling of concrete hydraulic fracturing with extended finite element method". In: *Science in China Series E: Technological Sciences* 52.3 (2009), pp. 559–565.

[51] G. Golewski, P. Golewski, and T. Sadowski. "Numerical modelling crack propagation under Mode II fracture in plain concretes containing siliceous fly-ash additive using XFEM method". In: *Computational Materials Science* 62 (2012), pp. 75–78.

[52] X. Zhang and T. Q. Bui. "A fictitious crack XFEM with two new solution algorithms for cohesive crack growth modeling in concrete structures". In: *Engineering Computations* 32.2 (2015), pp. 473–497.

[53] Z. P. Bažant. "Instability, ductility, and size effect in strain-softening concrete". In: *ASCE J Eng Mech Div* 102.2 (1976), pp. 331–344.

[54] Z. P. Bazant and T. B. Belytschko. "Wave propagation in a strain-softening bar: exact solution". In: *Journal of Engineering Mechanics* 111.3 (1985), pp. 381–389.

[55] K. Park, G. H. Paulino, and J. Roesler. "Cohesive fracture model for functionally graded er reinforced concrete". In: *Cement and concrete research* 40.6 (2010), pp. 956–965.

[56] S. H. Song, G. H. Paulino, and W. G. Buttlar. "A bilinear cohesive zone model tailored for fracture of asphalt concrete considering viscoelastic bulk material". In: *Engineering Fracture Mechanics* 73.18 (2006), pp. 2829–2848.

[57] J. Wang. "Cohesive zone model of intermediate crack-induced debonding of FRP-plated concrete beam". In: *International journal of solids and structures* 43.21 (2006), pp. 6630–6648.

[58] G. H. Paulino, S. H. Song, and W. G. Buttlar. "Cohesive zone modeling of fracture in asphalt concrete". In: *Proc., 5th RILEM International Conference on Cracking in Pavements: Mitigation, Risk Assessment, and Prevention*. 2004, pp. 63–70.

[59] K. Park and G. H. Paulino. "Cohesive zone models: a critical review of traction-separation relationships across fracture surfaces". In: *Applied Mechanics Reviews* 64.6 (2011), p. 060802.

[60] P. Grassl and M. Jirásek. "Plastic model with non-local damage applied to concrete". In: *International Journal for Numerical and Analytical Methods in Geomechanics* 30.1 (2006), pp. 71–90.

[61] G. Pijaudier-Cabot and Z. P. Bažant. "Nonlocal damage theory". In: *Journal of engineering mechanics* 113.10 (1987), pp. 1512–1533.

[62] M. Jirásek. "Non-local damage mechanics with application to concrete". In: *Revue française de génie civil* 8.5-6 (2004), pp. 683–707.

[63] Z. Bazant and B. Oh. "Crack band theory for fracture of concrete". In: *Materieaux and Structures* 16 (1983), pp. 155–77.

[64] R. De Borst and P. Nauta. "Non-orthogonal cracks in a smeared finite element model". In: *Engineering Computations* 2.1 (1985), pp. 35–46.

[65] O. Dahlblom and N. S. Ottosen. "Smeared crack analysis using generalized fictitious crack model". In: *Journal of engineering mechanics* 116.1 (1990), pp. 55–76.

[66] R. Faria, J. Oliver, and M. Cervera. "A strain-based plastic viscous-damage model for massive concrete structures". In: *International journal of solids and structures* 35.14 (1998), pp. 1533–1558.

[67] E. Benvenuti, A. Tralli, and G. Ventura. "A regularized XFEM model for the transition from continuous to discontinuous displacements". In: *International Journal for Numerical Methods in Engineering* 74.6 (2008), pp. 911–944.

[68] E. Benvenuti, G. Ventura, N. Ponara, and A. Tralli. "Accuracy of three-dimensional analysis of regularized singularities". In: *International Journal for Numerical Methods in Engineering* 101 (2015), pp. 29–53.

[69] S. Osher and J. Sethian. "Fronts Propagating with Curvature Dependent Speed: Algorithms Based on Hamilton-Jacobi Formulations". In: *Journal of Computational Physics* 79 (1988), pp. 12–49.

[70] H. Mihashi and N. Nomura. "Correlation between characteristics of fracture process zone and tension-softening properties of concrete". In: *Nuclear engineering and design* 165.3 (1996), pp. 359–376.

[71] K. Otsuka and H. Date. "Fracture process zone in concrete tension specimen". In: *Engineering Fracture Mechanics* 65.2-3 (2000), pp. 111–131.

[72] B. Ferracuti, M. Savoia, and C. Mazzotti. "Interface law for FRP concrete delamination". In: *Composite Structures* 80 (2007), pp. 523–531.

[73] P. Carrara, D. Ferretti, F. Freddi, and G. Rosati. "Shear tests of carbon fiber plates bonded to concrete with control of snap-back". In: *Engineering Fracture Mechanics* 78 (2011), pp. 2663–2678.

[74] E. Benvenuti. "A regularized XFEM framework for embedded cohesive interfaces". In: *Computer Methods in Applied Mechanics and Engineering* 197.49-50 (2008), pp. 4367–4378.

[75] M. Cervera, M. Chiumenti, and R. Codina. "Mixed stabilized finite element methods in nonlinear solid mechanics: Part ii: Strain localization". In: *Computer Methods in Applied Mechanics and Engineering* 199.37-40 (2010), pp. 2571–2589.

[76] M. A. Crisfield. *Non-linear finite element analysis of solids and structures*. Vol. 1. Wiley New York, 1991.

[77] L. Sluys and R. de Borst. "Computational methods in non-linear solid mechanics". In: *TU Delft* 21 (2001), p. 76.

[78] Intel. *Intel FORTRAN XE Compose numerical library*. 2018. URL: `https://software.intel.com/en-us/parallel-studio-xe/documentation/featured-documentation`.

[79] C. Geuzaine and J.-F. Remacle. "Gmsh: A 3-D finite element mesh generator with built-in pre-and post-processing facilities". In: *International journal for numerical methods in engineering* 79.11 (2009), pp. 1309–1331.

[80] N. Orlando and E. Benvenuti. "Advanced XFEM Simulation of Pull-out and Debonding of Steel Bars and FRP-Reinforcements in Concrete Beams". In: *America Journal of Engineering and Applied Sciences* 9 (2016), pp. 746–754.

[81] E. Benvenuti and N. Orlando. "Effective 3D Regularized Xfem for Pull-Out of Steel Bars in Concrete, bending and Shear Tests on FRP-Reinforced Concrete Beams". In: *7th European Congress on Computational Methods in Applied Sciences and Engineering*. Vol. 2. Crete Island, Greece, 2016, pp. 2726–2733.

[82] J. Xiao and H. Falkner. "Bond behaviour between recycled aggregate concrete and steel rebars". In: *Construction and Building Materials* 21.2 (2007), pp. 395–401.

[83] B. Täljsten. "Strengthening of concrete prisms using the plate-bonding technique". In: *International journal of Fracture* 82.3 (1996), pp. 253–266.

[84] S. E. Ashari and S. Mohammadi. "Delamination analysis of composites by new orthotropic bimaterial extended finite element method". In: *International Journal for numerical methods in engineering* 86.13 (2011), pp. 1507–1543.

[85] L. De Lorenzis. "Some recent results and open issues on interface modeling in civil engineering structures". In: *Materials and structures* 45.4 (2012), pp. 477–503.

[86] K. Benzarti, F. Freddi, and M. Frémond. "A damage model to predict the durability of bonded assemblies. Part I: Debonding behavior of FRP strengthened concrete structures". In: *Construction and building materials* 25.2 (2011), pp. 547–555.

[87] L. De Lorenzis, B. Miller, and A. Nanni. "Bond of FRP laminates to concrete". In: *ACI Materials Journal* 98.3 (2001), pp. 256–264.

[88] E. Martinelli, C. Czaderski, and M. Motavalli. "Modeling in-plane and out-of-plane displacement fields in pull-off tests on FRP strips". In: *Engineering Structures* 33 (2011), pp. 3715–3725.

[89] P. Carrara and D. Ferretti. "A finite-difference model with mixed interface laws for shear tests of FRP plates bonded to concrete". In: *Composites Part B: Engineering* 54 (2013), pp. 329–342.

[90] K. Subramaniam, C. Carloni, and L. Nobile. "Width effect in the interface fracture during shear debonding of FRP sheets from concrete". In: *Engineering Fracture Mechanics* 74 (2007), pp. 578–594.

[91] K. Subramaniam, C. Carloni, and L. Nobile. "An understanding of the width effect in FRP–concrete debonding". In: *Strain* 47.2 (2011), pp. 127–137.

[92] F. Freddi and M. Savoia. "Analysis of FRP–concrete debonding via boundary integral equations". In: *Engineering Fracture Mechanics* 75.6 (2008), pp. 1666–1683.

[93] V. Salomoni, G. Mazzucco, C. Pellegrino, and C. Majorana. "Three-dimensional modelling of bond behaviour between concrete and FRP reinforcement". In: *Engineering Computations* 28.1 (2011), pp. 5–29.

[94] J. Chen and W. Pan. "Three dimensional stress distribution in FRP-to-concrete bond test specimens". In: *Construction and Building Materials* 20.1-2 (2006), pp. 46–58.

[95] P. Neto, J. Alfaiate, and J. Vinagre. "A three-dimensional analysis of CFRP–concrete bond behaviour". In: *Composites Part B: Engineering* 59 (2014), pp. 153–165.

[96] M. J. Chajes, W. W. Finch, T. A. Thomson, et al. "Bond and force transfer of composite-material plates bonded to concrete". In: *Structural Journal* 93.2 (1996), pp. 209–217.

[97] CNR. " CNR 200/2004: Guide for the Design and Construction of Externally Bonded FRP Systems for Strengthening Existing Structures". In: (2004).

[98] T. Triantafillou and N. Plevris. "Strengthening of RC beams with epoxy-bonded fibre-composite materials". In: *Materials and Structures* 25 (1992), pp. 201–211.

[99] O. Buyukozturk, O. Gunes, and E. Karaca. "Progress on understanding debonding problems in reinforced concrete and steel members strengthened using FRP composites". In: *Construction and Building Materials* 18 (2004), pp. 9–19.

[100] C. Czaderski, K. Soudki, and M. Motavalli. "Front and side view image correlation measurements on FRP to concrete pull-off bond tests". In: *Journal of Composites for Construction* 14 (2010), pp. 451–463.

[101] T. Smith and J. Teng. "Interfacial stresses in plated beams". In: *Engineering structures* 23 (2001), pp. 857–871.

[102] T. Smith and J. Teng. "FRP-strengthened RC beams I: review of debonding strength models". In: *Engineering structures* 24 (2002), pp. 385–395.

[103] M. Aram, C. Czaderski, and M. Motavalli. "Debonding failure modes of flexural FRP-strengthened RC beams". In: *Composites part B: engineering* 39 (2008), pp. 826–841.

[104] H. Garden and L. Hollaway. "An experimental study of the influence of plate end anchorage of carbon fibre composite plates used to strengthen reinforced concrete beams". In: *Composite Structures* 42 (1998), pp. 175–188.

[105] H. Thomsen, E. Spacone, S. Limkatanyu, and G. Camata. "Failure Mode Analyses of Reinforced Concrete Beams Strengthened in Flexure with Externally Bonded Fiber-Reinforced Polymers". In: *Journal of Composites for Construction* 8 (2004), pp. 123–131.

[106] H. Rahimi and A. Hutchinson. "Concrete beams strengthened with externally bonded FRP plates". In: *Journal of composites for construction* 5 (2001), pp. 44–56.

[107] M. Maalej and K. Leong. "Effect of beam size and FRP thickness on interfacial shear stress concentration and failure mode of FRP-strengthened beams". In: *Composites Science and Technology* 65 (2005), pp. 1148–1158.

[108] X. Lu, J. Teng, L. Ye, and J. Jiang. "Intermediate crack debonding in FRP-strengthened RC beams: FE analysis and strength model". In: *Journal of Composites for Construction* 11 (2007), pp. 161–174.

[109] M. Achintha and C. Burgoyne. "Fracture energy of the concrete FRP interface in strengthened beams". In: *Engineering Fracture Mechanics* 110 (2013), pp. 38–51.

[110] N. Attari, S. Amziane, and M. Chemrouk. "Flexural strengthening of concrete beams using CFRP, GFRP and hybrid FRP sheets". In: *Construction and Building Materials* 37 (2012), pp. 746–757.

[111] J. Barros and J. Figueiras. "Flexural behavior of SFRC: testing and modeling". In: *Journal of Materials in Civil Engineering* 11 (1999), pp. 331–339.

[112] B. Täljsten. "Strengthening of beams by plate bonding". In: *Journal of Materials in Civil Engineering* 9 (1997), pp. 206–212.

[113] O. Rabinovitch and Y. Frostig. "Closed-form high-order analysis of RC beams strengthened with FRP strips". In: *Journal of Composites for Construction* 4 (2000), pp. 65–74.

[114] J. Teng, J. Chen, S. Smith, and L. Lam. *FRP: strengthened RC structures*. John Wiley and Sons Ltd, 2002, p. 266.

[115] A. Ingraffea and V. Saouma. "Numerical modelling of discrete crack propagation in reinforced and plain concrete". In: *In Fracture Mechanics of Concrete* (1985). Ed. by M. N. P. Dordrecht, pp. 171–225.

[116] Z. Yang, J. Chen, and D. Proverbs. "Finite element modelling of concrete cover separation failure in FRP plated RC beams". In: *Construction and Building Materials* 17 (2003), pp. 3–13.

[117] G. Barenblatt. "The mathematical theory of equilibrium cracks in brittle fracture". In: *Advances in Applied Mechanics* 7 (1962), pp. 55–129.

[118] A. Hillerborg, M. Modeer, and P. Petersson. "Analysis of crack formation and crack growth in concrete by means of fracture mechanics and finite elements". In: *Cement and Concrete Research* 6 (1976), pp. 773–782.

[119] A. Needleman. "A continuum model for void nucleation by inclusion debonding". In: *Journal of Applied Mechanics* 54 (1987), pp. 525–531.

[120] X. Lu, J. Teng, L. Ye, and J. Jiang. "Bond-slip models for FRP sheets/plates bonded to concrete". In: *Engineering Structures* 27 (2005), pp. 920–937.

[121] G. Chen, J. Chen, and J. Teng. "On the finite element modelling of RC beams shear-strengthened with FRP". In: *Construction and Building Materials* 32 (2012), pp. 13–26.

[122] G. Chen, J. Teng, J. Chen, and Q. Xiao. "Finite element modeling of debonding failures in FRP-strengthened RC beams: A dynamic approach". In: *Computers and Structures* 158 (2015), pp. 167–183.

[123] Y. Rashid. "Analysis of reinforced concrete pressure vessels". In: *Nuclear Engineering and Design* 7 (1968), pp. 334–344.

[124] N. Pešić and K. Pilakoutas. "Concrete beams with externally bonded flexural FRP-reinforcement: analytical investigation of debonding failure". In: *Composites Part B: Engineering* 34 (2003), pp. 327–338.

[125] N. Kishi, G. Zhang, and H. Mikami. "Numerical cracking and debonding analysis of RC beams reinforced with FRP sheet". In: *Journal of Composites for Construction* 9 (2005), pp. 507–514.

[126] G. Camata, E. Spacone, and R. Zarnic. "Experimental and nonlinear finite element studies of RC beams strengthened with FRP plates". In: *Composites Part B: Engineering* 38 (2007), pp. 277–288.

[127] G. Chen, J. Teng, and J. Chen. "Finite-element modeling of intermediate crack debonding in FRP-plated RC beams". In: *Journal of Composites for Construction* 15 (2010), pp. 339–353.

[128] N. Orlando and E. Benvenuti. "Advance Simulation of Debonding of FRP Plates from Steel-Fiber-Reinforced-Concrete beams under bending". In: *25th International Conference on Composites/Nano Engineering*. Roma, Italy, 2017.

[129] E. Benvenuti and N. Orlando. "Accurate XFEM simulation of failure and debonding of FRP-plate-reinforced beams of steel fiber reinforced concrete". In: *14th National Conference of the Aimeta*. Salerno, Italy, 2017.

[130] E. Benvenuti and N. Orlando. "Regularized XFEM for the failure analysis of FRP-reinforced concrete beams under bending". In: *5th International Conference on Computational Computational Modeling of Fracture and Failure of Materials and Structures*. Nantes, France, 2017.

[131] E. Benvenuti and N. Orlando. "Continuous-Discontinuous XFEM-based 3D procedure for Failure and Debonding of FRP-reinforced beams". In: *14th International Conference on Computational Plasticity, Fundamentals and Applications*. Barcelona, Spain, 2017.

[132] F. Altun, T. Haktanir, and K. Ari. "Effects of steel fiber addition on mechanical properties of concrete and RC beams". In: *Construction and Building Materials* 21 (2007), pp. 654–661.

[133] A. Carpinteri, E. Cadamuro, and G. Ventura. "Fiber-reinforced concrete in flexure: a cohesive/overlapping crack model application". In: *Materials and Structures* 48.1-2 (2015), pp. 235–247.

[134] D. Fanella and A. Naaman. "Stress-strain properties of fiber reinforced mortar in compression." In: *Journal of The American Concrete Institute* 82 (1985), pp. 475–483.

[135] A. Ezeldin and P. Balaguru. "Normal-and high-strength fiber-reinforced concrete under compression". In: *Journal of materials in civil engineering* 4 (1992), pp. 415–429.

[136] D. Özcan, A. Bayraktar, A. Şahin, T. Haktanir, and T. Türker. "Experimental and finite element analysis on the steel fiber-reinforced concrete (SFRC) beams ultimate behavior". In: *Construction and Building Materials* 23.2 (2009), pp. 1064–1077.

[137] E. Iarve. "Mesh independent modelling of cracks by using higher order shape functions". In: *International Journal for Numerical Methods in Engineering* 56 (2003), pp. 869–882.

[138] E. Iarve, M. Gurvich, and D. Mollenhauer. "Mechanism-Based Direct Simulation of Tensile Failure in Composite Laminates". In: *51st AIAA/ASME/ASCE/AHS/ASC Structures, Structural Dynamics, and Materials Conference. Orlando, Florida*. 2010.

[139] D. Motamedi and S. Mohammadi. "Fracture analysis of composites by time independent moving-crack orthotropic XFEM". In: *International Journal of Mechanical Sciences* 54 (2012), pp. 20–37.

[140] Y. Wang and H. Waisman. "Progressive delamination analysis of composite materials using XFEM and a discrete damage zone model". In: *Computational Mechanics* 55 (2015), pp. 1–26.

[141] C.-F. M. Code. "Model code for concrete structures". In: *Bulletin D'Information* 117-E (1990).

[142] T. Wee, M. Chin, and M. Mansur. "Stress-strain relationship of high-strength concrete in compression". In: *Journal of Materials in Civil Engineering* 8 (1996), pp. 70–76.

[143] J. Thomas and A. Ramaswamy. "Mechanical properties of steel fiber-reinforced concrete". In: *Journal of materials in civil engineering* 19 (2007), pp. 385–392.

[144] J. Yin and Z. Wu. "Structural performances of short steel-fiber reinforced concrete beams with externally bonded FRP sheets". In: *Construction and Building Materials* 17 (2003), pp. 463–470.

[145] L. Li, Y. Guo, and F. Liu. "Test analysis for FRC beams strengthened with externally bonded FRP sheets". In: *Construction and Building Materials* 22 (2008), pp. 315–323.

[146] C. Qian and P. Stroeven. "Fracture properties of concrete reinforced with steel-polypropylene hybrid fibres". In: *Cement and Concrete Composites* 22 (2000), pp. 343–351.

[147] Z. Bažant and P. Pfeiffer. "Shear fracture tests of concrete". In: *Matériaux et Constructions* 19 (1986), pp. 111–121.

[148] E. Benvenuti, G. Borino, and A. Tralli. "A thermodynamically consistent nonlocal formulation for damaging materials". In: *European Journal of Mechanics - A Solids* 21 (2002), pp. 535–553.

[149] C. Comi. "A non-local model with tension and compression damage mechanisms". In: *European Journal of Mechanics - A/Solids* 20 (2001), pp. 1–22.

[150] B. Patzák and M. Jirásek. "Process zone resolution by extended finite elements". In: *Engineering Fracture Mechanics* 70 (2003), pp. 957–977.

[151] J. Rots, P. Nauta, G. Kuster, and J. Blaauwendraad. "Smeared crack approach and fracture localization in concrete". In: *HERON* 30 (1985), pp. 1–48.

[152] J. Gálvez, M. Elices, G. Guinea, and J. Planas. "Mixed mode fracture of concrete under proportional and nonproportional loading". In: *International Journal of Fracture* 94 (1998), pp. 267–284.

[153] J. Lemaitre. "A continuous damage mechanics model for ductile fracture". In: *Transactions of the ASME Journal of Engineering Materials and Technology* 107 (1985), pp. 83–89.

[154] W. Ramberg and W. Osgood. "Description of Stress-Strain Curves by Three Parameters". In: *technical notes. Washington D.C: National Advisory Committee for Aeronautics* 902 (1943), pp. 1–29.

[155] J. Barros, S. D. JE, and J. Lima. "Efficacy of CFRP-based techniques for the flexural and shear strengthening of concrete beams". In: *Cement and Concrete Composites* 29 (2007), pp. 203–217.

[156] NTC08. "Norme tecniche per le costruzioni in zone sismiche". In: *Ministerial Decree DM* 14.08 (2008), pp. 9–04.

[157] FIB. "Externally bonded FRP reinforcement for RC structures". In: *Bulletin Fédération Internationale Du Béton* 14 (2001), pp. 1–138.

[158] W. Handbook. "Wood handbook-Wood as an engineering material". In: *General Technical Report FPL-GTR-190, Department of Agriculture, Forest Service, Forest Products Laboratory: USA* (2010).

[159] S. Franke. *Zur Beschreibung des Tragverhaltens von Holz unter Verwendung eines photogrammetrischen Messsystems*. Verlag der Bauhaus-Univ., 2008.

[160] J. Poulsen. *Compression in clear wood*. Technical University of Denmark, 1998.

[161] S. Franke, B. Franche, K.-U. Schoner, and K. Rautenstrauch. "The strength behavior of wood in experiment and simulations". In: *Proceedings of the 10th World Conference on Timber Engineering (WCTE 2008), Miyazaki, Japan*. 2008.

[162] K. Persson. *Micromechanical modelling of wood and fibre properties*. Lund University, Department of Mechanics and Materials, 2000.

[163] K. Murata, H. Nagai, and T. Nakano. "Estimation of width of fracture process zone in spruce wood by radial tensile test". In: *Mechanics of Materials* 43.7 (2011), pp. 389–396.

[164] M. Lukacevic, W. Lederer, and J. Füssl. "A microstructure-based multisurface failure criterion for the description of brittle and ductile failure mechanisms of clear-wood". In: *Engineering Fracture Mechanics* 176 (2017), pp. 83–99.

[165] S. W. Tsai and E. M. Wu. "A general theory of strength for anisotropic materials". In: *Journal of composite materials* 5.1 (1971), pp. 58–80.

[166] R. Hill. "A theory of the yielding and plastic flow of anisotropic metals". In: *Proc. R. Soc. Lond. A* 193.1033 (1948), pp. 281–297.

[167] A. Bouchair and A. Vergne. "An application of the Tsai criterion as a plastic flow law for timber bolted joint modelling". In: *Wood science and technology* 30.1 (1995), pp. 3–19.

[168] P. L. Clouston and F. Lam. "Computational modeling of strand-based wood composites". In: *Journal of Engineering Mechanics* 127.8 (2001), pp. 844–851.

[169] R. De Borst and P. H. Feenstra. "Studies in anisotropic plasticity with reference to the Hill criterion". In: *International journal for numerical methods in engineering* 29.2 (1990), pp. 315–336.

[170] O. Hoffman. "The brittle strength of orthotropic materials". In: *Journal of Composite Materials* 1.2 (1967), pp. 200–206.

[171] B. Xu, M. Taazount, A. Bouchaïr, and P. Racher. "Numerical 3D finite element modelling and experimental tests for dowel-type timber joints". In: *Construction and building materials* 23.9 (2009), pp. 3043–3052.

[172] P. Mackenzie-Helnwein, J. Eberhardsteiner, and H. A. Mang. "A multi-surface plasticity model for clear wood and its application to the finite element analysis of structural details". In: *Computational Mechanics* 31.1-2 (2003), pp. 204–218.

[173] J. Schmidt and M. Kaliske. "Models for numerical failure analysis of wooden structures". In: *Engineering Structures* 31.2 (2009), pp. 571–579.

[174] C. Sandhaas, J.-W. Van de Kuilen, and H. J. Blass. "Constitutive model for wood based on continuum damage mechanics". In: *WCTE, World conference on timber engineering, Auckland, New Zealand, 15-19 July 2012*. 2012.

[175] L. F. Sirumbal-Zapata, C. Málaga-Chuquitaype, and A. Y. Elghazouli. "A three-dimensional plasticity-damage constitutive model for timber under cyclic loads". In: *Computers & Structures* 195 (2018), pp. 47–63.

[176] A. Khennane, M. Khelifa, L. Bleron, and J. Viguier. "Numerical modelling of ductile damage evolution in tensile and bending tests of timber structures". In: *Mechanics of Materials* 68 (2014), pp. 228–236.

[177] G. Tampone and N. Ruggieri. "State-of-the-art technology on conservation of ancient roofs with timber structure". In: *Journal of Cultural Heritage* 22 (2016), pp. 1019–1027.

[178] C. Alessandri and V. Mallardo. "Structural assessments of the Church of the Nativity in Bethlehem". In: *Journal of Cultural Heritage* 13.4 (2012), e61–e69.

[179] R. Bainbridge, C. Mettem, K. Harvey, and M. Ansell. "Bonded-in rod connections for timber structures—development of design methods and test observations". In: *International journal of adhesion and adhesives* 22.1 (2002), pp. 47–59.

[180] R. Steiger, E. Serrano, M. Stepinac, V. Rajcic, C. O'Neill, D. McPolin, and R. Widmann. "Reinforcement with glued-in rods". In: *Reinforcement of Timber Structures, A State-of-the-art Report* (2015), pp. 133–159.

[181] M. A. Parisi and M. Piazza. "Restoration and strengthening of timber structures: Principles, criteria, and examples". In: *Practice periodical on structural design and construction* 12.4 (2007), pp. 177–185.

[182] M. Del Senno, M. Piazza, and R. Tomasi. "Axial glued-in steel timber joints—experimental and numerical analysis". In: *Holz als Roh-und Werkstoff* 62.2 (2004), pp. 137–146.

[183] R. Steiger, E. Gehri, and R. Widmann. "Pull-out strength of axially loaded steel rods bonded in glulam parallel to the grain". In: *Materials and structures* 40.1 (2007), pp. 69–78.

[184] G. Tlustochowicz, E. Serrano, and R. Steiger. "State-of-the-art review on timber connections with glued-in steel rods". In: *Materials and structures* 44.5 (2011), pp. 997–1020.

[185] J. Eberhardsteiner. *Mechanisches Verhalten von Fichtenholz: Experimentelle Bestimmung der biaxialen Festigkeitseigenschaften*. Springer-Verlag, 2013.

[186] T. Vallée, T. Tannert, and S. Fecht. "Adhesively bonded connections in the context of timber engineering–A Review". In: *The Journal of Adhesion* 93.4 (2017), pp. 257–287.

[187] M. Stepinac, F. Hunger, R. Tomasi, E. Serrano, V. Rajcic, and J.-W. van de Kuilen. "Comparison of design rules for glued-in rods and design rule proposal for implementation in European standards". In: *Proceedings of CIB-W18 meeting*. Vol. 46. 2013.

[188] E. C. for Standardization (CEN). *Eurocode 5: Design of timber structures–Part 1-1: General–Common rules and rules for buildings*. 2004.

[189] B. Pizzo, M. Gavioli, and M. P. Lauriola. "Evaluation of a design approach to the on-site structural repair of decayed old timber end beams". In: *Engineering Structures* 48 (2013), pp. 611–622.

[190] C. O'Neill, D. McPolin, S. E. Taylor, T. Martin, and A. M. Harte. "Glued-in basalt FRP rods under combined axial force and bending moment: An experimental study". In: *Composite Structures* 186 (2018), pp. 267–273.

[191] N. Gattesco, A. Gubana, M. Buttazzi, and M. Melotto. "Experimental investigation on the behavior of glued-in rod joints in timber beams subjected to monotonic and cyclic loading". In: *Engineering Structures* 147 (2017), pp. 372–384.

[192] A. Susini. *Ripristino strutturale di travi lignee: indagine sugli interventi di ricostruzione fi testata con protesi in legno connessa con barre incollate*. Firenze, 2013.

[193] B. Pizzo and M. P. Lauriola. "Repair of timber end-beams: some operational aspects". In: *Protection of Historical Buildings: Proceedings of the International Conference on Protection of Historical Buildings, PROHITECH 09, Rome, Italy, 21-24 june 2009: PROHITECH 09*. 2009, pp. 397–402.

[194] B. Pizzo and K. Schober. "On site interventions on decayed beam ends". In: *Core document of COST action E* 34 (2008).

[195] M. Kaliske, C. Jenkel, S. Saft, and E. Resch. "Computational models for wooden structures". In: *Computational Technology Reviews* 2 (2010), pp. 145–176.

[196] D. Konopka, C. Gebhardt, and M. Kaliske. "Numerical modelling of wooden structures". In: *Journal of Cultural Heritage* 27 (2017), S93–S102.

[197] N. Orlando, C. Gebhardt, M. Kaliske, and E. Benvenuti. "A Regularized eXtended Finite Element Framework coupled to a multi-surface damage-plasticity for wooden beams". In: *GIMC-GMA*. Ferrara, Italy, 2018.

[198] H. Danielsson and P. J. Gustafsson. "A three dimensional plasticity model for perpendicular to grain cohesive fracture in wood". In: *Engineering Fracture Mechanics* 98 (2013), pp. 137–152.

[199] M. De Moura, J. Morais, and N. Dourado. "A new data reduction scheme for mode I wood fracture characterization using the double cantilever beam test". In: *Engineering Fracture Mechanics* 75.13 (2008), pp. 3852–3865.

[200] N. Dourado, S. Morel, M. De Moura, G. Valentin, and J. Morais. "Comparison of fracture properties of two wood species through cohesive crack simulations". In: *Composites Part A: Applied science and manufacturing* 39.2 (2008), pp. 415–427.

[201] K. Rautenstrauch, B. Franke, S. Franke, and K. Schober. "A new design approach for end-notched beams: View in code". In: *Paper No. CIB-W18/41-6-2, Proc., Meeting*. Vol. 41. 2008.